JPRS L/10646

8 July 1982

USSR Report

PHYSICS AND MATHEMATICS

(FOUO 5/82)

FBIS FOREIGN BROADCAST INFORMATION SERVICE

NOTE

JPRS publications contain information primarily from foreign newspapers, periodicals and books, but also from news agency transmissions and broadcasts. Materials from foreign-language sources are translated; those from English-language sources are transcribed or reprinted, with the original phrasing and other characteristics retained.

Headlines, editorial reports, and material enclosed in brackets [] are supplied by JPRS. Processing indicators such as [Text] or [Excerpt] in the first line of each item, or following the last line of a brief, indicate how the original information was processed. Where no processing indicator is given, the information was summarized or extracted.

Unfamiliar names rendered phonetically or transliterated are enclosed in parentheses. Words or names preceded by a question mark and enclosed in parentheses were not clear in the original but have been supplied as appropriate in context. Other unattributed parenthetical notes within the body of an item originate with the source. Times within items are as given by source.

The contents of this publication in no way represent the policies, views or attitudes of the U.S. Government.

APPROVED FOR RELEASE: 2007/02/09: CIA-RDP82-00850R000500080020-6

JPRS L/10646

8 July 1982

USSR REPORT

PHYSICS AND MATHEMATICS

(FOUO 5/82)

CONTENTS

CRYSTALS AND SEMICONDUCTORS

FOUR-WAVE ACOUSTOELECTRONIC INTERACTION

Leningrad PIS'MA V ZHURNAL TEKHNICHESKOY FIZIKI in Russian Vol 8, No 3, 12 Feb 82 (manuscript received 30 Sep 81) pp 133-136

[Article by L. A. Slavutskiy and I. Yu. Solodov, Moscow State University imeni M. V. Lomonosov]

[Text] Acoustoelectric nonlinear effects are the basis for electronic devices used in convolution, correlation and other forms of signal processing [Ref. 1]. Such effects are usually studied on the basis of square-law nonlinearity of a medium with consideration of only three-wave interaction of acoustic waves. A report was given in Ref. 2 on the use of four-wave interaction of surface waves with an electric field for signal storage. Our paper is the first to report experimental observation of four-wave interaction of surface and body acoustic waves enabling realization of new functional operations: triple convolution and correlation of radio signals.

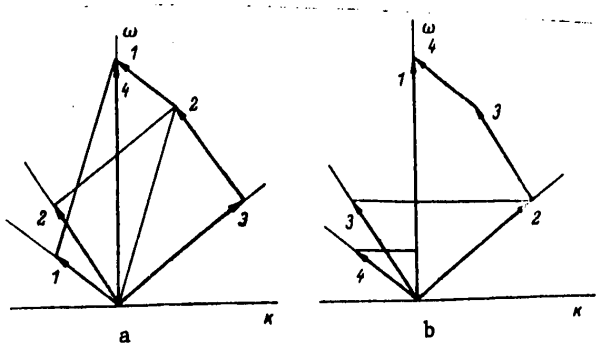

Fig. 1. ω-k diagrams of triple convolution (a) and correlation (b)

Fig. 1a shows an ω-k diagram of four-wave interaction of acoustic surface and body waves. The two dispersion branches of the diagram correspond to body (longitudinal) and surface waves with phase velocities that satisfy the approximate condition $c_{abw} \approx 2c_{asw}$. In the presence of the piezoelectric effect, the axis k = 0 of the diagram is a third dispersion branch of the system in which electromagnetic perturbations may occur. Conditions of synchronism with four-wave interaction take the form $k_4 = k_1 + k_2 + k_3$, $\omega_4 = \omega_1 + \omega_2 + \omega_3$, and

with consideration of the possibility of interaction of opposed acoustic waves are illustrated in Fig. 1a. It is clear from the diagram that when $\omega_2 = \omega_3 = 2\omega_1$ and $c_{abw} \cong 2c_{asw}$ we have $k_4 = 0$ and $\omega_4 = 5\omega_1$. Consequently, when a surface wave interacts with an accompanying body wave [Ref. 1, 2] and with an opposed surface wave [Ref. 3], for which $\omega_2 = \omega_3 = 2\omega_1$, a spatially homogeneous electric field is formed with frequency $5\omega_1$. Such interaction can be realized under conditions of cubic nonlinearity of the medium, or through two sequential three-wave processes on a quadratic nonlinearity.

The reverse third-order nonlinear effect -- generation of a surface wave with frequency ω_1 [Ref. 4] as a result of interaction of an electric field on frequency $5\omega_1$ [Ref. 1] with opposed longitudinal [Ref. 3] and surface [Ref. 2] waves ($\omega_2 = \omega_3 = 2\omega_1$) -- is shown in Fig. 1b. The conditions of synchronism for this process can be written in the following form: $\vec{k}_4 = \vec{k}_1 - \vec{k}_2 - \vec{k}_3$, $\omega_4 = \omega_1 - \omega_2 - \omega_3$.

The described four-wave processes were experimentally observed under conditions of acoustoelectric nonlinearity of a laminar $LiNbO_3$-Si structure. Acoustic surface waves with frequencies of 15 and 30 MHz were excited in yz-$LiNbO_3$ by interdigital transducers in the pulse mode (conversion losses of the order of 10 dB, band 3-5 MHz). A 30 MHz longitudinal acoustic wave pulse was excited by half-wave resonant transducers made of the same material and cemented to the end face of the specimen (losses ≅15 dB, band ≅3 MHz). To accomplish interaction of acoustic body and surface waves, the end face of the backing was cut at an angle of ≅10° to the axis y-$LiNbO_3$. In the region of the trail of the longitudinal wave on the surface of the backing between the surface wave transducers was a p-Si specimen measuring 5 x 20 x 2 mm with conductivity of $\cong 10^{-3}$ $(\Omega \cdot cm)^{-1}$. The resultant electric field was taken off by using solid metal electrodes on the upper surface of the semiconductor and the bottom plane of the backing; the signal from the electrodes went to the input of an amplifier tuned to a frequency of 75 MHz. Upon matching of time synchronization of the pulses to correspond to meeting of three interacting waves under the semiconductor, the signal of their interaction (triple convolution) was registered at the amplifier output.

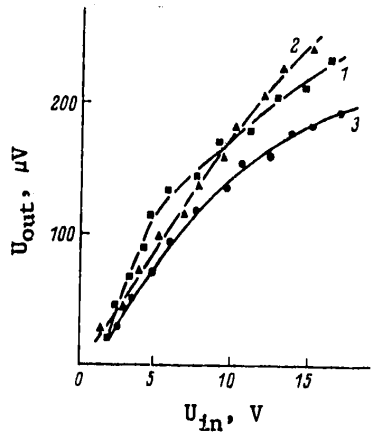

Fig. 2. Triple convolution voltage as a function of the voltage across the transducers: 1--transducer for 15 MHz surface waves; 2--body-wave transducer; 3--transducer for 30 MHz surface waves

Fig. 2 shows the experimentally obtained dependences of the triple convolution signal voltage amplitude on the voltage across each of the acoustic wave transducers (with voltage across the two others held constant). We can see from this figure that at an input voltage of ≅17 V, the output signal of the triple convolution has an amplitude of the order of 300 μV and varies linearly with increasing input signals up to 5 V. That there is a region of saturation of the curves on Fig. 2 can apparently be attributed to effective energy exchange as a result of three-wave interactions. Typically, since the efficiency of such processes is higher for surface waves [Ref. 3], it is for waves of this type that saturation regions appear on Fig. 2. We should also take note of rather high efficiency of the triple convolution process. At input voltages of 15 V, external losses to convolution $B = 20 \lg U_4/U_1$ do not exceed 90 dB.

We used the experimental technique described above to observe the third-order inverse nonlinear effect -- generation of surface waves as a result of four-wave interaction. Since the signal of the inverse surface wave is a function of acoustic correlation of the interacting waves, such a process represents triple correlation. The dependences on input voltage levels in this case are analogous to those shown on Fig. 2, and have characteristic saturation regions. External losses of triple correlation are comparatively low ($U_4 \cong 1$ mV at $U_1 \sim U_2 \sim U_3 \cong 10$ V), and amounted to ≅80 dB.

This level of effectiveness of four-wave interaction is completely acceptable in practical acoustoelectronics. Therefore the observed third-order nonlinear effects may find practical application in electronic devices that are associated with reciprocal processing of several signals.

REFERENCES

1. Kayno, G., TIIER, Vol 64, 1976, p 188.

2. Ralston, R. W., Stern, E., APPL. PHYS. LETT., Vol 35, No 2, 1979, p 150.

3. Bozhenko, V. V., Lyamov, V. Ye., Solodov, I. Yu., ZHURNAL TEKHNICHESKOY FIZIKI, Vol 51, No 3, 1981, p 650.

6610
CSO: 1862/139

FLUID DYNAMICS

UDC 621.373.826:533.951

SUBSONIC RADIATION WAVES IN AIR

Moscow KVANTOVAYA ELEKTRONIKA in Russian Vol 9, No 3(117), Mar 82 (manuscript received 6 Mar 81, after revision 25 Jun 81) pp 615-618

[Article by T. V. Loseva and I. V. Nemchinov, Institute of Physics of the Earth imeni O. Yu. Shmidt, USSR Academy of Sciences, Moscow]

[Text] It is shown that fast laser emission absorption waves (with pressure in the shock wave generated by the expanding plasma much higher than atmospheric) with predominant role of plasma self-radiation in the mechanism of propagation can exist at flux densities at least an order of magnitude lower than those at which they have been experimentally observed heretofore. The evolution of such subsonic radiation waves from the initial plasma layer is traced by numerical calculations of the corresponding spectral radiation-gasdynamic problem, and the authors determine the way that their major parameters depend on time (up to the quasi-steady stage of propagation) and on flux density of more than 0.1 MW/cm^2 for a CO_2 laser and 1 MW/cm^2 for a neodymium laser.

In Ref. 1, 2, an experimental and theoretical examination was made of the propagation of a laser spark in air of normal density in the slow-burning mode at rates of the order of 10 m/s. It was assumed that flame front propagation is due to ordinary heat conduction. For small radii of the laser beam (of the order of 1 mm) plasma radiation leads only to energy losses from the plasma layer.

It was shown in Ref. 3, 4 that with a sufficiently large irradiation spot size, plasma propagation relative to the barrier at which it arises will be determined by a hydrodynamic mechanism: as the plasma is heated, it expands and produces a shock wave. The rate of expansion of the hot plasma, which in essence displaces the cool air, may be fairly high, and pressure is correspondingly appreciable

$$v = 1{,}0 q_0^{1/3} \delta^{-1/3}, \quad p = 15 q_0^{2/3} \delta^{1/3}. \qquad (1)$$

Here v is plasma velocity, km/s, q_0 is laser emission flux density, MW/cm^2, δ is the ratio of air density to its normal value, p is pressure in bars.

Since the pressure in the plasma may be much greater than atmospheric, the optical thickness of the plasma layer will be large (for geometric dimensions that are not too small), and the self-radiation of this layer will determine the process of capture of gas particles by the plasma -- mass flow through the absorption wavefront, and with it the maximum temperature. The ideas of subsonic radiation waves [Ref. 3, 4] have been experimentally confirmed [Ref. 5-9]. Fast absorption waves (with velocities of more than 1 km/s) have been studied at $q_0 > 10$ MW/cm^2 for radiation with wavelength $\lambda = 1$ μm [Ref. 5-7] and at $q_0 > 1$ MW/cm^2 for $\lambda = 10$ μm [Ref. 8, 9]. Our estimates and calculations have shown that fast absorption waves generally speaking may exist at even lower radiation flux densities.

The problem of propagation of a subsonic radiation wave was solved by a method analogous to Ref. 3, 4. Detailed consideration was taken of the spectral makeup of the radiation, and detailed tables of absorption coefficients were used [Ref. 10]. Since analysis of Ref. 1, 2 shows that heat conductivity at low radiation flux densities may play an appreciable role, in contrast to Ref. 3, 4, molecular and electronic thermal conductivity were taken into consideration in addition to energy transport by hydrodynamic means and by radiation, using coefficients determined from tables of Ref. 11, 12. The process of plasma origination was not considered in this work. It was assumed that at the initial instant in the air above the barrier there existed a plasma layer with initial temperature of 1 eV at a pressure determined by relation (1). The initial optical thickness of the layer for radiation with $\lambda = 10$ μm at a mass of 20 μg/cm^2 is approximately 0.2-0.3.

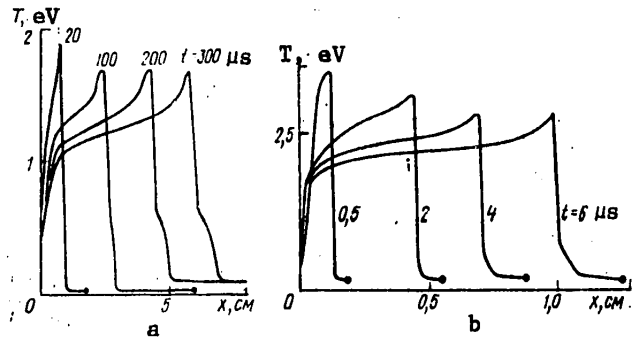

Fig. 1

The spatial distribution of temperature T at different times t is shown in Fig. 1 for a CO_2 laser at $q_0 = 0.1$ (a) and 5 MW/cm^2 (b). The qualitative pattern of the process of plasma heating and absorption wave advancement is the same for these values of q_0 and for intermediate values. Laser radiation is absorbed in a comparatively narrow zone. The gas is heated at temperatures below 1.1 eV by radiation of the continuous spectrum emitted by the plasma. At higher temperatures, absorption of laser radiation plays a major role. It was found that heat conduction does not play an appreciable role, which was determined both by analysis of profiles of temperature and energy release due to heat conduction and radiation effects, and by direct comparison of calculation with and without consideration of thermal conductivity. Radiation effects play a decisive part in advancement of the absorption wave.

Pressure and velocity in the steady state at $q_0 = 0.1$-5 MW/cm^2 are determined by relation (1) with accuracy of ±20%. The spatial maximum of temperature T_m, continuous-spectrum radiation flux density de-excited from the plasma to the wall q_w, and also the flux density emanating from the plasma toward the laser are similar functions of the specific energy E supplied up to the given instant t for all values of q_0 in the range considered. Fig. 2 shows curves of $T_m(E)$ for various q_0.

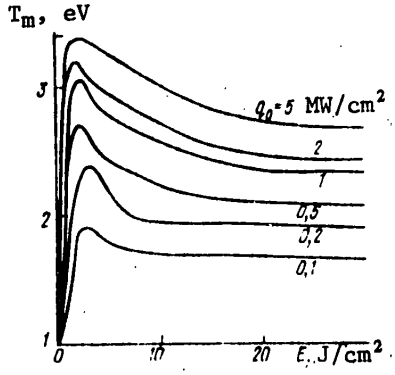

Fig. 2

At $E \gtrsim 20$ J/cm^2, the pattern becomes quasi-steady. Maximum temperatures in the quasi-steady stage change comparatively weakly with q_0:

$$T_m = [1 + 0.25 \lg (q_0/1 \text{ MW} \cdot \text{cm}^{-2})]2.3 \text{ K}. \quad (2)$$

Mass flowrate M is nearly proportional to q_0: at $q_0 = 0.1$ MW/cm^2 we have $M = 0.7$ g/cm$^2 \cdot$s. Total energy losses from the plasma layer to radiation increase with decreasing laser emission flux density and reach 45% at $q_0 = 0.1$ MW/cm^2. The values of M and T_m at $q_0 = 0.2$ MW/cm^2 (1.3 g/cm$^2 \cdot$s and 1.9 eV) and at $q_0 = 5$ MW/cm^2 (27 g/cm$^2 \cdot$s and 2.8 eV) differ somewhat from the values given in Ref. 4. The differences can be attributed to the fact that in Ref. 4 for these values of q_0 the problem was solved only in the multigroup approximation. At $q_0 = 1$-5 MW/cm^2 the calculated values of the parameters of the subsonic radiation wave are fairly close to the experimental values [Ref. 8, 9], especially if one considers the influence of the spike at the beginning of the CO_2 laser radiation pulse and the corresponding effects of unsteadiness. In the experiments of Ref. 13 at $q_0 \geqslant 0.2$ MW/cm^2 with millisecond pulses emitted by a CO_2 laser, propagation of slow combustion waves was observed. This is due to the small size of the irradiated spot ($\leqslant 1$ cm) and the correspondingly strong influence of two-dimensionality in expansion of the plasma jet, leading to nearly atmospheric pressure.

For large spots and shorter pulse durations after completion of the stage of plasma origination, the pattern should be close to that described by our calculations, which are in the nature of a theoretical prediction for such low flux densities and conditions of plane geometry of plasma expansion. In the case of pulses of smooth shape, the stage of plasma origination looms large for low laser radiation flux densities, according to calculations of Ref. 14 and experiments of Ref. 13. And in addition, if the amplitude of the spike is great enough, the specific energy of plasma initiation is correspondingly low (let us say, of the order of 2-3 J/cm^2), and absorption waves propagating due to the radiation mechanism may be observed right down to quite low flux densities in the main part of the laser pulse and up to the stage of quasi-steady pulse propagation. For example, at a flux density of 0.1 MW/cm^2, the thickness of the plasma layer by a time of 100-200 μs does not exceed 2-4 cm, i. e. at a spot area of the order of 50 cm^2 and specific energy of 10-20 J/cm^2, which is quite sufficient for reaching the quasi-steady stage of propagation, the total radiation energy of the CO_2 laser is approximately 0.1-1 kJ.

Estimates and calculations like those described above show that for a neodymium laser the threshold of maintaining quasi-steady fast laser radiation absorption waves is higher than for the CO_2 laser, but such waves can also exist at flux densities much lower than in the experiments of Ref. 5-7, and specifically at least at $q_0 \geqslant 1$ MW/cm^2. Qualitatively, the pattern of propagation of fast absorption waves for neodymium laser radiation is analogous to that given in Ref. 3, 4 and above for the CO_2 laser. The pressure and expansion rate found in the calculations also agree with relations (1). However, the ingition temperature (1.3 eV) is higher than for the CO_2 laser, and accordingly the maximum temperature of the plasma is somewhat higher than given by relation (2). Of course, in this case as well at low q_0 special plasma ignition is advisable, and the initial stage of development of the effect depends on the parameters of the "initiator." At laser radiation flux densities lower than those given in the calculations, the reduction of pressure in the initial plasma layer due to hydrodynamic expansion, and the corresponding cooling due to the amplified radiation may lead to transparency of the laser plasma and to a change in the nature of the processes occurring there. "Stalled" (decelerated) and "rushed" (accelerated) waves become possible, as well as pulsating modes of wave propagation with incomplete absorption of laser radiation.

Subsonic radiation waves propagating from a barrier under conditions of plane geometry have been considered above. However, such waves (with plasma pressure much greater than atmospheric) are possible in an unbounded gas medium as well when they propagate from an initial plasma layer that is initiated for example by an optical breakdown or electric discharge. The parameters of such waves in their quasi-steady stage are not much different from those of waves propagating from a wall. For example, velocities are only $2^{1/3}$ times less than those given by relations (1) for expansion in both directions rather than to one side only. The maximum temperature difference is even less significant. The only noticeable difference is in pressures -- they are $2^{2/3}$ times lower. The threshold of maintaining such quasi-steady fast absorption waves is correspondingly somewhat higher. However, all the same they may exist in the flux density region where only comparatively slow waves were observed under the conditions of the experiments of Ref. 1, 13, 15 (with pressure close to atmospheric), although hydrodynamic effects had already begun to play a part in their propagation as well.

REFERENCES

1. Bunkin, F. V., Konov, V. I., Prokhorov, A. M. et al., PIS'MA V ZHURNAL EKSPERIMENTAL'NOY I TEORETICHESKOY FIZIKI, Vol 9, 1969, p 609.

2. Rayzer, Yu. P., "Lazernaya iskra i rasprostraneniye razryadov" [Laser Spark and Discharge Propagation], Moscow, Nauka, 1974.

3. Bergel'son, V, I., Loseva, T. V., Nemchinov, I. V., ZHURNAL PRIKLADNOY MEKHANIKI I TEKHNICHESKOY FIZIKI, No 4, 1974, p 22.

4. Kozik, Ye. A., Loseva, T. V., Nemchinov, I. V. et al., KVANTOVAYA ELEKTRONIKA, Vol 5, 1978, p 2138.

5. Kozlova, N. N., Markovich, I. E., Nemchinov, I. V. et al., KVANTOVAYA ELEKTRONIKA, Vol 2, 1975, p 1930.

6. Berchenko, A. Ye., Sobolev, A. P., Fedyushin, B. T., KVANTOVAYA ELEKTRONIKA, Vol 6, 1979, p 1546.

7. Bessarab, A. V., Dolgaleva, G. V., Zhidkov, N. V. et al., FIZIKA PLAZMY, Vol 5, 1979, p 558.

8. Bakeyev, A. A., Vasil'yev, L. A., Nikolashkina, L. N. et al., KVANTOVAYA ELEKTRONIKA, Vol 2, 1975, p 1278.

9. Bakeyev, A. A., Nikolashkina, L. N., Prokopenko, N. V., KVANTOVAYA ELEKTRONIKA, Vol 7, 1980, p 1236.

10. Avilova, I. V., Kiberman, L. M., Vorob'yev, V. S. et al., "Opticheskiye svoystva goryachego vozdukha" [Optical Properties of Hot Air], Moscow, Nauka, 1970.

11. Stupochenko, Ye. V., Dotsenko, B. B., Stakhanov, I. P. et al., in: "Fizicheskaya gazovaya dinamika" [Physical Gas Dynamics], Moscow, Izd-vo AN SSSR, 1959, p 39.

12. Kalitkin, N. N., Kuz'mina, L. V., Rogov, V. S., "Tablitsiy termodinamicheskikh funktsiy i transportnykh koeffitsiyentov plazmy" [Tables of Thermodynamic Functions and Transport Coefficients of Plasma], Moscow, Izd-vo IPM AN SSSR, 1972.

13. Klosterman, E. L., Byron, S. R., J. APPL. PHYS., Vol 46, 1974, p 4751.

14. Golub', A. P., Nemchinov, I. V., KVANTOVAYA ELEKTRONIKA, Vol 7, 1980, p 1831.

15. Bufetov, I. A., Prokhorov, A. M., Fedorov, V. B., Fomin, V. K., PIS'MA V ZHURNAL EKSPERIMENTAL'NOY I TEORETICHESKOY FIZIKI, Vol 32, 1980, p 281.

6610
CSO: 1862/145

UDC 621.373.826.038.823

NUMERICAL STUDY OF VIBRATIONAL RELAXATION WITH TURBULENT JET MIXING IN SUPERSONIC NOZZLE

Minsk INZHENERNO-FIZICHESKIY ZHURNAL in Russian Vol 42, No 4, Apr 82 (manuscript received 27 Jan 81) pp 586-592

[Article by A. V. Lavrov and V. A. Pospelov, Leningrad Polytechnical Institute imeni M. I. Kalinin]

[Text] The paper gives the results of a computational study of the influence that different working parameters have on the characteristics of a CO_2 gasdynamic laser with selective thermal excitation.

Calculation of supersonic jet mixing with consideration of vibrational relaxation is of considerable interest in connection with the development of hypersonic wind tunnel equipment [Ref. 1], investigation of spontaneous emission in jet engine flows [Ref. 2], and creation of gasdynamic lasers (GDLs) with selective thermal excitation [Ref. 3-18]. Experimental research in recent years [Ref. 3-11] shows the possibility of using mixing in lasers to get higher gains and specific energy outputs than in GDLs with premixing. Alongside the further development of experimental research, a problem of some topicality is development of an adequate numerical model of the laser and using it as a basis for both parametric studies and analysis of the influence of separate factors on GDL operation. However, up until now the only extensive theoretical research that has been done on the mixing CO_2 GDL has been based on an instantaneous mixing model [Ref. 12-14]. Clearly, calculations using this model will agree well with experimental data if mixing takes place in the nozzle assembly [Ref. 6] or the mixer unit proposed in Ref. 5 is used. However, if the CO_2 + He is mixed through a central plug, where the injection itself takes place from a flat profiled nozzle [Ref. 11] or from circular orifices in the central plug (and the distance between orifices is approximately equal to their diameter), then two-dimensional mixing effects will play an appreciable role, and disregarding them may lead to considerable overstatement of the laser characteristics. Furthermore, in designing the optical cavity, data on density and gain profiles are needed.

There are currently examples in the literature on calculation of jet mixing in CO_2 GDLs with selective thermal excitation both on the basis of a system of boundary layer equations (narrow-channel) [Ref. 15-17], and with the use of

simplified Navier-Stokes equations [Ref. 11, 18]. In particular, in Ref. 17 the solution is based on using a semi-empirical model of turbulence relying on an equation of pulsation energy balance with a universal set of numerical coefficients, which had been successfully used previously in analyzing free shear flows [Ref. 19, 20]. Satisfactory agreement between the results of calculation [Ref. 17] and experimental data [Ref. 4] on distribution of small-signal gain g, CO_2 concentration γ and lasing power provides a basis for using the proposed technique in numerical parametric investigation of CO_2 GDLs with selective thermal excitation.

Comparison with Experimental Results. Ref. 10 gives abundant data on the influence of temperature and pressure in the gas generator chamber obtained by using a nozzle with central plug analogous in design to that of Ref. 4. In doing the corresponding calculations, it was assumed that the half-height of the CO_2 supply jet was $A_{01} = 0.2$ mm, height of the hot nitrogen jet $(A_{0E} - A_{01}) = 0.8$ mm, ratio of output cross section to critical cross section $A_E/A_{0E} = 15.7$, length of the supersonic part of the nozzle $x_c = 60$ mm. The nozzle contour was taken from Ref. 21, which gives the results of calculations of nozzles of minimum length with a corner point (the contour for Mach number $M = 4.5$ was used with ratio of specific heats $c_p:c_v = 1.4$). The Mach numbers at the beginning of the calculated region were equal to $M_{01} = M_{0E} = 1.2$, composition of the mixture of the secondary jet CO_2:He = 1:4 (by volume), initial temperature 300 K, and the values of the other parameters are given in the table. The flow length of the cavity was taken as $x_p = 24$ cm, distance between mirrors L = 17 cm, coefficients of absorption of the mirrors $\alpha_1 = \alpha_2 = 0.02$, coefficient of $t_1 = 0$, and t_2 was determined in an optimization process.

Parameters	γ (CO)							T_0, K (N_2)			
	0,05	0,1	0,15	0,2	0,25	0,3	0,4	2000	2500	3000	3500
T, K	207	213	218	223	227	231	237	1552	1940	2328	2720
V, m/s	823	710	634	575	533	495	441	964	1078	1180	1280

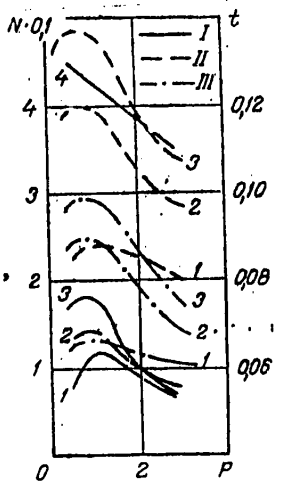

Fig. 1. Specific energy output and optimum transmission coefficient of output mirror as a function of the stagnation pressure: I--experiment [Ref. 10]; II--calculation, $\alpha = 0.02$; III--$(\alpha + \delta L) = 0.05$; nitrogen stagnation temperature: 1--$T_0 = 2000$; 2--2500; 3--3000 K; 4--t ($T_0 = 2500$ K), N, J/g; P, MPa

Results of comparing experimental data with calculations are shown in Fig. 1. The somewhat higher value of the specific energy output obtained in the calculation can be attributed to the fact that in the first place no consideration was taken of losses of vibrational energy during flow in the subcritical part of the nozzle, and in the second place the actual losses in the cavity were not considered (see Ref. 22). For example when the overall coefficient of losses per pass $(\alpha + \delta L)$ was increased to 0.05, the calculated curves agreed much better with experimental data. Fig. 1 also shows the results of computational optimization of the coefficient of transmission of the semitransparent mirror, evidencing the necessity for selecting t_2 in a multifactor optimization process. It is important to note that the t_2 obtained in the calculation lie in the range of mirror transmissions used in the experiment of Ref. 10.

Results of Numerical Parametric Study. Calculations were done using the nozzle contour taken from Ref. 4, Mach numbers $M_{01} = M_{0E} = 1.2$, static pressure at the beginning of the computational region $P_1 = P_E = 0.204$-1.632 MPa, which corresponds to pressure in the gas generator chamber of 0.5-4 MPa, temperature and flow velocity are given in the table, and the values of other parameters are given in Ref. 17. In order to reduce the number of parameters to be varied in the given section, the calculations were done for conditions of laser operation in the amplification mode, i. e. without consideration of the losses on the mirrors. The field intensity of the master laser was 10 kW/cm^2, and the flow length of the cavity was 8 and 40 cm.

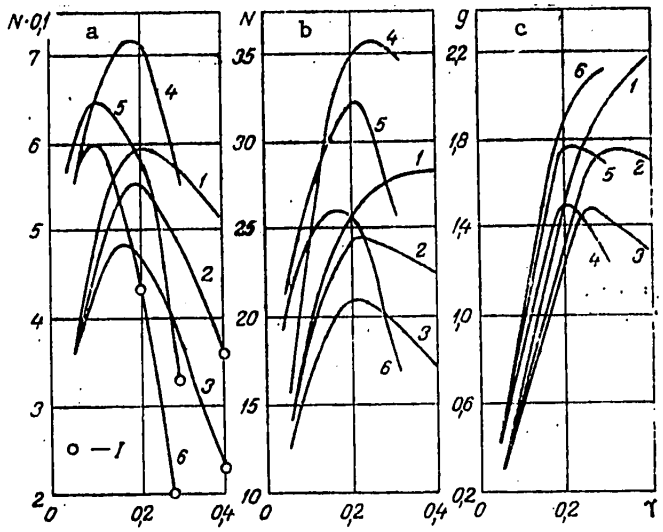

Fig. 2. Specific energy output (a, b) and average small-signal gain (c) at the nozzle tip as a function of CO_2 content in the secondary flow (a--$x_p = 40$; b--8 cm); 1-3--$T_0 = 2500$; 4-6--3000 K; 1, 4--P = 1; 2, 5--2; 3, 6--3 MPa; I--gain $g < 0$ at $x_p < 40$ cm, g, m^{-1}

Fig. 2 shows the results of calculation of specific energy output and average gain $g = \int_0^{\Lambda_E} g(y)\,dy/\Lambda_E$ at the nozzle tip for different values of working

parameters. Let us note that for some fairly large values of γ, the gain drops to 0 at $x_p < 40$ cm. As we can see from the figure, the optimum composition of the secondary jet depends appreciably both on pressure and on temperature, an increase in P and T entailing a reduction in the optimum value of γ. It is important to note that in operation of a laser with working parameters $P_0 = 3$ MPa, $T_0 = 3000$ K, the optimum mixture from the standpoint of maximizing energy output is CO_2:He = 1:9, and transition to the 1:4 mixture most often used in experiment reduces the energy output by 25%. It is interesting that for both short and long cavities the reduction in N with increasing γ at $\gamma > \gamma_{opt}$ is weaker at $T_0 = 2500$ K. This is because in the given case there is a reduction of gas temperature in the cavity, i. e. greater relaxation losses are possible, which increase with increasing CO_2 concentration. The results given on Fig. 2 show that for all working parameters the value of γ that is necessary for attaining maximum g is much greater than is necessary for maximizing the specific energy output. In application to GDLs with premixing, this fact has already been repeatedly mentioned in the literature (see for example Ref. 23). The results show that for the short cavity the specific energy output is about half that for the long cavity. Apparently increasing the field strength (by increasing the spacing between mirrors) does not appreciably increase N at $x_p = 8$ cm, since in addition to the limiting influence of the rate of transfer of vibrational energy from N_2 to $\nu_3 CO_2$, it is essential for the given mixing unit that mixing continues in the cavity.

The given results do not allow us to evaluate the influence of various factors on specific energy output. Therefore Fig. 3 shows data on the efficiencies

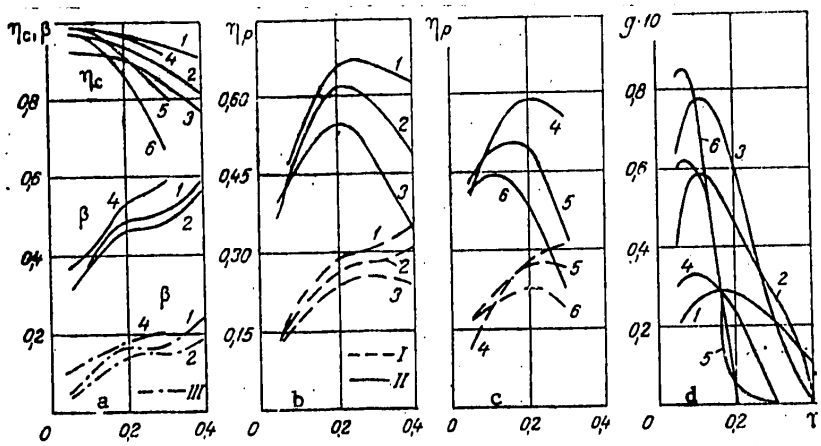

Fig. 3. Dependence of nozzle efficiency, mixing efficiency (a), cavity efficiency (b, c) and small-signal gain on the output of gas from the cavity (d) on CO_2 content in the secondary flow; I--$x_p = 8$; II--40 cm; III--mixing efficiency β on nozzle tip; 1-6--same as Fig. 2

of the nozzle η_c and the cavity η_p, mixing efficiency $\beta = c_{N_2}(y = 0) : c_{N_2}(y = A_E)$ and on the average gain as the gas leaves the cavity. As can be seen from this figure, η_c decreases with increasing CO_2 concentration, and in all cases exceeds the value $\eta_c = 0.65$. However, for GDLs with mixing this quantity does

not completely characterize nozzle efficiency, for the closeness of η_c to unity is evidence of poor mixing of N_2 and $CO_2 + He$. Therefore Fig 3a also shows the values of mixing efficiency β on the nozzle tip and at the end of the cavity. It can be seen that β increases with increasing CO_2 concentration. This is explained by the fact that at a fixed value of M_{01} an increase in γ leads to a reduction in the velocity of the secondary flow (see table); consequently there is an increase in the difference of velocities of the flows of N_2 and $CO_2 + He$ and accordingly in the effective coefficient of turbulent viscosity. The points of inflection on the curves can be attributed to the complexity of the process of turbulent mixing in the presence of a strong negative pressure gradient. Mixing efficiency does not exceed 60%, which shows the necessity for further improving the nozzle units used. Increasing the pressure leads to a slight drop in β, and a rise in nitrogen temperature causes somewhat of an increase in β, which is due to an increase in velocity V_E (see the table).

Fig. 3b and c show data on cavity efficiency. The efficiency of the cavity at $x_p = 8$ cm does not exceed the value $\eta_p = 0.35$. At $x_p = 40$ cm, efficiency reaches 65% for the flow mode with parameters $T_0 = 2500$ K, $P_0 = 1$ MPa, $\gamma = 0.25$. As we can see from comparing Fig. 2a and 3b, c, at $x_p = 40$ cm, similarity is observed in the curves for N and η_p as a function of γ. However, at $x_p = 8$ cm, such similarity is not observed. For example at $x_p = 8$ cm, $P_0 = 2$ MPa, $T_0 = 2500$ K, N reaches a maximum at $\gamma \cong 0.2$, whereas η_p continues to increase at even higher values.

Cavity efficiency can also be evaluated from the gain on gas output from the cavity. Therefore the corresponding calculated data are shown on Fig. 3d. We can see from the figure that for modes with maximum energy output a further increase in the gas-outlet gain is possible either by reducing the length of the cavity or by increasing field strength.

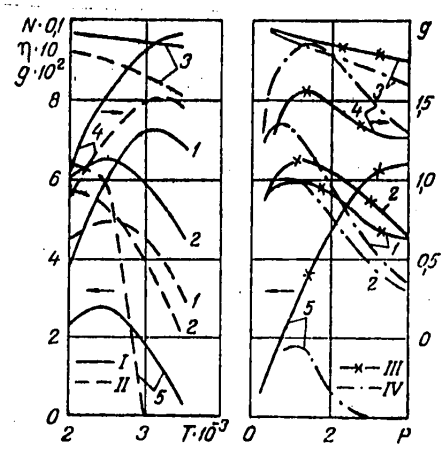

Fig. 4. Influence of stagnation temperature and pressure on GDL characteristics: I--$P_0 = 1$; II--3 MPa; III--$T_0 = 2500$; IV--3000 K; 1--N, J/g; 2--η_p; 3--η_c; 4--gain on nozzle tip; 5--gain at cavity outlet

Results of investigation of the influence that initial nitrogen temperature has on GDL characteristics are shown on Fig. 4. It is important to emphasize that at $P_0 = 3$ MPa the energy output at $T_0 = 3500$ K is little more than half the value at the optimum temperature of 2500 K, and at the same time the gain at the nozzle tip at the maximum temperature is slightly lower than the maximum gain. Analysis of the way that nozzle and cavity

efficiencies depend on T_0 shows that the reduction in N is due mainly to an increase in η_p as a consequence of rising gas temperature in the cavity.

It is of considerable interest to study the way that specific energy output depends on stagnation pressure since increasing P_0 simplifies the problem of restoring pressure in the flow to atmospheric level (see for example Ref. 11). Results of corresponding calculations are shown on Fig. 4. We can see that for $T_0 = 2500$, 3000 K the maximum energy output is reached at pressure of 1, 0.5 MPa respectively. Of considerable interest is the fact that when $P_0 > 2.2$ MPa the energy output for $T_0 = 2500$ K is higher than for 3000 K. In this case, the reduction of energy output is also caused chiefly by a drop in cavity efficiency, firstly due to the increase in gas temperature there, and secondly due to an increase in relaxation losses.

Thus the results given above show the feasibility of achieving high specific energy output in GDLs with selective thermal excitation when all working parameters are appropriately optimized. The computational data enable us to evaluate the mixing efficiency, as well as the nozzle and cavity efficiencies, and to make recommendations on improving them. The influence that nozzle shape and mixing cross section have on the energy output, and comparison of the CO_2 and N_2O GDLs are beyond the scope of this work and will be covered in future research.

Symbols

c--mass concentration; g--small-signal gain; t--mirror transmission coefficient; x_c--length of supersonic part of nozzle; x_p--length of cavity; A_{01}--half-height of CO_2 + He supply jet; A_{0E}--half-height of initial cross section of the nozzle; A_E--half-height of output cross section; L--spacing between mirrors; M--Mach number; N--specific energy output; P--pressure; T--temperature; P_0, T_0--nitrogen stagnation pressure and temperature; V--velocity; α--mirror absorption coefficient; β--mixing efficiency; γ--volumetric concentration of CO_2 in secondary flow; δ--coefficient of linear attenuation of radiation; η_c--nozzle efficiency; η_p--cavity efficiency.

REFERENCES

1. Muchnaya, M. I., "Calculating Flow of Viscous Gas in Hypersonic Nozzle With Consideration of Vibrational Nonequilibrium", IZVESTIYA AKADEMII NAUK SSSR: MEKHANIKA ZHIDKOSTI I GAZA, No 1, 1979, pp 165-168.

2. Jensen, D. E., Wilson, A. S., "Prediction of Rocket Exhaust Flame Properties", COMBUSTION AND FLAME, Vol 25, No 1, 1975, pp 103-109.

3. Korshko, V. N., Soloukhin R. I., "Optimum Conditions for Obtaining Inversion With Thermal Excitation by Mixing in Supersonic Flow", DOKLADY AKADEMII NAUK SSSR, Vol 211, No 4, 1973, pp 829-832.

4. Taran, J. P. E., Charpenel, M., Borghi, R., "Investigation of a Mixing CO_2 GDL", AIAA PAPER No 73-622, 1973, 9 pages.

5. Krauklis, A. V., Kroshko, V. N., Soloukhin R. I., Fomin, N. A., "Lasing Conditions in GDL With Thermal Excitation and Mixing in Supersonic Flow", FIZIKA GORENIYA I VZRYVA, Vol 12, No 5, 1976, pp 792-795.

6. Cassady, P. E., Newton, J., Rose, P., "A New Mixing Gasdynamic Laser", AIAA PAPER No 76-343, 1976, 11 pages.

7. Schall, W., Hoffman, P., Hugel, H., "Performance of N_2/CO_2 Gasdynamic Mixing Lasers", J. APPL. PHYS., Vol 48, No 2, 1977, pp 688-690.

8. Yefimov, B. G., Zaklyaz'minskiy, L. A., "Experimental Studies of the Influence of Mixing Conditions in Laval Nozzle on Gain in Supersonic Flow", FIZIKA GORENIYA I VZRYVA, Vol 15, No 1, 1979, pp 97-102.

9. Ostroukhov, N. N., Tkachenko, B. K., "Efficiency of CO_2 Excitation in Gasdynamic Laser With Gas Mixing", KVANTOVAYA ELEKTRONIKA, Vol 5, No 4, 1978, pp 924-926.

10. Vyskubenko, B. A. et al., "Experimental Studies of Mixing Gasdynamic CO_2 Laser", DOKLADY AKADEMII NAUK SSSR, Vol 248, 1979, pp 81-83.

11. Abakumov, B. V. et al., "High-Temperature cw Mixing GDL", in: "Kinetika khimicheskikh reaktsiy" [Kinetics of Chemical Reactions], Chernogolovka, Institute of Chemical Physics, USSR Academy of Sciences, 1980, pp 49-52.

12. Breyev, V. V., Kukharenko, A. T., Napartovich, A. P., Sharkov, V. F., "Feasibility of Improving GDL Efficiency", TEPLOFIZIKA VYSOKIKH TEMPERATUR, Vol 12, No 6, 1974, pp 1325-1327.

13. Achasov, O. V., Soloukhin R. I., Fomin, N. A., "Numerical Analysis of GDL With Selective Thermal Excitation" in: "Problemy teplo- i massoobmena-77" [Problems of Heat and Mass Exchange 77], Minsk, Institute of Heat and Mass Exchange, BSSR Academy of Sciences, 1977, pp 81-84.

14. Velikanov, A. G., Gorshunov, N. M., Kunin, Yu. A., Nemishchenko, O. P., "Optimizing Gain in Supersonic Flow by Mixing N_2 with CO_2-He", KVANTOVAYA ELEKTRONIKA, Vol 7, No 9, 1980, pp 1869-1874.

15. Charpenel, M., Taran, J. P. E., Borghi, R., "Laser thermique a melange", LA RECH. AEROSP., No 4, 1974, pp 189-197.

16. Markachev, Ye. S., "Iteration Algorithm for Calculating Steady-State Flow of Viscous Gas in Laval Nozzle", CHISLENNYYE METODY MEKHANIKI SPLOSHNOY SREDY, Vol 10, No 5, 1979, pp 75-80.

17. Akatnov, N. I., Lavrov, A. V., "Turbulent Mixing of Relaxing Jets in Supersonic Nozzle", IZVESTIYA AKADEMII NAUK SSSR: MEKHANIKA ZHIDKOSTI I GAZA, No 2, 1981, pp 156-160.

18. Golovichev, V. I., Manzhi, Sh., Soloukhin, R. I., Fomin, N. A., "Numerical Modeling of Mixing Processes in Obtaining Inversion by Gasdynamic Methods" in: "Chislennyye metody resheniya zadach perenosa" [Numerical Methods of

Solving Transfer Problems], Minsk, Institute of Heat and Mass Exchange, BSSR Academy of Sciences, 1979, pp 3-46.

19. Akatnov, N. I., "Influence of External Turbulence on Development of Turbulent Jet", IZVESTIYA AKADEMII NAUK SSSR: MEKHANIKA ZHIDKOSTI I GAZA, No 1, 1977, pp 24-29.

20. Akatnov, N. I., Lavrov, A. V., "Influence of Temperature Pulsations on Physicochemical Processes in High-Temperature Jet", TEPLOFIZIKA VYSOKIKH TEMPERATUR, Vol 16, No 5, 1978, pp 1005-1011.

21. Verkhovskiy, V. P., "Numerical Calculation of Flat Supersonic Nozzles With a Break in the Contour", TRUDY TSENTRAL'NOGO AERO-GIDRODINAMICHESKOGO INSTITUTA IMENI N. Ye. ZHUKOVSKOGO, No 1980, 1975, 42 pages.

22. Genich, A. P., Kulikov, S. V., Manelis, G. B., "Calculations of Energy Characteristics of Multicomponent Working Media in CO_2 GDL Using Combustion Products", ZHURNAL PRIKLADNOY MEKHANIKI I TEKHNICHESKOY FIZIKI, No 4, 1979, pp 11-16.

23. Losev, S. A., "Gazodinamicheskiye lazery" [Gasdynamic Lasers], Moscow, Nauka, 1977, 335 pages.

6610
CSO: 1862/151

UDC 518.517.944

METHODS OF SOLVING SIMPLIFIED STEADY-STATE VISCOUS GAS EQUATIONS

Novosibirsk METOD RESHENIYA STATSIONARNYKH UPROSHCHENNYKH URAVNENIY VYAZKOGO GAZA (PREPRINT NO 42) in Russian 1981 (signed to press 7 Nov 81) pp 1-52

[Preprint No 42, Institute of Theoretical and Applied Mechanics, Siberian Department, USSR Academy of Sciences, "Method of Solving Simplified Steady-State Viscous Gas equations", by V. M. Kovenya and S. G. Chernyy, 200 copies, 52 pages]

[Text] The authors consider numerical modeling of problems of aerodynamics in the approximation of simplified viscous gas equations. They discuss problems of choosing coordinate systems and unknown functions, and investigate the correctness of parabolized equations. An economic iteration scheme is proposed for solving simplified Navier-Stokes equations that is based on decomposition with respect to physical processes and spatial directions. The accuracy of the method is studied, and numerical solutions are compared for simplified and complete Navier-Stokes equations.

Introduction

The principal difficulties in numerical modeling of multidimensional supersonic steady-state viscous flows based on complete Navier-Stokes equations of compressible heat-conductive gas are due to considerable expenditures of computer time and memory. Therefore in addition to complete equations, extensive use is made of simplified models obtained from these equations by various assumptions about the nature of the flow (see Ref. 1). The advantage of simplified models is the possibility of finding solutions for steady-state problems by a multistep method along some coordinate direction. This reduces expenditures of computer time and memory, and enhances efficiency of numerical soltuion.

The simplest and most thoroughly studied simplified method is provided by boundary layer equations for which effective solution methods have been developed (e. g. see bibliography of Ref. 2). The use of boundary layer equations requires breaking down the region of flow disturbed by a solid into a zone of inviscid flow and a boundary layer, which is not always feasible.

Another approach is based on considering a unified system of simplified equations that are valid throughout the region of flow, but at the same time have an evolutionary type relative to one of the spatial coordinates. The viscous shock layer model is such a system in which the initial equations are split into two subsystems: parabolic equations and inviscid equations of first order. The former are solved by finite difference methods developed for solving boundary layer equations. The inviscid equations are solved in the blunting region by the method of straight lines [Ref. 3], and further down by a multistep finite-difference method. Davis was the first to use a viscous shock layer method to calculate flow around a paraboloid of revolution [Ref. 4], and this model was subsequently used by various authors to calculate flow around blunt bodies [Ref. 5-8].

The model next in complexity that describes viscous supersonic flow is obtained by eliminating the second derivatives along the flow from complete Navier-Stokes equations. The resultant equations are called parabolized Navier-Stokes equations. Having an elliptical nature relative to transverse directions, they enable calculation of flows with the presence of lateral separations (across the flow). This model was first used by Lin and Rubin to calculate three-dimensional flows [Ref. 9-11]. They proposed a semi-implicit method of solving parabolized Navier-Stokes equations using an iteration process. The system of resultant difference equations is resolved on each ray normal to the solid by vector sweeps that require inversion of 5 x 5 matrices at each node of the grid. The method was used by the authors to calculate three-dimensional flows at a longitudinal corner [Ref. 9], around a cone [Ref. 10] and near bodies of the fuselage-wing type [Ref. 11]. Subsequently a similar approach was used by Lubard and Helliwell to calculate laminar flows without axial separation at angles of attack around cones [Ref. 12, 13] and solids of complex shape [Ref. 14]. In Ref. 14 an approach is suggested in which the step coordinate is chosen in a direction close to a streamline, and the transverse coordinates are selected orthogonal to the step coordinate in the region of appreciable influence of viscous effects, which enables expansion of the region of applicability of the model of parabolized Navier-Stokes equations. A similar approach that is more general than that mentioned is proposed in Ref. 15.

Since the given methods of solving parabolized Navier-Stokes equations are semi-implicit, they have limitations on step size in the direction of improvement. To eliminate this inadequacy, an implicit method is considered in Ref. 16 that is based on decomposition with respect to spatial directions and is realized by vector sweeps. The method is applied to the problem of flow around a plate of finite width at an angle of attack. The Briley-McDonald method [Ref. 17] is used to realize the nonlinear difference scheme.

A combination of the viscous shock layer model and parabolized Navier-Stokes equations is considered in Ref. 7 for flow around a blunt cone at an angle of attack. The viscous shock layer equations are used in the region of blunting and on the windward side, while the parabolized Navier-Stokes equations are used on the leeward side. This cuts down on computer time.

Thus the use of simplified Navier-Stokes equations by appreciably reducing computer time and memory volume enables numerical computer simulation of an extensive class of problems of importance for practice in supersonic viscous flow around solids over a wide range of flow parameters. However, the problem of developing asymptotic methods of solving simplified viscous gas equations remains topical.

This paper is devoted to questions of numerical modeling of aerodynamics problems in the approximation of simplified viscous gas equations. The problems of selecting coordinate systems and unknown functions are discussed, and an investigation is made of the correctness of parabolized equations. An economic iteration method is proposed for solving simplified Navier-Stokes equations based on decomposition with respect to physical processes and spatial directions. An investigation is made of the accuracy of the method and numerical solutions by simplified and complete Navier-Stokes equations are compared.

§1. Selecting the form for recording equations

The principal assumption in deriving approximate models is that of smallness of the longitudinal components of the viscous stress tensor as compared with normal and azimuthal components. Therefore the coordinate system in which the principal equations are being considered must satisfy a number of requirements (see Ref. 15), chief among which are the following:

a) the family of coordinate lines q^1 that is selected as the direction field must coincide insofar as possible with streamlines;

b) the normal q^2 and azimuthal q^3 families of coordinate lines must be orthogonal to family q^1 in the zone of appreciable influence of viscous effects;

c) the surfaces of the solid and of the head shock wave must be coordinate surfaces.

To satisfy these requirements it is necessary to write the principal equations in an arbitrary curvilinear coordinate system.

Consider the problem of choosing the components of the velocity vector. The simplest form of recording is exemplified by simplified equations with covariant or contravariant components of the velocity vector. Let $\vec{e}_i = \partial\vec{R}/\partial q^i$ ($i = 1, 2, 3$) be a covariant basis, and $\vec{v} = v^i\vec{e}_i$ be the resolution of the velocity vector in this basis. Here $\vec{R}$ is the radius vector of a given point of space, v^i are the contravariant components of the velocity vector, and pairwise summation of like indices conventional for tensor analysis is assumed. The vector $\vec{v}$ is the diagonal of a parallelepiped with sides coinciding with the moving basis $\vec{e}_1$, $\vec{e}_2$, $\vec{e}_3$ and having length $\sqrt{g_{ii}}v^i$ (there is no summation with respect to i), where g_{ii} are diagonal elements of the covariant metric tensor. In the case of appreciable curvatures of the coordinate lines, the vectors $\vec{e}_i$ will change appreciably both in direction and in length, leading to non-physical changes of quantities v^i when there is a change of position in space even for a homogeneous vector field. Consequently the use of contravariant components of the velocity vector will introduce additional errors into the algorithm in finite difference approximation of equations.

For orthogonal coordinate systems close to rectilinear, it is possible to use as components of the velocity vector the physical components $v^{(i)}$ introduced by the formulas $v^{(i)} = \sqrt{g_{ii}}v^i$ (there is no summation with respect to i). The physical components of the velocity vector have dimensionality coinciding with the physical dimensionality of the velocity field, and are components of the resolution of the velocity vector in the moving orthonormalized unit basis $\vec{v} = v^{(i)}\vec{e}_i/\sqrt{g_{ii}}$. This enables use of physical velocity components for such systems of coordinates as for example spherical, cylindrical, natural, normally fixed to the surface of the solid. However, for coordinate systems that satisfy the requirements formulated above, physical contravariant components selected as unknown functions may not meet with success. We illustrate this statement by the following example.

Consider a region in which a coordinate system is plotted (Fig. 1), which is a model representation for many flow problems. Let the left-hand boundary Γ_1 of the given region be assigned by the equation $x = 0$, the upper boundary Γ_2 by $y = 2 + x$, the right-hand boundary Γ_3 by $x = 1$, and the lower boundary Γ_4 by $y = 1$. Let us introduce the coordinates ξ, η related to cartesian coordinates x, y by the formulas

$$\xi = x \ , \quad \eta = \frac{y-1}{x+1}$$

In such an assignment of the coordinate system, values $\eta = 0$ correspond to the lower boundary, and $\eta = 1$ -- to the upper boundary. The coordinate lines $\eta = c$, where $0 < c < 1$ are straight lines that diverge from the lower to the upper boundary. Coordinate lines $\xi = \text{const}$ form a family of curves perpendicular to the lower boundary. If we take boundary Γ_4 as the surface of the solid, Γ_2 as the surface of the head shock wave, and Γ_1 as the boundary on which the flow is incident, the coordinate system ξ, η satisfies the requirements formulated in the beginning of this section.

Let u^1, u^2 be components of the velocity vector in the cartesian coordinate system in directions on the axis Ox and Oy respectively. Consider the contravariant components v^1, v^2 of the velocity vector for homogeneous flow parallel to boundary Γ_4.

We have

$$v^i = u^m z^i_m \ , \quad i, m = 1, 2 \ ,$$

where

$$\begin{pmatrix} z^1_1 & z^1_2 \\ z^2_1 & z^2_2 \end{pmatrix} = \begin{pmatrix} \frac{\partial \xi}{\partial x} & \frac{\partial \xi}{\partial y} \\ \frac{\partial \eta}{\partial x} & \frac{\partial \eta}{\partial y} \end{pmatrix} = \begin{pmatrix} 1 & 0 \\ -\frac{\eta}{\xi+1} & \frac{1}{\xi+1} \end{pmatrix}.$$

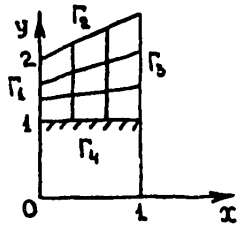

Fig. 1

Since $(u^1, u^2) = (1, 0)$, we find

$$(v^1, v^2) = \left(1, -\frac{\eta}{\xi+1}\right).$$

Setting $\xi = 0$ for the sake of definiteness, we find that the contravariant component $v^2 = -\eta$ varies along input boundary Γ_1 from 0 on Γ_4 to -1 on Γ_2. Let us find the physical contravariant components $v^{(1)}$, $v^{(2)}$. The matrix of the coefficients of the covariant metric tensor is

$$\begin{pmatrix} g_{11} & g_{12} \\ g_{21} & g_{22} \end{pmatrix} = \begin{pmatrix} 1+\eta^2 & \eta(\xi+1) \\ \eta(\xi+1) & (\xi+1)^2 \end{pmatrix}$$

Then

$$v^{(1)} = \sqrt{g_{11}}\,v^1 = \sqrt{1+\eta^2}\,, \quad v^{(2)} = \sqrt{g_{22}}\,v^2 = -\eta\,.$$

Thus even for a model region with the simplest coordinate system the contravariant velocity components (physical and mathematical) of a homogeneous flow are strongly changing functions of coordinates ξ, η, and in the first place cannot directly characterize the flow, and secondly they introduce additional errors in finite-difference approximation of equations.

Therefore in this paper the velocity vector components are taken as those in the cylindrical coordinate system. Density and pressure are taken as the other two dependent functions. Such a choice of thermodynamic quantities enables solution of the equation of continuity separately from the other equations (of momentum and energy), and on this basis a more economic algorithm can be constructed (see §4).

To derive simplified equations, let us consider the complete equations of motion of a viscous heat-conducting gas written in the cylindrical coordinate system z, θ, r (Fig. 2) in non-divergent form:

$$u\rho_z + \frac{V}{r}\rho_\theta + w\rho_r + \rho\left(u_z + \frac{V_\theta}{r} + w_r + \frac{w}{r}\right) = 0,$$

$$uu_z + \frac{V}{r}u_\theta + wu_r + \frac{1}{\rho}p_z = \frac{1}{Re\,\rho}\left(\tau^{11}_z + \frac{1}{r}\tau^{12}_\theta + \tau^{13}_r + \frac{\tau^{13}}{r}\right),$$

$$uV_z + \frac{V}{r}V_\theta + wV_r + \frac{1}{r\rho}p_\theta + \frac{wV}{r} = \frac{1}{Re\,\rho}\left(\tau^{12}_z + \frac{1}{r}\tau^{22}_\theta + \tau^{23}_r + 2\frac{\tau^{23}}{r}\right),$$

$$uw_z + \frac{V}{r}w_\theta + ww_r + \frac{1}{\rho}p_r - \frac{V^2}{r} = \frac{1}{Re\,\rho}\left(\tau^{13}_z + \frac{1}{r}\tau^{23}_\theta + \tau^{33}_r + \frac{\tau^{33}-\tau^{22}}{r}\right),$$

$$u\rho_z + \frac{V}{r}\rho_\theta + w\rho_r + \gamma\rho\left(u_z + \frac{1}{r}V_\theta + w_r + \frac{w}{r}\right) = \frac{\gamma}{R_r Re}\left\{(\mu\chi_z)_z + \right.$$

$$\left. + \frac{1}{r^2}(\mu\chi_\theta)_\theta + (\mu\chi_r)_r + \frac{\mu}{r}\chi_r\right\} + \frac{\gamma-1}{Re}\Phi\,,$$

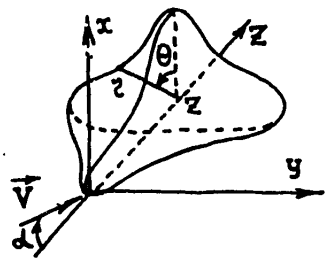

Fig. 2

$$\tau^{11} = (\lambda + 2\mu)u_z + \frac{\lambda}{r}V_\theta + \lambda w_r + \frac{\lambda}{r}w\,,$$

$$\tau^{22} = \lambda u_z + \frac{\lambda+2\mu}{r}V_\theta + \lambda w_r + \frac{\lambda+2\mu}{r}w\,,$$

$$\tau^{33} = \lambda u_z + \frac{\lambda}{r}V_\theta + (\lambda+2\mu)w_r + \frac{\lambda}{r}w\,,$$

$$\tau^{12}=\mu(V_z+\frac{u_\theta}{r}),\ \tau^{13}=\mu(W_z+u_r),\ \tau^{23}=\mu(\frac{W_\theta}{r}+V_r-\frac{V}{r}),$$

$$\Phi=\tau^{11}u_z+\frac{\tau^{12}}{r}(V_\theta+W)+\tau^{33}W_r+$$

$$+\frac{1}{\mu}\left[(\tau^{12})^2+(\tau^{13})^2+(\tau^{23})^2\right].$$

Here ρ is density; u, v, w are the components of the velocity vector in directions z, θ, r; p is pressure, $\varkappa=p/\rho$, $\lambda=\mu'-{}^2/_3\mu$, μ' is the second viscosity coefficient, μ is the dynamic viscosity coefficient. To close the system of equations, the equation of state of a perfect gas $p=(\gamma-1)\rho\varepsilon$ is given together with the power-law form of dependence of the dynamic viscosity coefficient on internal energy $\mu/\mu_\infty=(\varepsilon/\varepsilon_\infty)^\omega$, where $0.5\leqslant\omega\leqslant1$, $\gamma=c_p/c_v$ (c_p and c_v are the specific heats of the gas at constant pressure and volume respectively), μ_∞, ε_∞ are the values of the dynamic viscosity coefficient and internal energy of the undisturbed oncoming flow.

In converting to dimensionless form, all lengths are referred to the characteristic linear dimension of the solid L, velocities u, v, w are referred to the velocity U_∞ of the oncoming flow, pressure is normalized to the quantity $\rho_\infty U_\infty^2$, and density and viscosity coefficients are referred to ρ_∞ and μ_∞.

The Reynolds number Re and Prandtl number Pr are defined by the formulas

$$Re=\frac{U_\infty L\rho_\infty}{\mu_\infty},\quad Pr=\mu c_p/\varkappa,$$

where $\varkappa$ is the thermal conductivity coefficient.

Let us introduce the coordinate transformation

$$q^i=q^i(z,\theta,r)\quad(i=1,2,3),$$

that converts cylindrical coordinates z, θ, r to coordinates q^1, q^2, q^3 satisfying requirements a)-c) considered at the beginning of this section. The derivatives in the initial equations are transformed by the formulas

$$\frac{\partial}{\partial z}=z_1^i\frac{\partial}{\partial q^i},\quad\frac{\partial}{\partial\theta}=z_2^i\frac{\partial}{\partial q^i},\quad\frac{\partial}{\partial r}=z_3^i\frac{\partial}{\partial q^i},$$

where

$$z_1^i=\frac{\partial q^i}{\partial z},\quad z_2^i=\frac{\partial q^i}{\partial\theta},\quad z_3^i=\frac{\partial q^i}{\partial r}.$$

Eliminating from the resultant equations all viscous terms that contain derivatives with respect to q^1, we get a system of Navier-Stokes equations consisting of the equation of continuity

$$a\frac{\partial\rho}{\partial q^1}+b\frac{\partial\rho}{\partial q^2}+c\frac{\partial\rho}{\partial q^3}+\rho d=0\qquad(I)$$

and the equations of momentum and energy

$$A\frac{\partial \vec{f}}{\partial q^1} + B\vec{f} + C\vec{f} + D\vec{f} = G\vec{f} + Q\vec{f} + \vec{F} . \qquad (2)$$

In writing equations (1) and (2), the following notation is introduced:

$$a = uz_1^1 + v\frac{z_2^1}{r} + wz_3^1 ,$$
$$b = uz_1^2 + v\frac{z_2^2}{r} + wz_3^2 ,$$
$$c = uz_1^3 + v\frac{z_2^3}{r} + wz_3^3 ,$$
$$d = \frac{w}{r} + z_1^i\frac{\partial u}{\partial q^i} + \frac{z_2^i}{r}\frac{\partial v}{\partial q^i} + z_3^i\frac{\partial w}{\partial q^i} ,$$

$$A = \begin{pmatrix} a & 0 & 0 & z_1^1/\rho \\ 0 & a & 0 & z_1^2/\rho r \\ 0 & 0 & a & z_3^1/\rho \\ \gamma p z_1^1 & \gamma p\frac{z_2^1}{r} & \gamma p z_3^1 & a \end{pmatrix}, \quad B = \begin{pmatrix} b & 0 & 0 & z_1^2/\rho \\ 0 & b & 0 & z_2^2/\rho r \\ 0 & 0 & b & z_3^2/\rho \\ \gamma p z_1^2 & \gamma p\frac{z_2^2}{r} & \gamma p z_3^2 & b \end{pmatrix}\frac{\partial}{\partial q^2},$$

$$C = \begin{pmatrix} c & 0 & 0 & z_1^3/\rho \\ 0 & c & 0 & z_2^3/\rho r \\ 0 & 0 & c & z_3^3/\rho \\ \gamma p z_1^3 & \gamma p\frac{z_2^3}{r} & \gamma p z_3^3 & c \end{pmatrix}\frac{\partial}{\partial q^3}, \quad D = \begin{pmatrix} 0 & 0 & 0 & 0 \\ 0 & 0 & \frac{v}{r} & 0 \\ 0 & -\frac{v}{r} & 0 & 0 \\ 0 & 0 & 0 & \gamma\frac{w}{r} \end{pmatrix},$$

$$G\vec{f} = \begin{pmatrix} G_1 \\ G_2 \\ G_3 \\ G_4 \end{pmatrix}, \quad Q\vec{f} = \begin{pmatrix} Q_1 \\ Q_2 \\ Q_3 \\ Q_4 \end{pmatrix}, \quad \vec{F} = \begin{pmatrix} F_1 \\ F_2 \\ F_3 \\ F_4 \end{pmatrix}, \quad \vec{f} = \begin{pmatrix} u \\ v \\ w \\ p \end{pmatrix}.$$

The quantities G_k and Q_k include respectively the viscous terms with iterated derivatives with respect to q^2 and q^3 of the functions: u for k = 1, v for k = 2, w for k = 3, and p/ρ for k = 4. The remaining viscous terms with iterated and mixed derivatives with respect to q^2 and q^3 are included in vector $\vec{F}$.

§2. Formulation of the problem

1. The correctness of formulation of the initial boundary value problem relative to coordinate q^1 for the resultant simplified equations is investigated on the basis of the two-dimensional model system of equations

$$A\frac{\partial \vec{f}}{\partial x} + B\frac{\partial \vec{f}}{\partial y} = C\frac{\partial^2 \vec{f}}{\partial y^2} , \qquad (I)$$

where

$$A=\begin{pmatrix} u & \rho & 0 & 0 \\ 0 & u & 0 & 1/\rho \\ 0 & 0 & u & 0 \\ 0 & \gamma p & 0 & u \end{pmatrix},\quad B=\begin{pmatrix} v & 0 & \rho & 0 \\ 0 & v & 0 & 0 \\ 0 & 0 & v & 1/\rho \\ 0 & 0 & \gamma p & v \end{pmatrix},$$

$$C=\begin{pmatrix} 0 & 0 & 0 & 0 \\ 0 & m & 0 & 0 \\ 0 & 0 & m & 0 \\ 0 & 0 & 0 & \frac{\gamma}{\Pr} m \end{pmatrix},\quad \vec{f}=\begin{pmatrix} \rho \\ u \\ v \\ p \end{pmatrix},\quad m=\frac{\mu}{\rho \mathrm{Re}}\ .$$

For equations (1) we formulate the Cauchy problem with initial data on line $x = x_0$

$$\vec{f}(x,y)\big|_{x=x_0} = \vec{f}_0(y)\ , \qquad (2)$$

that determine the solution for $x \geqslant x_0$, $|y| < \infty$.

We rewrite system (1) as

$$\frac{\partial \vec{f}}{\partial x} + A^{-1}B\frac{\partial \vec{f}}{\partial y} = A^{-1}C\frac{\partial^2 \vec{f}}{\partial y^2}\ . \qquad (3)$$

and consider the two subsystems of equations

$$\frac{\partial \vec{f}}{\partial x} + A^{-1}B\frac{\partial \vec{f}}{\partial y} = 0\ , \qquad (3a)$$

$$\frac{\partial \vec{f}}{\partial x} = A^{-1}C\frac{\partial^2 \vec{f}}{\partial y^2}\ , \qquad (3b)$$

that correspond to flows in two limiting cases: negligibly small forces of viscosity ($\mathrm{Re} \to \infty$), and large forces of viscosity (small Reynolds number).

The eigenvalues of matrix $A^{-1}B$

$$\lambda_{1,2} = \frac{v}{u}\ ,\quad \lambda_{3,4} = \frac{uv \pm c\sqrt{u^2 + v^2 - c^2}}{u^2 - c^2}$$

($c = \sqrt{\gamma p/\rho}$ is the speed of sound in a perfect gas) are real, and the corresponding system of equations (3a) is hyperbolic when condition

$$u^2 + v^2 > c^2$$

is met. In this case, Cauchy problem (3a), (2) is correct (e. g. see Ref. 1), and may be solved by a multistep method of integration along coordinate x from cross section to cross section. In doing this, it is necessary that the line

of initial data $x = x_0$ and the lines of advancement of the solution $x = \text{const}$ have the spatial type of Ref. 18, i. e. that condition $M_x = u/c > 1$ be met. In the case of subsonic flows, system of equations (3a) becomes elliptical, and Cauchy problem (3a), (2) becomes incorrect. Since there are always local subsonic flow zones in supersonic viscous flow around solids near a wall, system of equations (3a) must be regularized near these zones. In this paper, the simplified Navier-Stokes equations are regularized by the method proposed in Ref. 19, 20. In accordance with this method, we introduce one of the possible regularizing functions in the equation of momentum in the projection of system (3a) on the Ox axis, after which matrix A assumes the form

$$A = \begin{pmatrix} u & \rho & 0 & 0 \\ 0 & u & 0 & \tilde{\chi}/\rho \\ 0 & 0 & u & 0 \\ 0 & \gamma p & 0 & u \end{pmatrix}, \qquad (5)$$

where $\tilde{x}$ is a regularizing function (see Ref. 20) such that

$$\begin{aligned} \tilde{\chi} &\to 1 \quad \text{when} \quad M_x > 1 \\ \tilde{\chi} &\to 0 \quad \text{when} \quad M_x < 1 . \end{aligned} \qquad (6)$$

Let us consider the eigenvalues of matrix $A^{-1}B$ after regularization (5), (6). Two of the four eigenvalues λ_1 and λ_2 will remain as before, equal to v/u. The others will take the form

$$\lambda_{3,4} = \frac{uV \pm c\sqrt{u^2 + \tilde{\chi}(V^2 - c^2)}}{u^2 - \tilde{\chi}c^2} . \qquad (7)$$

Expression (7) implies that problem (3a), (2) is correct in the subsonic zone as well if condition

$$\tilde{\chi}\left(1 - \frac{V^2}{c^2}\right) < M_x^2 \qquad (8)$$

is met, which can be realized by appropriate choice of function $\tilde{x}$.

Let us now consider the eigenvalues of matrix $A^{-1}C$ of system (3b):

$$\lambda_1 = 0 , \quad \lambda_2 = m/u ,$$
$$\lambda_{3,4} = \frac{m}{c(M_x^2 - 1)}\left[0.5M_x\left(1 + \frac{\gamma}{\rho_r}\right) \pm \sqrt{0.25M_x^2\left(1 - \frac{\gamma}{\rho_r}\right)^2 + \frac{\gamma}{\rho_r}}\right] . \qquad (9)$$

System of equations (3b) is not completely parabolic (see Ref. 1), and problem (3b), (2) is correct if eigenvalues (9) have non-negative real parts. It is implied by (9) that λ_1 and λ_2 are real and non-negative when $u > 0$. Eigenvalues λ_3 and λ_4 will also be real and positive when $M_x > 1$, since in this case

$$0.25M_x^2\left(1 - \frac{\gamma}{\rho_r}\right)^2 + \frac{\gamma}{\rho_r} < 0.25M_x^2\left(1 + \frac{\gamma}{\rho_r}\right)^2$$

However, if $M_x < 1$, then $\lambda_3 < 0$ and problem (3b), (2) is incorrect. Let us introduce regularizing functions $\tilde{\varphi}$ and $\tilde{\varkappa}$ in the second equation of system (3b), after which matrix A will be written as

$$A = \begin{pmatrix} u & \rho & 0 & 0 \\ 0 & \tilde{\varphi} u & 0 & \tilde{\varkappa}/\rho \\ 0 & 0 & u & 0 \\ 0 & \gamma p & 0 & u \end{pmatrix}$$

The eigenvalues of matrix $A^{-1}C$ in this case are equal to

$$\lambda_1 = 0, \quad \lambda_2 = m/u$$

$$\lambda_{3,4} = \frac{m}{c(\tilde{\varphi} M_x^2 - \tilde{\varkappa})}\left[0.5 M_x\left(1 + \frac{\gamma}{p}\tilde{\varphi}\right) \pm \sqrt{0.25 M_x^2\left(1 + \frac{\gamma}{p}\tilde{\varphi}\right)^2 - \frac{\gamma}{p}\left(\tilde{\varphi} M_x^2 - \tilde{\varkappa}\right)}\right]. \quad (10)$$

Choosing functions $\tilde{\varphi}$ and $\tilde{\varkappa}$ such that when $M_x > 1$

$$\tilde{\varphi} \to 1, \quad \tilde{\varkappa} \to 1,$$

and when $M_x < 1$

$$\frac{\tilde{\varkappa}}{\tilde{\varphi}} < M_x^2$$

we find that eigenvalues (10) will be real and non-negative. System (3b) regularized in this way will be everywhere not completely parabolic, and problem (3b), (2) will be correct.

Thus Cauchy problem (2) for system of equations (1) with corresponding regularization in zones where $M_x < 1$ is correct and the equations can be integrated by a multistep method.

The given analysis of correctness of formulation of Cauchy problem for model system of equations (1) allows us to hope that the initial boundary value problem formulated relative to coordinate q^1 for general system of equations (1.1), (1.2) with regularization in subsonic zones will be correct. The validity of this assumption has been confirmed by numerous calculations and comparisons with results by other techniques. Thus, the following initial boundary value problem is formulated for simplified three-dimensional equations (1.1), (1.2).

2. Initial data -- distributions of density, velocities and pressure -- are assigned on coordinate surface $q^1 = q_0^1$, which is a surface of spatial type (except for a narrow zone near the body). On coordinate surface $q^2 = q_b^2$, which is the surface of the body, we have the conditions of sticking

$$u = V = W = 0$$

and one of the modes of heat exchange:

thermal indulation $\partial\varepsilon/\partial q^2 = 0$
or wall cooling $\varepsilon = \varepsilon_w$.

In choosing the external boundary $q^2 = q^2_{ext}$, two cases are possible. In the first, the external boundary is situated in such a way that perturbations from the body do not reach it, and conditions of undisturbed flow are assigned on this surface:

$$\rho = 1,\ u = \cos\alpha,\ V = \sin\alpha\sin\theta,\ W = -\sin\alpha\cos\theta,\ p = \frac{1}{\gamma M_\infty^2}$$

where α is angle of attack (Fig. 2), and M_∞ is the Mach number of the undisturbed flow.

In the second case, it is assumed that the head shock wave is a surface of discontinuity, and it is taken as the external boundary. On this surface we have the Rankine-Hugoniot conditions

$$\begin{gathered}\rho_1 V_{1n} = \rho_2 V_{2n}\ ,\\ p_1 + \rho_1 V_{1n}^2 = p_2 + \rho_2 V_{2n}^2\ ,\\ \frac{\gamma}{\gamma-1}\frac{p_1}{\rho_1} + \frac{V_{1n}^2}{2} = \frac{\gamma}{\gamma-1}\frac{p_2}{\rho_2} + \frac{V_{2n}^2}{2}\ ,\\ \vec{V}_{1\tau} = \vec{V}_{2\tau}\ ,\end{gathered} \qquad \text{(II)}$$

where subscript "1" corresponds to values in front of the shock wave (undisturbed flow), and "2" -- to parameters behind the shock wave; subscript "n" denotes the velocity vector component normal to the wave surface, and "τ" -- the tangential component of the velocity vector. At comparatively low Reynolds numbers conditions (11) may be replaced by generalized Rankine-Hugoniot relations that account for viscous effects (see Ref. 21).

Assignment of conditions of the "side" boundaries of the integration region depends on the nature of the flow to be simulated. In the case of flow around asymmetric bodies or around bodies at a non-zero angle of attack, the flows do not have symmetry. In such cases, it is necessary to consider the region of flow near the body in its entirety, i. e. to assume that boundaries $q^3 = q^3_\Lambda$ and $q^3 = q^3_\Pi$ coincide, and to assign on these boundaries the cyclicity conditions

$$\vec{g}\big|_{q^3 = q^3_\Lambda} = \vec{g}\big|_{q^3 = q^3_\Pi}$$

where vector $\vec{g}$ has components (ρ, u, v, w, p). If flow is symmetric relative to a plane of symmetry, then boundaries $q^3 = q^3_\Lambda$ and $q^3 = q^3_\Pi$ coincide with the plane of symmetry, and conditions

$$\frac{\partial V_\tau}{\partial n} = \frac{\partial \rho}{\partial n} = \frac{\partial p}{\partial n} = V_n = 0 \qquad \text{(I2)}$$

hold there, where n is the normal to the plane of symmetry, v_n and v_τ are the velocity vector components normal and tangential to the plane of symmetry.

In this formulation, the problem is solved by a finite-difference iteration method, in which equations (1.1), (1.2) are integrated from one coordinate surface $q^1 = \text{const}$ to the other, beginning with the initial data surface $q^1 = q_0^1$.

The equations are regularized in the subsonic wall zones. In doing this, the regularizing functions are introduced into each momentum equation, since in the curvilinear coordinate system q^1, q^2, q^3 each of these equations contains terms with gradient $\partial p/\partial q^1$ that describe propagation of perturbations upstream in the subsonic zones.

§3. Scheme for two-dimensional equations

Let us introduce a difference grid Q_h into the computation region Q with steps h_1 and h_2 in directions x and y respectively. We define values of grid functions at the nodes of the grid (n, j), i. e. we take $f_j^n = f(x^n, y_j)$, where superscript n denotes the number of the node of the grid in direction x, and the subscript denotes the node number in direction y. Let us introduce difference operators Λ_2^k, Λ_{22} that approximate derivatives $\partial/\partial y$ and $\partial^2/\partial y^2$ respectively at grid node (j). As operator Λ_2^k we can take symmetric Λ_2^2 or asymmetric Λ_2^k operators that approximate the first derivative with second order or with order k.

Consider the difference scheme

$$A^* \frac{\vec{f}_j^{n+1} - \vec{f}_j^n}{h_1} + \left[B^* \Lambda_2^k - C^* \Lambda_{22}\right]\left[\sigma \vec{f}_j^{n+1} + (1-\sigma)\vec{f}_j^n\right] = 0, \qquad (I)$$

that approximates system of equations (2.1) with order $O(h_1^r + h_2^k)$, where $k = 1, 2$ and $r = 2$ at $\sigma = 0.5$, and $r = 1$ at $\sigma \neq 0.5$, and is nonlinear at $\sigma \neq 0$ relative to $n+1$ layers. Here A*, B*, C* are grid matrices coinciding with matrices A, B, C at grid nodes $\sigma(n+1) + (1-\sigma)n$, j. To simplify the notation, subscript j will henceforth be omitted.

To realize scheme (1), let us consider the iterational difference scheme

$$\frac{\vec{f}^{\nu+1} - \vec{f}^{\nu}}{\tau} + A^* \frac{\vec{f}^{\nu+1} - \vec{f}^n}{h_1} + \left(B^* \Lambda_2^k - C^* \Lambda_{22}\right)\left[\sigma \vec{f}^{\nu+1} + (1-\sigma)\vec{f}^n\right] = 0, \qquad (2)$$

that approximates system of equations (2.1); the convergence of the iterations has the same order as in initial scheme (1). Scheme (2) is derived from (1) by adding terms $(\vec{f}^{\nu+1} - \vec{f}^{\nu})/\tau$ that are equivalent to fictitious time derivatives. Here τ is an iteration parameter, ν is the iteration number in section $n+1$, i. e. $\vec{f}^{\nu} = \vec{f}^{(n+1)^{\nu}}$. Matrix operators A^{ν}, B^{ν}, C^{ν} are taken at grid nodes $\sigma(n+1) + (1-\sigma)n$, j, i. e.

$$\mathcal{D}^{\nu} = \sigma \mathcal{D}^{(n+1)^{\nu}} + (1-\sigma)\mathcal{D}^n$$

where D is any of the matrices A, B or C. Iteration scheme (2) is linear relative to iteration $\nu+1$, and its solution can be found by vector sweeps.

Let us write system of difference equations (2) as

$$\vec{\Pi}^{\nu} \frac{\vec{f}^{\nu+1} - \vec{f}^{\nu}}{\tau} = -\vec{\Omega}^{\nu}, \qquad (3)$$

where E is the unit matrix,

$$\tilde{\Pi}^{\nu} = E + \frac{\tau}{h_1} A^{\nu} + \tau\sigma\left(B^{\nu}\Lambda_2^{\frac{1}{2}} - C^{\nu}\Lambda_{22}\right),$$

$$\vec{\Omega}^{\nu} = A^{\nu}\frac{\vec{f}_1^{\nu} - \vec{f}_1^{\nu}}{h_1} + \left(B^{\nu}\Lambda_2^{\frac{1}{2}} - C^{\nu}\Lambda_{22}\right)\left[\sigma\vec{f}^{\nu} + (1-\sigma)\vec{f}^{n}\right],$$

Let us factor operator $\tilde{\Pi}^{\nu}$ approximately, representing it as

$$\tilde{\Pi}^{\nu} \approx \Pi^{\nu} = \Pi_1^{\nu}\Pi_2^{\nu}\Pi_3^{\nu} \qquad (4)$$

where

$$\Pi_1^{\nu} = E + \frac{\tau}{h_1}A^{\nu},\ \Pi_2^{\nu} = E + \tau\sigma\left(B_1^{\nu}\Lambda_2^{\frac{1}{2}} - C^{\nu}\Lambda_{22}\right),\ \Pi_3^{\nu} = E + \tau\sigma B_2^{\nu}\Lambda_2^{\frac{1}{2}},$$

$$A^{\nu} = \begin{pmatrix} u^{\nu} & \rho^{\nu} & 0 & 0 \\ 0 & u^{\nu} & 0 & 1/\rho^{\nu} \\ 0 & 0 & u^{\nu} & 0 \\ 0 & \gamma p^{\nu} & 0 & u^{\nu} \end{pmatrix},\quad B_1^{\nu}\Lambda_2^{\frac{1}{2}} = \begin{pmatrix} v^{\nu} & 0 & 0 & 0 \\ 0 & v^{\nu} & 0 & 0 \\ 0 & 0 & v^{\nu} & 0 \\ 0 & 0 & 0 & v^{\nu} \end{pmatrix}\Lambda_2^{\frac{1}{2}},$$

$$B_2^{\nu}\Lambda_2^{\frac{1}{2}} = \begin{pmatrix} 0 & 0 & \rho^{\nu}\Lambda_2^{\frac{1}{2}} & 0 \\ 0 & 0 & 0 & 0 \\ 0 & 0 & 0 & 1/\rho^{\nu}\Lambda_2^{\frac{1}{2}} \\ 0 & 0 & \gamma p^{\nu}\Lambda_2^{\frac{1}{2}} & 0 \end{pmatrix},\quad C^{\nu} = \begin{pmatrix} 0 & 0 & 0 & 0 \\ 0 & m^{\nu} & 0 & 0 \\ 0 & 0 & m^{\nu} & 0 \\ 0 & 0 & 0 & \frac{\gamma}{p_r}m^{\nu} \end{pmatrix}.$$

Representation of operator $\tilde{\Pi}^{\nu}$ in form (4) corresponds to decomposition by physical processes: operator A^{ν} accounts for gasdynamic terms in direction x, $B_1^{\nu}\Lambda_2^{\frac{1}{2}}$ accounts for transfer terms in direction y, $B_2^{\nu}\Lambda_2^{\frac{1}{2}}$ accounts for terms with pressure in direction y, and $C^{\nu}\Lambda_{22}$ accounts for viscous terms. Here $\Lambda_2^{\frac{1}{2}}$ is a unilateral operator, and Λ_2^2 is a symmetric operator. Decomposition of this kind enables us to construct iteration schemes that are realizable by scalar sweeps. With consideration of representation (4), iteration scheme

$$\Pi^{\nu}\frac{\vec{f}^{\nu+1} - \vec{f}^{\nu}}{\tau} = -\vec{\Omega}, \qquad (5)$$

or its equivalent in fractional steps

$$\begin{aligned} \Pi_1^{\nu}\vec{\xi}^{1/3} &= -\vec{\Omega}, \\ \Pi_2^{\nu}\vec{\xi}^{2/3} &= \vec{\xi}^{1/3}, \\ \Pi_3^{\nu}\vec{\xi}^{\nu+1} &= \vec{\xi}^{2/3}, \\ \vec{f}^{\nu+1} &= \vec{f}^{\nu} + \tau\vec{\xi}^{\nu+1} \end{aligned} \qquad (6)$$

approximates system of equations (1) with convergence of iterations with order $O(h_1^2 + h_2^{\frac{1}{2}})$. Let us discuss realization of scheme (6) in fractional steps.

On the first step, the system of difference equations can be resolved explicitly, since operator Π_1^{ν} does not contain derivatives, and its inversion is equivalent to finding an inverse 4 x 4 matrix. On the second fractional step, each difference equation of the system is solved independently by scalar sweeps, since operator Π_2^{ν} is diagonal.

On the third fractional step the difference equations

$$\begin{aligned} &\xi_\rho^{\nu+1} + \tau\alpha\rho\Lambda_1^2\xi_v^{\nu+1} = \xi_\rho^{1/3}, \\ &\xi_u^{\nu+1} = \xi_u^{1/3}, \\ &\xi_v^{\nu+1} + \frac{\tau\alpha}{\rho}\Lambda_1^2\xi_\rho^{\nu+1} = \xi_v^{1/3}, \\ &\xi_\rho^{\nu+1} + \tau\alpha\gamma\rho\Lambda_1^2\xi_v^{\nu+1} = \xi_\rho^{1/3} \end{aligned} \qquad (7)$$

are solved in the following sequence: using the third equation to eliminate $\xi_v^{\nu+1}$ from the fourth equation, we get a second-order difference equation for determination of $\xi_\rho^{\nu+1}$:

$$\xi_\rho^{\nu+1} - (\tau\alpha)^2\gamma\rho\Lambda_1^2\frac{1}{\rho}\Lambda_1^2\xi_\rho^{\nu+1} = \xi_\rho^{1/3} - \tau\alpha\gamma\rho\Lambda_1^2\xi_v^{1/3},$$

which is resolved by a scalar sweep. With respect to the known discrepancy of $\xi_\rho^{\nu+1}$, we find $\xi_v^{\nu+1}$ from the third equation, and then $\xi_\rho^{\nu+1}$ from the first.

Thus resolution of system of difference equations (6) reduces to a sequence of scalar sweeps and direct recalculations by explicit formulas, which results in a considerable savings of machine time when this method is computerized.

After finding vector

$$\vec{f}^{\nu+1} = \vec{f}^{\nu} + \tau\vec{\xi}^{\nu+1}$$

the cycle of computations is repeated. The iteration is continued until the specified norm of the quantity

$$(\vec{f}^{\nu+1} - \vec{f}^{\nu})/\tau$$

is less than a predetermined positive number ε that characterizes the degree of convergence of the interation process.

Let us consider the question of convergence of iterations in section $n+1$. For the sake of simplicity in the presentation, here and below we will take weight σ as equal to 1. Taking the coefficients of matrices A, B, C as constant (principle of frozen coefficients), let us subtract system of equations (1) from (2). As a result we get the system of difference equations

$$\frac{\vec{\psi}_j^{\nu+1} - \vec{\psi}_j^{\nu}}{\tau} + A\frac{\vec{\psi}_i^{\nu+1}}{h_1} + B\Lambda_2^{\kappa}\vec{\psi}_j^{\nu+1} = C\Lambda_{12}\vec{\psi}_j^{\nu+1}, \qquad (8)$$

where

$$\vec{\psi}_j^{\nu+1} = \vec{f}_j^{\nu+1} - \vec{f}_j^{n+1}$$

is the difference of solutions of iteration scheme (2) and difference scheme (1). Let us study the behavior of deflection vector $\vec{\psi}_j^{\nu}$ with increasing ν for a solution of the form

$$\vec{\psi}_j^{\nu} = \vec{\psi}_0\lambda^{\nu}e^{i\kappa jh_2}. \qquad (9)$$

Substituting (9) in (8) we get a system of equations

$$\left(\frac{\lambda-1}{\tau}E + \frac{\lambda}{h_1}A + d_1\lambda B_1 + d_2\lambda B_2 - d_3\lambda C\right)\vec{\psi}_0 = 0, \quad (10)$$

that implies the characteristic equations

$$\det\left\|\lambda\left(E + \frac{\tau}{h_1}A + \tau d_1 B_1 + \tau d_2 B_2 - \tau d_3 C\right) - E\right\| = 0, \quad (11)$$

where

$$d_1 = d_1^{\pm} = \begin{cases} d_1^+, & \text{if } V \geq 0 \\ d_1^-, & \text{if } V < 0 \end{cases}, \quad d_1^{\pm} = \pm\frac{1-\cos\varkappa h_2}{h_2} + i\frac{\sin\varkappa h_2}{h_2},$$
$$d_2 = \frac{i}{h_2}\sin\varkappa\frac{h_2}{2}, \quad d_3 = -\frac{4}{h_2}\sin^2\varkappa\frac{h_2}{2}.$$

With regularization (2.5) and assuming $\gamma/Pr = 1$, the roots of equation (11) are

$$\lambda_1 = \frac{1}{1 + \frac{\tau}{h_1}u + \tau V d_1^+}, \quad \lambda_2 = \frac{1}{1 + \frac{\tau}{h_1}u + \tau V d_1^+ - \tau m d_3},$$
$$\lambda_{3,4} = \frac{1}{1 + \frac{\tau}{h_1}u + \tau V d_1^+ - \tau m d_3 \pm \tau c\sqrt{(d_2)^2 + \varkappa^2/h_1^2}}.$$

This implies that $|\lambda_j| \leq 1$. Thus the solution of iteration scheme (2) converges to the solution of system (1) on each layer $x = \text{const}$.

Let us consider the stability of difference scheme (1) with transition from section to section. The characteristic equation corresponding to (1) takes the form:

$$\det\left\|A\frac{\lambda-1}{h_1} + d_1\lambda B_1 + d_2\lambda B_2 - d_3\lambda C\right\| = 0. \quad (12)$$

The first two roots of equation (12) are

$$\lambda_1 = \frac{1}{1 + h_1 d_1^{\pm}\frac{V}{u}}, \quad \lambda_2 = \frac{1}{1 + h_1 d_1^{\pm}\frac{V}{u} - h_1 d_3\frac{m}{u}}$$

and obviously $|\lambda_\ell| \leq 1$ ($\ell = 1, 2$) for all $u > 0$. The remaining two roots for $\gamma/Pr = 1$, $v = m = 0$ (flow weakly diverging from Ox axis at high Reynolds numbers)

$$\lambda_{3,4} = 1 \Big/ \left[1 \pm \frac{h_1 d_2}{\sqrt{M_x^2 - \varkappa^2}}\right]$$

are also less than unity in absolute value with regularization (2.6). In the case where the effect of the transverse pressure gradient in the stream is small ($P_y = 0$), we have the following values of the third and fourth roots of equation (12)

$$\lambda_{3,4} = \frac{1}{1 + \frac{h_1(d_1^{\pm}V - d_3 m)}{c(M_x \pm \sqrt{\varkappa^2})}}$$

that also are no greater than 1 in absolute value if condition (2.6) is met. Consequently difference scheme (2) for system of equations (2.1) with appropriate regularization in the approximation of "frozen" coefficients is stable relative to iterations and advancement of the solution in the direction of improvement (direction x in our case).

§4. Scheme for three-dimensional equations

Let us go on to construction of an iteration difference scheme for a system of three-dimensional equations of viscous gas (1.1), (1.2) in curvilinear coordinates q^i ($i = 1, 2, 3$). By analogy with the two-dimensional case (see §3), we consider the implicit difference schemes

$$a^{n+1}\frac{\rho^{n+1}-\rho^n}{h_t}+(b^{n+1}\Lambda_1^{k}+c^{n+1}\Lambda_3^{k}+d^{n+1})\rho^{n+1}=0, \quad (I)$$

$$A^{n+1}\frac{\vec{f}^{n+1}-\vec{f}^n}{h_t}+(B^{n+1}+C^{n+1}+D^{n+1}-G^{n+1}-Q^{n+1})\vec{f}^{n+1}=\vec{F}^{n+1}, \quad (2)$$

that approximate equations (1.1) and (1.2) with order $O(h_1+h_2^k+h_3^k)$. Here and below we take the notation of §3 (difference operator Λ_2^k approximates differential operator $\partial/\partial q^2$, and Λ_3^k approximates $\partial/\partial q^3$). Where possible, we omit the subscripts for grid nodes in directions q^2 and q^3. Since schemes (1) and (2) are nonlinear relative to layer $n+1$, for their realization we consider iteration schemes

$$\frac{\vec{f}^{s+1}-\vec{f}^s}{\tau}+A^s\frac{\vec{f}^{s+1}-\vec{f}^n}{h_t}+(B^s+C^s+D^s-G^s-Q^s)\vec{f}^{s+1}=\vec{F}^s, \quad (3)$$

$$\frac{\rho^{s+1}-\rho^s}{\tau}+a^{s+1}\frac{\rho^{s+1}-\rho^n}{h_t}+(b^{s+1}\Lambda_2^{k}+c^{s+1}\Lambda_3^{k}+d^{s+1})\rho^{s+1}=0, \quad (4)$$

that are resolvable on each iteration in two stages. On the first stage the equations of momentum and energy (3) are solved. In doing this, the densities are taken from the preceding iteration. Then using the resultant velocities and pressure the density is found from the difference analog of the continuity equation (4). This marks the end of the iteration, and the cycle is repeated. Let us consider the solution of the equations on each of the stages.

We rewrite system of equations (3) as

$$\tilde{\Pi}^s\frac{\vec{f}^{s+1}-\vec{f}^s}{\tau}=-\vec{\Omega}^s, \quad (5)$$

where

$$\tilde{\Pi}^s=E+\frac{\tau}{h_t}A^s+\tau B^s+\tau C^s+\tau D^s-\tau G^s-\tau Q^s, \quad (6)$$

$$\vec{\Omega}^s=A^s\frac{\vec{f}^s-\vec{f}^n}{h_t}+(B^s+C^s+D^s-G^s-Q^s)\vec{f}^s-\vec{F}. \quad (7)$$

Let us factor operator $\tilde{\Pi}^{\nu}$ approximately, representing it as

$$\tilde{\Pi}^{j} \approx \Pi^{j} = \Pi_1^{j} \Pi_2^{j} \Pi_3^{j} \Pi_4^{j} \Pi_5^{j} . \tag{8}$$

Here

$$\Pi_1^{j} = E + \frac{\tau}{h_1} A^{j} + \tau D^{j}, \quad \Pi_2^{j} = E + \tau B_1^{j} - \tau G^{j}, \quad \Pi_3^{j} = E + \tau B_2^{j}$$

$$\Pi_4^{j} = E + \tau C_1^{j} - \tau Q^{j}, \quad \Pi_5^{j} = E + \tau C_2^{j} ,$$

$$B_1 = \begin{pmatrix} b & 0 & 0 & 0 \\ 0 & b & 0 & 0 \\ 0 & 0 & b & 0 \\ 0 & 0 & 0 & b \end{pmatrix} \Lambda_2^{k}, \quad B_2 = \begin{pmatrix} 0 & 0 & 0 & z_1^1/\rho \\ 0 & 0 & 0 & z_2^1/\rho r^2 \\ 0 & 0 & 0 & z_3^1/\rho \\ r\rho z_1^1 & r\rho \frac{z_2^1}{r^2} & r\rho z_3^1 & 0 \end{pmatrix} \Lambda_2^{2},$$

$$C_1 = \begin{pmatrix} c & 0 & 0 & 0 \\ 0 & c & 0 & 0 \\ 0 & 0 & c & 0 \\ 0 & 0 & 0 & c \end{pmatrix} \Lambda_3^{k}, \quad C_2 = \begin{pmatrix} 0 & 0 & 0 & z_1^2/\rho \\ 0 & 0 & 0 & z_2^2/\rho r^2 \\ 0 & 0 & 0 & z_3^2/\rho \\ r\rho z_1^2 & r\rho \frac{z_2^2}{r^2} & r\rho z_3^2 & 0 \end{pmatrix} \Lambda_3^{2},$$

Λ_j^k and Λ_j^2 are unilateral and symmetric difference operators that approximate the differential operators $\partial/\partial q^1$ ($j = 2, 3$). The representation of operator $\tilde{\Pi}^{\nu}$ in form (8), which corresponds to decomposition with respect to physical processes and spatial directions, enables resolution of scheme (5) by scalar sweeps. With consideration of representation (8), the iteration scheme

$$\Pi^{j} \frac{\vec{f}^{j+1} - \vec{f}^{j}}{\tau} = - \vec{\Omega}^{j}, \tag{9}$$

or its equivalent in fractional steps

$$\begin{aligned} &(E + \frac{\tau}{h_1} A + \tau D) \vec{\xi}^{1/5} = - \vec{\Omega}, \\ &(E + \tau B_1 - \tau G) \vec{\xi}^{2/5} = \vec{\xi}^{1/5}, \\ &(E + \tau B_2) \vec{\xi}^{3/5} = \vec{\xi}^{2/5}, \\ &(E + \tau C_1 - \tau Q) \vec{\xi}^{4/5} = \vec{\xi}^{3/5}, \\ &(E + \tau C_2) \vec{\xi}^{j+1} = \vec{\xi}^{4/5}, \\ &\vec{f}^{j+1} = \vec{f}^{j} + \tau \vec{\xi}^{j+1} \end{aligned} \tag{10}$$

approximates system of equations (2) with convergence of iterations with order $O(h_1 + h_2^k + h_3^k)$.

Let us consider realization of scheme (10). In order to start computation in a "new" section $n+1$, $q^1 = \text{const}$, we have to assign a zeroth iteration, using one of the following extrapolation formulas:

$$\vec{f}^{\circ} = \vec{f}^{n} + O(h_1),$$
$$\vec{f}^{\circ} = 2\vec{f}^{n} - \vec{f}^{n-1} + O(h_1^2).$$

Calculations showed that either of these formulas gives the same rate of convergence and results, and the first formula was used in further computations. Realization of scheme (10) starts with calculation of the vector $\vec{\Omega}$ of the right-hand members at internal grid nodes. After computing the right-hand member, the first fractional step is realized

$$(E + \frac{\tau}{h_1}A + \tau D)\vec{\xi}^{1/5} = -\vec{\Omega}$$

which is equivalent to the system of algebraic equations

$$\begin{aligned}
&(1 + \tfrac{\tau}{h_1}a)\xi_u^{1/5} + \tfrac{\tau}{h_1}\tfrac{\bar{z}_1^1}{\rho}\xi_p^{1/5} = -\Omega_1,\\
&(1 + \tfrac{\tau}{h_1}a)\xi_v^{1/5} + \tau\tfrac{v}{2}\xi_w^{1/5} + \tfrac{\tau}{h_1}\tfrac{\bar{z}_2^1}{\rho^2}\xi_p^{1/5} = -\Omega_2,\\
&(1 + \tfrac{\tau}{h_1}a)\xi_w^{1/5} - \tau\tfrac{v}{2}\xi_v^{1/5} + \tfrac{\tau}{h_1}\tfrac{\bar{z}_3^1}{\rho}\xi_p^{1/5} = -\Omega_3, \qquad (11)\\
&(1 + \tfrac{\tau}{h_1}a + \tau\tfrac{\gamma w}{2})\xi_p^{1/5} + \tfrac{\tau}{h_1}\gamma\rho(\bar{z}_1^1\xi_u^{1/5} + \tfrac{\bar{z}_2^1}{2}\xi_v^{1/5} + \bar{z}_3^1\xi_w^{1/5}) = -\Omega_4.
\end{aligned}$$

On the second fractional step the system of difference equations

$$(E + \tau B_1 - \tau G_1)\vec{\xi}^{2/5} = \vec{\xi}^{1/5} \qquad (12)$$

is resolved by scalar three-point sweeps, since B_1 and G are diagonal operators.

The third fractional step

$$(E + \tau B_2)\vec{\xi}^{3/5} = \vec{\xi}^{2/5}$$

corresponds to the following system of difference equations

$$\begin{aligned}
&\xi_u^{3/5} + \tfrac{\tau\bar{z}_1^1}{\rho}\Lambda_2^2\xi_p^{3/5} = \xi_u^{2/5},\\
&\xi_v^{3/5} + \tfrac{\tau\bar{z}_2^1}{\rho^2}\Lambda_2^2\xi_p^{3/5} = \xi_v^{2/5},\\
&\xi_w^{3/5} + \tfrac{\tau\bar{z}_3^1}{\rho}\Lambda_2^2\xi_p^{3/5} = \xi_w^{2/5}, \qquad (13)\\
&\xi_p^{3/5} + \tau\gamma\rho(\bar{z}_1^1\Lambda_2^2\xi_u^{3/5} + \tfrac{\bar{z}_2^1}{2}\Lambda_2^2\xi_v^{3/5} + \bar{z}_3^1\Lambda_2^2\xi_w^{3/5}) = \xi_p^{2/5}.
\end{aligned}$$

Eliminating the quantities $\xi_u^{3/5}$, $\xi_v^{3/5}$, $\xi_w^{3/5}$ from the last equation of system (13), we get a three-point difference equation relative to $\xi_p^{3/5}$:

$$\xi_p^{3/5} - \tau^2\gamma\rho\left[z_1^2\Lambda_2^2\frac{z_1^2}{\rho}\Lambda_2^2\xi_p^{3/5} + \frac{z_2^2}{2}\Lambda_2^2\frac{z_2^2}{\rho^2}\Lambda_2^2\xi_p^{3/5} + z_3^2\Lambda_2^2\frac{z_3^2}{\rho}\Lambda_2^2\xi_p^{3/5}\right] = \xi_p^{2/5} - \tau\gamma\rho\left(z_1^2\Lambda_2^2\xi_u^{2/5} + \frac{z_2^2}{2}\Lambda_2^2\xi_v^{2/5} + z_3^2\Lambda_2^2\xi_w^{2/5}\right),$$

that are solved by a scalar sweep.

The fourth

$$(E + \tau C_1 - \tau Q)\vec{\xi}^{4/5} = \vec{\xi}^{3/5} \qquad (I4)$$

and fifth

$$(E + \tau C_2)\vec{\xi}^{j+1} = \vec{\xi}^{4/5} \qquad (I5)$$

fractional steps coincide in structure with the second and third steps, and can be realized by analogous formulas.

The new values $u^{\nu+1}$, $v^{\nu+1}$, $w^{\nu+1}$, $p^{\nu+1}$ are computed by the formula

$$\vec{f}^{j+1} = \vec{f}^{j} + \tau\vec{\xi}^{j+1}. \qquad (I6)$$

The resultant velocity field satisfies sticking conditions on the surface of the body since it is assumed that

$$\xi_{u_{ij}} = \xi_{v_{ij}} = \xi_{w_{ij}} = 0. \qquad (I7)$$

To calculate pressure on the surface of the body, we use one of the following formulas:

$$p_{1j}^{j} = p_{2j}^{j} \qquad (I8)$$

or

$$p_{1j}^{j} = p_{2j}^{j} - \frac{\mu_{ij}^{j}}{3}\left[8\frac{(v^2)_{2j}^{j}}{h_2} + \frac{(v^1)_{2j}^{j} - (v^1)_{1j}^{n}}{h_1} + \frac{(v^3)_{2j+1}^{j} - (v^3)_{2j-1}^{j}}{2h_3}\right] - (v^1)_{2j}^{j}\frac{\mu_{2j}^{j} - \mu_{1j}^{n}}{h_1} - (v^3)_{2j}^{j}\frac{\mu_{2j+1}^{j} - \mu_{2j-1}^{j}}{2h_3}, \qquad (I9)$$

$$v^k = uz_1^k + v\frac{z_2^k}{2} + wz_3^k, \quad k = 1,2,3$$

that are difference approximations of different orders for the equation of momentum in the projection on the normal to the solid.

After realizing scheme (10) by one of the above-mentioned formulas, we calculate the pressure on the surface of the body. The choice of representation

of pressure on the body depends on the nature of flow (detached, undetached) and on the necessary accuracy. As an example, for undetached flows near bodies of the sphere and cone type representation (18) gives completely satisfactory results even for considerable angles of attack (up to 20°).

Let us consider the second stage of the numerical method of solving system of equations (3), (4) -- solution of continuity equation (4).

Let us rewrite equation (4)

$$\tilde{\Pi}_\rho^{\nu+1}\frac{\rho^{\nu+1}-\rho^\nu}{\tau} = -\Omega_\rho , \qquad (20)$$

where

$$\tilde{\Pi}_\rho^{\nu+1} = 1 + \frac{\tau}{h_1}a^{\nu+1} + \tau b^{\nu+1}\Lambda_2^\kappa + \tau c^{\nu+1}\Lambda_3^\kappa + \tau d^{\nu+1} , \qquad (21)$$

$$\Omega_\rho = a^{\nu+1}\frac{\rho^\nu-\rho^h}{h_1} + (b^{\nu+1}\Lambda_2^\kappa + c^{\nu+1}\Lambda_3^\kappa + d^{\nu+1})\rho^\nu . \qquad (22)$$

Let us factor operator $\tilde{\Pi}_\rho^{\nu+1}$ approximately,

$$\tilde{\Pi}_\rho^{\nu+1} \approx \Pi_\rho = (1 + \frac{\tau}{h_1}a^{\nu+1} + \tau d^{\nu+1} + \tau b^{\nu+1}\Lambda_2^\kappa)(1 + \tau c^{\nu+1}\Lambda_3^\kappa)$$

and replace equation (20) by the scheme in fractional stepa

$$\begin{aligned}(1 + \frac{\tau}{h_1}a^{\nu+1} + \tau d^{\nu+1} + \tau b^{\nu+1}\Lambda_2^\kappa)\xi_\rho^{\nu+1/2} &= -\Omega_\rho ,\\ (1 + \tau c^{\nu+1}\Lambda_3^\kappa)\xi_\rho^{\nu+1} &= \xi_\rho^{\nu+1/2} ,\\ \rho^{\nu+1} &= \rho^\nu + \tau\xi_\rho^{\nu+1} .\end{aligned} \qquad (23)$$

Scheme (23) is realized on each fractional step by scalar sweeps. The values of coefficients α_1 and β_1 in the sweep formula

$$\xi_{\rho ij}^{\nu+1/2} = \alpha_i\xi_{\rho i+1,j}^{\nu+1/2} + \beta_i , \quad i = I-1, \ldots, 1$$

on the first fractional step depend on the given mode of heat exchange, and are equal to:

for thermal isolation

$$\alpha_1 = \frac{\rho_{1j}^{\nu+1}}{\rho_{2j}^{\nu+1}} , \quad \beta_1 = \rho_{2j}^\nu\left(\frac{p_{1j}^{\nu+1}}{\rho_{2j}^{\nu+1}} - \frac{p_{1j}^\nu}{\rho_{2j}^\nu}\right) ;$$

for cooling of the wall

$$\alpha_1 = 0 , \quad \beta_1 = \frac{1}{(\gamma-1)\varepsilon_w}\xi_{p1j}^{\nu+1} .$$

The second stage concludes with calculation of density $\rho^{\nu+1}$ by formula

$$\rho^{\nu+1} = \rho^\nu + \tau\xi_\rho^{\nu+1} .$$

If the upper bound is chosen in the region of undisturbed flow, calculation of a single iteration concludes here. If the outer bound of the calculated region is the head shock wave, the gasdynamic quantities there must be recalculated after computing values inside the region on each iteration, and in the same way with transition to the next cross section $q^1 = \text{const}$.

§5. Algorithm for isolating head shock wave

The head shock wave is isolated in the following sequence:

1) the position of the head shock wave on the n-th layer of cross section $q^1 = \text{const}$ is extrapolated to the n+1-th layer and taken as the outer bound of the computational region;

2) from the known configuration of the wave and parameters of the oncoming flow, the parameters behind the wave are determined from the Rankine-Hugoniot conditions and taken as the values of the gasdynamic functions on the outer boundary on the "zeroth" iteration;

3) gasdynamic parameters are calculated inside the region by the scheme described above;

4) pressure on the outer boundary behind the wavefront is determined by extrapolation from the values calculated inside the region, and the values of the remaining gasdynamic functions behind the wavefront and the position of the wave itself are determined from the Rankine-Hugoniot relations.

Let us consider points 1), 2) and 4) in more detail in the algorithm for isolating the head shock wave.

1. Coordinate system q^1, q^2, q^3 that is used in finally writing out the principal equations is adjusted by successive coordinate transformations, the first of which

$$\tilde{q}^i = \tilde{q}^i(z, \theta, r), \quad i = 1, 2, 3 \qquad (1)$$

transforms the initial cylindrical coordinates z, θ, r to curvilinear coordinates $\tilde{q}^i$ satisfying requirements a) and b) of §1. Besides this, coordinate $\tilde{q}^2$ is the length of a segment of a coordinate line of the second family included between the surface of the body and a point of space. The surface of the body is a coordinate surface $\tilde{q}^2 = 0$. Let $\tilde{q}^2 = \bar{x}(\tilde{q}^1, \tilde{q}^3)$ be the equation of the surface of the head shock wave. Transformation

$$\hat{q}^1 = \tilde{q}^1, \quad \hat{q}^2 = \tilde{q}^2 / \bar{\tilde{x}}(\tilde{q}^1, \tilde{q}^3), \quad \hat{q}^3 = \tilde{q}^3 \qquad (2)$$

converts coordinates $\tilde{q}^i$ to $\hat{q}^j$ in which the surface of the head shock wave is a coordinate surface $\hat{q}^2 = 1$. Finally, the third transformation

$$q^1 = \hat{q}^1, \quad q^2 = q^2(\hat{q}^2), \quad q^3 = q^3(\hat{q}^3) \qquad (3)$$

enables us to crowd coordinate surfaces $\tilde{q}^2 = \text{const}$ and $\tilde{q}^3 = \text{const}$ in regions of high gradients while leaving the difference grid uniform on coordinates q^1.

Thus the equation of the wave surface enters into the coordinate transformation coefficients z_j^i, and it must be assigned on a new cross section before starting the iterations. Let us set

$$\tilde{x}(\tilde{q}^1, \tilde{q}^3) = \tilde{x}(\tilde{q}^1(q^1), \tilde{q}^3(q^3)) = x(q^1, q^3) .$$

Then the initial position of the head shock wave surface is assigned by extrapolating the wave position from preceding cross sections $q^1 = \text{const}$ using one of the formulas

$$x_j^{n+1} = x_j^n + O(h_1), \tag{4}$$

$$x_j^{n+1} = 2x_j^n - x_j^{n-1} + O(h_1) \tag{5}$$

(j is the node number in the direction of coordinate q^3).

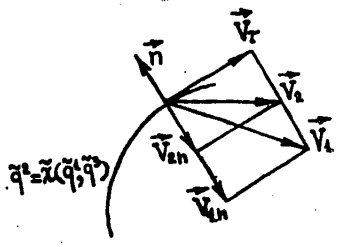

Fig. 3

In extrapolation, we must meet a requirement stemming from the properties of the compression shock that is as follows. The normal component of the velocity vector of the incident flow to the wave surface, and the outer normal to this surface must be opposite in direction (Fig. 3), i. e. we must satisfy the inequality

$$\vec{V}_1 \cdot \vec{n} < 0 , \tag{6}$$

where $\vec{v}_1$ is the vector of the incident flow, $\vec{n}$ is the vector of the outer unit normal to the surface of the shock wave. The results of calculations and rates of convergence of iterations with the use of extrapolation formulas (4) and (5) when condition (6) is met were nearly the same. Moreover, no appreciable differences were observed in results or rates of convergence when x_j^{n+1} was taken as the position obtained from x_j^n by formula

$$x_j^{n+1} = x_j^n + ch_1 , \tag{7}$$

where c is some non-negative quantity selected in accordance with condition (6).

2. After determining the position of the upper bound x_j^{n+1}, a new distribution of nodes of the grid is assigned in cross section n + 1. The initial values of gasdynamic functions in the inner nodes of this grid and in those lying on the surface of the body are taken (see §4) from the corresponding nodes of cross section n. To determine the quantities on the outer boundary of the cross section, we use the Rankine-Hugoniot relations (2.11) from which we get an expression for the gas parameters behind the wavefront

$$p_2 = \frac{2\rho_1 V_{1n}^2 - (\gamma-1)p_1}{\gamma+1} , \tag{8}$$

$$\rho_2 = \rho_1 \frac{1}{1 + \frac{p_1 - p_2}{\rho_1 V_{1n}^2}} , \tag{9}$$

$$V_{2n} = \frac{\rho_1}{\rho_2} V_{1n} . \tag{10}$$

The modulus of the normal component of the velocity vector $\vec{v}_{1n}$ is equal to

$$V_{1n} = |\vec{V}_1 \cdot \vec{n}| \quad . \tag{II}$$

The unit normal vector $\vec{n}$ is determined from the known wave equation. Let $\vec{i}_1$, $\vec{i}_2$, $\vec{i}_3$ be the orthonormalized basis in the cylindrical coordinate system z, θ, r. Then, having the implicit equation of the wave surface

$$\begin{aligned} &\tilde{f}(\tilde{q}^1, \tilde{q}^2, \tilde{q}^3) = \tilde{q}^2 - \tilde{\chi}(\tilde{q}^1, \tilde{q}^3) = \\ &= \tilde{q}^2(q^1, q^2, q^3) - \chi(q^1, q^3) = f(q^1, q^2, q^3) = \\ &= \hat{f}(z, \theta, r) = 0 \ , \end{aligned} \tag{I2}$$

we get an expression for vector $\vec{n}$

$$\vec{n} = \frac{1}{K}\left(\hat{f}_z \vec{i}_1 + \frac{\hat{f}_\theta}{r}\vec{i}_2 + \hat{f}_r \vec{i}_3\right) , \tag{I3}$$

where

$$K = \sqrt{\hat{f}_z^2 + \left(\frac{\hat{f}_\theta}{r}\right)^2 + \hat{f}_r^2} \ . \tag{I4}$$

Since the equations are integrated in the standard mathematical domain of variation of variables q^i, the derivatives with respect to other variables must be converted to derivatives with respect to q^i. Let us set

$$\begin{aligned} &\tilde{q}^2 = \hat{q}^2\tilde{\chi}(\tilde{q}^1, \tilde{q}^3) = \hat{q}^2(q^2)\,\tilde{\chi}(\tilde{q}^1(q^1), \tilde{q}^3(q^3)) = \\ &= \eta(q^2)\chi(q^1, q^3) = \pi(q^1, q^2, q^3) \ . \end{aligned} \tag{I5}$$

With consideration of (12) and (15) we get

$$\begin{aligned} \hat{f}_z &= \pi_1 z_1^1 + \pi_2 z_1^2 + \pi_3 z_1^3 - \chi_1 z_1^1 - \chi_3 z_1^3 \ , \\ \hat{f}_\theta &= \pi_1 z_2^1 + \pi_2 z_2^2 + \pi_3 z_2^3 - \chi_1 z_2^1 - \chi_3 z_2^3 \ , \\ \hat{f}_r &= \pi_1 z_3^1 + \pi_2 z_3^2 + \pi_3 z_3^3 - \chi_1 z_3^1 - \chi_3 z_3^3 \ , \end{aligned} \tag{I6}$$

where

$$\pi_i = \frac{\partial \pi}{\partial q^i} \ , \ i = 1,2,3 \ ; \quad \chi_\alpha = \frac{\partial \chi}{\partial q^\alpha} \ , \ \alpha = 1,3 \ .$$

To find the velocity vector components u_2, v_2, w_2 behind the wavefront, we use the geometric decomposition

$$\vec{V}_2 = \vec{V}_{2n} + \vec{V}_\tau \ . \tag{I7}$$

This, and the obvious equality

$$\vec{V}_\tau = \vec{V}_1 - \vec{V}_{1n}$$

imply that

$$\vec{V}_2 = \vec{V}_1 + \vec{V}_{2n} - \vec{V}_{1n} = \vec{V}_1 - |V_{2n}|\vec{n} + |V_{1n}|\vec{n} = \\ = \vec{V}_1 + (|V_{1n}| - |V_{2n}|)\vec{n} \ . \tag{I8}$$

Substituting (10) in (18), we get

$$\vec{V}_2 = \vec{V}_1 + |V_{1n}|\left(1 - \frac{\rho_1}{\rho_2}\right)\vec{n} \ ,$$

from which we finally find

$$u_2 = u_1 + g\hat{\xi}_x \ , \\ v_2 = v_1 + g\frac{\hat{\xi}_\theta}{r} \ , \tag{I9} \\ w_2 = w_1 + g\hat{\xi}_z \ ,$$

where

$$g = \frac{|V_{1n}|}{K}\left(1 - \frac{\rho_1}{\rho_2}\right) \ ,$$

and the absolute value $|v_{1n}|$ is found from (11) and is equal to

$$|V_{1n}| = \frac{1}{K}\left|u_1\hat{\xi}_x + v_1\frac{\hat{\xi}_\theta}{r} + w_1\hat{\xi}_z\right| .$$

The algorithm for calculating quantities (16) uses the following finite-difference formulas

$$\chi_1 \approx \frac{\chi_j^{j+1} - \chi_j^n}{h_1} \ , \quad \chi_3 \approx \frac{\chi_{i+1}^{j+1} - \chi_{i-1}^{j+1}}{2h_3} \ , \\ \pi_1 \approx \eta^{j+1}\frac{\chi_j^{j+1} - \chi_j^n}{h_1} \ , \quad \pi_2 \approx \dot{\eta}^{j+1}\chi^{j+1} \ , \\ \pi_3 \approx \eta^{j+1}\frac{\chi_{i+1}^{j+1} - \chi_{i-1}^{j+1}}{2h_3} \ .$$

Function $\eta(q^2)$ that sets the crowding of coordinate surfaces $\tilde{q}^2 = \text{const}$, and its derivative are defined and analytically calculated by the formulas

$$\eta(q^2) = \frac{\exp(q^2) - 1}{\beta} \ , \\ \dot{\eta}(q^2) = \frac{d\eta}{dq^2} = \frac{\exp(q^2)}{\beta}$$

where β is a parameter that determines the degree of crowding of surfaces toward the body.

4. The unknown functions on the outer boundary on each iteration (with the exception of the first) are ρ_2, u_2, v_2, w_2, p_2, x. We have five Rankine-Hugoniot relations (2.11) to determine these six unknowns. To close this system, we extrapolate the newly calculated pressures inside the region to the wave. The extrapolation formula is

$$p^{j+1}_{i,j} = 3\left(p^{j+1}_{i-1,j} - p^{j+1}_{i-2,j}\right) + p^{j+1}_{i-3,j} \,. \qquad (20)$$

Using the known pressure p_2 behind the wavefront, we find from the Rankine-Hugoniot relations (2.11)

$$\rho_2 = \rho_1 \frac{\frac{p_2}{p_1} + \frac{\gamma-1}{\gamma+1}}{\frac{\gamma-1}{\gamma+1}\frac{p_2}{p_1} + 1} \,, \qquad (21)$$

$$V^2_{1n} = \frac{\gamma+1}{2}\frac{p_1}{\rho_1}\left[\frac{p_2}{p_1} + \frac{\gamma-1}{\gamma+1}\right] \,. \qquad (22)$$

From (11) we have the expression

$$V^2_{1n} = \frac{\left[u_1\hat{\xi}_x + v_1\frac{\hat{\xi}_\theta}{r} + w_1\hat{\xi}_z\right]^2}{\hat{\xi}^2_x + \left(\frac{\hat{\xi}_\theta}{r}\right)^2 + \hat{\xi}^2_z} \,,$$

Substituting formulas (16) and (22) in this expression gives us a quadratic equation relative to x_1

$$\tilde{a}(x_1)^2 - 2\tilde{b}x_1 + \tilde{c} = 0 \,, \qquad (23)$$

where

$$\tilde{a} = V^2_{1n}g^{11} - (\hat{V}^1)^2 \,,$$
$$\tilde{b} = V^2_{1n}(\pi_i g^{i1} - x_3 g^{13}) - \hat{V}^1(\pi_i\hat{V}^i - x_3\hat{V}^3) \,,$$
$$\tilde{c} = V^2_{1n}(\pi^2_i g^{ii} + x^2_3 g^{33} - 2\pi_i g^{i3}x_3) - (\pi_i\hat{V}^i - x_3\hat{V}^3)^2 \,,$$
$$g^{kl} = z^k_1 z^l_1 + \frac{z^k_2 z^l_2}{r^2} + z^k_3 z^l_3 \,,$$
$$\hat{V}^k = u_1 z^k_1 + v_1\frac{z^k_2}{r} + w_1 z^k_3 \,.$$

Since vector $\vec{v}_\tau$ tangent to the wave surface forms a positive angle with the direction of improvement, and the quantity

$$\tilde{a} < 0 \,,$$

the following root of equation (23) is chosen:

$$x_1 = \frac{\tilde{b} - \sqrt{\tilde{b}^2 - \tilde{a}\tilde{c}}}{\tilde{a}} \qquad (24)$$

Calculating the right-hand member of (24) by using the quantities computed on iteration ν, and replacing the derivative of x_1 with the unilateral difference, we get a formula for calculating the position of the wave on iteration $\nu+1$:

$$x^{\nu+1} = x^{n} + h_1 \frac{\tilde{b}^{\nu} - \sqrt{(\tilde{b}^{\nu})^2 - \tilde{a}^{\nu}\tilde{c}^{\nu}}}{\tilde{a}^{\nu}} . \qquad (25)$$

Taking $x^{\nu+1}$ as the new outer boundary of the cross section, we find the coefficients of transformation of variables $(z\frac{1}{2})^{\nu+1}$, after which the components of the velocity vector behind the wavefront on iteration $\nu+1$ are calculated from formulas (19).

This concludes calculation of all gasdynamic functions on iteration $\nu+1$, and we go on to the new iteration $\nu+2$.

§6. Results of calculations

As the initial model we take simplified Navier-Stokes equations in which only the iterated derivatives along the normal to the surface of the body are retained from all the viscous terms. In the first part of the section we consider flow around a plate, sphere and blunt cone. Based on the solution of these problems an investigation is made of the accuracy of the proposed method, its effectiveness, and the applicability of the given model. In the second part an examination is made of the flow around a spherically blunted cone at a non-zero angle of attack.

1°. The problem of longitudinal flow of a compressible heat-conductive gas around a flat plate has numerous numerical and analytical solutions that agree well with experimental data. Therefore we verified the proposed technique by applying it to solution of this problem, which at $\mathrm{Pr} = \omega = 1$ reduces to an ordinary third-order differential equation [Ref. 22]

$$2f''' + ff'' = 0 \qquad (I)$$

with boundary conditions

$$f = f' = 0 \quad \text{when} \quad \zeta = 0$$
$$f' = 1 \quad \text{when} \quad \zeta = \infty , \qquad (2)$$

where $u = f'(\zeta)$ is the longitudinal component of the velocity vector in Dorodnitsyn variables

$$\zeta = \eta\sqrt{\frac{\mathrm{Re}}{x}} , \qquad (3)$$

$$y = \int_0^{\eta} T\,d\eta . \qquad (4)$$

Here x, y are cartesian coordinates, $y = 0$, $x \geq 0$ is the equation of the plate, $T = 1/\rho$ is absolute temperature related to internal energy by the expression

$$\varepsilon = c_v T \ .$$

Temperature is reduced to dimensionless form by normalization to its value in the undisturbed flow, and the other notation is the same as in §1. The profile of the longitudinal component u of the velocity vector was determined from the solution of problem (1), (2) taken from the table in Ref. 23, and the distribution of temperature T was calculated from the formulas:

for a cooled wall

$$T = (1 + \frac{\gamma-1}{2}M_\infty^2 - \frac{T_w}{T_\infty})u + \frac{T_w}{T_\infty} - \frac{\gamma-1}{2}M_\infty^2 u^2 , \quad (5)$$

for a heat-insulated wall

$$T = 1 + \frac{\gamma-1}{2}M_\infty^2 (1-u^2) \ . \quad (6)$$

The transverse component v of the velocity vector was found by using the equation of continuity

$$\frac{\partial \rho u}{\partial x} + \frac{\partial \rho v}{\partial y} = 0 \ .$$

The resultant parameters were assigned as the initial data in cross section x = 1. The calculation was done up to the control cross section x = const, and the results were compared with data found for this cross section from solution of equations (1)-(6). In direction y, 50 nodes were taken, and the grid was considered as uniformly crowded toward the surface of the body. The step along the Ox axis was assigned as uniform and equal to $\Delta x = 0.01$.

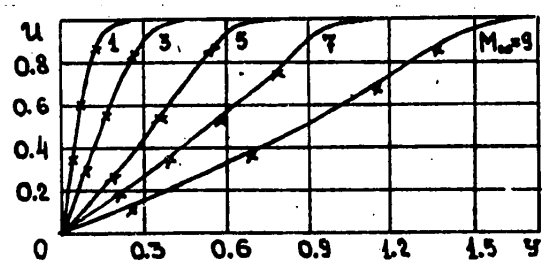

Fig. 4. Distribution of longitudinal component of velocity vector on heat-insulated plate

Fig. 4-7 show the profiles of the longitudinal component of the velocity vector and the temperature in the boundary layer on heat-insulated and cooled plates at different Mach numbers in cross section x = 1.1. The solid lines correspond to the solution of (1)-(6), and the crosses show the results by

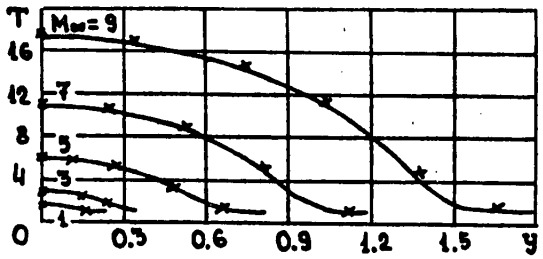

Fig. 5. Temperature distribution on heat-insulated plate

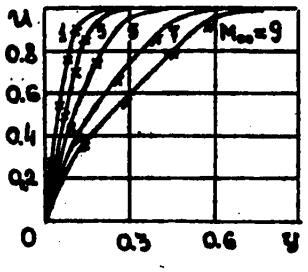

Fig. 6. Distribution of longitudinal component of velocity vector on cooled plate ($T_w = 1$)

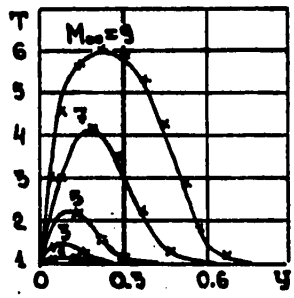

Fig. 7. Temperature distribution on cooled plate ($T_w = 1$)

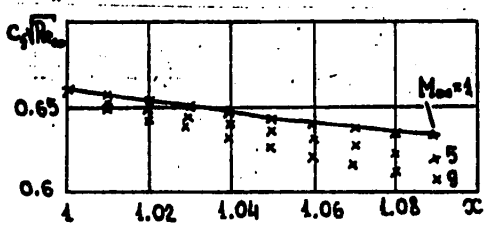

Fig. 8. Distribution of friction coefficient along heat-insulated plate

Fig. 8 shows distributions of the friction coefficient along a heat-insulated plate for different Mach numbers as obtained at $\omega = 1$ from the approximate formula [Ref. 22] (solid lines)

$$c_f = \frac{0.664}{\sqrt{Re_x}}$$

and by our method (crosses). These figures show that the difference in results increases with increasing Mach number (the maximum relative error at $M_\infty = 1$

is ≈0.3%, and at $M_\infty = 9$ it is about 10%), which can be attributed to two causes. In the first place, as the Mach number increases there is an increase in the gradients of gasdynamic functions in the boundary layer, and this leads to an increase in the error of the difference approximation of the scheme. This is confirmed by Fig. 9, which shows a graph of the change in friction coefficient as a function of the parameter β in the formula (see §5)

$$\eta(q^2) = \frac{\exp(q^2) - 1}{\beta}$$

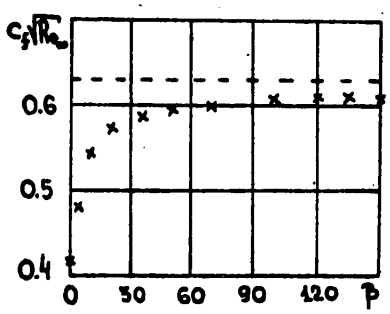

Fig. 9. Friction coefficient as a function of crowding parameter β ($M_\infty = 10$, --- approximate formula from Ref. 22)

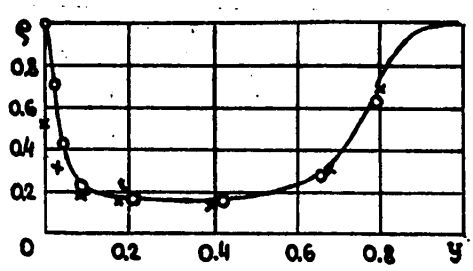

Fig. 10

With increasing parameter β there is an increase in the degree of crowding of longitudinal coordinate lines near the plate. In the second place, as the gradients of the functions in the transverse direction increase, there is an increase in the influence of convective terms in the equation of momentum in the projection on the normal to the plate. These terms are missing in the boundary layer equations, but are present in our model. Their influence on the results of calculations is clear from Fig. 10, which shows the density profiles obtained from (1)-(6) (solid line), by the given method (crosses), and also by this method but without consideration of convective terms in the equation of momentum in the projection on the normal to the plate (circles) for $M_\infty = 10$, $T_w = 1$, $x = 1.3$.

The next series of calculations was done for axisymmetric flows around a sphere and a spherically blunted cone. In the former case, data were used from Ref. 21, obtained on the basis of complete Navier-Stokes equations by the method of integral relations. A table of gasdynamic parameters of flow around a cooled sphere ($M_\infty = 6$, $\gamma = 1.4$, $Re_\infty = 3550$, $Pr = 0.7$, $\omega = 0.5$, $\varepsilon_w = 0.142$) gave the profiles of parameters in cross section $s = 0.9425$ (s is the length of the arc measured along the outline of the sphere), which were taken as initial data for the given method. Calculation was continued to cross section $s = 1.5708$, and the solution there was compared with tabulated data. On rays

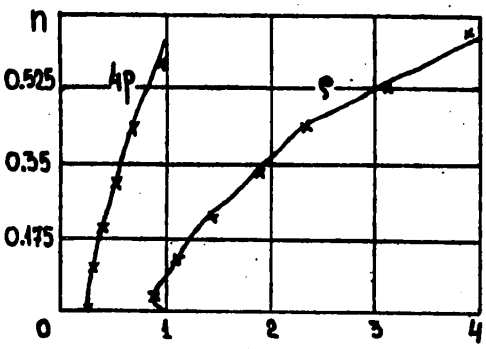

Fig. 11. Distribution of density and pressure across the shock layer at a sphere (—— data from Ref. 21, × -- data by our method)

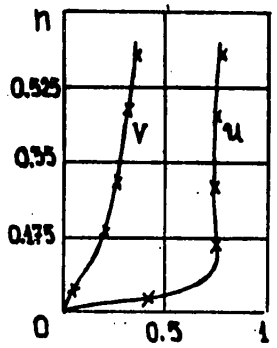

Fig. 12. Distribution of velocity components across shock layer at a sphere

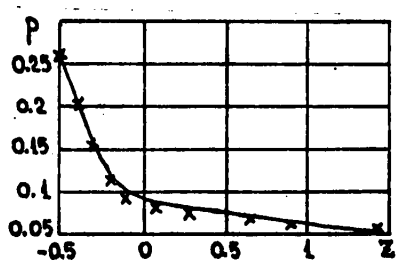

Fig. 13. Pressure distribution on spherically blunted 10° cone

s = const between the body and the shock wave there were 26 nodes of the difference grid crowded toward the body with crowding parameter (see §5) $\beta = 100$. The profiles of density, pressure and velocity components are compared on Fig. 11 and 12. Maximum relative error is ≈2%, occurring near the upper boundary, rather than near the body as might have been assumed from incorrectness of the problem in the subsonic region near the wall. This can be attributed to the fact that strong crowding of the grid in the transverse direction was used in the calculation (the minimum step in this direction near the body being of the order of 1% of the maximum step at the upper boundary).

Fig. 13 compares pressure distributions on a cooled spherically blunted 10° cone at $M_\infty = 15$, $Re_\infty = 10^4$, $\gamma = 1.4$, $Pr = 0.72$, $\omega = 0.75$, $\varepsilon_w = 0.214$. Plotted on the axis of abscissas is the distance along the axis of the body reduced to dimensionless form by reference to the blunting radius (center of the sphere at 0). The initial data and pressures for comparison (shown by the solid line on the figure) were taken from tables in Ref. 24. The crosses show the pressures on the surface as determined by our method. The maximum relative

error was ≈5%. Computing time on the given interval of the axis of the body was no more than 6 minutes on a BESM-6 for a grid with 20 nodes across the shock layer and a step $\Delta z = 0.05$ in the direction of improvement.

The resultant data show that the method considered in this paper can be successfuly used for calculations of supersonic viscous flows around a wide class of bodies.

2°. Calculations were done on supersonic viscous flow around a cooled spherically blunted cone at angle of attack α. Conical surfaces orthogonal to the surface of the body in cross sections $z = \text{const}$ were taken as the cross sections $q^1 = \text{const}$ (Fig. 14). The surface of the initial data was selected on the blunted section. Initial data on each ray of the surface were assigned from solution of the problem that is axisymmetric relative to the direction of the incident flow (Fig. 15). Initial data were taken from Ref. 21 for calculations of axisymmetric flow of a gas with parameters $M_\infty = 6$, $\gamma = 1.4$, $Re_\infty = 3550$, $Pr = 0.7$, $\omega = 0.5$, $\varepsilon_w = 0.142$ around a sphere. The angle α and the semi-aperture angle of the cone were given as 20° and 15° respectively.

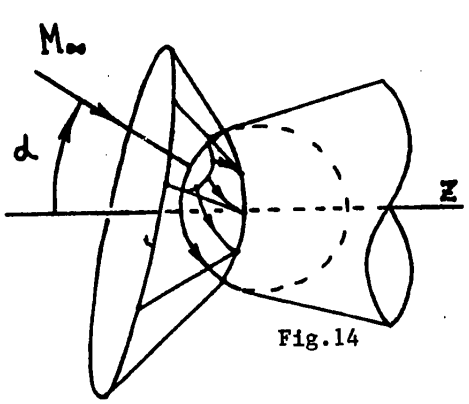

Fig.14

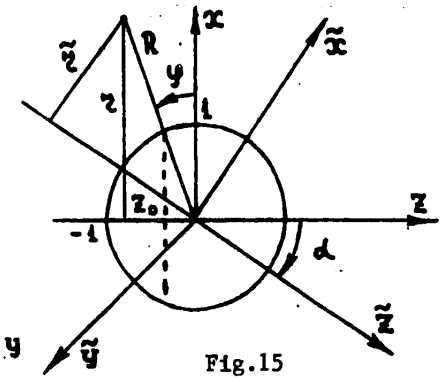

Fig.15

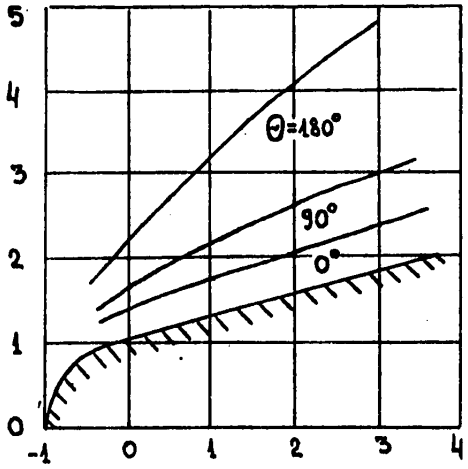

Fig. 16

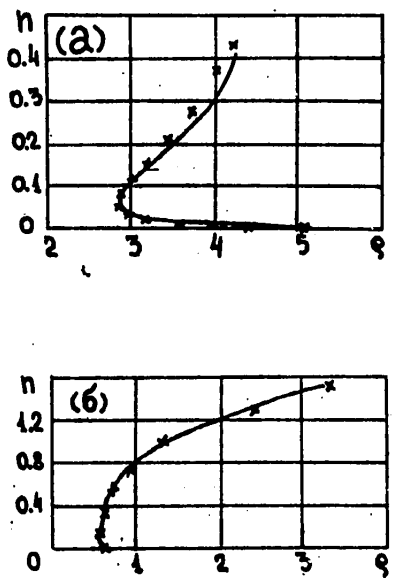

Fig. 17. Transverse density distribution on windward side (plane $\theta = 0°$, Fig. a) and on the leeward side (plane $\theta = 180°$, Fig. b) in cross section $z = 1$ (—— $h_1 = 0.06$, × -- $h_1 = 0.2$)

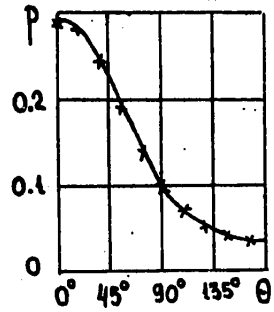

Fig. 18. Pressure distribution on surface of cone in azimuthal direction in cross section $z = 0.6$ (—— $h_1 = 0.24$, × -- $h = 0.06$)

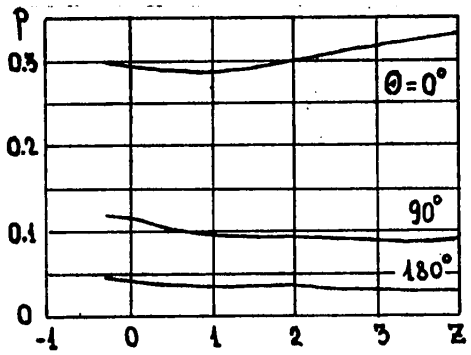

Fig. 19. Surface pressure distribution along the body

Fig. 16 shows a plan view of the geometry of the body and the position of the head shock wave at various angles θ. Since the results of the calculation could not be compared with the parameters of analogous calculations obtained by other methods (due to absence of the latter in the available literature), calculations were done on different grids to check accuracy and the influence of parameters of the scheme. Fig. 17, 18 compare the density distributions across the shock layer and pressure on the surface of the cone in the azimuthal direction obtained at different values of the step in the direction of improvement. Fig. 19 shows pressure distribution on the surface along the body at different angles θ.

REFERENCES

1. Kovenya, V. M., Yanenko, N. N., "Metod rasshchepleniya v zadachakh gazovoy dinamiki" [Method of Decomposition in Problems of Gas Dynamics], "Nauka", 1981.

2. Shevelev, Yu. D., "Trekhmernyye zadachi teorii laminaronogo pogranichnogo sloya" [Three-Dimensional Problems of Laminar Boundary Layer Theory], Moscow, "Nauka", 1977.

3. Gilinskiy, S. M., Telenin, G. F., Tinyakov, G. P., "Method of Calculating Supersonic Flow Around Bodies With Departing Shock Wave", IZVESTIYA AKADEMII NAUK SSSR: MEKHANIKA I MASHINOSTROYENIYE, No 4, 1964, pp 9-28.

4. Davis, "Numerical Solution of Equations of a Hypersonic Viscous Shock Layer", RAKETNAYA TEKHNIKA I KOSMONAVTIKA, No 5, 1970, pp 3-13.

5. Voronkin, V. G., "Calculation of Viscous Shock Layer on Blunt Cones", IZVESTIYA AKADEMII NAUK SSSR: MEKHANIKA ZHIDKOSTI I GAZA, No 6, 1974, pp 99-105.

6. Ankudinov, A. L., "Viscous Shock Layer Near Paraboloid of Revolution", TRUDY TSENTRAL'NOGO AERO-GIDRODINAMICHESKOGO INSTITUTA, No 1448, 1973.

7. Gogineni, P. R., Lewis, C. H., "Hypersonic Viscous Shock-Layer Flows Including Leeside Separation", J. SPACECRAFT, Vol 17, No 4, Jul-Aug 80, pp 316-322.

8. Karyakin, V. Ye., Popov, F. D., "Calculating Three-Dimensional Supersonic Flow of a Viscous Heat-Conductive Gas Around Blunt Bodies", ZHURNAL VYCHISLITEL'NOY MATEMATIKI I MATEMATICHESKOY FIZIKI, Vol 17, No 6, 1977, pp 1545-1555.

9. Rubin, S. G., Lin, T. C., "Numerical Methods for Two- and Three-Dimensional Viscous Flow Problems: Application to Hypersonic Leading Edge Equations", JOURNAL OF COMPUTATIONAL PHYSICS, Vol 9, No 2, Apr 72, pp 339-364.

10. Lin, T. C., Rubin, S. G., "Viscous Flow Over a Cone at Moderate Incidence--1: Hypersonic Tip Region", J. COMPUTERS AND FLUIDS, Vol 1, 1973, pp 37-57.

11. Lin, T. C., Rubin, S. G., "A Numerical Method for Supersonic Viscous Flow Over a Slender Reentry Vehicle", AIAA PAPER, No 19-0205, 1979, pp 1-10.

12. Lubard, S. C., Helliwell, W. S., "Calculation of the Flow on a Cone at High Angle of Attack", AIAA JOURNAL, Vol 12, No 7, 1974, pp 965-974.

13. Helliwell, W. S., Lubard, S. C., "An Implicit Method for Three-Dimensional Viscous Flow With Application to Cones at Angle of Attack", JOURNAL OF COMPUTERS AND FLUIDS, Vol 3, 1975, pp 83-101.

14. Helliwell, W. S., Dickinson, R. P., Lubard, S. C., "Viscous Flow Over Arbitrary Geometries at High Angle of Attack", AIAA PAPER, 80-0064.

15. Chernyy, S. G., "O vybore sistemy koordinat dlya chislennogo resheniya uravneniy Nav'ye-Stoksa marshevym metodom" [Choosing Coordinate System for Numerical Solution of Navier-Stokes Equations by Multistep Method], (in press).

16. Li, C. P., "A Computational Procedure for Supersonic Flows Governed by the Parabolic Navier-Stokes Equations", JOURNAL OF COMPUTATIONAL PHYSICS, 1980(35), pp 365-380.

17. Briley, W. R., McDonald, H., "Solution of the Multi-Dimensional Compressible Navier-Stokes Equations by a Generalized Implicit Method", JOURNAL OF COMPUTATIONAL PHYSICS, Vol 24, 1977, pp 372-397.

18. Gabenko, K. I., Voskresenskiy, G. P., Lyubimov, A. A., Rusanov, V. V., "Prostranstvennoye obtekaniye gladkikh tel ideal'nym gazom" [Three-Dimensional Flow of Ideal Gas Around Smooth Bodies], Moscow, "Nauka", 1964.

19. Kovenya, V. M., Chernyy, S. G., Yanenko N. N., "Simplified Equations for Describing Viscous Gas Flows", DOKLADY AKADEMII NAUK SSSR, Vol 245, No 6, 1979, pp 1322-1324.

20. Kovenya, V. M., Chernyy, S. G., "Solving Simplified Equations of Viscous Gas by Multistep Method", CHISLENNYYE METODY MEKHANIKI SPLOSHNOY SREDY, Novosibirsk, Vol 10, No 1, 1979, pp 71-87.

21. Belotserkovskiy, O. M., ed., "Chislennoye issledovaniye zadach gazovoy dinamiki" [Numerical Investigation of Problems in Gas Dynamics], Moscow, "Nauka", 1974.

22. Abramovich, G. N., "Prikladnaya gazovaya dinamika" [Applied Gas Dynamics], Moscow, "Nauka", 1969.

23. Shikhting, G., "Teoriya pogranichnogo sloya" [Boundary Layer Theory], Moscow, "Nauka", 1974.

24. Kokoshinskaya, P. S., Pavlov, B. M., Paskonov, V. M., "Chislennoye issledovaniye sverkhzvukogo obtekaniya tel vyazkim gazom" [Numerical Study of Supersonic Viscous Gas Flow Around Solids], Moscow, Moscow State University, 1980.

Contents page

6610
CSO: 1862/137

LASERS AND MASERS

THEORETICAL AND EXPERIMENTAL DETERMINATION OF VIBRATIONAL TEMPERATURES AND GAINS IN GASDYNAMIC CO_2 LASER WITH ADDITIVES OF CO AND NO, PART 2: EXPERIMENTAL TECHNIQUE AND RESEARCH RESULTS

Novosibirsk FIZIKA GORENIYA I VZRYVA in Russian Vol 17, No 5, Sep-Oct 81 (manuscript received 25 Sep 80) pp 56-61

[Article by V. M. Doroshenko, N. N. Kudryavtsev and S. S. Novikov, Moscow]

[Text] Experimental Results. Vibrational temperatures and gains were measured in a quasi-cw gasdynamic laser on a shock tube with nozzle on the end of the low-pressure section. The inside diameter of the shock tube was 74 mm. A flat Laval nozzle was used in which the hypersonic part consisted of an arc of a circle with radius of 90 mm smoothly joined to a semicircle with radius of 2 mm in the region of the critical cross section of the nozzle. The height of the critical cross section of the nozzle was $h_* = 1.5$ mm, degree of expansion of the flow $h/h_* = 38$. The measurements were made directly at the output of the supersonic nozzle.

The gain on wavelength of $\lambda = 10.6$ μm was determined by the method of probing the flow with a power-stabilized electric-discharge CO_2 laser beam. The total power of the probe laser emission was measured 0.5-1.0 ms after beginning of the gas discharge process. For this purpose, the radiation of the probe laser was shut off by an electro-optical shutter. The intensity of spontaneous emission of the gas flow was measured simultaneously in two spectral regions. The optical systems for recording the intensity of infrared radiation were a combination of a flat and a spherical mirror. They focused the radiation of the flow on the sensing element of photoresistors.

The necessary spectral regions were isolated by infrared filters with the following passbands: for the 2.7 μm band--$\lambda = 2.9 \pm 0.5$ μm; 4.3 μm--4.37 ± 0.05 μm; 4.7 μm--4.75 ± 0.4 μm; 5.3 μm--5.3 ± 0.6 μm; in measurement of gain on transition $00°1 \rightarrow 10°0CO_2$--$10.6 \pm 0.6$ μm. The transmission curve of the filter used in the radiation intensity channel of the 4.3 μm band is displaced somewhat relative to its central part toward greater wavelengths. A filter with such a transmission curve was selected to suppress radiation of the most intense rotational lines of the main vibrational transition that are situated in the central part of the 4.3 μm band. According to Ref. 16, the coefficient of absorption in the central parts of these lines under the conditions of CO_2 laser cavities reach values corresponding to total absorption of the

incident radiation at distances of 1-5 mm. Therefore, absorption of radiation of rotational lines of transition $00°1 \rightarrow 00°0$ in the wall layers of the supersonic flow may have an appreciable effect on the results of determining vibrational temperatures.

In measurements of emission intensity in the CO band of 4.7 μm and the NO band of 5.3 μm, the investigated radiation went past the filter through a cell with mixture of CO_2 and N_2O at atmospheric pressure. This totally eliminated transmission of emission of the 4.3 μm band through the filters used in the channels for measuring radiation intensity in the 4.7 and 5.3 μm bands.

In calibrating the channels of infrared radiation intensity, the cylindrical channel of the shock tube was extended to the viewing ports. In this way, all components of the optical systems could be kept the same as in the measurements.

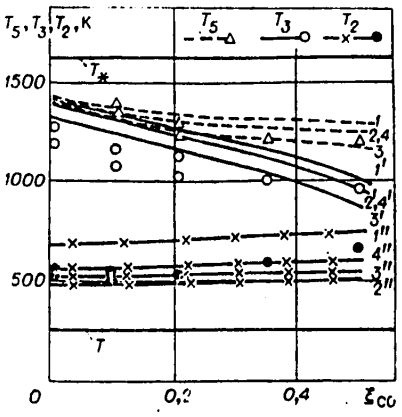

Fig. 1. Vibrational temperatures of CO_2 and CO in a mixture of $0.1\ CO_2 + (0.5 - \xi_{CO})N_2 + \xi_{CO}CO + 0.4$ He; gas parameters in front of the nozzle: $p_0 = 9.4 \pm 0.4$ atm and $T_0 = 2000 \pm 80$ K; T_* is the temperature in the critical cross section of the nozzle; T is translational temperature of the gas at the nozzle outlet

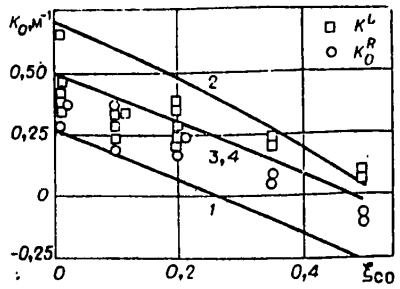

Fig. 2. Gain in mixture of $0.1\ CO_2 + (0.5 - \xi_{CO})N + \xi_{CO}CO + 0.4$He. Experimental conditions correspond to Fig. 1: K_0^L--results of gain measurements by the laser probing method; K_0^R--corresponding values reconstructed for the center of line P20 of the laser transition $00°1 \rightarrow 10°0$ CO_2 from measured T_3 and T_2. Line numbering corresponds to the version of calculation

Results of Studying Carbon Monoxide Additives. Results of measurements of vibrational temperatures of asymmetric (T_3) and collective (T_2) modes of CO_2 and the vibrational temperature of CO (T_5) when carbon monoxide is substituted for nitrogen in mixture $0.1CO_2 + 0.5N_2 + 0.4$He are shown in Fig. 1. It can be seen that the vibrational temperature of CO is 200-250 K higher than T_3. The vibrational temperatures of carbon monoxide and the asymmetric mode of CO_2 are considerably lower than the gas temperature T_* in the critical cross section of the nozzle. When carbon monoxide is substituted for nitrogen, there is a monotonic drop in T_3 and T_5.

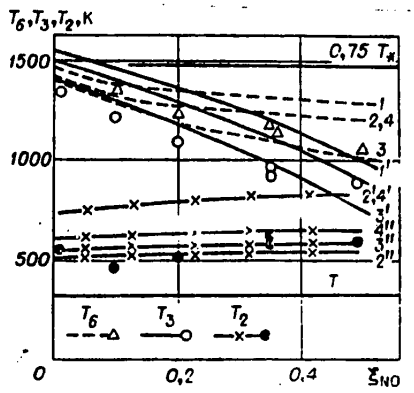

Fig. 3. Vibrational temperatures of CO_2 and NO in mixture $0.1CO_2 + (0.5 - \xi_{NO})N_2 + \xi_{NO}NO + 0.4$ He at gas parameters in front of the nozzle $p_0 = 10.9 \pm 0.5$ atm and $T_0 = 2250 \pm 100$ K

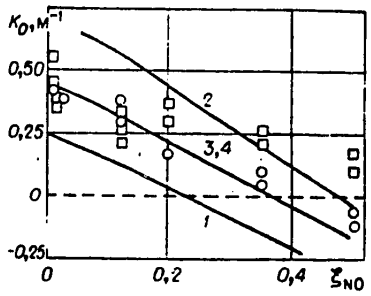

Fig. 4. Gain in mixture $0.1CO_2 + (0.5 - \xi_{NO})N_2 + \xi_{NO}NO + 0.4$He (symbols as in Fig. 2)

The collective mode of carbon dioxide is characterized by excitation considerably in excess of equilibrium; the vibrational temperature T_2 is more than 200 K higher than the translational gas temperature. As the carbon monoxide concentration increases over a range of 0-0.5, T_2 increases by approximately 200 K.

The results of theoretical calculation of the vibrational temperatures of CO (T_5) or NO (T_6) and CO_2 (T_3 and T_2) when rate constants and characteristic times are chosen in accordance with data given in Ref. 1 (tables 1 and 2) are represented on Fig. 1, 3 by curves 1, 1' and 1" respectively. The numbers 1-4 on Fig. 1 denote the results of calculations of the vibrational temperature of CO (NO on Fig. 3), while 1'-4' and 1"-4" on Fig. 1 and 3 denote the results of calculations of the vibrational temperatures of CO_2 -- T_3 and T_2 respectively. The numerical designations of the curves on Fig. 1-4 define the versions of selecting rate constants of the relaxation processes described below.

It is clear from the data of Fig. 1 that the theoretical and experimental dependences of vibrational temperatures on carbon monoxide content correlate well with each other. The values of the theoretically calculated vibrational temperatures of CO_2 are 100-200 K higher than the experimental values. In most cases this exceeds the error of measurements of vibrational temperatures in this research. The calculation of T_5 coincides with the results of the experiment within the limits of measurement error.

Vibrational temperatures of CO_2 and CO were calculated at doubled rate constants of the processes of V-V' exchange of asymmetric and collective modes of CO_2 ($Q_{23} \cdot 2$) and V-T relaxation of the collective mode ($Q_{20} \cdot 2$). The results are shown on Fig. 1-4 by curves 2 (curves 3 -- calculation at $Q_{23} \cdot 5$ and $Q_{20} \cdot 2$). The data of Fig. 1 show that satisfactory agreement of experimental measurements with theoretically calculated vibrational temperatures of CO_2 (T_2) is observed with an increase in Q_{20} by 30-70% depending on the CO content. Doubling and quintupling Q_{23} brings theory and experiment into agreement in the region of higher CO contents $\xi_{CO} \geq 0.3$.

The influence that the possible uncontrollable water vapor content in mixtures considered has on vibrational temperatures of CO_2 and CO is illustrated by curves 4 on Fig. 1-4. The calculations were done for $\xi_{H_2O} = 1.005$. In this calculation version, the T_2 coincide with experimental data, and the theoretical values of T_3 are somewhat higher, as before.

Thus if consideration is taken of the attendant uncertainties in the rate constants of relaxation processes (see citations 32, 36 in Ref. 1), possible uncontrollable trace amounts of water vapor in the investigated mixture, and errors in measurements of vibrational temperatures, the agreement between calculated and measured values of vibrational temperatures of CO_2 and CO can be considered satisfactory. An exception is the discrepancy for T_3 at $\xi_{CO} < 0.2$ that cannot be attributed to these factors.

The results of measurements and calculation of gain for the investigated mixtures are shown on Fig. 2. Based on results of measurements of T_3 and T_2, we can determine the gain in the center of the rotational line of laser transition $00°1 \rightarrow 10°0$ of carbon dioxide from the intensity of spontaneous infrared emission in the 4.3 and 2.7 μm bands

$$K_0^R = \frac{\lambda^2 A}{8\pi}\left(N_{00°1,J'} - \frac{2J'+1}{2J+1} N_{10°0,J}\right)\frac{a}{\sqrt{\pi}\gamma_L} H(a, 0), \qquad (1)$$

where $A = 0.187\ s^{-1}$ is the probability of spontaneous emission on the laser transition; $a = \gamma_L\sqrt{\ln 2}/\gamma_D$; $H(a, 0)$ is the value of the Voigt function in the center of the line; $N_{00°1,J'} = (2J'+1) N_{CO_2} Q_v^{-1} Q_R^{-1} \exp[-\Theta_3/T_3 - E_r(J')/kT]$, $N_{10°0,J} = (2J+1) N_{CO_2} Q_v^{-1} Q_R^{-1} \exp\left[-\frac{\Theta_1}{T_2} - \frac{E_r(J)}{kT}\right]$ are the populations of the corresponding vibrational-rotational levels; N_{CO_2} is the number of CO_2 molecules in a unit of volume; $\Theta_3 = 3380$ K, $\Theta_1 = 1997$ K are the characteristic temperatures of vibrational levels 00°1 and 10°0; Q_V and Q_R are respectively the vibrational and rotational statistical sums of CO_2; $E_r(J)$ is rotational energy. In this paper, the gain was reconstructed for the most intense line P20 of transition $00°1 \rightarrow 10°0$, which corresponds to $J' = 19$, $J = 20$ in (1). The theoretical calculation of gain was done with the use of calculated values of vibrational temperatures T_3 and T_2 for the center of line P20 of transition $00°0 \rightarrow 10°1$ by relation (1).

Using the estimates given above for the error in determining T_3 and T_2, we can establish that for the boundary conditions of the given paper, the accuracy of reconstruction of gain K_0^R is approximately $\pm 0.1\ m^{-1}$. The loss of sensitivity of the given method of determining gain in the region of small values of $|K_0| \leq 0.1$ is due to a reduction in the population difference of laser levels $N_{00°1}$-$N_{10°0}$ to values comparable with the error of measurements of $N_{00°1}$ and $N_{10°0}$.

The data of Fig. 2 confirm the good correlation of values of K^L and K_0^R measured by two independent methods. A monotonic reduction of K_0 is observed as nitrogen is replaced by carbon monoxide from the carbon monoxide content with $K_0 = 0.5\ m^{-1}$ at $\xi_{CO} = 0$ to near-zero values at $\xi_{CO} = 0.5$.

The results of theoretical calculation of gain when the rate constants of vibrational relaxation processes are selected according to versions 3 and 4 agree well with measurements. Calculations by version 1 somewhat understate the values of K_0, and version 2 overstates them.

The data of Fig. 2 show the relatively weak influence that a symbatic change in relaxation rates of upper and lower laser levels of CO_2 has on gain. The difference in results of K_0 calculations for versions 2-4, characterized by appreciably different process relaxation rates, approximately corresponds to the experimental error of gain measurements -- 20-30% [Ref. 3].

Measurements of vibrational temperatures of CO_2 and CO showed that the reduced amplification when nitrogen is replaced by carbon monoxide is determined by two factors: an increase in the rate of relaxation of vibrational energy of $CO_2(\nu_3)$ molecules in process (7)† and consequently of CO and N_2 as carbon monoxide is added to the mixture, since $Q_{23}(M = CO) > Q_{23}(M = N_2)$ (see table 2 from Ref. 1), and development of an additional channel for relaxation of vibrational energy of molecules of $CO_2(\nu_3)$, N_2 and CO (see formula (10) in Ref. 1). These factors lead to reduction of vibrational temperatures of CO T_5 and the asymmetric mode of CO_2 T_3, and to an increase in vibrational temperature of the collective mode of CO_2 T_2.

The experimental and theoretical data shown on Fig. 1, curves 1-4, indicate approximately identical effectiveness of molecules CO and N_2 in the process of relaxation of the collective mode of carbon dioxide gas (6). Actually, when nitrogen is replaced by carbon monoxide up to concentrations $\xi_{CO} \cong 0.2$, T_2 remains practically unchanged. This result agrees with the data of measurements of rate constant Q_{20} with M = CO (see citations 60, 61 in Ref. 1), and contradicts studies [Ref. 4] in which it was established that the quantity Q_{20} when M = CO is approximately two orders of magnitude higher than when $M = N_2$.

Results of Investigation of Nitric Oxide Additives. The nitric oxide molecule has a lower vibrational quantum than the carbon monoxide molecule. The defect of the first vibrational level of NO with the first level of the asymmetric mode of CO_2 increases to 450 cm^{-1} as compared with the CO molecule (243 cm^{-1}). For the NO molecule, just as for CO, quasi-resonant exchange may take place with the collective mode of CO_2 in (10).

The results of measurements of vibrational temperatures of NO T_6 and CO_2 T_3 and T_2 when nitric oxide is substituted for nitrogen in mixture $0.1CO_2 + 0.5N_2 + 0.4He$ are shown in Fig. 3. The reduction in T_6 and T_3 as nitric oxide is added is more appreciable than with the addition of carbon monoxide (see Fig. 1, 3). An increase is noted in the rate of vibrational relaxation of $CO_2(\nu_3)$, N_2 and NO as compared with mixtures that contain carbon monoxide. This is evidenced by the reduction of vibrational temperatures: $\Delta T_6 = T_6(\xi_{NO} = 0) - T_6(\xi_{NO} = 0.5) \cong 500$ K and $\Delta T_3 = T_3(\xi_{NO} = 0) - T_3(\xi_{NO} = 0.5) \cong 500$ K when nitrogen is replaced by nitric oxide as compared with corresponding quantities $\Delta T_5 \cong 200$ K and $\Delta T_3 \cong 300$ K with analogous substitution of carbon dioxide for nitrogen.

†Here and below, reactions are numbered as in Ref. 1.

Just as in mixtures with carbon monoxide, the calculated values of T_3 are overstated by 100-250 K depending on the NO content. To correlate calculations and experiments on determining T_3, the rate constant Q_{23} must be approximately quintupled. The calculated values of temperature T_6 coincide with experiment in the concentration region $\xi_{NO} \lesssim 0.2$, and are 150-250 K higher than the experimental values at $\xi_{NO} \gtrsim 0.2$

An increase in T_2 is observed theoretically and experimentally with systematic substitution of NO for N_2. The theoretical calculation of T_2 is also overstated (see curve 1" of Fig. 3). To bring theory and experiment into line, it is necessary to approximately double the rate constant of reaction (6) $Q_{20}(M = NO)$, or to have water vapor in the mixture in an amount of $\xi_{H_2O} = 0.005$.

Results of measurements and calculation of gain with the addition of nitric oxide are shown in Fig. 4. Addition of nitric oxide leads to a reduction of K_0 from 0.4 cm^{-1} at $\xi_{NO} = 0$ to 0.1-0.15 m^{-1} at $\xi_{NO} = 0.5$, which corresponds in order of magnitude to a reduction of gain with equivalent substitution of carbon monoxide for nitrogen. Good agreement with experiment is obtained with theoretical calculation of K_0 when the rate constants of relaxation processes are taken according to versions 3 and 4. Choosing the rate constants in accordance with version 1 gives understated values of K_0 as compared with experiments. Use of the rate constants of version 2 overstates K_0 in region $\xi_{NO} \lesssim 0.2$.

On the whole, the influence of NO molecules on the kinetics of formation of population inversions in the active medium of a CO_2 gasdynamic laser is in large measure analogous to the influence of CO molecules. Just like CO molecules, the NO molecules cause a reduction in stored vibrational energy of the upper laser level of $CO_2(\nu_3)$, $N_2(\nu)$ and $NO(\nu)$ as a result of an increase in the relaxation rate of this this energy in the process of V-V exchange (7) in CO_2 and as a result of development of an additional relaxation channel (10) that in fact couples the antisymmetric and collective modes of CO_2. The relaxation rate of the collective mode (6) and consequently of the lower laser level is not considerably increased as compared with collisions of CO_2 molecules with nitrogen. The noted factors considerably reduce the gain when nitric oxide is added to the CO_2 laser mixture, just as in the case of carbon monoxide.

The following comments can be made concerning the discrepancy between experiment and theory in determination of vibrational temperatures. In most cases these discrepancies can be attributed to attendant uncertainties in choosing the rate constants of processes of vibrational relaxation of the multicomponent medium of the CO_2 laser, or to the presence of uncontrollable trace amounts of water molecules in the mixture that appreciably accelerate processes of vibrational relaxation. The more appreciable discrepancies noted in some cases in the given paper for vibrational temperatures of the asymmetric mode T_3 may apparently be due to the occurrence of atomic components such as oxygen in the medium at high temperatures. Such components are strong deactivators of molecular vibrations [Ref. 5]. It is also possible that the explanation of this discrepancy under conditions of considerable vibrational excitation

of the molecules requires examination of a more detailed scheme of vibrational relaxation in the active medium of the CO_2 laser that takes consideration of occurrence of additional channels of energy exchange.

REFERENCES

1. Doroshenko, V. M., Kudryavtsev, N. N., Novikov, S. S., FIZIKA GORENIYA I VZRYVA, Vol 17, 1981, p 2.

2. Biryukov, A. S.,Volkov, Yu. A. et al., KVANTOVAYA ELEKTRONIKA, Vol 3, 1976, p 1748.

3. Soloukhin, R. I., Yakobi, Yu. A., ZHURNAL PRIKLADNOY MEKHANIKI I TEKHNICHESKOY FIZIKI, No 3, 1974.

4. Levis, M., Bernstein, L., AERONAUT. RES. COUN. CURRENT. PAPERS, No 1294, London, 1974.

5. Buchwald, M. I., Wolga, G. J., J. CHEM. PHYS., Vol 62, 1975, p 2828.

6610
CSO: 1862/153

UDC 621.373.826.038.823

HIGH-EFFICIENCY PHOTOINITIATED D_2-F_2-CO_2 LASER

Moscow KVANTOVAYA ELEKTRONIKA in Russian Vol 9, No 3(117), Mar 82 (manuscript received 2 Jul 81) pp 624-625

[Article by A. S. Bashkin, N. P. Vagin, L. V. Kulakov, A. N. Orayevskiy, Yu. P. Podmar'kov, O. Ye. Porodinkov, M. I. Prishchepa and N. N. Yuryshev, Physics Institute imeni P. N. Lebedev, USSR Academy of Sciences, Moscow]

[Text] A report on investigation of a photoinitiated D_2-F_2-CO_2 chemical laser. A specific energy output of 37 J/liter, corresponding to a technical laser efficiency of 18% is achieved on a mixture of $D_2:F_2:CO_2:He = 1:5.5:4:9.5$ ($[O_2]/[F_2] = 0.03$, $p = 1$ atm) at degree of initiation $\Delta[F_2]/[F_2] = 0.05\%$.

One of our preceding papers [Ref. 1] reported on attainment of high technical efficiencies η_t in a large-volume H_2-F_2 laser with photoinitiation by standard flashlamps IFP-20000 ($\eta_t = 36\%$ at specific energy output $\varepsilon = 25$ J/liter). The results of comparative experiments on initiation of D_2-F_2-CO_2 and H_2-F_2 lasers with small volumes by a beam of fast electrons has shown that the energy parameters of these lasers are approximately the same [Ref. 2], which leads us to hope for high η_t in the photoinitiated D_2-F_2-CO_2 laser as well. As pointed out in Ref. 1, the high values of η_t and ε in chemical lasers based on the fluorine-hydrogen chain reaction can be realized only when using a medium with large cross sections that assure effective capture of emission of the photosource (diameter of the laser cell must be of the order of 150 mm or more for the usual partial pressures of fluorine of the order of 200 mm Hg or less). Therefore the experiments were done on the same laser cell as in Ref. 1; active volume was about 7.3 liters.

Operation with the D_2-F_2-CO_2 laser requires the use of NaCl windows, which could not withstand more than one use under the conditions of the experiments done. Therefore we were unable to work with laser windows of $\emptyset$ 160 mm as in the case of the H_2-F_2 laser. However, this is not important for determining the energy parameters of the D_2-F_2-CO_2 laser since special studies on the H_2-F_2 laser showed uniformity of laser energy distribution over the cross section of the cell (cell diameter was 150 mm) throughout the entire range of fluorine working pressures ($\lesssim$200 mm Hg). This demonstrates the possibility of investigations of the D_2-F_2-CO_2 laser with the use of medium-sized optics and subsequent scaling of the results to the full cross section of the laser cell. Therefore all experiments were done with optics of $\emptyset$ 70 mm and laser beam diameter of ~60 mm.

The purpose of our research was to determine the feasibility of getting high technical efficiencies and specific energy outputs on a chemical D_2-F_2-CO_2 laser initiated by flashlamp emission. In the course of the experiments, the above-mentioned laser output parameters were optimized with respect to composition and pressure of the mixture, oxygen content, degree of initiation and Q of the optical cavity. The best result was attained on a mixture of $D_2:F_2:CO_2:He = 1:5.5:4:9.5$ ($[O_2]/[F_2] = 0.03$) at atmospheric pressure. Specific energy output $\varepsilon = 37$ J/liter was attained at a degree of initiation $\Delta[F_2]/[F_2] = 0.05\%$. Considering the above statement regarding the possibility of scaling up to the entire cross section of the cell, we find that the given specific energy output should correspond to energy from the entire active volume of the laser of 270 J. The energy of a capacitor bank supplying the necessary degree of initiation $\Delta[F_2]/[F_2] = 0.05\%$ was 1.5 kJ. Consequently, at the attained energy output of 37 J/liter, the technical efficiency of the laser is 18%.

It is interesting to note that on the given facility in experiments with the H_2-F_2 laser an energy output of ~40 J/liter was achieved at efficiency of ~19% (mixture $H_2:F_2:He:O_2 = 22:150:15:563$, $p = 1$ atm). This shows that under certain conditions the photoinitiated D_2-F_2-CO_2 laser is on a par with the photoinitiated H_2-F_2 laser with respect to specific energy output and technical efficiency.

REFERENCES

1. Bashkin, A. S., Oraevsky, A. N., Paziuk, V. S., Porodinkov, O. E., Yuryshev, N. N., Vagin, N. P., "Investigation of a Large Volume H_2-F_2 Laser With Flashlamp Initiation", Lectures, Symposium Optika-80, Budapest, November 1980, p 106.

2. Bashkin, A. S., Orayevskiy, A. N., Tomashov, V. N., Yuryshev, N. N., KVANTOVAYA ELEKTRONIKA, Vol 7, 1980, p 1357.

6610
CSO: 1862/145

UDC 621.373.826.038.823

INFLUENCE OF SPECIFIC PUMPING POWER ON WORKING EFFICIENCY OF ATMOSPHERIC-PRESSURE ELECTRON-BEAM CONTROLLED CO_2 LASER

Moscow KVANTOVAYA ELEKTRONIKA in Russian Vol 9, No 2(116), Feb 82 (manuscript received 16 Apr 81, after revision 17 Jul 81) pp 413-415

[Article by V. G. Vostrikov, V. G. Naumov and L. V. Shachkin]

[Text] An experimental study is done on the influence that specific pumping power has on operating efficiency of an atmospheric-pressure electron-beam controlled CO_2 laser at fixed near-optimum values of other parameters that influence laser output energy. It is shown that an increase in specific pumping power from 2 to 7 kW/cm^3 leads to an increase in the output energy by 40% for a mixture of $CO_2:N_2:He = 1:6:3$.

The problem of the influence that specific pumping power has on the working efficiency of electron-beam controlled lasers is a timely question when selecting optimum duration in pulse-periodic laser systems. It is evident from general arguments that a reduction in pulse duration τ_p (while retaining the specific pumping energy ε that is limited by heating of the gas mixture) should lead to an increase in the efficiency of the electron-beam controlled laser due to reduced collisional relaxation as compared with radiative, and on the other hand the reduction is limited by complication of the ionization device and its supply system, as well as by an increase in the radiation power density on the target, leading to gas breakdown at its surface. Besides, when the pumping power is increased, there is an increase in the rate of electron losses in proportion to the square of electron concentration, which leads in turn to a reduction of efficiency in utilization of the electron beam.

Theoretically the problem of complex optimization of the excitation pulse parameters was considered in Ref. 1, 2. Research has now been done on experimental investigation of the way that emission energy P_e and efficiency η depend on the normalized electric field strength E/N and composition of the working mixture [Ref. 3, 4]. However, in all these papers, simultaneous variation of several parameters that influence P_e and η (such as ε, E/N, specific pumping power and so on) has precluded a detailed analysis of the influence that any parameter has at fixed values of the other parameters near optimum.

To determine the influence of specific pumping power on output emission energy and efficiency on an electron-beam controlled laser using carbon dioxide, we

did an experimental study of the way that P_e depends on η and q at fixed values of pumping energy and E/N for mixtures of $CO_2:N_2:He = 1:6:3$ and 1:4:5 (in parts by volume) at pressure of 1 atmosphere and initial temperature of the gas mixture ~300 K. The experiments were done on a facility described in Ref. 5. The source of ionization was an electron beam with initial energy of ~200 keV, coupled through an aluminum foil 35 μm thick into the gas-discharge chamber. To guarantee constant composition, the working mixture was continuously circulated through the mixing chamber. The discharge current was measured by a Rogowski loop. The research used a two-pass telescopic unstable cavity with magnification M = 1.3, the length of the active zone along the optical axis of the cavity was $L_c = 2 \times 0.75$ m. Radius of curvature of the output mirror was 33 m, and of the opaque mirror -- 43 m. Reflectivity of the mirrors $\kappa \cong 0.985$. Output energy was measured by a matrix of EP-40 cells. Lasing pulse shape was recorded by an FSG-223 sensor with signal fed to the S8-11 two-beam memory oscilloscope; the signal from the Rogowski loop was sent to the same oscilloscope. The energy input in each pulse was determined by approximate numerical integration over the course of the pumping pulse. Since the pulse shape for the specific pumping power is practically the same as that of the discharge current, this recording technique enabled us to determine the time of termination of the lasing pulse relative to completion of the pumping pulse. Fig. 1 shows oscillograms of current and lasing pulses. The

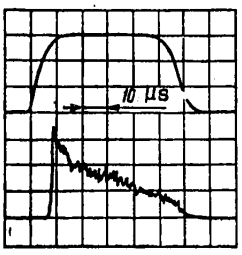

Fig. 1. Typical oscillograms of discharge current (top) and lasing pulse (bottom)

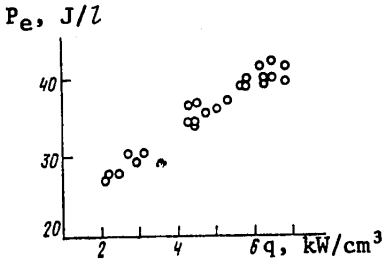

Fig. 2. Emission output energy as a function of specific pumping power

variation in specific pumping power with fixed electric field and energy input was achieved by varying the beam current and pumping pulse duration. The voltage across the discharge chamber (and accordingly the value of the electric field) was the maximum permissible for each mixture with consideration of stability of the working mode at which no breakdowns were observed in the discharge chamber either during the pulse or after its completion.

Fig. 2 shows how specific energy output depends on the pumping power density for a mixture of $CO_2:N_2:He = 1:6:3$ at $E/N = 1.5 \cdot 10^{-16}$ W·cm². Output energy was measured at two fixed values of specific energy input $\varepsilon_1 = 0.25$ and $\varepsilon_2 = 0.30$ J/cm³. Under our conditions, lasing practically ceased at the end of the pumping pulse at ε_1, and therefore a further increase in specific energy

input to ε_2 does not increase energy output. (A similar effect was observed for the mixture $CO_2:N_2:He = 1:4:5$ as well.) As can be seen from Fig. 2, an increase in specific pumping power from 2 to 7 kW/cm^2 leads to an increase in output energy by approximately 40-50%. The maximum attained output energy was $P_{e_{max}} = 42$ J/ℓ. For a mixture of $CO_2:N_2:He = 1:4:5$ the dependence of output energy on q is similar as a whole to that observed on Fig. 2.

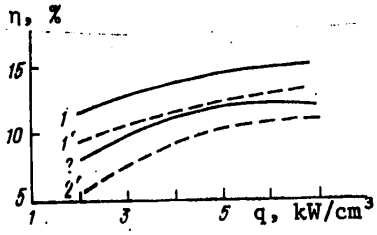

Fig. 3. Laser efficiency as a function of specific pumping power: 1, 1'--$CO_2:N_2:He = 1:6:3$ ($E/N = 1.5 \cdot 10^{-16}$ W·cm^2, 1--$\varepsilon_1 = 0.25$ J/cm^3, 1' $\varepsilon_2 = 0.30$ J/cm^3); 2, 2'--$CO_2:N_2:He$ 1:4:5 ($E/N = 1.3 \cdot 10^{-16}$ W·cm^2, 2--$\varepsilon_1 = 0.25$ J/cm^3, 2'--$\varepsilon_2 = 0.30$ J/cm^3)

Fig. 3 shows how laser efficiency depends on specific power input for both mixtures at two values of specific energy input. The curves were obtained by averaging experimental data. As we can see from Fig. 3, the most effective of the investigated mixtures was a mixture of $CO_2:N_2:He = 1:6:3$ (curves 1, 1'). The maximum value of $\eta = 15\%$ is attained at $\varepsilon_1 = 0.25$ J/cm^3 and $q \cong 7$ kW/cm^3. The higher value of η for mixture $CO_2:N_2:He = 1:6:3$ cannot be attributed to the fact that the volumetric heat capacity (J/ℓ·deg) for the mixture with volumetric ratio of components of 1:6:3 is greater than that for the mixture with ratio 1:4:5 at about the same effectiveness of excitation of vibrational levels under our conditions for the given mixtures [Ref. 6, 7]. It is completely possible that the decisive factor is that the optical axis of the unstable cavity was situated near the cathode (at a distance of the order of 1 cm) and other things being equal (due to comparatively greater inhomogeneity of the discharge in the cathode zone for mixture 1:4:5), the operation of the optical cavity was affected more by the strong influence of inhomogeneity of the gain and of the index of refraction. More detailed investigation of the dependence of output energy on the composition of the working mixture and pumping conditions requires a series of experimental studies of homogeneity of the active medium and calculations with consideration of the configuration of the discharge chamber, the cavity and homogeneity of the active medium.

In conclusion the authors thank A. V. Korneyev and I. D. Dzhigaylo for assisting with the experiments, and A. G. Krasyukov and P. A. Svotin for constructive discussion of the results.

REFERENCES

1. Avrov, A. I., Glotov, Ye. P., Danilychev, V. A., Cheburkin, N. V., KVANTOVAYA ELEKTRONIKA, Vol 7, 1980, p 1979.

2. Avrov, A. I., Glotov, Ye. P., Danilychev, V. A., Kamenets, F. F., Krasovskiy, V. M., Soroka, A. M., KVANTOVAYA ELEKTRONIKA, Vol 8, 1981, p 424.

3. Basov, N. G., Danilychev, V. A., Ionin, A. A., Kovsh, I. B., Sobolev, V. A., Suchkov, A. F., Urin, B. M., KVANTOVAYA ELEKTRONIKA, Vol 2, 1975, p 2458.

4. Basov, N. G., Danilychev, V. A., Ionin, A. A., Kovsh, I. B., Sobolev, V. A., Suchkov, A. F., Urin, B. M., KVANTOVAYA ELEKTRONIKA, Vol 1, 1974, p 2529.

5. Krasyukov, A. G., Naumov, V. G., Shachkin, L. V., Shashkov, V. M., FIZIKA PLAZMY, Vol 7, 1981, p 100.

6. Lobanov, A. N., Orlov, V. K., Suchkov, A. F., Urin B. M., Preprint No 199, Lebedev Physics Institute, Moscow, 1977.

7. Karlov, N. V., Konev, Yu. B., Kochetov, I. V., Pevgov, V. G., Preprint No 91, Lebedev Physics Institute, Moscow, 1976.

6610
CSO: 1862/133

UDC 621.373.826.038.823

INVESTIGATION OF CHEMICAL HF LASER BASED ON HIGH-PRESSURE H_2-SF_6 MIXTURE

Moscow KVANTOVAYA ELEKTRONIKA in Russian Vol 9, No 3(117), Mar 82 (manuscript received 7 Jul 81) pp 625-628

[Article by A. S. Bashkin, A. N. Orayevskiy, V. N. Tomashov and N. N. Yuryshev, Physics Institute imeni P. N. Lebedev, USSR Academy of Sciences, Moscow]

[Text] An investigation is made of the energy characteristics of a chemical HF laser using a mixture of H_2-SF_6 excited by a relativistic electron beam. Effective lasing is achieved at a mixture pressure up to 4.5 atm. Specific energy output of 50 J/liter is obtained at a mixture pressure of 1.5 atm. The authors note the capability of continuous tuning of the lasing frequency over a range of 2.2 cm^{-1} about the center of each of the vibrational-rotational lines, which enables development of a powerful tunable laser necessary for laser-chemical research.

The solution of laser-chemical problems has necessitated development of powerful lasers that emit radiation over a wide wavelength range. Radiation with wavelength near 3 μm is needed for resonant excitation of molecules that have hydrocarbon bonds. Quite promising in this band is a chemical HF laser based on a mixture of SF_6-H_2 that has a broad lasing spectrum. The use of a stable gas mixture as the active medium of the laser enables reliable operation at high pressures, which not only shortens the duration of the lasing pulse, but also enables expansion of the continuous tuning range.

Ref. 1 experimentally demonstrated the feasibility of tuning the frequency of the HF laser in a range of 0.5 cm^{-1} around each vibrational-rotational transition. However, the energy characteristics of this laser were very low. Besides, expansion of the continuous tuning band of the laser is quite desirable.

The possibility of operation of the laser using an SF_6-H_2 mixture at pressures up to 10 atm was demonstrated in Ref. 2. However, the explanation of the abrupt drop in energy characteristics of the laser at mixture pressures above 3 atm by relaxation of vibrationally excited HF molecules by H_2 and HF molecules is unconvincing. Therefore the question of getting efficient lasing on an SF_6-H_2 mixture at pressures of several atmospheres remains open.

In high-gain lasers, including chemical HF lasers, a reduction in energy characteristics may be caused by "parasitic" lasing or superluminescence [Ref. 3, 4]; however, direct observation of parasitic lasing and the possibility of overcoming it have apparently not been described in the literature as yet.

Our research is dedicated to solving all these problems. The SF_6-H_2 mixture was excited by an electron beam from an accelerator described in Ref. 5. Transverse excitation was used because of the low electron energy (200 keV). The use of an external magnetic field of 6 kGs intensity eliminated electron scattering, increased current density in the laser cell, and also permitted more exact determination of the active volume of the laser and the input energy. The electron energy lost in the laser gas medium was measured as previously in Ref. 5 by a moving angle calorimeter.

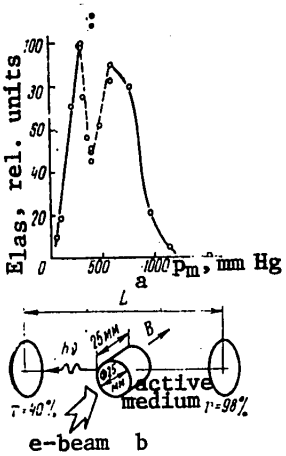

Fig. 1. Lasing energy as a function of pressure of a mixture of $SF_6:H_2 = 7:1$ (a) and general diagram of the experiment (b): B--direction of external magnetic field; the axis of the "parasitic" cavity coindices with the direction of B

Development of parasitic lasing was checked on the experiment diagrammed in Fig. 1. Laser output energy was measured at different mixture pressures. The occurrence of a "dip" at the top of the curve can be attributed to parasitic lasing. Since emission was not observed in the presence of the opaque mirror alone, it can be assumed that in the given case there was no superluminescence. Aluminum surfaces spaced 2.5 cm apart and parallel to one another could serve as the mirrors of the "parasitic" cavity. The electron beam from the accelerator was coupled in through one of these foil sheets, and the beam was extracted from the laser cell for measurement of its parameters through the other foil sheet. Of course, the Q of this cavity was lower than that of the main optical cavity, but since it had a short base (2.5 cm) compared with the main cavity (120 cm), the field was established in much shorter times. The occurrence of the dip at the top of the curve is due to the fact that it was at the top that the lasing threshold was surpassed for the parasitic cavity. The situation is aggravated by the fact that the length of the laser active zone in these two directions was about the same (see Fig. 1).

To check out the above arguments, the length of the main cavity was reduced to 40 cm. When this was done, the laser output energy at a mixture pressure of 500 mm Hg more than doubled upper point ● on Fig. 1a). Also to suppress parasitic lasing for a cavity base of L = 120 cm, a screen was introduced into the active medium bent into a cylinder 2.5 cm in diameter, which strongly

reduced the Q of the parasitic cavity. The current of the electron beam in the gas medium showed insignificant change. In this case as well, a sharp increase was observed in the lasing pulse energy (lower point • on Fig. 1).

Thus the given experiment was a kind of imitation of conditions that may arise in lasers with large active volumes. In such lasers, large transverse dimensions may lead to spurious emission even with much lower gain than in this case.

To eliminate the further possibility of parasitic lasing, the shape of the cathode was altered: the circular form was replaced by a strip measuring 63x 4 mm. The track of the electron beam [photo not reproduced] and the general setup of the experiment are shown in Fig. 2. Laser output energy

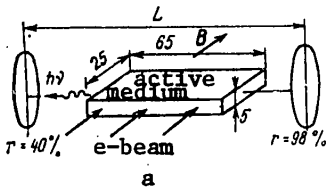

Fig. 2. General diagram of experiment with strip cathode (a) and track of electron beam on surface of tin-plated sheet located directly in the gas medium of the laser cell (b) [photo not reproduced]

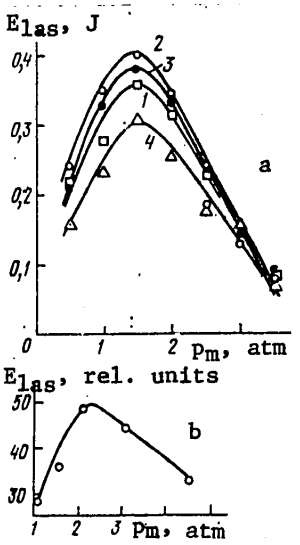

Fig. 3. Output energy of laser using mixture of $SF_6:H_2 = 5:1$ (1), 20:1 (2), 54:1 (3) and 100:1 (4) as a function of mixture pressure for entire lasing cross section (a) and for a layer of Ø 4 mm closest to the point of entry of electrons into the laser gas (b)

was measured as a function of the pressure of mixtures with different SF_6/H_2 ratios (Fig. 3). At pressure of 1.5 atm and ratio $SF_6:H_2 = 20:1$, the lasing pulse energy reached 0.4 J. Considering that the cross section of the lasing spot as determined from the burn left on blackened photographic paper corresponded to the cross section of the electron beam, we can assume that the active volume of the laser was about 8 cm^3. However, because of the small laser dimensions, the accuracy of determining the active volume is no better than 20-25%. Thus the specific lasing energy is $\varepsilon_{las} = 50$ J/liter. Such a high value of ε_{las} shows that high energy parameters are attainable even when a chemical reaction of other than chain type is used under conditions of intense initiation.

The level of initiation of the mixture was determined on the basis of data on measurement of the electron beam energy contributed to the active volume of the laser, and also with consideration of the fact that energy of 4.5 eV

is expended on formation of a single fluorine atom [Ref. 6]. These estimates give a concentration of atomic fluorine of $(1.1 \pm 0.2)\ 10^{18}$ cm^{-3} at SF_6 pressure of 1.5 atm, with laser efficiency η_e of 6.6% relative to the electron energy contributed to the active volume of the laser. Defining the chemical efficiency η_{chem} of the laser as the ratio of the laser pulse energy to the energy released in reaction of atomic fluorine with hydrogen, we find that at $p = 1.5$ atm and a ratio of $SF_5:H_2 = 20$, $\eta_{chem} = 21\%$. Increasing the ratio of $SF_6:H_2$ from 20 to 100 while maintaining the pressure constant at 1.5 atm causes a drop in laser energy to 0.3 J (see Fig. 3a). There is a corresponding drop in η_e. However, since such a reduction in the hydrogen content of the mixture causes a sharp reduction in its energy reserve, there is an increase in η_{chem}. For example, at $SF_6:H_2 = 54$, $\eta_{chem} = 29\%$, and at $SF_6:H_2 = 100$, η_{chem} is 40%. Increasing the pressure of the mixture above 1.5 atm (see Fig. 3a) causes the output energy of the laser to drop for any mixture composition that is used.

In principle, this effect may be caused by the influence of relaxation of excited HF* molecules upon collision with hydrogen molecules [Ref. 2]. However, an estimate of the characteristic times of the process ($k = 2.4 \cdot 10^4$ $(s \cdot mm\ Hg)^{-1}$ [Ref. 6]) at mixture pressures of ~1.5 atm shows that the drop in output energy of the laser cannot be entirely explained by relaxation of HF* molecules. In these estimates we have assumed that lasing pulse duration is commensurate with the duration of an electron beam current pulse [Ref. 7]. The fact that the maximum laser output energy is observed at the same pressure (see Fig. 3a) regardless of mixture composition is likewise indirect proof of the weak influence of relaxation of HF* by H_2 molecules. Apparently relaxation begins to have an effect at more appreciable values of mixture pressure. This is possibly manifested by the intersection of the curves on Fig. 3 at a pressure in excess of 3 atm. The abrupt drop in output energy with pressure at $p > 1.5$ atm to all appearances is due mainly to the nonuniformity of initiation, which shows up most strongly at high pressures. To check out this assumption, 2 diaphragms were introduced into the cavity with aperture of 4 mm, producing lasing in a narrow layer closest to the point of entry of the laser beam into the laser cell. The output energy of the lasing pulse was plotted as a function of the pressure of a mixture of $SF_6:H_2 = 20$ (Fig. 3b). In this case, the maximum output energy was no longer observed at 1.5 atm, but at 2.5 atm. An increase in pressure to 4.5 atm causes a drop in laser output energy by only 1.5 times. A further increase in the pressure was limited by the mechanical strength of the foil through which the beam was coupled into the laser cell.

The attainment of effective lasing at such high pressures may be of interest from the standpoint of tuning the laser frequency over the line width of the vibrational-rotational transition. The laser line width $\Delta\nu$ in the given case is determined by impact broadening and is related to the pressure of the mixture by the expression $\Delta\nu = \delta_{SF_6} p_{SF_6}$ [Ref. 1]. Line broadening by hydrogen can be disregarded.

Since $\delta_{He}/\delta_{SF_6} = 0.2$ [Ref. 8], increasing the pressure of the mixture by SF_6 is more advantageous than by using a buffer gas such as helium. Since $\delta_{SF_6} \cong 0.5$ $(cm \cdot atm)^{-1}$, under the given experimental conditions ($p \cong 4.5$ atm)

laser frequency can be tuned over a range of 2.2 cm^{-1} around the center of each of the vibrational-rotational lines in the emission range of the laser ($\lambda = 2.7-3.0$ μm). Increasing pressure by means of the principal reagents (SF_6 and H_2) without the use of buffer gases also produced lasing with rather high power (~10 mW) despite a small active volume of the laser (~8 cm^3).

The electron beam technique provides the capability of considerably increasing the active volume of the laser not only by increasing cathode area, but by increasing the electron beam energy. The latter also gives the possibility for increasing the pressure of the gas medium.

REFERENCES

1. Bagratashvili, V. N., Knyazev, I. N., Kudryavtsev, Yu. A., Letokhov, V. S., PIS'MA V ZHURNAL EKSPERIMENTAL'NOY I TEORETICHESKOY FIZIKI, Vol 18, 1973, p 110.

2. Vol'nov, A. M., Dovbysh, L. Ye., Kazakevich, A. T., Mel'nikov, S. P., Sinyanskiy, A. A., KVANTOVAYA ELEKTRONIKA, Vol 4, 1977, p 426.

3. Suchard, S. N., Kerber, R. L., Emanuel, G., Whitier, J. S., J. CHEM. PHYS., Vol 57, 1972, p 6065.

4. Chen, H. L., Taylor, R. L., Wilson, J., Lewis, P., Fyfe, W., J. CHEM. PHYS., Vol 61, 1974, p 306.

5. Bashkin, A. S., Konoshenko, A. F., Tomashov, V. N., Yuryshev, N. N., KVANTOVAYA ELEKTRONIKA, Vol 6, 1979, p 2166.

6. Wilson, J., Chen, H. L., Fyfe, W., Taylor, R. L., Little, R., Lowell, R., J. APPL. PHYS., Vol 44, 1973, p 5447.

7. Patterson, E. L., Gerber, R. A., Blair, L. S., J. APPL. PHYS., Vol 45, 1974, p 1822.

8. Wiggins, T. A., Griffen, N. C., Arlin, E. M., Kerstetter, D. L., J. MOL. SPECTR., Vol 37, 1970, p 77.

6610
CSO: 1862/145

UDC 621.378.33

FEASIBILITY STUDY ON MAXIMIZING SPECIFIC EMISSION PARAMETERS OF CHAIN REACTION HF LASER

Moscow KVANTOVAYA ELEKTRONIKA in Russian Vol 9, No 3(117), Mar 82 (manuscript received 7 Jul 81) pp 628-630

[Article by A. S. Bashkin, A. N. Orayevskiy, V. N. Tomashov and N. N. Yuryshev, Physics Institute imeni P. N. Lebedev, USSR Academy of Sciences, Moscow]

[Text] An examination is made of the energy parameters of an H_2/F_2 laser excited by electron beam at a pressure of the active volume of up to 3 atm. A specific energy output of 180 J/liter is achieved at efficiency of 500% with respect to the electron beam energy contributed to the active volume. An increase in initiation achieved by substituting sulfur hexafluoride for helium gave a specific energy output of 400 J/liter at efficiency of ~140% and chemical efficiency of 22% on a mixture at atmospheric pressure.

The development of pulsed chemical lasers is inseparably connected with increasing the pressure of the active gas medium. In principle, increasing the pressure enables us to raise the specific energy output both by increasing the energy content of the gas mixture, and by initiation, since the concentration of radicals (such as F) that "drive" the chain reaction of fluorine and hydrogen increases with increasing pressure of the medium at a constant electron or photon flux of the initiation source. The rise in pressure also increases the chemical reaction rate, shortening duration of the lasing pulse and thereby increasing lasing power along with energy output. Shortening of the laser pulse necessitates the use of a short-duration pumping source. From this standpoint, electron beams are most convenient for pumping the active media of high-pressure lasers.

The use of high-current, high-energy beams (55 kA, 1 MeV) gave lasing energy of 2.3 kJ [Ref. 1, 2] on a hydrogen-fluorine mixture at pressure of 700 mm Hg, and even 4.2 kJ at mixture pressure of 1340 mm Hg. The efficiency η_e with respect to beam energy invested in the active volume of the laser was 180%, and maximum chemical efficiency η_{chem} was 10%. All these results admirably demonstrate the feasibility of efficient laser operation on a fluorine-hydrogen chain reaction at high reagent pressure. Unfortunately, Ref. 1, 2 do not give

data on specific energy outputs, initiation level, or the way that laser parameters depend on mixture composition. All this makes it difficult, if not impossible, to do an in-depth physical analysis of the research results.

In this paper, we study the possibility of getting effective lasing on a fluorine-hydrogen chain reaction at high reagent pressure by using a comparatively low-energy electron beam (less than 200 keV) as the pumping source. The experimental facility is described in detail in Ref. 3. Let us note that the use of an external magnetic field in transverse configuration of the experiment eliminated electron beam scattering, enabled exact measurement of the beam energy invested in the active volume of the laser by a moving calorimeter [Ref. 4], and precise formation of the geometry of the excited volume in the laser gas mecium [Ref. 3].

The size of the active volume was determined on the basis of measurements of the electron beam cross section in the gas medium and the lasing spot, the cross section of the lasing spot corresponding to the electron beam cross section in the appropriate direction. On the basis of these measurements we can estimate the active volume of the laser: $\sim 8 \pm 2$ cm^3.

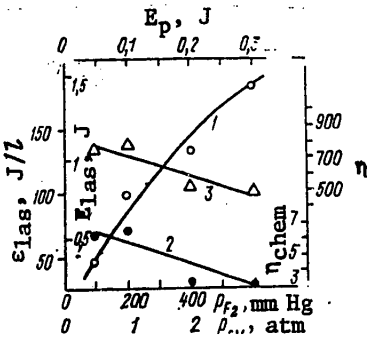

Fig. 1. Laser output energy E_{las} (1), chemical efficiency η_{chem} (2) and efficiency η_e with respect to electron beam energy invested in active volume (3) as functions of mixture pressure

Measurements were made of the output energy of a laser on a mixture of $F_2:O_2:H_2:He = 2:0.16:0.48:5$, as well as η_e and η_{chem} at different pressures of the mixture (Fig. 1). As the pressure is increased up to 3 atm, an increase is observed in the laser output energy while η_e drops from 900% at a pressure of 1 atm to 500% at 3 atm with a corresponding drop in η_{chem} from 6.6 to 3.2%. It is interesting to note that the data obtained at atmospheric pressure correspond almost completely to the data found in Ref. 4 for a similar mixture in a laser with longitudinal pumping by an electron beam of the same energy.

The influence of the hydrogen content in the mixture was studied at atmospheric pressure (the change in hydrogen pressure was compensated by changing the helium pressure in the mixture). The results are shown in Fig. 2. Despite the fact that increasing the ratio p_{H_2}/p_{F_2} to ½ did increase the laser output energy, subsequent experiments were done for mixtures with $p_{H_2}/p_{F_2} = ¼$ since increasing this ratio reduced the value of η_{chem} as well as considerably increasing the pressure developed as a result of the reaction, which often led

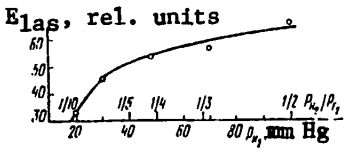

Fig. 2. Laser output energy as a function of hydrogen content in the mixture

to rupture of the foil and damage of the cell windows. Since the active volume of the laser retained a small fraction of the electron beam energy even at a mixture pressure of 3 atm, and a further increase in the pressure of the mixture was limited by the mechanical strength of the laser cell, an investigation was made of the possibility of increasing the degree of initiation of the mixture by increasing the density of the medium. This was done by adding sulfur hexafluoride, a gas with high molecular weight that is also a donor of atomic fluorine [Ref. 4]. The total pressure of the mixture (1 atm) was not changed, and the increased pressure was compensated by reducing the helium content in the mixture. The resultant curves are shown on Fig. 3. Addition of 400 mm Hg of SF_6 led to an increase in output energy by a factor of 2.5. Efficiency η_{chem} reached a very high value (~16%). However, the increase in E_{las} and η_{chem} was accompanied by a drop in η_e to 200%. This can be attributed to a reduction in the length of the chain reaction due to a break in the chain in trimolecular reactions of the type $F(H) + O_2 + M \rightarrow F(H)O_2 + M$, where M is is a molecule of SF_6, which is quite effective in reactions of this type.

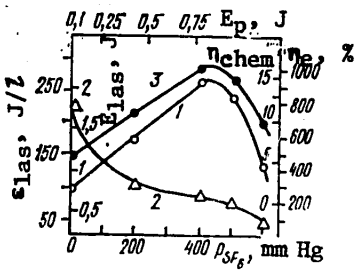

Fig. 3. Influence of SF_6 content in mixture of $F_2:O_2:H_2:SF_6 = 200:16:48:p_{SF_6}$ on E_{las} (1), η_e (2) and on η_{chem} (3)

Despite the reduction in η_e, the addition of SF_6 may be advantageous from the viewpoint of increasing the specific energy output, chemical efficiency, and also more efficient utilization of beam energy. Besides, the presence of SF_6 in the mixture considerably increases its stability, and experiments have shown that it reduces the pressure developed as a result of the reaction, which in turn reduces the requirements for strength of structural components of the cell, especially the foil and windows.

By optimizing the cavity and increasing the accelerator beam current density through a reduction in the thickness of the coupling foil, a laser emission energy of 3.3 J was attained on a mixture of $F_2:O_2:H_2:He:3F_6 = 200:8:48:100:400$ mm Hg. Beam energy of 2.4 J was absorbed in the active volume of the laser, which corresponds to a concentration of $1.25 \cdot 10^{17}$ fluorine atoms per cm^3 that are formed during initiation at $\varepsilon_F = 12$ eV [Ref. 5]. The value of η_e was 140%, and $\eta_{chem} \sim 22\%$. As the fluorine pressure in this mixture is increased to 400 mm Hg, laser output energy rises to 4 J. Measurements of laser beam divergence made for a cavity with base of 34 cm formed by an opaque mirror with radius of curvature of 10 m and a flat output mirror gave a value of 4 mrad, which is ten times the diffraction limit. However, no experiments were done on imporving the divergence as this was beyond the scope of our research.

The results demonstrate the feasibility of getting very high specific energy outputs of ~400 J/liter at $\eta_e \gtrsim 100\%$.

The use of an external magnetic field in transverse configuration of the experiment gives high initiation of the active laser medium even at low electron beam energy. The main impediment to increasing the pressure of working mixtures at present is the problem of increasing the strength of laser structural components, whereas the active volumes of the laser can be increased both by increasing electron beam energy and by enlarging the cross section of the beam, which is completely feasible considering the current state of accelerator engineering.

REFERENCES

1. Gerber, R. A., Patterson, E. L., Blair, L. S., Greiner, N. R., APPL. PHYS. LETTS, Vol 25, 1974, p 281.

2. Patterson, E. L., Gerber, R. A., IEEE, Vol QE-11, 1975, p 642.

3. Bashkin, A. S., Orayevskiy, A. N., Tomashov, V. N., Yuryshev, N. N., KVANTOVAYA ELEKTRONIKA, Vol 9, 1982, p 630.

4. Bashkin, A. S., Konoshenko, A. F., Tomashov, V. N., Yuryshev, N. N., KVANTOVAYA ELEKTRONIKA, Vol 6, 1979, p 2166.

5. Wilson, J., Chen, H. L., Fyfe, W., Taylor, R. L., Little, R., Lowel, R., APPL. PHYS., Vol 44, 1973, p 5447.

6610
CSO: 1862/145

UDC 621.378.33

INFLUENCE OF STARTING INITIATION ON H_2/F_2 LASER PARAMETERS

Moscow KVANTOVAYA ELEKTRONIKA in Russian Vol 9, No 3(117), Mar 82 (manuscript received 7 Jul 81) pp 630-632

[Article by A. S. Bashkin, A. N. Orayevskiy, V. N. Tomashov and N. N. Yuryshev, Physics Institute imeni P. N. Lebedev, USSR Academy of Sciences, Moscow]

[Text] Parameters of a chemical H_2/F_2 laser are studied as a function of the level of starting initiation of the mixture by electron beam. It is shown that conditions of maximizing efficiency do not coincide with conditions of maximizing output energy.

The principal initial parameters that determine the characteristics of the emission pulse of a chemical laser are mixture composition and initiation. Knowledge of the starting initiation enables prediction of lasing parameters as well as verification and correction of known theoretical models of chemical lasers. Therefore it is of considerable interest to study the way that such laser parameters as specific energy output ε_{las}, laser efficiency η_e, chemical efficiency η_{chem} and lasing pulse duration τ_{las} depend on starting initiation, i. e. the concentration of fluorine atoms [F] at different pressures of working mixtures. Unfortunately, the question of the influence of initiation level on the lasing parameters of H_2/F_2 chemical lasers has been practically untouched in experimental research.

We have carried out such research with a relativistic electron beam for dissociation of molecular fluorine. Since in the given case $\tau_{init} \ll \tau_{las}$, the investigation of the influence of [F] on lasing parameters becomes simpler and clearer. The degree of dissociation of F_2 was varied by changing the electron beam current density with the insertion of mesh filters in the path of the electron beam. The use of foil of different thicknesses to do this may cause a change in the energy spectrum of electrons, and therefore is undesirable.

The general setup and parameters of the accelerator are given in Ref. 1. The use of an external magnetic field prevented scattering of electrons and enabled more accurate measurement of beam energy by an angle calorimeter. The active volume of the laser was ~8 cm^3. Based on calorimetric measurements of beam energy absorption in gas media, the initiation energy was determined. The initial concentration of atomic fluorine was calculated from these measurements, assuming that 12 eV is used to produce a single fluorine atom [Ref. 2].

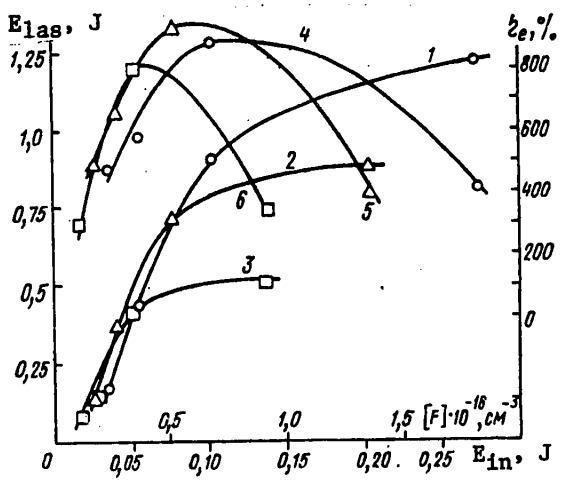

Fig. 1. Laser emission energy E_{las} (1-3) and efficiency η_e (4-6) as functions electron beam energy invested in the active volume: mixture $F_2:O_2:He:H_2$=200:16:500:48 (1, 4), 150:12:376:36 (2, 5) and 100:8:250:24 mm Hg (3, 6)

A mixture of $F_2:O_2:He:H_2 = 2:0.16:5:0.48$ was selected for the experiments. A mixture of similar composition had been studied previously. At a pressure of 0.8-1 atm this mixture gave $\varepsilon_{las} \approx 100$ J/liter at efficiency $\eta_e \approx 900\%$ [Ref. 3]. Some decrease of hydrogen in the mixture, as shown by the experiment, increased η_{chem} with a slight reduction in energy output. At the same time, there was also a reduction in the possibility of damage to structural components of the laser by explosion of the mixture.

The experiments were done at a total pressure of 1, 0.75 and 0.5 atm. Fig. 1 shows both the laser emission energy and efficiency (η_e) as functions of the energy E_{in} invested in the active volume. An increase in the level of initiation increases the output energy of the laser, although there is a tendency to saturation of this dependence in the region of high input energies. This effect shows up most strongly as the pressure of the working mixture decreases.

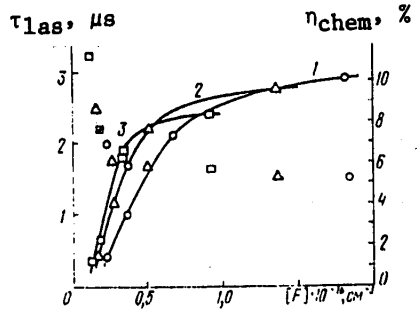

Fig. 2. Chemical efficiency η_{chem} (curves) and lasing pulse duration τ_{las} (points) as dependent on the electron beam energy invested in the active volume of the laser (notation as in Fig. 1)

Specific energy output of 155 J/liter is attained at the maximum possible initiation in the given experiments on a mixture with pressure of 1 atm. It is interesting that in the region of low values of initiation the lasing energy is higher on mixtures of lower pressure. Efficiency η_{chem} behaves similarly (Fig. 2). This may be due to the fact that the length of the chemical reaction chain is greater for low-pressure mixtures at low-level initiation. Increasing the pressure of the mixture while retaining the concentration of initial centers leads to an increase in acts of chain breaking, which in turn reduces the lasing characteristics.

Fig. 2 also shows the dependences of lasing pulse duration at different pressures on the level of initiation of the mixture. They are characterized by weak dependence of τ_{las} on the pressure of the working mixture and are steep only in the region of low E_{in}. The behavior of η_e (see Fig. 1) is characterized by a maximum with position that depends on the pressure of the working mixture, and shifts toward increasing initiation levels for the higher-pressure mixtures. The maximum values of η_e for all mixtures used are 800-900%. The specific energy output for a mixture at atmospheric pressure reaches 110 J/liter.

Since it was impossible to increase initiation by raising the current density in the given experiments, we attempted to increase the initial concentration of fluorine atoms by substituting sulfur hexafluoride for some of the helium [Ref. 3]. A specific energy output of $\varepsilon_{las} \cong 400$ J/liter was attained at $\eta_e \cong 140\%$ on a mixture of $F_2:O_2:H_2:He:SF_6 = 200:8:48:100:400$ mm Hg. Here the energy input to the active mixture was 2.4 J. If these results are compared with those of our research obtained on a mixture of atmospheric pressure at $E_{in} > 0.075$ J (see Fig. 1), it can be seen that the product $\eta_e E_{las}$ changes by a factor of only 1.7 as E_{in} is changed by a factor of 30. This shows that the optimum conditions of initiation are appreciably different for maximizing η_e and ε_{las}.

Thus our research has led us to the following conclusions. 1. With increasing initiation energy there is an increase in output energy and chemical efficiency of the laser, although there is a tendency toward saturation that is most pronounced for low-pressure mixtures. 2. The optimum values of laser efficiency η_e are reached at certain values of initiation energy E_{in}, and as the pressure of the working mixture is increased, the optimum region of E_{in} shifts toward higher values. 3. At low initiation energies the efficiency of the chemical chain reaction drops with increasing pressure of the working mixture, leading to a reduction in η_e, η_{chem} and the laser output energy.

REFERENCES

1. Bashkin, A. S., Orayevskiy, A. N., Tomashov, V. N., Yuryshev, N. N., KVANTOVAYA ELEKTRONIKA, Vol 9, 1982, p 628.

2. Wilson, J., Chen, H. L., Fyfe, W., Taylor, R. L., Little, R., Lowell, R., J. APPL. PHYS., Vol 44, 1973, p 5447.

3. Bashkin, A. S., Konoshenko, A. F., Orayevskiy, A. N., Tomashov, V. N., Yuryshev, N. N., KVANTOVAYA ELEKTRONIKA, Vol 6, 1979, p 2166.

6610

CSO: 1862/145

UDC 621.373.8.038.825.3

NEW PHOSPHATE GLASS FOR LASERS WITH HIGH EMISSION PULSE RECURRENCE RATE

Moscow KVANTOVAYA ELEKTRONIKA in Russian Vol 9, No 3(117), Mar 82 (manuscript received 1 Jul 81) pp 622-624

[Article by N. Ye. Alekseyev, A. K. Gromov, A. A. Izyneyev and V. B. Kravchenko, Institute of Radio Physics and Electronics, USSR Academy of Sciences, Moscow]

[Text] The paper gives some lasing characteristics of new LGS-T phosphate glass based on Na-Al that has higher thermal conductivity and heat resistance than known grades, as well as a rather high coefficient of thermal expansion, making it suitable as a base for synthesizing athermal glasses. The authors demonstrate absence of concentration quenching of neodymium luminescence in such a base at a content of up to 6 wt.% Nd_2O_3. Average lasing power of more than 20 W at a frequency of 15 Hz is attained on active elements with Ø 8 x 100 mm. The glass has good technological characteristics and can be produced in large volumes.

Active elements made of phosphate glasses are used in pulse-periodic lasers due to high efficiency and low lasing thresholds. The possibilities for increasing the lasing power taken from the active element are limited for a predetermined size chiefly due to thermal stability of the elements, which can be increased either by hardening [Ref. 1-3] or by improving the mechanical characteristics of the glass and improving its thermal conductivity.

Use of the first method on heat-treated active elements measuring Ø 10 x 130 mm made of GLS22 athermal glass has yielded a free lasing power of 15 W [Ref. 3]. An output power of 8 W in the free lasing mode and 5 W in the Q-switched mode has been attained on hardened active elements measuring Ø 8 x 100 mm made from LGS-I athermal glass on a frequency of 10 Hz [Ref. 4]. At the present time, we have obtained a free lasing power of 96 W at a frequency of 1 Hz at efficiency of 3% on a hardened rectangular active element with size of 10 x 40 x 300 mm made of LGS-I glass. However, the hardening of active elements involves an additional technological operation that increases cost. Therefore the second method of improving thermal stability of glass is preferable for high-power process lasers.

It is known [Ref. 5] that the thermal stability of an active element increases with a reduction in the coefficient of linear thermal expansion α, which for

phosphate athermal glasses lies in a range of $(105-130)\cdot10^{-7}$ K^{-1} [Ref. 6, 7]. Laser glasses are known with lower values of α, including Li-Nd-La ultraphosphate glass. Lasing power of 15 W at frequency of 6-8 Hz has been attained on an active element with Ø 6.3x100 mm made of such glass [Ref. 8]. In this paper we give some results of investigation of the laser characteristics of active elements made of a new Na-Al glass that has elevated thermal conductivity [Ref. 9] and thermal stability. The value of α for glasses of this type is $(108-120)\cdot10^{-7}$ K^{-1}, and consequently this base (LGS-T glass) can be used to make athermal glasses.

The glasses were founded in platinum crucibles with volume of 3 liters with bottom branch pipe; the concentration of Nd_2O_3 was 3 and 6 wt.%. Cylindrical active elements with Nd_2O_3 concentration of 3 wt.% measured Ø 8x100 mm, and with 6 wt.% -- Ø 5x100 mm ($\alpha = 108\cdot10^{-7}$ K^{-1}). Nd^{3+} luminescence lifetime for both concentrations was 270-280 μs, which shows the possibility for further increasing the neodymium content in the glass. The half-width of the Nd^{3+} luminescence band for transition $F_{3/2}$- $I_{11/2}$ is 18 nm. The lasing characteristics of the glasses were studied in a monoblock quartz illuminator with mirror coating. Pumping was by an ISP-600 stroboscopic flashlamp, capacitance of the capacitor bank was 200 μF, the lamp and the active element were cooled by a 0.2% solution of K_2CrO_4 at a flowrate of at least 30 liters/minute, pumping energy in a pulse was 100 J. The transmission of the output mirror was taken as the optimum for each type of active element, and was 30% for an element measuring Ø 8x100 mm, and 50% for Ø 5x100 mm. The average power was measured by the IMO-2 instrument with wedge-shaped reflecting plate serving as a beam splitter. The results of measurements of the output power as a function of the pumping pulse recurrence rate are shown on the Figure (curves 1, 2). Given here for comparison are the parameters of a hardened LGS-I glass active element Ø 8x100 mm (curve 3). It can be seen that on a frequency of 15 Hz at pumping energy of 100 J we get an average lasing power of more than 20 W with the active element Ø 8x100 mm, and more than 15 W with Ø 5x100 mm. It should be noted that the active elements were not subjected to any hardening operations other than ordinary pickling, and that they were capable of operation at a pumping power of 1.5 kW for an arbitrarily prolonged time. As a rule, deterioration of output parameters was caused by sputtering of the lamp electrodes and reduction of light output. The element with Ø 5x100 mm was tested in the same illuminator with the LTI-PCh industrial laser as the light source. Under these conditions, an average emission power of 9 W was attained at a lasing pulse recurrence rate of 50-100 Hz.

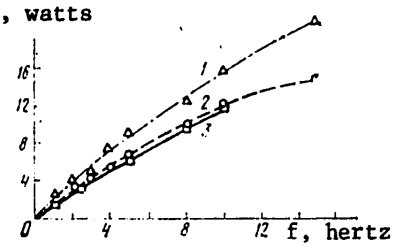

Radiation power as a function of the pumping pulse recurrence rate: 1--LGS-T glass (3 wt.% Nd_2O_3); 2--LGS-T (6 wt.% Nd_2O_3); 3--hardened LGS-I glass

Thus, LGS-T laser glass is a quite promising material for use in lasers with emission pulse recurrence rates at least up to 100 Hz and average emission power of 100 W or more. In addition, it has good technological properties and can be made in large volumes.

REFERENCES

1. Mak, A. A., Mit'kin, V. M., Polukhin, V. N., Stepanov, A. I., Shchavelev, O. S., KVANTOVAYA ELEKTRONIKA, Vol 2, 1975, p 850.

2. Mit'kin, V. M., KVANTOVAYA ELEKTRONIKA, Vol 8, 1981, p 484.

3. Buzmakov, A. G., Kovrishkin, V. S., Mit'kin, V. M., Polukhin, V. N., Stel'makh, M. F., Stepanov, A. I., Pozdnyakov, A. Ye., Chel'nyy, A. A., in: "Tezisy dokladov na Vtoroy Vse oyuznoy konferentsii 'Optika lazerov'" [Abstracts of Reports to Second All-Union Conference on Laser Optics], Leningrad, GOI, 1979, p 7.

4. Alekseyev, N. Ye., Gruzdev, V. V., Izyneyev, A. A., Kopylov, Yu. L., Kravchenko, V. B., Milyavskiy, Yu. S., Mikhaylov, Yu. N., Rozman, S. P., Fisher, A. M., KVANTOVAYA ELEKTRONIKA, Vol 5, 1978, p 2354.

5. Mit'kin, V. M., Shchavelev, O. S., Zheltov, V. B., OPTIKO-MEKHANICHESKAYA PROMYSHLENNOST', No 9, 1978, p 39.

6. Avakyants, L. A., Buzhinskiy, I. M., Koryagina, Ye. I., Surkova, V. F., KVANTOVAYA ELEKTRONIKA, Vol 5, 1978, p 725.

7. Alekseyev, N. Ye., Gapontsev, V. P., Zhabotinskiy, M. Ye., Kravchenko, V. B., Rudnitskiy, Yu. P., "Lazernyye fosfatnyye stekla" [Laser Phosphate Glasses], Moscow, Nauka, 1970.

8. Avanesov, A. G., Basov, Yu. G., Garmash, V. M., Denker, B. I., Il'ichev, N. N., Maksimova, G. V., Malyutin, A. A., Osiko, V. V., Pashinin, P. P., Prokhorov, A. M., Sychev, V. V., KVANTOVAYA ELEKTRONIKA, Vol 7, 1980, p 1120.

9. Alekseyev, N. Ye., Volkonskaya, T. I., Izyneyev, A. A., Kravchenko, V. B., Kulikova, I. N., Parfenova, L. S., Smirnov, I. A., "Tezisy dokladov Pyatoy Vsesoyuznoy konferentsii 'Fiziko-khimicheskiye issledovaniya fosfatov' ('Fosfaty-81')" [Abstracts of Reports to the Fifth All-Union Conference on Physical-Chemical Phosphate Research (Phosphates-81)], Leningrad, 1981, part 1, p 10.

6610
CSO: 1862/145

UDC 621.385.325

PICOSECOND PULSE GENERATION IN ALEXANDRITE LASER IN 0.7-0.8 μm RANGE WITH PASSIVE MODE LOCKING

Moscow KVANTOVAYA ELEKTRONIKA in Russian Vol 9, No 3(117), Mar 82 (manuscript received 6 Jul 81) pp 607-609

[Article by V. N. Lisitsyn, V. N. Matrosov, V. P. Orekhova, Ye. V. Pestryakov, B. K. Sevast'yanov, V. I. Trunov, V. N. Zenin and Yu. L. Remigaylo, Institute of Thermal Physics, Siberian Department, USSR Academy of Sciences, Novosibirsk; Institute of Geology and Geophysics, Siberian Department, USSR Academy of Sciences, Novosibirsk; Institute of Crystallography, USSR Academy of Sciences, Moscow]

[Text] A report on picosecond pulse generation in an alexandrite laser in the range of 0.7-0.8 μm on vibronic transitions $^4T_2 \rightarrow {}^4A_2 + h\omega_{phon}$ in passive mode locking using saturable absorbers DS1 and DTTS. The pulse duration with DS1 in the range of 0.725-0.745 μm was 8 ps, and with DTTS in the range of 0.75-0.775 μm -- 90 ps.

Of particular interest among new laser materials that have now been synthesized is alexandrite $BeAl_2O_4:Cr^{3+}$ [Ref. 1, 2]. A distinctive feature of this material is lasing on vibronic transitions $^4T_2 \rightarrow {}^4A_2 + h\omega_{phon}$, and as a consequence the capability for continuous tuning of the lasing frequency in the region of 0.7-0.8 μm at room temperature [Ref. 2, 3]. Relatively low thresholds, high efficiency with lamp pumping and a considerable increase in efficiency when the active element is heated to 70°C, as well as the capability for continuous-wave operation or with a high pulse recurrence rate open up extensive possibilities for its use in science experiments and engineering, and in particular for generating ultrashort pulses with tunable frequency.

As we know [Ref. 4], ultrashort pulses can be produced in a laser with mode locking if the spectral width of amplification is wide enough. In alexandrite the amplification band with lasing on vibronic transitions is 100 nm. The situation is analogous in organic dye lasers, which enables generation of sub-picosecond pulses with tunable frequency.

In this paper we are the first to report on frequency-tunable picosecond pulse generation in a solid-state alexandrite laser with passive mode locking by saturable organic dyes.

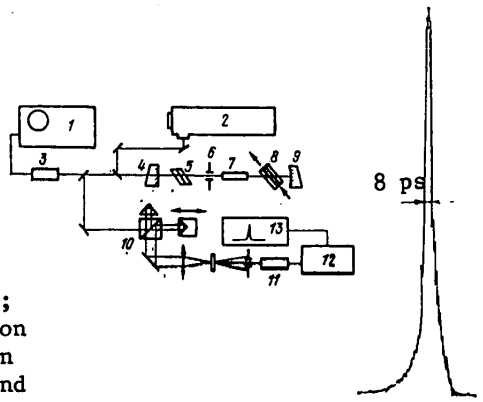

Fig. 1. Diagram of the experimental setup: 1--oscilloscope; 2--spectrograph; 3--FEK-09; 4--output mirror; 5--Lio filter; 6--diaphragm; 7--active element; 8--cell; 9--opaque mirror; 10--correlation device for measuring pulse duration; 11--photomultiplier; 12--peak-to-peak voltmeter; 13--two-coordinate chart recorder; on the right is the correlation function of the laser pulse in vector generation of the second harmonic

The diagram of the experimental setup for mode locking is shown in Fig. 1. The active element with Ø 6 x 70 mm with chromium concentration of 10^{19} cm^{-3} and antireflection-coated end faces and an INP 5/60 flashlamp were placed in a monoblock quartz illuminator. The ultraviolet part of the pumping (shorter than 350 nm) lying in the region of inactive absorption of alexandrite and detrimental to the efficiency of laser operation due to the development of photochemical and thermal processes in the active element was cut off by an aqueous solution of sodium nitrate and a thin pyrex tube so that laser efficiency during operation was not decreased. The axis of the active element coincided with direction <001> of alexandrite, and stimulated emission was polarized along <010>. The laser cavity with length of 0.5 m was formed by an opaque mirror with radius of curvature of 3 m and a flat output mirror with transmission Tr = 3%.

Measurement of the threshold characteristics of the active medium in single-mode operation without frequency tuning or selectors showed that the threshold of free lasing is 48 J, which coincides with the value given in Ref. 2. Let us note that the measurements made in our research were done on the crystal used in Ref. 3. The high values of lasing thresholds in Ref. 3 can be attributed to the fact that the design of the illuminator for studying the temperature dependences of lasing characteristics did not give high pumping efficiency or optimization of lasing parameters. In the illuminator used in our research, at a pulse recurrence rate of 12.5 Hz and pumping energy of 80 J (τ_p = 250 μs) on wavelength of 70 nm the average output power was 1.1 W at output mirror transmission Tr = 8%. The dependence of output energy on pumping energy is shown in Fig. 2. In the mode of generation of the TEM_{00q} mode with spectral selector (Lio filter) and diaphragm of Ø 1.2 mm, tuning was accomplished over a range of 718-780 nm (Fig. 3).

It is to be noted that at high levels of excitation in the active element, considerable thermally induced stresses arise that give rise to a heat lens. The dependence of the effective focal length of the heat lens on the average pumping power is approximated in our case by the expression $F(P_{av}) = 1.5/P_{av}^{\frac{1}{2}}$ [kW]. With consideration of this, the design of the optical cavity was changed

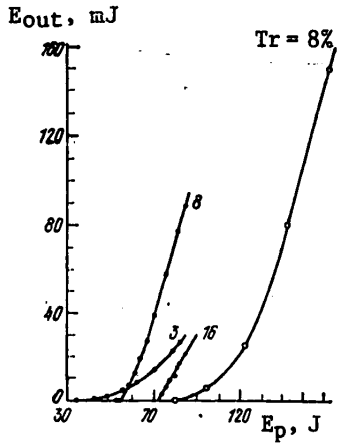

Fig. 2. Free lasing output energy of alexandrite as a function of pumping energy for $\lambda = 750$ nm: rod temperature T = 50 (●) and 15°C (○)

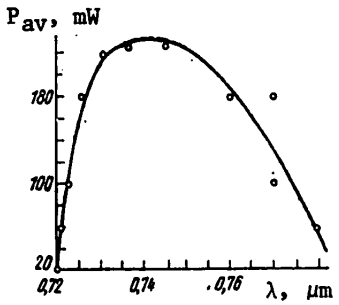

Fig. 3. Spectral dependence of free lasing output power for laser with Lio filter at Tr = 3%

to compensate for thermal effects. Induced thermal birefringence was disregarded since it was less than the natural level of $\Delta n \cong 0.002$, which was confirmed by polarization interference in crossed polaroids. As a result of using the geometry optimum for our case (the concave mirror with radius of curvature of 300 cm was replaced with a convex mirror with radius of curvature of 200 cm), the output power was increased to 2.5 W.

Mode locking in the alexandrite laser was accomplished by two saturable absorbers -- DS1 and DTTS -- with relaxation times of 22 and 130 ps respectively in ethanol solutions [Ref. 4]. The absorption spectrum of DS1 in ethanol is shifted relative to the center of the lasing band of alexandrite (750 nm) into the short-wave region, and has a maximum on 709 nm with half-width of 40 nm, which makes it difficult to use this substance as a saturable absorber in the 700-750 nm band. Because of this, the DS1 absorption line was shifted by replacing the ethanol with dimethyl sulfoxide by 8 nm into the longer-wave region. DTTS in ethyl alcohol, despite its considerable relaxation time, is admirably suitable with respect to absorption spectrum for mode locking in the long-wave part of the alexandrite lasing spectrum (>750 nm).

The cell with saturable absorber oriented at the Brewster angle was placed in front of the opaque mirror; the dye solution was circulated at a rate of 10 liters per minute, enabling operation at a pulse recurrence rate of 12.5 Hz. All the studies described below were done in this mode. Wavelength was tuned by a Lio filter, and the TEM_{00q} mode was isolated by a diaphragm. The end faces of the active element were turned through an angle of 2-3° relative to the axis of the optical cavity. Mode locking was matched by changing the density of the saturating absorber and the pumping level. The envelope of the pulse train and the mode locking were checked by an FEK-09 coaxial photocell and an oscilloscope with overall time resolution of 3 ns. The average duration of ultrashort pulses in the train was measured by the correlation

technique of vector generation of the second harmonic in $LiIO_3$ [Ref. 4]. In the two-threshold mode [Ref. 5] with DS1 in dimethyl sulfoxide, the duration of the pulse train was 200-300 ns with average duration of a pulse in the train of 20 ps; in the mode close to autostabilization [Ref. 6], in a somewhat modified cavity geometry, where shaping was done from a series of free lasing spikes, the average duration of the pulse was shortened to 8 ps, and considerable modulation of the train envelope was observed. With DS1, tuning was accomplished in the range of 725-745 nm at a spectral width of 0.2 nm. The absence of structure in the emission spectrum at high contrast of the correlation curve shows that there were no additional pulses on the axial period [Ref. 7]. On Fig. 1 we have shown the correlation curve for generation of the second harmonic on a wavelength of 730 nm, and have indicated the pulse duration as adjusted for a gaussian profile.

With use of an ethanol solution of DTTS, ultrashort pulses with 90 ps duration were generated in the 750-775 nm range. Average output power of the laser with DS1 on a wavelength of 735 nm was 20 mW. When the temperature of the active element was increased to 50°C (checked by a differential thermocouple on the rod), mode locking became more stable due to increased gain of the active medium.

There is no doubt that when the concentration of active centers in the alexandrite matrix is increased, we can count on a considerable increase in the output power of the laser in mode-locked operation.

Our research was not aimed at getting ultrashort pulses in the isolated pulse mode at high pumping energies. Our principal attention was concentrated on the feasibility of operation at a high pulse recurrence rate (up to 100 Hz), enabling active use of the alexandrite laser both in spectroscopic work and in technological devices.

REFERENCES

1. Bukin, G. V., Volkov, S. Yu., Matrosov, V. N., Sevast'yanov, B. K., Timoshechkin, M. I., KVANTOVAYA ELEKTRONIKA, Vol 5, 1978, p 1168.

2. Walling, J. C., Peterson, O. J., Jenssen, H. P., Morris, R. C., O'Dell, E. W., IEEE J., Vol QE-16, 1980, p 1302.

3. Sevast'yanov, B. K., Remigaylo, Yu. L., Orekhova, V. P., Matrosov, V. N., Tsvetkov, Ye. G., Bukin, G. V., DOKLADY AKADEMII NAUK SSSR, Vol 256, 1981, p 373.

4. Shapiro, S., ed., "Sverkhkorotkiye svetovyye impul'sy" [Ultrashort Light Pulses], Moscow, Mir, 1981.

5. Zherikhin, A. N., Kovalenko, V. A., Kryukov, P. G., Matveyets, Yu. A., Chekalin, S. V., Shatverashvili, O. B., KVANTOVAYA ELEKTRONIKA, Vol 1, 1974, p 377.

6. Milenkevich, A. V., Savva, V. A., Samson, A. M., ZHURNAL PRIKLADNOY SPEKTROSKOPII, Vol 25, 1976, p 618.

7. Sychev, A. A., TRUDY FIZICHESKOGO INSTITUTA IMENI P. N. LEBEDEVA AKADEMII NAUK SSSR, Vol 84, No 3, 1975.

6610
CSO: 1862/145

UDC 537.876.23.029.7:551.510.5

ESTIMATING POSSIBILITIES FOR USING PHASE CONJUGATE ADAPTIVE SYSTEMS TO COMPENSATE LASER BEAM THERMAL DEFOCUSING

Moscow RADIOTEKHNIKA I ELEKTRONIKA in Russian Vol 26, No 11, Nov 81 (manuscript received 24 Mar 80) pp 2334-2341

[Article by V. V. Vorob'yev]

[Text] Based on representation of the action of a nonlinear medium as an extended aberration-free heat lens, the author calculates the process of compensating defocusing by phase conjugate adaptive systems. Use of such systems is effective only in the case of weak thermal nonlinearity when the length of the nonlinear heat lens is less than the characteristic length of thermal self-stress.

1. Recently there has been extensive discussion of the question of feasibility of compensating the distortions of laser beams that arise on propagation in the atmosphere by using adaptive coherent optics systems [Ref. 1-4]. Generalization of the results of numerical calculations and experimental research has led to the conclusion [Ref. 1] that these systems may satisfactorily correct distortions introduced by turbulence, but are poor at correcting thermal defocusing. An exact solution for the problem of compensating thermal defocusing in the real atmosphere can be found only by numerical methods, and in the general case this requires repeated solution of a four-dimensional problem of beam propagation to the target and propagation of the reflected wave to the reception aperture. This does not permit calculations with sufficient accuracy and over wide changes in parameters. Therefore it is advisable to consider simple models of propagation and compensation that give an analytical solution of the problem. One such model consists in replacing the action of the nonlinear medium on beam propagation by the action of thin aberration-free lenses located at different distances from the input aperture [Ref. 5]. It has been demonstrated that it is not always possible to compensate even the defocusing of such lenses. The given model has the disadvantage that the results depend strongly on the position of the nonlinear thin lenses on the propagation path. It is not clear where to place them in the case of an extended nonlinear medium. In this paper, an investigation is made of the possibilities of using a phase conjugate system to compensate for defocusing by an extended heat lens. It has been shown by various examples that compensation is impossible when the extent l of the nonlinear medium is greater than the characteristic length L_T of thermal self-stress.

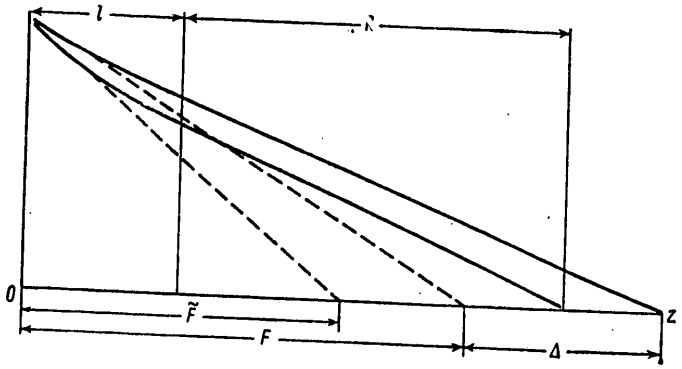

Fig. 1. Qualitative pattern of correction: l--thickness of nonlinear layer; $R+l$--distance to the target; F--initial radius of curvature of the wavefront; $F+\Delta$--distance at which focusing to correction occurs; $\tilde{F}$--radius of curvature of the reflected wave

2. The following problem is considered (see Fig. 1). A beam with radius of curvature of the phase front F on boundary $z=0$ is incident in the direction of the z-axis on a nonlinear medium occupying layer $(0, l)$. Due to thermal nonlinearity, the distance at which the beam is focused behind the layer (if such is possible) will differ from F by an amount Δ. A diverging wave passing through the nonlinear layer is reflected from a target located at distance R from the layer. The reflected wave will have radius of curvature $-\tilde{F}$. If there were no change in perturbations of the index of refraction in the layer with time, focusing on the target could be realized by changing the radius of curvature of the incident wavefront from F to $\tilde{F}$. However, in a nonlinear medium, a change in F leads to a change of the medium, and as a result, when F is changed to $\tilde{F}$ the focal point may shift away from the target. Our task is to determine conditions under which repetition of this procedure leads to focusing on the target, and to find the number of repetitions of the procedure (or the time interval required to adjust focusing) to get the desired focusing accuracy.

Assuming that the thickness of the layer l is much less that the diffraction length $L_д = ka^2$, where k is the wave number, a is beam size, and disregarding attenuation of intensity due to absorption, we will describe beam propagation in the layer by the equations

$$2\frac{\partial\varphi}{\partial z}+(\nabla_\perp\varphi)^2=\varepsilon_н(J), \tag{1}$$

$$\frac{\partial J}{\partial z}+\nabla_\perp\varphi\nabla_\perp J+\Delta_\perp\varphi J=0, \tag{2}$$

where ϕ is the eikonal, J is the light field intensity, $\varepsilon_н$ is the nonlinear part of permittivity, which in the general case is some functional of J(x, y, z, t).

3. Let us first consider compensation in a medium with nonlinearity of the form

$$\varepsilon_n(J) = -\varepsilon_2 J, \tag{3}$$

where the coefficient ε_2 and intensity J may depend parametrically on time. This dependence may approximate the integral

$$\varepsilon_n(J) = \frac{\partial \varepsilon}{\partial T}\frac{\alpha}{\rho c_p}\int_0 J(x, y, z, t')\,dt' \tag{4}$$

when intensity J changes slowly in time ($t(\partial J/\partial t) \ll J$). In this case, $\varepsilon_2 = -(\partial\varepsilon/\partial T)\cdot(\alpha t/\rho c_p)$. For reasons of simplicity, a dependence of form (3) is often used in thermal self-stress problems (e. g. see Ref. 2, 5). Its applicability to compensation problems will be discussed below.

In the aberration-free approximation [Ref. 6], solution of equations (1), (2) reduces to solution of equations for curvature S of the phase front and beam radius a, which in the case $\varepsilon_H = -\varepsilon_2 J$ will have the form

$$S' - S^2 = -\frac{a_0^4}{L_T^2 a^4}, \quad a' = -aS, \tag{5}$$

where $L_T = a_0/\sqrt{\varepsilon_2 J_0}$, a_0 is beam radius, J_0 is intensity at the center of the beam at the input of the medium. The initial curvature S_0 of the phase front may be arbitrary. We determine S_0 from the condition that $S(l) = R^{-1}$ on the output of the layer, i. e. so that focusing takes place on the target. The solution of equations (5) will be

$$a^2(z) = a_0^2\left[(1 - S_0 z)^2 + \frac{z^2}{L_T^2}\right], \tag{6}$$

$$S(z) = \frac{a_0^2}{a^2(z)}\left(S_0 - S_0^2 z - \frac{z}{L_T^2}\right).$$

From condition $S(l) = R^{-1}$ we get

$$S_0 = \frac{2l + R\left(1 \mp \sqrt{1 - 4l^2(R+l)^2 R^{-2} L_T^{-2}}\right)}{2l(l+R)}. \tag{7}$$

Formula (7) implies that focusing at distance R behind the layer is possible if

$$\frac{l}{L_T}\frac{R+l}{R} \leqslant \frac{1}{2}. \tag{8}$$

Let us compare this condition with the analogous expression

$$4S_H \frac{R_1(R+l)}{R+l-R_1} \leqslant 1, \tag{9}$$

obtained in Ref. 5 on the basis of a thin-lens model; R_1 is the distance to the nonlinear lens from the transmitting aperture; S_H is the lens power, which

as implied by (6) is equal to $S_H = z/L_T^2$. At $l \ll R$ and $R_1 = l$, i. e. when the thin lens is located at the end of the nonlinear medium, there is insignificant difference between (8) and (9).

Let us note that condition $S(l) = R^{-1}$ may be satisfied at two different values of S_0. It is natural that condition (8) is necessary for convergence of the compensation scheme. However, in the general case it is insufficient. To demonstrate this, it is necessary to calculate the compensation in accordance with the scheme described in the previous section.

The change in curvature of the phase front S of the wave from a point source situated at distance R from the nonlinear medium is described by the first equation of system (5) with given function $a(z)$

$$(10) \qquad S' - S^2 = -\frac{a_0^4}{L_T^2 a^4(z)}$$

and boundary condition $\tilde{S}(l) = -R^{-1}$. Let us make the substitution of variables $\tilde{S} = -b'/b$ in (10). Then for function b(z) we get the linear equation

$$(11) \qquad b'' - \frac{a_0^4}{L_T^2 a^4} b = 0.$$

Considering that function $a(z)$ is a solution of the equation

$$a'' - \frac{a_0^4}{L_T^2 a^3} = 0,$$

the solution of equation (11) can be written as

$$(12) \qquad b = f(z)[C_1 + C_2 \operatorname{arctg} g(z)],$$

where

$$f(S_0, z) = a(S_0, z)/a_0; \; g(S_0, z) = -L_T[f^2(S_0, z) S(S_0, z)];$$

Functions $a(z)$ and S(z) are defined by formulas (6); C_1, C_2 are arbitrary constants. Considering condition $\tilde{S}(l) = -1/R$, we get

$$(13) \qquad \tilde{S}(0) = -S_0 - \frac{f^2(l)[1 - RS(l)]}{R + L_T f^2(l)[1 - RS(l)][\operatorname{arctg}(S_0 L_T) + \operatorname{arctg}(g(l))]}.$$

The phase conjugate compensation scheme corresponds to ar iteration scheme for finding solution $\tilde{S}(0) = -S_0$ of equation (13). Fig. 2 gives curves for

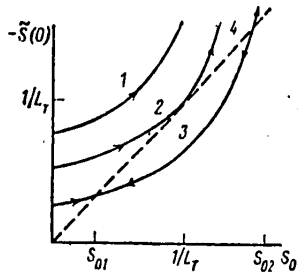

Fig. 2. Qualitative dependence of the curvature $\tilde{S}(0)$ of the phase front of the reflected wave on curvature S(0) of the incident wavefront at $l/L_T > \frac{1}{2}$ (1); $l/L_T = \frac{1}{2}$ (2); $l/L_T < \frac{1}{2}$ (3) and $\tilde{S}(0) = -S_0$ (4)

$\tilde{S}(0)$ as a function of S_0. The iteration series converges to solution S_{01} if $l \leqslant l_0 = (L_T/2)(R/(R+l))$ and $S_0 < S_{02}$, where S_{01}, S_{02} are solutions of equation (13) that are determined by formula (7). Thus, in the general case, satisfaction of condition (8) alone is insufficient for convergence of the compensation scheme; the iteration series will diverge even when (8) is satisfied if the initial curvature of the phase front $S_0 > S_{02}$. The number of iterations necessary for finding a solution with given accuracy increases strongly as $l \to l_0$. For example, at $l \ll R$ ($l_0/L_T = 0.5$), the accuracy of finding S_{01} equal to 1% is attained in 4 iterations with corresponding numbers of 6 at $l/L_T = 0.4$, 15 at $l/L_T = 0.45$, and 30 at $l/L_T = 0.48$.

4. Let us consider compensation of thermal defocusing in a moving medium.

If the time change in the field is sufficiently slow, beam propagation in a medium moving at constant velocity V directed along the x-axis is described by system of equations (1), (2), where

$$\varepsilon_n = \frac{1}{V}\frac{\partial e}{\partial T}\frac{\alpha}{\rho c_p}\int_{-\infty} J(x', y, z, t)\,dx'. \tag{14}$$

In the aberration-free approximation (e. g. see Ref. 7), nonlinearity of the medium has no effect on beam broadening along the x-axis. However, the equations for curvature of the wave front and beam radius along the y-axis take the form

$$S' - S^2 = -\frac{a_0^3}{2L_{TV}^2 a^3}; \quad a' = -aS, \tag{15}$$

where

$$L_{TV} = \sqrt{\frac{\rho c_p V a_0}{(-\partial e/\partial T)\alpha J_0 \sqrt{\pi}}}$$

is the characteristic length of thermal self-stress in the moving medium. The solution of equations (15) can be written as

$$SL_{TV} = \frac{\sqrt{C_1 - 1/f}}{f}; \quad C_2 - \frac{z}{L_{TV}} = \frac{1}{C_1}\left\{f\sqrt{C_1 - 1/f} + \right. \tag{16}$$

$$\left. + \frac{1}{\sqrt{C_1}}\ln\left[f\left(\sqrt{C_1} + \sqrt{C_1 - 1/f}\right)\right]\right\},$$

where

$$f = \frac{a(z)}{a_0}; \quad C_1 = 1 + L_{TV}^2 S_0^2;$$

$$C_2 = \frac{\sqrt{C_1 - 1}}{C_1} + \frac{\ln\left(\sqrt{C_1} + \sqrt{C_1 - 1}\right)}{C_1^{3/2}}.$$

The value of the initial curvature S_0 at which $S(l) = R^{-1}$ will be determined by the relation

$$S_0 L_{TV} = \sqrt{\frac{1}{f} + f^2 \frac{L_{TV}^2}{R^2}},$$

where f is the solution of the second equation of (16) at $z = l$,

$$C_1 = C_1(f) = \frac{1}{f} + \frac{f^2 L_{TV}^2}{R^2}; \quad C_2 = C_2(C_1(f)).$$

Numerical calculations for the case $l/R \ll 1$ show that under condition

$$(17) \qquad l/L_{TV} \leqslant 0{,}836$$

this equation has two real roots, and it has no real roots if inequality (17) is not satisfied. Therefore it should be expected that the conditions of convergence of the iteration sequence simulating the compensation scheme will be analogous to the conditions of convergence in the case of local thermal nonlinearity, i. e. in addition to satisfaction of (17) it is further required that $S_0 < S_{02}$, where S_{02} is the value of curvature corresponding to the smaller of the roots f_1, f_2.

Let us compare the results of the aberration-free approximation with the results of exact calculations of stability of the phase conjugate algorithm for compensating thermal defocusing in a moving medium [Ref. 3, 4]. These calculations for length of the nonlinear layer $l = (1/2)k\alpha_0^2$ (k is the wave number) showed that the algorithm is stable at values of the parameter $R_V = k^2 a_0^4 \sqrt{\pi}/L_{TV}^2$ of 7 or less. In our notation, this condition can be written as $l/L_{TV} \leqslant 0.99$, which agrees well with (17).

5. In considering the previous problems, we have assumed a slow time change in beam intensity and temperature field. This assumption is valid for compensation of defocusing in a moving medium if the time interval τ_k over which compensation takes place is much greater than the time of settling of the steady temperature field in the beam region ($\tau_k \gg a/V$). Applicability of the assumption that intensity changes slowly requires special consideration for compensation of nonstationary defocusing. Clearly, the characteristic time of intensity variation in this case is determined by the magnitude of nonlinearity.

To resolve this question, let us study the time process of defocusing compensation in a medium with intensity dependence of permittivity defined by relation (4). For phase front curvature and beam radius we have the equations

$$(18) \qquad S' - S^2 = -\frac{1}{L_{T0}^2} \frac{1}{\tau} \int_0^t \frac{a_0^4 \, dt'}{a^4(z, t')}, \quad a' = -aS$$

with boundary conditions $a(0, t) = a_0$, $S(l, t) = 1/R$, where τ is pulse duration, $0 \leqslant t \leqslant \tau$,

$$L_{T0} = \left(-\frac{\partial \varepsilon}{\partial T} \frac{J_0 \tau}{\rho c_p a_0^2} \right)^{-1/4}$$

is the characteristic length of thermal self-stress, which is related to the quantity L_T introduced in section 3 by the expression

$$L_T=\sqrt{\tau/l}\,L_{T0}.$$

The solution of system of equations (18) is found numerically. In doing this, a computational scheme is used that corresponds to a discrete compensation scheme consisting in the following. At the initial instant $t=0$, the curvature of the phase front at the inlet of the medium was assigned equal to $S_0=(R+l)^{-1}$. Then the time change in quantities $\alpha(z, t)$, $S(z, t)$ at constant $S(0, t)$ was calculated up to the instant $\tau_k=\tau/N$ when correction of the curvature of the phase front occurs. Curvature of the phase front at inlet of the medium at the instant of correction was taken as equal (with reversed sign) to the curvature of a wavefront from a point source situated at distance R upon transmission through a medium with index of refraction formed by the beam up to the instant of correction. A similar procedure was then repeated.

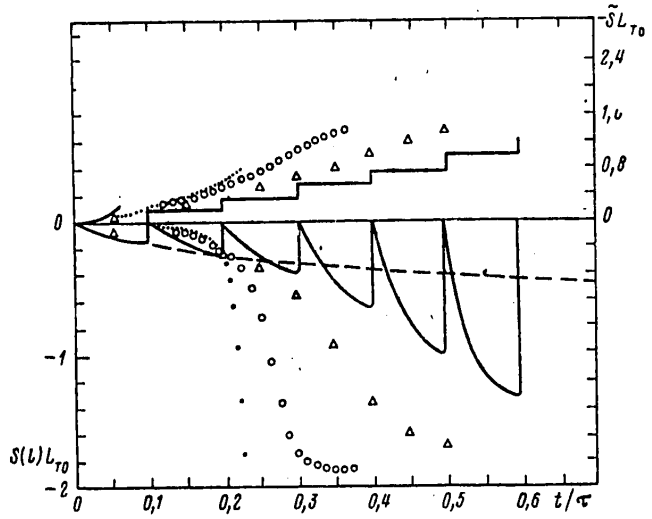

Fig. 3. Time change in curvature of phase fronts of beam at output of layer $S(l)$ and of the reflected wave at the input $\tilde{S}(0)$ at $l/L_{T0}=2$ for different intervals τ_k. Solid lines--$\tau_k/\tau=1/10$, Δ--$\tau_k/\tau=1.40$, o--1/80, • -1/200 (only the values of S and S at the end of interval τ_k are shown for $\tau_k/\tau\leqslant 40$). The dotted line shows $S(l, t)$ without compensation

Fig. 3 shows time dependences of the phase front curvature at the outlet from the nonlinear medium for case $l/R\ll 1$, $l/L_{T0}=2$. Under condition $l/R\ll 1$, the optimum phase correction should be such that a collimated beam $S(l)=0$ is produced at the outlet of the layer. Condition $S(l)=0$ is satisfied exactly at instants of correction. For the rest of the time, compensation is not complete, there is some error that depends on time t, length l of the nonlinear layer, and interval τ_k. Dependence of the compensation error on τ_k is of interest. With decreasing τ_k, the compensation error decreases for $t\leqslant t^*=0.193\tau$

and increases for $t > t^*$. Calculations show that as layer length l increases, there is a reduction in the time interval t^* in which reducing τ_k reduces the compensation error. Dependence of interval t^* on l can be approximately written as

$$t^*/\tau \simeq 0{,}8(L_{T0}/l)^2 \quad \text{or} \quad l/L_T(t^*) \simeq 0{,}9. \tag{19}$$

Let us note that when

$$\frac{l}{L_r} = \frac{l}{L_{T0}}\sqrt{\frac{t}{\tau}} \leqslant 0{,}5$$

The time dependence of curvature $\tilde{S}(0, t)$ of the phase front (as $\tau_k \to 0$) is linear with good accuracy (at least 5%)

$$S(0,t) = \frac{l}{L_{T0}^2}\frac{t}{\tau}, \tag{20}$$

whereas when $l/L_T \leqslant 0.5$, using the approximation of section 3,

$$S_0(0,t) = \frac{1}{2l}\left(1 - \sqrt{1 - 4\frac{l^2}{L_{T0}^2}\frac{t}{\tau}}\right). \tag{21}$$

Ratio $S_0(t)/\tilde{S}(0, t)$ is equal to 1.11 at $\xi = 0.3$; 1.25 at $\xi = 0.4$; 2 at $\xi = 0.5$, where $\xi = l/L_T$. Hence we can conclude that in compensation problems, the applicability of the integral approximation $\int_0^t J\,dt = Jt$ is limited to the case of weak nonlinear effects.

Conclusions. Phase conjugate systems can provide beam focusing behind a layer of nonlinear medium upon condition that thermal nonlinear effects are small ($l < L_T$). The capability of focusing at a given distance does not mean that the influence of nonlinearity can be completely compensated. Since the beam dimensions at the outlet of the nonlinear medium in the presence of compensation are less than its dimensions with focusing in a linear medium, the diffraction divergence behind the layer is increased, and consequently the maximum intensity in the focal plane is reduced.

Calculations of thermal defocusing also show low effectiveness of compensation at discrete instants of time. Apparently compensation will be more effective with continuous correction of the phase front using information on derivatives of the process $\tilde{S}(0, t)$, the moreso as the dependence of $\tilde{S}$ on t is linear at small times.

In the stationary case as well, with nonlinearity of form (3) or (14), the number of iterations can also be reduced if information is used on the derivative $d\tilde{S}(0)/dS_0$, e. g. in a compensation scheme that corresponds to solution of equation (13) by Newton's iteration method

$$S_0^{n+1} = S_0^n - (S_0^n + \tilde{S}^n(0))\frac{S_0^n - S_0^{n-1}}{\tilde{S}^n(0) - \tilde{S}^{n-1}(0)},$$

where n is the number of the iteration. This latter sum has the additional advantage over the iteraction scheme $S_0^{n+1} = -\bar{S}^n(0)$ used in section 3 that it guarantees convergence to the solution even at initial values $S_0 > S_{02}$, if condition (8) is satisfied.

The author thanks V. I. Tatarskiy, A. P. Sukhorukov and M. A. Vorontsov for discussing the results and constructive criticism.

REFERENCES

1. Bakut, P. A., Ustinov, K. D., Troitskiy, I. I., Sviridov, K. I., "Methods of Handling Light Fields With Observation Through a Turbulent Medium: Part 4", ZARUBEZHNAYA RADIOELEKTRONIKA, No 3, 1977, pp 55-86.

2. Karamzin, Yu. I., Sukhorukov, A. P., "Nonlinear Adaptive Optics", IZVESTIYA AKADEMII NAUK SSSR: SERIYA FIZICHESKAYA, Vol 42, No 12, 1978, pp 2547-2559.

3. Vorontsov, M. A., Chesnokov, S. S., "Optimizing Light Beam Focusing in Moving Nonlinear Media", IZVESTIYA VYSSHIKH UCHEBNYKH ZAVEDENIY: RADIOFIZIKA, Vol 22, No 11, 1979, pp 1318-1323.

4. Akhmanov, S. A., Vorontsov, M. A., Kandidov, V. P. et al., "Thermal Self-Stress of Light Beams and Compensation Methods", IZVESTIYA VYSSHIKH UCHEBNYKH ZAVEDENIY: RADIOFIZIKA, Vol 23, No 1, 1980, pp 1-37.

5. Herrmann, J., "Property of Phase Conjugate Adaptive Systems", J. OPT. SOC. AMER., Vol 67, No 3, 1977, pp 290-295.

6. Akhmanov, S. A., Sukhorukov, A. P., Khokhlov, R. V., "Self-Focusing and Diffraction of Light in Nonlinear Medium", USPEKHI FIZICHESKIKH NAUK, Issue 93, No 1, 1967, pp 19-70.

7. Vorob'yev, V. V., Shemetov, V. V., "Thermal Self-Focusing of Laser Beams in Moving Media", IZVESTIYA VYSSHIKH UCHEBNYKH ZAVEDENIY: RADIOFIZIKA, Vol 22, No 4, 1979, pp 441-448.

6610
CSO: 1862/152

UDC 621.375.826

EFFICIENCY OF COPPER VAPOR LASERS

Moscow TEPLOFIZIKA VYSOKIKH TEMPERATUR in Russian Vol 20, No 1, Jan-Feb 82 (manuscript received 10 Mar 81) pp 177-180

[Article by V. M. Batenin, P. A. Vokhmin, I. I. Klimovskiy and L. A. Selezneva, Institute of High Temperatures, USSR Academy of Sciences]

[Text] Copper vapor laser research has dealt with both theoretical [Ref. 1, 2] and experimental [Ref. 3, 4] analysis of efficiency. The theoretical papers consider the coefficient of conversion of electric energy introduced into the discharge up to the point of cessation of the lasing pulse to lasing energy (η_p), while the factor in experimental papers is the coefficient of conversion of the energy available in the storage device to lasing energy--the so-called practical efficiency ($\eta_{пр}$). It is obvious that because of energy losses in commutating elements (e. g. Ref. 5), noncorrespondence between the durations of excitation and lasing pulses and so on, $\eta_{пр}$ is always less than η_p. Thus it is incorrect to compare these efficiencies.

In this paper, an attempt is made to compare the results of calculation and experiment with consideration of losses associated with the discharge loop, leading to a reduction in $\eta_{пр}$ as compared with η_p. In addition, we give results of theoretical analysis of the feasibility of increasing the η_p of a copper vapor laser to values in excess of 10%.

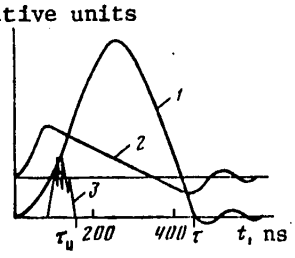

Fig. 1. Oscillograms of pulses of current (1), voltage across the electrodes of the discharge tube (2) and lasing (3). Neon pressure--13.3 kPa; power consumed from the supply source--1.8 kW. Maximum current and voltage--260 A and 8.6 kV

The facility on which the studies were done is described in Ref. 5, 6. The measurements of η_p were made under the same conditions as those used for gas temperature measurements on the discharge tube axis in Ref. 7. Fig. 1 shows typical oscillograms of the pulses of discharge current i, voltage U across the discharge tube electrodes and the lasing pulse on two wavelengths λ_1 = 510.5 nm and λ_2 = 578.2 nm. We can see from these oscillograms that the

discharge is inductive, i. e. the voltage across the discharge gap is divided between inductance L and resistance R of the discharge as

$$U = iR + Ldi/dt. \quad (1)$$

Conversion coefficient η_p corresponding to the theoretical value in Ref. 2 should be calculated from the relation

$$\eta_p = Q \Big/ \int_0^{\tau_и} i^2 R\, dt, \quad (2)$$

where Q is lasing energy, $\tau_и$ is the instant of cessation of the lasing pulse.

The quantity iR was calculated from equation (2) with the use of measured currents and voltages, assuming L = const, the value of L being determined by using equation (1) for the instant τ (see Fig. 1) when i = 0.

Mode	Power $W_п$ invested in discharge per unit of length, W/cm	Lasing power $W_г$, W	Discharge length, cm	η_p, %	$\eta_{пр}$, %	Ne buffer gas pressure p, kPa	E/p V/(cm·kPa)	Electron temperature, T_e eV
I	13	1.03	70	1	0.06	13.3	68	5
II	12	1.9	100	1.3	0.08	3.3	113	6
III	18	1.3	70	2	0.05	3.3	113	6

Results of calculating η_p using experimental data in accordance with (2) in different modes of copper vapor laser operation are summarized in the table. Also given here are the values of $\eta_{пр}$, which for laser operation in the periodic mode are equal to the ratio of the average lasing power to the power consumed from the source of supply. We can see that the values of $\eta_{пр}$ are appreciably different from the values of η_p.

To compare the results of the given experiment with calculation, it is necessary to know such parameters as the concentration of copper and neon atoms in the discharge, and also the average value of electron energy over the lasing pulse time. The concentration of neon atoms n_{Ne} averaged over the cross section of the discharge tube was calculated from the pressure measured in the experiment and the gas temperature in the discharge tube, whose value was determined from curves given in Ref. 7 for the gas temperature on the discharge tube axis $T_г(0)$ as a function of the level of power invested in the discharge per unit of length of the discharge tube $W_п$ (see table).

Under the conditions of this experiment, just as in Ref. 8, copper atoms are completely ionized in the paraxial region of the discharge by the end of the excitation pulse. Therefore the concentration of copper atoms in the paraxial zone can be determined from the known electron concentration $n_e(0)$ on the

discharge axis at the instant of termination of the excitation pulse. We should point out that it was established in Ref. 9 that ionization of neon atoms during the excitation pulse is negligible compared with that of copper atoms.

The value of $n_e(0)$ was calculated from the resistance R of the discharge as determined from current and voltage pulses in the following sequence: discharge conductivity was calculated from the current and voltage pulses, and then the average electron concentration n_e over the cross section of the discharge tube was calculated from the conductivity. With consideration of the data of Ref. 8, $n_e(0)$ was defined as $n_e(0) \cong 2n_e$. Considering the difference of the temperature T_r of heavy particles averaged over the cross section of the discharge tube from $T_r(0)$, the average concentration of copper atoms n_{Cu} can be estimated from the relation

$$n_{Cu} = T_r(0)\, n_e(0)/T_r. \qquad (3)$$

The average value of electron energy during the lasing pulse was calculated from data of Ref. 10 for the ratio $E/\sqrt{n_{Cu}/n_{He}}$ averaged over the given time interval, where E is the field strength in the discharge.

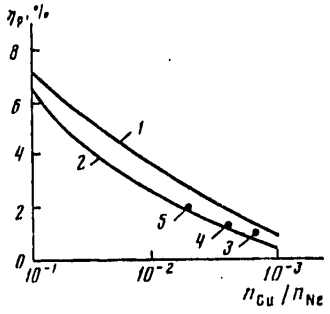

Fig. 2. Dependence of η_p on the ratio n_{Cu}/n_{Ne}. Calculation according to Ref. 2: 1--T_e = 5 eV; 2--T_e = 6 eV. Experiment: 3--mode I; 4--II; 5--III (see table)

Dependences of η_p on the ratio n_{Cu}/n_{He} were calculated by the method of Ref. 2 with consideration of the fact that lasing occurs on two wavelengths. Fig. 2 shows the comparison of results of the calculation and experiment. It can be seen that agreement between calculation and experiment is totally satisfactory, from which we can conclude that in a copper vapor laser at $T_e \sim 5$ eV with ratio $n_{Cu}/n_{He} \sim 0.1$ the coefficient of conversion of energy invested in the discharge to the energy of induced emission may reach ~7%.

Let us note that the results of calculation and experiment given above apply to the case where the lasing energy from a cubic centimeter of active medium is the maximum possible, i. e. where the maximum number of copper atoms participate in lasing. Given below are the results of calculation of η_p for conditions where fewer than the maximum possible number of copper atoms participate in lasing. In this case, within the formalism of the model of Ref. 2 that assumes simultaneity of termination of the lasing and excitation pulses, the specific lasing energy on one wavelength is determined by the relation

$$W_r = h\nu \frac{n_{Cu}}{\xi} \frac{q_{0p}}{q_p - \mu q_0} [\exp(-\mu q_0 F) - \exp(-q_p F)],$$

$$F = \int_0^{\tau_n} n_e\, dt, \quad \xi = \frac{g_p}{g_M}, \quad \mu = 1 + \frac{1}{\xi},$$

where $h\nu$ is the energy of an induced quantum; n_{Cu} is the concentration of copper atoms; q_0, q_{0p}, q_p are the rate constants of dissolution of the ground state, excitation and dissolution of the resonant level of the copper atom respectively; g_p, g_M are the statistical weights of the resonant and metastable levels; τ_B is the instant of termination of the lasing pulse.

The specific energy input to the discharge is determined by the relation

$$W_{вкл} = (n_{Cu} - n_{Cu}')I - \sum_j (1+\xi_j) W_{rj}(I - \varepsilon_{pj}) + A n_{Ne} F, \qquad (5)$$

$$n_{Cu}' = n_{Cu} e^{-q_0 F}, \quad A = \sum_i q_i \varepsilon_i,$$

where in addition to the conventional symbols, the j = 1, 2 refer to levels $P_{1/2}$ and $P_{3/2}$ respectively of the copper atom; n_{Ne} is the concentration of neon atoms; ε_i, q_i are respectively the energy and rate constant of inelastic interaction of the i-th electron with a neon atom; I is the ionization potential of the copper atom.

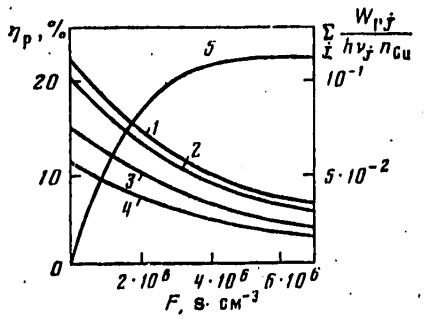

Fig. 3. Dependence of η_p (1-4) and the fraction of atoms participating in lasing (5) on F (T_e = 5 eV) at n_{Cu}/n_{He} of: 1--∞; 2--10^{-1}; 3--$2 \cdot 10^{-2}$; 4--10^{-2}

The dependences of η_p on parameter F were calculated with consideration of (4), (5) (Fig. 3). Given on this same figure is the F-dependence of the percentage of atoms participating in lasing, calculated as $\alpha = \sum_j \frac{W_{rj}}{h\nu_j n_{Cu}}$.

From the curves shown on Fig. 3, we see that coefficients of conversion of energy invested in the discharge to lasing energy can be achieved on the 20% level in copper vapor lasers at specific energy outputs that are an order of magnitude less than the maximum possible. It should be noted that the increase in η_p observed on Fig. 3 with a reduction in the number of atoms participating in the lasing is due to a reduction in energy losses by electrons associated with excitation and ionization of resonantly excited copper atoms.

REFERENCES

1. Yeletskiy, A. V., Zemtsov, Yu. K., Rodin, A. V., Starostin, A. N., "Optimum Characteristics of High-Pressure Copper Vapor Laser", DOKLADY AKADEMII NAUK SSSR, Vol 220, 1975, p 318.

2. Vokhmin, P. A., Klimovskiy, I. I., "Ultimate Characteristics of Lasers Based on Self-Limiting Transitions", TEPLOFIZIKA VYSOKIKH TEMPERATUR, Vol 16, No 5, 1978, p 1080.

3. Isayev, A. A., Lemerman, G. Yu., "Investigation of Copper Vapor Pulse Laser at Elevated Powers", KVANTOVAYA ELEKTRONIKA, Vol 4, No 7, 1977, p 1413.

4. Bokhan, P. A., Solomonov, V. I., Shcheglov, V. B., "Investigation of Energy Characteristics of Copper Vapor Laser With Longitudinal Discharge", KVANTOVAYA ELEKTRONIKA, Vol 4, No 8, 1977, p 1812.

5. Klimovskiy, I. I., Selezneva, L. A., "Some Particulars of Operation of a Circuit With Storage-Capacitance Resonant Charge Exchange Used for Excitation of Lasers Based on Self-Limiting Transitions", TEPLOFIZIKA VYSOKIKH TEMPERATUR, Vol 17, No 1, 1979, p 27.

6. Batenin, V. M., Burmakin, V. A. et al., "Gas Temperature in Copper Vapor Laser", TEPLOFIZIKA VYSOKIKH TEMPERATUR, Vol 16, No 6, 1978, p 1145.

7. Batenin, V. M., Klimovskiy, I. I., Selezneva, L. A., "Ultimate Average Emission Powers of Copper Vapor Lasers", TEPLOFIZIKA VYSOKIKH TEMPERATUR, Vol 18, No 4, 1980, p 707.

8. Batenin, V. M., Klimovskiy, I. I., Lesnoy, M. A., Selezneva, L. A., "Plasma Parameters in Discharge Afterglow in Copper Vapor Laser", KVANTOVAYA ELEKTRONIKA, Vol 7, No 5, 1980, p 988.

9. Batenin, V. M., Burmakin, V. A., et al., "Time Behavior of Electron Concentration in Copper Vapor Laser", KVANTOVAYA ELEKTRONIKA, Vol 4, No 7, 1977, p 1572.

10. Mnatsakanyan, A. Kh., Naydis, G. V., Shternov, N. P., "Electron Energy Distribution in Mixtures of Copper Vapor With Neon and Helium", KVANTOVAYA ELEKTRONIKA, Vol 5, No 3, 1978, p 597.

11. Winkler, R., "Die kinetischen Eigenschaften der Elektronen des anisothermen homogenen stationären Neon-Plasmas in Ionisierungs gradbereich von 10^{-9} bis 10^{-2}", ANN. PHYS., Vol 29, 1973, p 37.

6610
CSO: 1862/149

UDC 621.373.021.7.001.5

THERMOELASTIC ACTION OF PERIODICALLY PULSED LASER RADIATION ON SOLID SURFACE

Moscow KVANTOVAYA ELEKTRONIKA in Russian Vol 9, No 2(116), Feb 82 (manuscript received 12 Aug 81) pp 343-353

[Article by V. V. Apollonov, A. M. Prokhorov, V. Yu. Khomich and S. A. Chetkin, Physics Institute imeni P. N. Lebedev, USSR Academy of Sciences, Moscow]

[Text] The authors consider the phenomenon of thermoelastic action of powerful pulse-periodic laser emission on the surface of a solid. The analysis is based on relations between the characteristics of the heat-stressed state under the action of cw and arbitrarily time-variable laser radiation that are analogous to Duhamel integrals. Relations are calculated for the maximum intensities of laser radiation that lead to impermissible elastic distortions of the surface, plastic flow of the material with formation of residual stresses, fatigue fracture and melting of the surface layer.

Various fields of science and engineering are now making extensive use of laser systems that generate powerful unsteady radiation fluxes. The approximation of uncoupled thermoelasticity is used in Ref. 1-4 to examine the quasistatic problem of the action of laser radiation on the surface of a solid with determination of the unsteady fields of temperatures and stresses in the process of reaching the steady heat-stressed state. A topic that is quite timely is generalization of the problem of thermoelastic behavior of a solid when its surface is acted on by laser radiation that varies arbitrarily in time.

1. Description of the Heat-Stressed State of a Body When Laser Emission Acts on its Surface

Consider an isotropic body with fixed temperature at time zero. Axisymmetric radiant flux of variable intensity is incident on the surface (with coefficient of absorption A). It is assumed that the intensity distribution in the cross section of the laser beam conforms to Gauss law: $I(\vec{r})=I_0 \exp(-K_0 r^2)$, where $K_0 = 2/r_0^2$, and energy absorption takes place directly on the irradiated surface, since the depth of the skin layer is much less than the depth of penetration of the temperature field for characteristic times of change in beam intensity t_x.

The problem of determining the temperature field is treated in the linear approximation: it is assumed that the thermophysical and mechanical characteristics of materials are independent of temperature, and the energy losses due to radiation and convection are disregarded.

Under condition that the characteristic dimension of the beam $r_0 < L$, and time of energy input $r_0^2/a^2 \leqslant t \leqslant L^2/a^2$, the model of a half-space can be used in solving the problem. Then the heating of the material is described by the equation of heat conduction

$$\frac{\partial T}{\partial t} = a^2 \Delta T \qquad (1)$$

with the following initial and boundary conditions

$$\left.\frac{\partial T}{\partial z}\right|_{z=0} = -\frac{I_0 A}{\lambda} f(t) \exp(-K_0 r^2),$$
$$T|_{t=0} = 0, \quad \lim_{z, r \to \infty} T < M,$$

where a^2, λ are the coefficients of thermal diffusivity and heat conduction of the material respectively, M is a finite quantity, f(t) is the time function of laser intensity normalized to unity.

Solving the formulated problem by the method of sequential Hankel and Laplace transformations, we get

$$T^* = \frac{2\lambda\sqrt{K_0}}{I_0 A} T = \frac{1}{2\pi i\sqrt{K_0}} \int_{\sigma-i\infty}^{\sigma+i\infty} \varphi(p) e^{pt}\, dp \int_0^\infty \xi \frac{e}{\gamma}^{-\xi^2/4K_0} e^{-\gamma z} J_0(\xi r)\, d\xi, \qquad (2)$$

where p and ξ are the parameters of the Laplace and Hankel transforms, $\gamma^2 = \xi^2 + p/a^2$, $\phi(p)$ is the Laplace transform of f(t). The given expression enables us to describe the thermal state of a solid with surface exposed to laser radiation that varies arbitrarily in time, and also to get a solution to the uncoupled problem of thermoelasticity in integral form.

In the general case, analysis of phenomena of thermoelasticity is based on consideration of a system of equations of coupled thermoelasticity [Ref. 5-7, 10]. When the inequalities

$$\max\left(\frac{\rho a^2}{\lambda'};\ \frac{\rho a^2}{\mu};\ \sqrt[3]{\frac{\rho^2 a^2}{K_0 E^2}}\right) \ll \tau \ll \sqrt[3]{\frac{\rho^4 c^4 a^2}{\mu^2 \alpha_T^4 (I_0 A)^2}}$$

are satisfied, the description of the resultant heat-stressed state of the elastic half-space can be based on equations of quasi-steady thermoelasticity:

$$\mu\nabla^2 u + (\lambda' + \mu)\,\text{grad div}\, u - \alpha_T(3\lambda' + 2\mu)\nabla T = 0,$$
$$\nabla^2 T - \frac{1}{a^2}\frac{\partial T}{\partial t} = 0, \qquad (3)$$

where λ', μ are Lamé coefficients, $\vec{u}$ is the strain vector, ρ is density, α_T is the coefficient of linear thermal expansion, E is Young's modulus.

Elastic perturbations in solids propagate at the speed of sound c, and therefore to attain a "steady" stressed state it is necessary that the rate of attainment be greater than the rate of attainment of thermal equilbrium, i. e. $\sqrt{a^2 t} \ll ct$. For real solids that have finite dimensions there is a set of natural frequencies of mechanical vibrations. Consequently the conditions of quasi-steadiness also include the stipulation that frequencies that are multiples of the laser pulse recurrence rate must not coincide with the natural frequencies of the solid to avoid consideration of resonance phenomena that cannot be analyzed without accounting for a term $\rho\partial^2\vec{u}/\partial t^2$ in equilibrium equation (3).

The general form of the components of the stress tensor has the representation

$$\sigma_{zz}^{\lambda} = 2GD\int_0^{\infty} \xi^2 J_0(\xi r)\,\psi(\xi)\,[e^{-\gamma z} - e^{-\xi z}(1 + z(\xi - \gamma))]\,d\xi,$$

$$\sigma_{rr}^{\lambda} = 2GD\int_0^{\infty} \psi(\xi)\left\{J_0(\xi r)\,[\xi(\xi z - 2)(\xi - \gamma)e^{-\xi z} + \xi^2 e^{-\xi z} - \gamma^2 e^{-\gamma z}] + \right.$$

$$\left. + \frac{J_1(\xi r)}{r}\,[\xi e^{-\gamma z} - \{(\xi - \gamma)(z\xi - 2(1 - \nu)) + \xi\}e^{-\xi z}]\right\} d\xi,$$

$$\sigma_{rz}^{\lambda} = 2GD\int_0^{\infty} \xi\psi(\xi)\,J_1(\xi r)\,[\gamma(e^{-\gamma z} - e^{-\xi z}) - \xi z(\xi - \gamma)\,e^{-\xi z}]\,d\xi,$$

$$\sigma_{\varphi\varphi}^{\lambda} = 2GD\int_0^{\infty} \psi(\xi)\left\{J_0(\xi r)[(\xi^2 - \gamma^2)e^{-\gamma z} - 2\nu\xi(\xi - \gamma)e^{-\xi z}] + \right.$$

$$\left. + \frac{J_1(\xi r)}{r}\,[(\xi - \gamma)(\xi z - 2(1 - \nu)) + \xi)\,e^{-\xi z} - \xi e^{-\gamma z}]\right\} d\xi, \qquad (4)$$

where G is the shear modulus, J_n is a Bessel function of n-th order,

$$D = \frac{\alpha_T}{2}\,\frac{1+\nu}{1-\nu}\,\frac{I_0 A a^2}{K_0 \lambda p}\,\varphi(p);\quad \psi(\xi) = \frac{\xi}{\gamma}\,e^{-\xi^2/4K_0}$$

A distinguishing feature (as a consequence of cylindrical symmetry) of the problem is equality of the components σ_{rr} and $\sigma_{\phi\phi}$ to one another, and $\sigma_{rz} = 0$ on the Z axis. The given expressions describe the nature of the unsteady stressed state of the solid. Analysis of expressions (4) enables determination of the nature of these changes in time for any point of the half-space.

The stressed state that arises in a solid is accompanied by deformation, the greatest strain being reached on the irradiated surface. In the formalism of the half-space model, the amount of displacement of the surface as a result of laser action takes the form

$$W^* = \frac{\lambda K_0 W}{(1+\nu)\alpha_T I_0 A} = -\frac{FO}{2\pi i}\int_{\sigma - i\infty}^{\sigma + i\infty} dp\,\frac{\varphi(p/l)}{p} \times$$

$$\times \int_0^{\infty} e^{v - v}\,J_0(\sqrt{v}\,\delta_r)\,\frac{\sqrt{v + p/FO} - \sqrt{v}}{\sqrt{v + p/FO}}\,dv, \qquad (5)$$

where $\delta_r = 2\sqrt{K_0}r$, $FO = 4K_0a^2t$. The resultant expressions enable us to trace the change in shape of the surface during exposure to laser action.

Thus we have completely described the nature of the thermal, heat-stressed and deformational states that arise in a solid as a result of surface irradiation by a powerful laser beam that varies arbitrarily in time. In this situation, the following relations hold between the quantities that characterize the heat-stressed state in the cw ($\phi(p) = 1/p$) or any other unsteady state of input of laser energy to the solid:

$$\sigma_{ik}^{\text{нест}} = \int_0^t f(\tau) \frac{\partial \sigma_{ik}^{\text{ст}}}{\partial \tau}\Big|_{t-\tau} d\tau, \qquad W^{\text{нест}} = \int_0^t f(\tau) W^{\text{ст}}\Big|_{t-\tau} d\tau, \tag{6}$$

which is a consequence of formulas of the Laplace transform type for components of the heat stress tensor and the heat strain vector:

$$\hat{L}(\sigma_{ik}^{\text{нест}}) = p\varphi(p)\hat{L}(\sigma_{ik}^{\text{ст}}), \hat{L}(W^{\text{нест}}) = p\varphi(p)\hat{L}(W^{\text{ст}}),$$

where L is the Laplace transformation operator.

These relations are analogous to relations of the Duhamel integral type that are known from the theory of heat conduction. The non-triviality of the given fact for quantities that characterize the heat-stressed state consists in the following: time t figures in these equations as a parameter rather than as an independent variable with respect to which differentiation is carried out (as for example in the equation of heat conduction), which is a consequence of the uncoupled nature of the quasi-steady problem of thermoelasticity.

On the basis of the developed technique we have made a comparative examination of effects of thermal deformation of an elastic half-space in the cw, pulsed and pulse-periodic modes of action of laser radiation on a solid surface.

2. Action of Continuous Laser Emission on Solid Surface

If the times of laser exposure satisfy inequality $r_0^2/a^2 \ll t \ll L^2/a^2$ a steady temperature field may be set up in the solid. In this case, the process of establishment of this field in the center of the zone of irradiation is described by the expression $T^* = \frac{2}{\sqrt{\pi}} \operatorname{arctg}(\sqrt{FO})$.

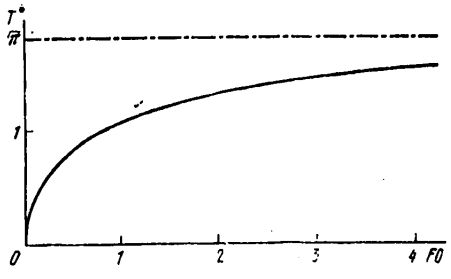

Fig. 1. Temperature on the surface of a specimen in the center of the zone of irradiation as a function of time (number FO) under the action of cw radiation

This expression implies (Fig. 1) that for times such that $FO \leqslant 4$, the instantaneous temperature differs by no more than 10% from the steady-state value. Therefore

we have assumed that a steady thermal state is set up in the material when $FO \geqslant 4$.

The expression for the temperature field in the half-space [Ref. 12] is

$$T^* = \int_0^\infty J_0(\sqrt{v}\,\delta_r)\exp(-\sqrt{v}(\sqrt{v}+\delta_z))\frac{dv}{\sqrt{v}}, \qquad (7)$$

where $\delta_z = 2\sqrt{K_0}z$. Analysis of the expression shows the local nature of the temperature field, whose intensity drops off sharply with increasing distance from the center of the zone of irradiation over the surface and into the material. The half-width of the intensity distribution is several times narrower than the half-width of the corresponding temperature profile on the irradiated surface. In the very center of the zone, the maximum value of $\sqrt{\pi}$ is reached.

In the steady stressed state ($p \to 0$) only components σ_{rr} and $\sigma_{\phi\phi}$ of the heat stress tensor are different from zero:

$$\sigma^*_{rr} = -2(1-\nu)\int_0^\infty \exp(-\sqrt{v}(\sqrt{v}+\delta_z))\frac{J_1(\sqrt{v}\,\delta_r)}{v\,\delta_r}dv,$$

$$\sigma^*_{\varphi\varphi} = -2(1-\nu)\int_0^\infty \exp(-\sqrt{v}(\sqrt{v}+\delta_z))\left[J_0(\sqrt{v}\,\delta_r) - \frac{J_1(\sqrt{v}\,\delta_r)}{\delta_r\sqrt{v}}\right]\frac{dv}{\sqrt{v}}, \qquad (8)$$

where $\sigma^*_{ik} = \lambda\sqrt{K_0}(1-\nu)\sigma_{ik}/I_0 AG\alpha_\tau(1+\nu)$. The depth of penetration of σ_{ii} into the material is $\sim r_0$. On the surface, the steady-state stress field is

$$\sigma^*_{rr} = -\frac{\sqrt{\pi}(1-\nu)}{2}\,{}_1F_1\left(-\frac{1}{2},\ 2,\ -\frac{\delta_r^2}{4}\right),$$

$$\sigma^*_{\varphi\varphi} = \frac{\sqrt{\pi}(1-\nu)}{2}\left[{}_1F_1\left(\frac{1}{2},\ 2;\ -\frac{\delta_r^2}{4}\right) - 2\,{}_1F_1\left(\frac{1}{2},\ 1,\ -\frac{\delta_r^2}{4}\right)\right]. \qquad (9)$$

The maximum of the heat-stress field is reached in the center of the zone of irradiation: $\sigma^*_{ii} = -\sqrt{\pi}(1-\nu)/2$. The steady stressed state is characterized by the relation (Fig. 2)

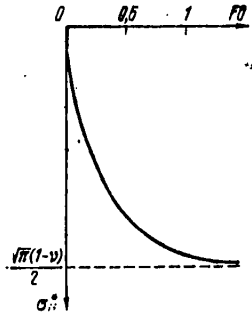

$$\sigma^*_{ii} = -\frac{1+\nu}{\sqrt{\pi}}\left[FO\left(\operatorname{arctg}\frac{1}{\sqrt{FO}} - \frac{1}{\sqrt{FO}}\right) + \frac{1-\nu}{1+\nu}\operatorname{arctg}\sqrt{FO}\right].$$

Fig. 2. Settling of steady stressed state on the surface of the specimen in the center of the zone of irradiation

The amount of thermal deformation of a reflecting surface in the steady state in the half-plane model approaches infinity, which can be attributed to the

infinite volume of the region of effective heating of the material (Fig. 3). It is of interest to evaluate the thermal deformation within the limits of long laser beam exposure times (FO>>1):

$$W^* = -\frac{1}{2}\left[FO\exp\left(-\frac{\delta_r^2}{4}\right) - \left(\frac{4\sqrt{FO}}{1+FO} - 2\ln\left(\sqrt{FO}+\sqrt{FO+1}\right)\right)\times \right.$$
$$\left. \times {}_1F_1\left(\frac{3}{2},\ 1;-\frac{\delta_r^2}{4}\right)\right] \approx -{}_1F_1\left(\frac{3}{2},\ 1;-\frac{\delta_r^2}{4}\right)\ln 2\sqrt{FO}. \qquad (10)$$

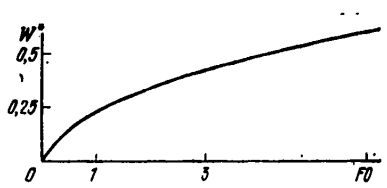

Fig. 3. Settling of quasi-steady deformation state on surface of specimen in the center of the zone of irradiation

Deformation surface profiles for different times are described in Ref. 1, 3.

3. Action of Pulsed Laser Emission on Solid Surface

We will deal below with times of action for which $FO_1 = 4K_0a^2\tau \ll 1$, which is often the case in practice when studying the interaction of pulsed laser radiation with matter.

At short exposure times, the depth of penetration of the temperature field is proportional to $\sqrt{a^2\tau} \ll r_0$, and therefore radial heat leakages can be disregarded, and the temperature distribution over the surface follows the profile of laser beam intensity distribution:

$$T^* = \frac{2}{\sqrt{\pi}}\left[\theta(t^*)\operatorname{arctg}\sqrt{FO_1 t^*} - \theta(t^*-1)\operatorname{arctg}\sqrt{FO_1(t^*-1)}\right]\times$$
$$\times \exp(-K_0 r^2), \qquad (11)$$

where $\theta(t^*)$ is the Heaviside function, $t^* = t/\tau$, τ is pulse duration, $FO_1 = 4K_0a^2\tau$. Expression (11) reaches a maximum at the instant of termination of the action of the pulse in the center of the zone of irradiation:

$$T^* = 2\operatorname{arctg}(\sqrt{FO_1})/\sqrt{\pi}.$$

The components of the stress tensor in this case have form (4) with representation of parameter γ^2 as p/a^2 because when inequality $FO_1 \ll 1$ is met, the process of heat propagation in a solid is "quasi-one-dimensional" and radial heat runoffs can be disregarded.

The maximum values of components σ^*_{rr} and $\sigma^*_{\phi\phi}$ are reached on the surface, and take the form

$$\sigma^*_{rr} = \sigma^*_{\phi\phi} = -\frac{2}{\sqrt{\pi}}\left[\theta(t^*)\sqrt{FO_1 t^*} - \theta(t^*-1)\sqrt{FO_1(t^*-1)}\right]\exp(-K_0 r^2),$$

i. e. the distribution of components σ^*_{ii} on the surface follows the distribution of laser beam intensity.

The behavior of heat stress tensor components σ^*_{zz} and σ^*_{rz} is more complicated. On surface $z = 0$, component $\sigma^*_{zz} = 0$, and it reaches its maximum value at some $z = z_0$, after which it approaches zero. The value of σ_{rz} is zero on surface $z = 0$ and on the Z axis; moreover, $\sigma_{rz} \to 0$ as $r, z \to \infty$. Therefore this component reaches its maximum value at certain values of z_0' and r_0'.

Let us evaluate $\sigma^{*\max}_{rz}$ and $\sigma^{\max}_{zz}$, and also z_0, r_0', z_0', utilizing the fact that the parameter $z_0/r_0 \ll 1$ at $FO_1 \ll 1$, and expanding the expressions for σ^*_{rz} and σ^*_{zz} in a series with respect to this parameter. The values of z_0, r_0', z_0' for σ^*_{zz} and σ^*_{rz} are determined from conditions $\partial\sigma_{iz}/\partial i = 0$: for σ^*_{zz}, $z_0 = \sqrt{12}$, and for σ^*_{rz}, $z_0' = 2\sqrt{a^2\tau}$ and $r_0 = (2/K_0)^{1/2}$. Here

$$\sigma^{*\max}_{zz} = {}^{8}/_{9}\sqrt{\pi}\, FO_1,\ \sigma^{*\max}_{rz} = FO_1/2, \tag{12}$$

where e is the base of natural logarithms.

The expression for thermal deformation of a reflecting surface in the case of exposure to a pulse of arbitrary shape [Ref. 11] is

$$W^* = -{}^{1}/_{2} FO_1 [0\ (t^*)t^* - 0\ (t^* - 1)(t^* - 1)] \exp(-K_0 r^2)/2. \tag{13}$$

The distribution of deformation over the reflecting surface follows the distribution of laser beam intensity, and the maximum is proportional to the Fourier number.

4. Particulars of Thermal Deformation of a Solid by Pulse-Periodic Laser Radiation

Analysis of thermoelastic behavior of a solid exposed to pulse-periodic laser action is based on our relations of the Duhamel integral type (6). The time-variable radiation flux takes the form of a train of square pulses of duration τ with period T (frequency 1/T) and off-duty factor $SQV = \tau/T$. It is assumed that $FO_2 = 4K_0 a^2 T \ll 1$.

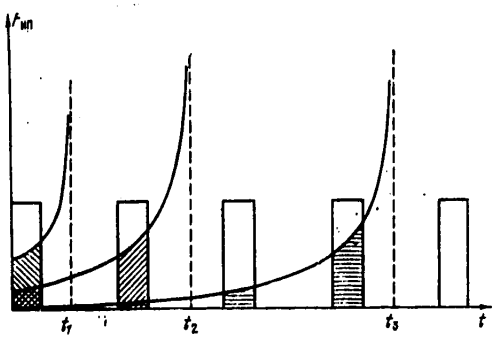

Fig. 4. Geometric interpretation of integrals of Duhamel type

At initial instants ($FO < 1$), features of the pulsed mode are typical of the pulse-periodic mode of laser action. Actually, the geometric sense of integrals of type (6) is characterized by the area of the shaded figures on Fig. 4.

For long times ($FO > 1$) the temperature and thermal stresses reach their quasi-steady values, i. e. there is a constant component of these quantities just as for the cw mode of energy input with adjusted intensity $I_0 SQV$ (I_0 is the maximum of intensity for a separate pulse) and against the background of this component (in time with the change of laser beam intensity)

we observe a peak in temperature and stress of approximately the same shape (accuracy ~SQV) as for pulsed action.

For the quantity W, an individual "pulse" of thermal deformation of the reflecting surface appears against the "steady-state component" approaching infinity. The expression for the temperature field in this case

$$T^* = SQV \int_0^\infty \frac{J_0(\sqrt{v}\delta_r)}{\sqrt{v}} \exp\left(-\sqrt{v}\left(\sqrt{v}+\delta_z\right)\right) dv + \frac{2}{\sqrt{\pi}} \exp\left(-\frac{\delta_r^2}{4}\right) \times$$
$$\times \sum_{n=0}^{N} \left[\theta(t^*-n) \operatorname{arctg} \sqrt{FO_2(t^*-n)} - \theta(t^*-n-SQV) \times\right.$$
$$\left. \times \operatorname{arctg} \sqrt{FO_2(t^*-n-SQV)}\right] \theta(n+1-t^*) \qquad (14)$$

is obtained directly from generalized expression (2), since for our assumed train of laser pulses

$$f(t) \div \varphi(p) = \frac{(1-\exp(-p\tau))(1-\exp(-p(N+1)T)}{1-\exp(-pT)},$$

where N is the number of elapsed pulses. In the center of the zone of irradiation where the temperature reaches its maximum value by the time of termination of the next pulse, $T^* = SQV\sqrt{\pi} + 2 \operatorname{arctg} \sqrt{FO_1}/\sqrt{\pi}$.

Analysis of the heat-stressed state shows that the maximum values of the radial and peripheral stresses are reached in the center of the zone of irradiation and can be represented as

$$\sigma_{ii}^{*\,\text{ип}} = \int_0^t f(t-\tau) \frac{\partial \sigma_{ii}^{\text{непр}}}{\partial \tau} d\tau,$$
$$\sigma_{ii}^{*\,\text{непр}} = -\frac{1+\nu}{\sqrt{\pi}} \left[FO\left(\operatorname{arctg}\frac{1}{\sqrt{FO}} - \frac{1}{\sqrt{FO}}\right) + \frac{1-\nu}{1+\nu} \operatorname{arctg}\sqrt{FO}\right]. \qquad (15)$$

When the quasi-steady state is reached, the expression for $\sigma_{ii}^*(0, 0, FO)$ is considerably simplified:

$$\sigma_{ii}^{*\,\text{ип}} = -\frac{\sqrt{\pi}}{2}\left[(1-\nu)SQV + \frac{4}{\pi}\sqrt{FO_2}\sum_{n=0}^{N}\left[\theta(t^*-n)\sqrt{t^*-n}-\right.\right.$$
$$\left.\left.-\theta(t^*-n-SQV)\sqrt{t^*-n-SQV}\right]\theta(n+1-t^*)\right], \qquad (16)$$

and the distribution of the stress field on the surface by the instant of termination of pulse action

$$\sigma_{ii}^* = \sigma_{ii}^{*(1)} + \sigma_{ii}^{*(2)},$$
$$\sigma_{\varphi\varphi}^{*(1)} = \frac{\sqrt{\pi}(1-\nu)SQV}{2}\left[{}_1F_1\left(\frac{1}{2}, 2; -\frac{\delta_r^2}{4}\right) - 2\,{}_1F_1\left(\frac{1}{2}, 2, -\frac{\delta_r^2}{4}\right)\right], \qquad (17)$$
$$\sigma_{rr}^{*(2)} = -\frac{\sqrt{\pi}}{2}(1-\nu)SQV\,{}_1F_1\left(\frac{1}{2}, 1; -\frac{\delta_r^2}{4}\right),$$
$$\sigma_{\varphi\varphi}^{*(2)} = \sigma_{rr}^{*(2)} = -2\sqrt{FO1/\pi}\exp(-\delta_r^2/4).$$

In the steady stressed state $\sigma^*_{rz} = \sigma^*_{zz} = 0$ (as a consequence of axial symmetry of the problem), and therefore their values in the case of pulse-periodic laser action will be the same as for pulsed radiation.

The amount of displacement of the solid surface in the pulse-periodic mode has steady and pulsed components:

$$W^* = SQV W^{*(1)} + W^{*(2)}, \tag{18}$$

$$W^{*(1)} = -\frac{1}{2}\left[FO \exp\left(-\delta_r^2/4\right) - \left(\frac{4\sqrt{FO}}{1+FO} - 2 \ln\left(\sqrt{FO} + \sqrt{FO+1}\right)\right) {}_1F_1\left(\frac{3}{2},\ 1; -\delta_r^2/4\right)\right],$$

$$W^{*(2)} = -\frac{FO_2}{2} e^{-K_0 r^2} \sum_{n=0}^{N} \theta(n+1-t^*)\left[\theta(t^*-n)(t^*-n) - \theta(t^*-n-SQV)(t^*-n-SQV)\right].$$

For the quasi-steady heat-stressed state in the center of the zone of irradiation, the amount of thermal deformation is

$$W^* = -\left[SQV \ln 2\sqrt{FO} + \frac{FO_2}{2} \sum_{n=0}^{N} \theta(n+1-t^*)\left[\theta(t^*-n) \times (t^*-n) - \theta(t^*-n-SQV)(t^*-n-SQV)\right]\right]. \tag{19}$$

Conclusions

Thus we have completely described the nature of the heat-stressed state that arises in an elastic half-space when its surface is exposed to cw, pulsed and pulse-periodic laser radiation. Let us note the typical peculiarities of the process of thermal deformation that are implied by the expressions derived.

1. The process is localized. The characteristic dimension of the localization of fields of stresses, temperatures and strains is of the order of the characteristic dimension of the zone of irradiation r_0.

2. For short times of laser beam exposure in the cw and pulse-periodic modes, and also in the pulsed mode ($FO_1 \ll 1$), the rates of increase in temperature, thermal stresses and deformations are proportional to laser beam intensity I_0, whereas for $FO \geqslant 3$-4 these quantities (in the cw and pulse-periodic modes) reach their "quasi-steady" level in the general case, which is proportional to I_0.

3. The resultant expressions enable determination of the laser beam parameters I_0, A, K_0, t, τ, SQV that typify the stage of elastic behavior of the material characterized by total recovery of the initial surface state when the laser beam is switched off. However, in some cases with cw and pulse-periodic laser action, the thermal deformation of an optical surface becomes impermissibly large ($W > \lambda/20$). Accounting for deformations is extermely

important for such laser systems as quasioptical transmission lines, telescopes, stable and unstable optical cavities, focusing systems.

4. This analysis enables us to determine the laser beam intensity at which the material goes into the inelastic region as a result of stresses that arise during exposure that exceed the yield stress of the material in the cw and pulsed modes, or that exceed the fatigue limit in the pulse-periodic mode.

The values of the maximum intensities $I_{\lambda/20}$, $I_{\sigma_т}$, $I_{T_{пл}}$ [$T_{ПЛ}$ is the melting point] with cw laser action are

$$I_{T_{пл}}=2\lambda\sqrt{K_0}\,T_{пл}/(\sqrt{\pi}A),\ I_{\sigma_т}=2\lambda\sqrt{K_0}\,\sigma_т/[\sqrt{3\pi}(1+\nu)AG\alpha_т],$$
$$I_{\lambda/20}=\lambda K_0\lambda_{CO_2}/[20(1+\nu)\alpha_т A\ln(2\sqrt{FO})]. \qquad (20)$$

If the physical characteristics of metals satisfy the inequality

$$\sigma_т/[(1+\nu)G\alpha_т T_{пл}]<1, \qquad (21)$$

then $I_{\sigma_т}<I_{T_{пл}}$. If the times of laser exposure are such that

$$\ln(2\sqrt{FO})>\sqrt{3\pi K_0}\,\lambda_{CO_2}G/40\,\sigma_т, \qquad (22)$$

then $I_{\lambda/20}<I_{\sigma_т}$.

In the case of pulsed action of radiation, the expressions for the maximum laser beam intensities take the form

$$I_{T_{пл}}=\sqrt{\pi}\,\lambda\,T_{пл}/(2A\sqrt{a^2\tau}),$$
$$I_{\sigma_т}(\sigma_{rr})=\sqrt{\pi}\,(1-\nu)\lambda\sigma_т/(2\sqrt{3}\,AG\alpha_т(1+\nu)\sqrt{a^2\tau}),$$
$$I_{\sigma_т}(\sigma_{zz})=(\pi e/(2\sqrt{3a^2\tau}))[(1-\nu)\,\sigma_т\,\lambda/(AG\alpha_т(1+\nu))], \qquad (23)$$
$$I_{\sigma_т}(\sigma_{rz})=\tfrac{1}{3}\sqrt{\pi e/(2a^2\tau)}\,(1-\nu)\,\lambda\sigma_т/[AG\alpha_т(1+\nu)],$$
$$I_{\lambda/20}=\lambda\lambda_{CO_2}/[40(1+\nu)A\alpha_т a^2\tau].$$

In this case, we have $I_{\sigma_т}(\sigma_{zz})>I_{\sigma_т}(\sigma_{rz})>I_{\sigma_т}(\sigma_{rr})$, since $I_{\sigma_т}(\sigma_{rz})/I_{\sigma_т}(\sigma_{zz})=\sqrt{2/(3\pi e)}$, $I_{\sigma_т}(\sigma_{zz})/I_{\sigma_т}(\sigma_{zz})=\sqrt{\pi}\,e$. If the physical characteristics of the material satisfy inequality $\sqrt{3}G\alpha_т(1+\nu)T_{пл}/[(1-\nu)\sigma_т]>1$ (for reference, $G/\sigma_т\sim10^3$), the quantity $I_{T_{пл}}>I_{\sigma_т}$, and for time

$$\tau>3\lambda^2_{CO_2}G/[400\,\pi a^2(1-\nu)^2\sigma_т^2], \qquad (24)$$

in addition $I_{\sigma_т}>I_{\lambda_{CO_2}/20}$.

In the case of pulse-periodic action on the solid surface, the maximum intensities are determined from the relation

$$(I_i^{ип})^{-1}=(SQVI_i^{непр})^{-1}+(I_i^{имп})^{-1}, \qquad (25)$$

where $I_i^{непр}$ is determined from (20), and $I_i^{имп}$ is determined from (23).

As a result of the unsteady, cyclically repeated stressed state that arises with irradiation of the material, irreversible fatigue changes may occur if the amplitude of oscillations of one of the components of the heat-stress tensor σ_{ik} exceeds the fatigue limit $\sigma^{0.1}_{ycT}$ as determined for compression or bending respectively.

The expressions for limiting intensities determined for each of the components σ_{ik}:

$$I_{ycT}(\sigma_{rr}) = \frac{(1-\nu)\lambda\sigma^{(0)}_{ycT}\sqrt{K_0}}{AG\,\alpha_T(1+\nu)}\sqrt{\frac{\pi}{3FO_1}},$$
$$I_{ycT}(\sigma_{rz}) = \frac{(1-\nu)\lambda\sigma^{(1)}_{ycT}\sqrt{K_0}}{AG\,\alpha_T(1+\nu)}\frac{2\sqrt{2e}}{FO_1}, \qquad (26)$$
$$I_{ycT}(\sigma_{zz}) = \frac{(1-\nu)\lambda\sigma^{(0)}_{ycT}\sqrt{K_0}}{AG\,\alpha_T(1+\nu)}\frac{9}{8\sqrt{\pi}}(FO_1)^{-1}.$$

If the duration of an individual laser pulse is such that $0.02 = 81/(512\pi e) \leqslant FO_1 \leqslant \sqrt{3}/8\pi = 0.62$ [sic], then $I_{ycT}(\sigma_{rr}) \leqslant I_{ycT}(\sigma_{zz}) \leqslant I_{ycT}(\sigma_{rz})$; if $FO_1 \leqslant 81/(512\pi e)$, then $I_{ycT}(\sigma_{zz}) \leqslant I_{ycT}(\sigma_{rr}) \leqslant I_{ycT}(\sigma_{rz})$, and if $1 > FO_1 > 9\sqrt{3}/8\pi$, then $I_{ycT}(\sigma_{zz}) \leqslant I_{ycT}(\sigma_{rz}) \leqslant I_{ycT}(\sigma_{rr})$. In this connection, since $\sigma^{0.1}_{ycT} \sim 0.1\sigma_T$, fatigue fractures of the irradiated surface (formation of micro- and macro-cracks, peeling of the surface layer, structural and phase changes of matter) will occur at laser beam intensities an order of magnitude lower than those at which the material passes into the inelastic region [Ref. 14-17].

However, it should be borne in mind that the resultant estimates are true for ideal surfaces in vacuum since the presence of air, slight contamination of the irradiated surface, microcracks that arise as a consequence of stress concentration on grain boundaries and the like may lead to breakdown of the gas near the surface, and consequently to destruction of the surface at laser emission intensities much lower than the calculated values.

6. Summary

The results enable us to evaluate the role of the thermoelastic mechanism of destruction in the process of interaction of intense cw, pulsed and pulse-periodic laser fluxes with the surface of solids. The temperature, stress and displacement fields have been defined in fairly general form. On the basis of the resultant expressions, an investigation has been made of the typical features of thermal and stressed states that arise in a solid upon laser exposure of its surface; a system of parameters of stability of the heat-stressed state has been introduced for different mechanisms of destruction.

Appendix

The expressions derived in this paper for characteristics of the heat-stressed state of an elastic half-plane with surface exposed to the action of cw, pulsed and pulse-periodic laser radiation have been represented as functions of

coordinates and time. However, in experiments involving the interaction of laser radiation with matter, the magnitude of thermal stresses and strains is determined from the magnitude of temperatures.

The relation between stresses in the center of the zone of irradiation and temperature in the process of establishment of the steady state in the case of continuous irradiation of the surface by a laser beam takes the form

$$\sigma_{ii}^{*}=-\frac{1+\nu}{\sqrt{\pi}}\left[\operatorname{tg}^{2}\left(\frac{\sqrt{\pi}}{2}T^{*}\right)\left(\operatorname{arctg}\frac{1}{\operatorname{tg}\left(\frac{\sqrt{\pi}}{2}T^{*}\right)}-\frac{1}{\operatorname{tg}\left(\frac{\sqrt{\pi}}{2}T^{*}\right)}\right)+\right.$$
$$\left.+\frac{\sqrt{\pi}}{2}\frac{1-\nu}{1+\nu}T^{*}\right],$$
$$W^{*}=-\frac{1}{2}\left[\operatorname{tg}^{2}\left(\frac{\sqrt{\pi}}{2}T^{*}\right)-\left(\frac{4\operatorname{tg}\left(\frac{\sqrt{\pi}}{2}T^{*}\right)}{1+\operatorname{tg}^{2}\left(\frac{\sqrt{\pi}}{2}T^{*}\right)}-\right.\right.$$
$$\left.\left.-2\ln\left(\operatorname{tg}\left(\frac{\sqrt{\pi}}{2}T^{*}\right)+\frac{1}{\cos\left(\frac{\sqrt{\pi}}{2}T^{*}\right)}\right)\right)\right]. \qquad (\Pi.\ 1)$$

As temperature T* approaches its steady-state value $\sqrt{\pi}$

$$\sigma_{ii}^{*}=-(1-\nu)T^{*}/2. \qquad (\Pi.\ 2)$$

The expression for the magnitude of thermal strain as a function of temperature

$$W^{*}=-\ln[2\operatorname{tg}(\sqrt{\pi}T^{*}/2)]. \qquad (\Pi.\ 3)$$

A distinguishing feature of the stressed state that arises under pulsed action is that the components of the thermal stress tensor on the surface in the center of the zone of irradiation

$$\sigma_{ii}^{*}=-T^{*}, \qquad (\Pi.\ 4)$$

$$\sigma_{zz}^{*\max}=\frac{2\sqrt{2}}{9}\pi T^{*} \text{ and } \sigma_{rz}^{*\max}=-\sqrt{\frac{\pi}{2e}}\frac{T^{*}}{4}. \qquad (\Pi.\ 5)$$

The relation between thermal deformation and temperature

$$W^{*}=-\frac{\pi}{8}T^{*2}. \qquad (\Pi.6)$$

The difference in signs of σ_{ii}^{*}, σ_{rz}^{*} and σ_{zz}^{*} is due to the fact that compression of the material takes place on the surface in the center of the zone of irradiation, whereas component σ_{zz}^{*} at distance z_0 expresses tension.

In the case of pulse-periodic action of laser emission on a solid surface, by the instant of termination of pulse action

$$\sigma_{ll}^{*} = {}^{1}/_{8}\sqrt{\pi}(1+\nu)\,SQV - T^{*} \tag{П.7}$$

$$\sigma_{zz}^{*} = \sigma_{zz}^{*\max} = \frac{\pi}{9}\left(\frac{T^{*}}{SQV} - \sqrt{\pi}\right)^{2}, \tag{П.8}$$

$$\sigma_{rz}^{*} = \sigma_{rz}^{*\max} = \frac{\pi}{8\sqrt{2e}}\left(\frac{T^{*}}{SQV} - \sqrt{\pi}\right)^{2}.$$

REFERENCES

1. Apollonov, V. V., Shefter, E. M., Preprint No 105, Physics Institute imeni P. N. Lebedev, USSR Academy of Sciences, Moscow, 1974.

2. Apollonov, V. V., Barchukov, A. I., Konyukhov, V. I., Prokhorov, A. M., PIS'MA V ZHURNAL EKSPERIMENTAL'NOY I TEORETICHESKOY FIZIKI, Vol 15, 1972, p 248.

3. Apollonov, V. V., Barchukov, A. I., Prokhorov, A. M., IEEE, T. Vol QE-10, 1974, p 505.

4. Barchukov, A. I., Konev, Yu. B., Preprint No 158, Physics Institute imeni P. N. Lebedev, USSR Academy of Sciences, Moscow, 1973.

5. Melan, E., Parkus, G., "Termouprugiye napryazheniya, vyzyvayemyye statsionarnymi temperaturnymi polyami" [Thermoelastic Stresses Caused by Steady-State Temperature Fields], Moscow, Fizmatgiz, 1958.

6. Parkus, G., "Neustanovivshiyesya temperaturnyye napryazheniya" [Unsteady Temperature Stresses], Moscow, Fizmatgiz, 1963.

7. Novatskiy, V., "Voprosy termouprugosti" [Problems of Thermoelasticity], Moscow, Izd-vo AN SSSR, 1962.

8. Doetsch, G., "Rukovodstvo k prakticheskomu primeneniyu preobrazovaniy Laplasa" [Handbook on Practical Use of Laplace Transforms], Moscow, Fizmatgiz, 1958 [German edition: "Anleitung zum praktischen Gebrauch der Laplace-Transformation", Oldenburg, Munich, 1956].

9. Gradshteyn, I. S., Ryzhik, I. M., "Tablitsy integralov, summ, ryadov i proizvedeniy" [Tables of Series, Products and Integrals, (English translation, Academic Press, New York, 1964)], Moscow, Nauka, 1971.

10. Kovalenko, A. D., "Termouprugost'" [Thermoelasticity], Kiev, Naukova dumka, 1975.

11. Apollonov, V. V., Bunkin, F. V., Khomich, V. Yu., Chetkin, S. A., PIS'MA V ZHURNAL TEKHNICHESKOY FIZIKI, Vol 1978, p 1017.

12. Lösch, F., Jahnke, E., Emde, F., "Spetsial'nyye funktsii" [Special Functions], Moscow, Nauka, 1964.

13. Krylov, V. I., Shul'gina, L. T., "Spravochnaya kniga po hislennomu integrirovaniyu" [Handbook on Numerical Integration], Moscow, Nauka, 1966.

14. Yekorbi, T., "Fizika i mekhanika razrusheniya i prochnosti tverdykh tel" [Physics and Mechanics of Destruction and Strength of Solds], Moscow, Mir, 1971.

15. Konovalov, Ye. G., Drozdov, V. M., Tyavlovskiy, M. D., "Dinamicheskaya prochnost' metallov" [Dynamic Strength of Metals], Minsk, Nauka i tekhnika, 1969.

16. Ivanoiv, V. S., "Ustalostnoye razrusheniye metallov" [Fatigue Fracture of Metals], Moscow, GTI, 1963.

17. Apollonov, V. V., Barchukov, A. I., Karlov, N. V., Prokhorov, A. M., Khomich, V. Yu., Shefter, E. M., PIS'MA V ZHURNAL TEKHNICHESKOY FIZIKI, Vol 1, 1975, p 522.

6610
CSO: 1862/133

UDC 621.378.8

REGENERATING WORKING MIXTURE OF IODINE LASER WITH OPEN-DISCHARGE PUMPING

Moscow KVANTOVAYA ELEKTRONIKA in Russian Vol 9, No 2(116), Feb 82 (manuscript received 4 Aug 81) pp 368-369

[Article by L. K. Gavrilina, V. S. Zuyev, V. A. Katulin, N. N. Korzhavina, Yu. S. Leonov, Yu. I. Morozov and A. L. Petrov]

[Text] A chromato-mass-spectrometric analysis is done on the depleted mixture in an iodine laser and an iodine amplifier with pumping by an open high-current discharge. It is shown that there is a difference between the driven mode (amplifier) and free-running mode (laser). This difference should lead to accumulation of large amounts of I_2 in the driven mode, which may lead in turn to a difference in designs of the regeneration system for these two modes.

Ref. 1 reported on a short-pulse iodine laser with repeated use of the regenerated mixture. Analysis of the products of photolysis of such a laser showed that the main poisoning component of the depleted mixture is I_2, which was removed in purification and regeneration. Similar iodine lasers with high output energy (~10^3 J) can operate in the free-running mode as well. The question arises as to how the compositions of the depleted gas mixture will differ when the powerful iodine laser is operated in the modes of free running and amplification of short pulses (driven mode). This problem is topical for developing a purification system for the closed gas loop of a powerful iodine laser. A preliminary answer to the question is given in Ref. 2, 3, where it is shown that much less I_2 is accumulated in the free-running mode than in the driven mode. However, the results of these papers cannot be directly transferred to iodine lasers with pumping by emission from an intense open electric discharge [Ref. 4] since the pumping power and spectral makeup differ considerably from low-power lamp pumping [Ref. 2, 3].

In pumping by an open discharge (without a quartz discharge tube), the active substance is also absorbed by hard UV radiation ($\lambda < 200$ nm) with subsequent dissociation [Ref. 5]. In principle, all this may considerably alter the kinetics of processes compared with lamp pumping.

Experiments were done on a facility described in Ref. 1, 4. A powerful iodine laser was used with volume of ~1 m^3 pumped by an open electric discharge with capacitor bank energy of 270 kJ in both amplification and free lasing (1800 J at the output).

In laser operation in the free-running mode, the optical cavity was formed by mirrors with reflectivities of 100 and 30%. After each discharge, samples of the gas mixture were taken and the final products were analyzed. The depleted mixture after one-time laser action was condensed in a metal tank that had been pre-evacuated to a pressure of 1 μm Hg; condensation was done at liquid nitrogen temperature.

The SN-8 ("Varian") mass spectrometer was used for analyzing the photolysis products after doing laser experiments in the two modes. This mass spectrometer can be interfaced with a chromatograph, enabling isolation of individual components of the mixture that are then introduced directly into the mass spectrometer so that each component is analyzed separately. A column with length of 3.6 m was used in doing the chromatographic analysis.

Composition of mixture	Concentration of total number of molecules, %		
	In initial mixture	In photolysis products	
		Free-running operation	Driven mode
CF_4	-	$6 \cdot 10^{-3}$	$2.2 \cdot 10^{-1}$
SF_6	95.2	95.5	94.6
SOF_2	-	$2.8 \cdot 10^{-2}$	$3.7 \cdot 10^{-1}$
C_2F_5I	-	$4.5 \cdot 10^{-2}$	$3 \cdot 10^{-2}$
C_6F_{14}	-	$8.2 \cdot 10^{-1}$	1.15
C_3F_7I	4.8	4.2	2.8
I_2^*, μg	-	11	46

*Amount of I_2 determined by titration

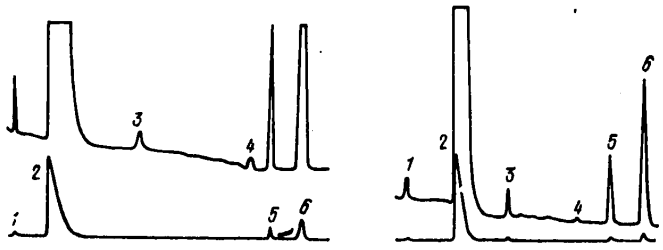

a b

Chromatograms of photolysis products in free-running (a) mode and driven (b) mode:
1--CF_4, 2--SF_6, 3--SOF_2, 4--C_2F_5I, 5--C_6F_{14}, 6--C_3F_7I

The results of the chromatographic analysis are presented in the table and the figure. As compared with the initial mixture of SF_6-C_3F_7I after laser operation in the two modes, new products appear: CF_4, SOF_2, C_2F_5I, C_6F_{14}. It can be seen from the table that the qualitative composition in both modes of laser operation is the same, being a mixture of the initial substances and products of decomposition, although when the laser is operated in the free-running mode the amount of reacted C_3F_7I is less than in the driven mode. In accordance with this, there is also a reduction in the quantitative accumulation of the above-mentioned products.

The amount of I_2 that is formed cannot be analyzed by the chromatographic method because of the high absorptivity of iodine. Therefore we used an analytical method that we had developed previously in application to our own conditions [Ref. 2]. Just as we had assumed, much less molecular iodine was formed in the free lasing mode (see table).

Thus our results are analogous to those found in experiments with lamp pumping, although with certain stipulations. Their gist is that in the case of pumping by an open discharge, SF_6 is entrained into the region of chemical interaction, which apparently does not occur with lamp pumping. This is proved first of all by the formation of SOF_2 that takes place only in pumping by an open discharge. Let us note that binding of oxygen in SOF_2 may be quite useful as oxygen is also a strong quenchant of excited iodine atoms and is practically always present in the mixture.

It seems to us that the major processes leading to formation of CF_4 and C_6F_{14} proceed analogously with pumping by an open discharge and by lamps. This becomes clear if we take consideration of the strong dilution of the working gas with the SF_6 buffer gas that has a high specific heat precluding pyrolysis, and self-shielding of hard radiation by the working gas as a consequence of the larger absorption cross section in the UV region (by a factor of 10-100) than in the pumping band.

The process of I_2 formation in the two modes is described in Ref. 3. The difference can be attributed to the different lifetimes of the excited iodine in the driven mode (100 μs) and in the free lasing mode (0.1-1 μs).

In the free lasing mode, where stimulated emission brings about rapid transition of the atomic iodine to the ground state, the reaction of reverse recombination takes place at a high rate ($C_3F_7 + I \rightarrow C_3F_7I$), the initial substance is restored, and molecular iodine is not accumulated (there is partial "self-regeneration"). The reaction of reverse recombination of excited iodine occurs much more slowly.

In the driven mode with prolonged existence of excited iodine atoms, the radicals recombine rapidly $C_3F_7^* + C_3F_7^* \rightarrow C_6F_{14}$, since there is practically no atomic iodine in the ground state. Therefore at the end of pumping when a short pulse passes that transfers iodine from the excited to the ground state, there are no $C_3F_7^*$ radicals, and reverse recombination does not occur. The de-excited iodine atoms in this case are constrained to recombine into molecular iodine.

Thus, closed-loop regeneration systems for iodine lasers in free-running and cavity Q-switched (driven) modes may be quite different. It is clear from what we have said that a great deal of molecular iodine is accumulated in a powerful iodine laser in the driven mode, which necessitates additional purification for subsequent use [Ref. 1]. In the free lasing mode, reverse recombination takes place, and purification of the initial material need not be so thorough.

REFERENCES

1. Gavrilina, L. K., Katulin, V. A., Korzhavina, N. N., Leonov, Yu. S., Morozov, Yu. I., Nosach, V. Yu., Petrov, A. L., KVANTOVAYA ELEKTRONIKA, Vol 6, 1979, p 1495.

2. Basov, N. G., Gavrilina, L. K., Leonov, B. S., Sautkin, V. A., PIS'MA V ZHURNAL EKSPERIMENTAL'NOY I TEORETICHESKOY FIZIKI, Vol 8, 1968, p 178.

3. Andreyeva, G. L., Malyshev, V. I., Maslov, A. I., Sobel'man, I. I., Sorokin, V. A., PIS'MA V ZHURNAL EKSPERIMENTAL'NOY I TEORETICHESKOY FIZIKI, Vol 10, 1969, p 429.

4. Zuyev, V. S., Katulin, V. A., Nosach, V. Yu., Petrov, A. L., TRUDY FIZICHESKOGO INSTITUTA IMENI P. N. LEBEDEVA AKADEMII NAUK SSSR, Moscow, Vol 125, 1980, p 3.

5. Borovich, B. L., Zuyev, V. S., Katulin, V. A., Mikheyev, L. D., Nikolayev, F. A., Nosach, O. Yu., Rozanov, V. B., "Khimicheskiye lazery" [Chemical Lasers], ITOGI NAUKI I TEKHNIKI, SERIYA RADIOTEKHNIKA, Vol 15, Moscow, VINITI AN SSSR, 1978.

6610
CSO: 1862/133

UDC 621.373.826.038

INFLUENCE OF SOUND WAVES ON PULSED GAS-DISCHARGE LASER EMISSION POWER

Moscow KVANTOVAYA ELEKTRONIKA in Russian Vol 9, No 2(116), Feb 82 (manuscript received at ZHURNAL TEKHNICHESKOY FIZIKI 25 Sep 80, and at KVANTOVAYA ELEKTRONIKA 12 Mar 81) pp 270-274

[Article by V. F. Kravchenko, E. K. Karabut, A. A. Gudkov and V. Ye. Bogoslavskiy, Scientific Research Institute of Physics, Rostov-na-Donu State University]

[Text] It is shown that in pulsed gas-discharge lasers at high specific energy inputs in the pulse, acoustic oscillations are excited in the active medium. It is demonstrated that when working the pulse-periodic mode, the buildup of acoustic oscillations leads to redistribution of the density of the active medium in the discharge tube, which is responsible for resonant dependence of the average lasing power on the recurrence rate of the stimulating pulses.

1. Introduction

One of the important problems in the investigation and design of pulsed gas discharge lasers is raising the average emission power. Solution of this problem by simultaneously increasing the pulse power and pulse recurrence rate runs up against a number of difficulties, among which some of the most important are the low rates of cooling of the active medium and deionization. It is known [Ref. 1, 2] that increasing the excitation energy leads to gas-dynamic forces that accompany transmission of the current pulse in the discharge chamber, causing shock and acoustic waves and associated mass transfer, which may have an appreciable effect on the laser output characteristics. The sound waves that arise in the gas when the current pulse passes through it were first used to accelerate cooling of the active medium of nitrogen lasers in Ref. 3, and convective carbon dioxide lasers in Ref. 4.

In the case of periodic pulse energy input, depending on the pulse recurrence rate there may be oscillations of the gas density in the discharge gap, which is associated with excitation of standing waves [Ref. 5]. The influence of these effects on operation of pulsed gas discharge lasers has not been studied up until now, although it is known that the formation of a standing sound wave in the discharge gap leads to low-frequency oscillations of radiation

intensity [Ref. 6], and consequently may cause changes in the emission power of pulsed gas discharge lasers.

In this paper we investigate the influence that sound waves arising in two-pulse and pulse-periodic operation have on the emission power of strontium and copper chloride vapor lasers.

2. Experimental Facility

Experiments with an ionic self-limited strontium vapor laser used a discharge tube of alundum ceramic with inside diameter of 10 mm and length of 65 cm; the distance between electrodes was 20 cm. The strontium vapor pressure optimum for lasing was set by the temperature of an external heater. Helium at pressures of 1.3-2.0 kPa was used as the buffer gas. Discharge excitation was either in the doubled pulse mode with delay between pulses adjustable over a wide interval, or in the pulse-periodic mode. In the latter case to prevent overheating of the active medium the discharge was switched on for a short period (10-20 s). A storage capacitor of 1-1.5 nF was discharged through a TGI1-500/16 thyratron. Change in lasing power on line Sr II with $\lambda = 1.03$ μm was monitored in the two-pulse mode by an FEU-28 photomultiplier with output fed to an oscilloscope; in the pulse-periodic mode the radiation receiver was a calibrated FSD-1 photoresistor.

Experiments with the copper chloride vapor laser were done in a sectionalized quartz discharge tube of diameter D with internal cylindrical water-cooled electrodes. The segments were ceramic inserts of thickness d and inside diameter of 6 mm separated by distance l. Parameters D, d and l in the different tubes were varied. The discharge was excited by a Blumlein circuit with TGI1-1000/25 thyratron as a commutator. The capacitance of the storage capacitor varied from 220 to 1500 nF. The tube was filled with neon in the pressure range of 5.3-8.0 kPa. CuCl vapor was introduced into the discharge by self-heating of the tube in the pulse-periodic mode. The average emission power on the green ($\lambda = 510.5$ nm) and yellow ($\lambda = 578.2$ nm) CuI lines was measured on the IMO-2 instrument.

In all experiments the shape and amplitude of the voltage across the discharge tube and the current through the tube were monitored by non-inductive capacitive divider and shunt with output signal sent to the input of a VM-450 oscilloscope.

3. Experimental Results and Discussion

In double-pulse operation of the Sr-He laser, periodic changes are observed in the lasing power in the second pulse as the time delay between pulses is changed (Fig. 1). The magnitude of changes in lasing power increases with increasing input of electric power to the discharge and with increasing buffer gas pressure. Stepwise dependence of average lasing power on stimulating pulse recurrence rate is observed in the pulse-periodic mode (Fig. 2).

In the investigation of the CuCl-Ne laser with sectionalized discharge tube, the average lasing power shows multiresonant dependence on stimulating pulse

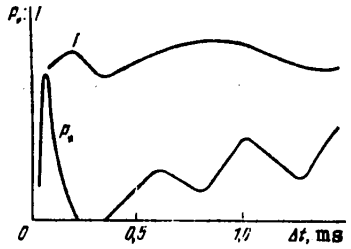

Fig. 1. Lasing pulse power P_H and intensity I of spontaneous emission on Sr I line $\lambda = 460.7$ nm in the pulse mode as functions of the time delay between pulses

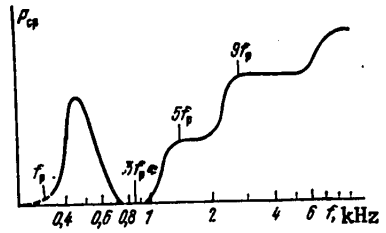

Fig. 2. Average lasing power of Sr-He laser as a function of pulse recurrence rate; $f_p \approx 0.3$ kHz is the lower resonant frequency

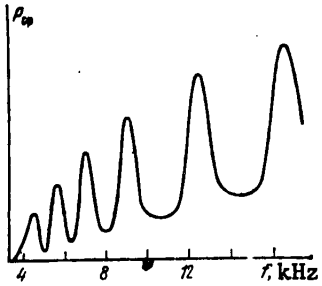

Fig. 3. Average lasing power P_{cp} of CuCl-Ne laser as a function of pulse recurrence rate

recurrence rate (Fig. 3). On a frequency of 16.5 kHz at discharge gap length of 14 cm, the overall average lasing power on both lines was 1.1 W, efficiency was about 0.35% with respect to energy stored in the storage capacitors. It was established that the frequencies of observed resonances do not depend on the length of the discharge zone, the geometry of the end sections of the tube, thickness or number of segments, but are determined solely by the parameter D of the expansion zone. A change in D from 2 to 1.2 cm increased the number of observed resonances; the nature of the behavior of average lasing power remained analogous to Fig. 3. With a further reduction in the ratio D/d, the amplitudes of resonance peaks decrease so much that the emission power is no longer a resonant function of the recurrence rate, and the relation between them becomes monotonic. The amplitudes of the resonance peaks increase with increasing ratio l/d and power input to the discharge, and also with decreasing neon pressure. On high resonance frequencies one observes stabilization of the discharge along the axis of the tube, and contraction of the discharge column and lasing spot. This is most noticeable when the active medium is overheated. During heating, the lasing spot is at first annular

in structure, and then gradually fills the whole cross section of the discharge channel. With underheating, the structure of the spot on resonance frequencies abruptly changes from annular to a uniform cross section of smaller diameter.

Before going on to analyze each of the results, let us note that in a gas discharge in cylindrical tubes at large specific pulse energy inputs, density oscillations may arise [Ref. 5]. These oscillations have the nature of shock waves [Ref. 7] and sound waves [Ref. 2]. Analysis of the above results has shown that the intensity of the fluctuations is determined by the parameter W/p, where W is specific energy introduced in the pulse into the discharge, and p is the pressure of the active medium. An increase in the value of W/p leads to buildup of strong oscillations of gas density in the discharge tube. Also of importance is the geometry of cool and hot (plasma-filled) zones of the discharge tube. Particles of metal dust are configured lengthwise of the discharge tube in periodic clots that change position with a change in geometry of the discharge tube and recurrence rate of the stimulating pulses. The frequency band of lasing power oscillations, absence of fluctuations in voltage across the discharge tube and current through it as the pulse recurrence rate changes, and also the behavior of metal dust particles in the tube show the acoustic nature of the observed oscillations.

The observed dependence of oscillations on energy input to the discharge suggests that the principal mechanism of buildup of sound waves can be attributed to the weak shock waves that arise upon thermal expansion of the plasma column. Actually, the energy released in the volume occupied by the plasma causes an abrupt increase of pressure in this space in a process that can be considered isochronic. in virtue of the considerable inertia of the process of heat transfer, the equalization of pressures occurs gasdynamically as a consequence of the shock wave. Two cases are possible.

1. *Small energy input* ($W/p \leqslant 0.75$). Gas expands isentropically. The size of the zone of expansion can be determined from the expressions $V_н/V_0=K_p^{1/\gamma}$ for longitudinal waves and $V_н/V_0=K_p^{1/\gamma}[V_0(K_p^{1/\gamma}-1)/V_c]^{-1}$ for radial waves, where $K_p=1+(\gamma-1)\,W/p$; $\gamma=c_p/c_V$; $V_н$, V_0 and V_c are the volumes of the heated zone at the end of the flare, the discharge channel and the discharge tube respectively.

After equalization of pressures in the hot and cool zones of the tube, the directional pulse acquired by the gas propagates as a sound wave.

2. *Large energy input* ($W/p > 0.75$). In this case, as established in Ref. 7, the shock wave causes a periodic change of gas density in the discharge region. As the gas intermixes, equalization of pressures takes place, and subsequent processes in the tube occur analogously to the propagation of sound waves.

The sound waves in propagating along the discharge tube are reflected from its walls. In this process, they may be either damped out by interference and absorption, or built up due to establishment of a standing wave. In the case of strict consideration of the process of sound wave propagation, it is necessary to account for its reflection at interfaces of different temperature zones of the discharge tube. The reflectivity at such an interface

depends on the temperature ratio of gas in the hot and cool zones of the tube. Under conditions typical of pulsed gas discharge lasers $T_0 \cong 300$ K, $T_g \cong 2$-4 kK, reflectivity in this case is about 0.3.

It is known that a cylindrical cavity has a set of eigenfrequencies that can be found from the expressions $f_n = nc/(2L)$ for longitudinal modes, and $f_{mn} = \kappa_{mn}c/(2\pi R)$ for radial modes of oscillations, where κ_{mn} is the root of the equation $J_m'(kR) = 0$; c is the speed of sound; J_m is a Bessel function of m-th order.

If the radius of the cylinder $R < 0.293\lambda$, where λ is the wavelength of the sound propagating in the cylinder, then radial wave modes do not arise, and longitudinal waves have a planar front. At $R > 0.293\lambda$ the excited mode of radial waveforms depends on geometry and location of the source; if the source is in the middle of the cylindrical tube on its axis, mainly longitudinal waves with odd n and radial waves of type f_{0n} will be excited.

When the cavity is subjected to an exciting force with frequency f_{ex}, formation of standing waves is possible on frequencies $f_{ex} = f_{cav}/s$, where f_{cav} is the lower frequency of the cavity, $s = 1, 2, 3, \ldots$

The proposed model readily explains observed experimental data.

In the case of the Sr-He laser in the double-pulse mode, a weak shock wave arises. As it expands, the hot gas radiates an acoustic wave to both sides, the pressure of the active medium falls, and lasing is interrupted. With the arrival of the reflected wave, the pressure of the active medium in the active zone increases, reaches a maximum, and then falls off.

The behavior of spectral lines of neutral strontium atoms excited by direct electron impact agrees with the assumed model of redistribution of density of the active medium of the laser due to formation of longitudinal standing sound waves. The intensities of ionic lines of strontium and stimulated emission of the laser in virtue of the stepwise mechanism of excitation [Ref. 8] have different maxima depending on strontium vapor pressure. For example at the Sr vapor pressure that is optimum for lasing, stimulated emission has two maxima since the system passes twice through optimum conditions during a half-period. In the regular pulse mode, excitation of odd modes of longitudinal waveforms is observed (see Fig. 2).

In the case of the CuCl-Ne laser, the expanding discharge channel (which is a linear sound source in virtue of the chosen geometry of the tube) pumps up standing sound waves on resonance frequencies that are multiples of the fundamental radial wave of mode f_{01}. The frequency dependence on Fig. 3 is given for the case where $c = (7\text{-}7.5)\cdot 10^2$ m/s (which corresponds to the value of the pre-pulse temperature of the gas in a range of 700-800 K), D = 2.5 cm, $\kappa_{01} = 3.83$ [Ref. 2]; the frequency of the fundamental radial mode is 34-36 kHz. It can be seen that the set of frequencies of observed resonances fits into a series f_{01}/s, where $s = 2, 3, 4, 5, 6, 7$. The distance between the dust clots (nodes) formed in operation on resonance frequencies in the extended end sections of the discharge tube, which is equal to the wavelength of the standing sound waves, is about 1 cm, which corresponds to a wavelength of the

fundamental mode $\lambda = c/f_{01}$. The change in structure of the lasing spot agrees with the change in density of the active medium for the given mode of oscillations.

The observed frequency responses of the CuCl-Ne laser are due to selection of conditions that are optimum for pumping up sound waves. In particular, the parameter W/p was in a range of 1-2, whereas published data on the operation of metal-vapor pulsed gas discharge lasers give typical values of $W/p \leqslant 0.1$-0.3.

Thus when operating pulsed gas discharge lasers in the pulse-periodic mode at large specific energy inputs in a pulse, sound waves are pumped up in the active medium, leading to redistribution of the density of the active medium in the tube, which causes complicated dependence of the average lasing power on the recurrence rate of the exciting pulses. By taking the recurrence rate as a multiple of the fundamental radial mode of the wound waves excited in the discharge tube, it is possible in many cases to increase the average power of stimulated emission of pulsed gas discharge lasers with segmented active element.

REFERENCES

1. Stricker, S. D., Stewart, A. S., PHYS. REV. LETTS, Vol 11, 1963, p 527.

2. Kozlov, Yu. G., Shukhtin, A. M., ZHURNAL TEKHNICHESKOY FIZIKI, Vol 38, 1968, p 1465.

3. Kravchenko, V. F., Il'yushko, V. G., Mikhalevskiy, V. S., Polunin, V. A., IZVESTIYA SEVERNOGO KAVKAZSKOGO NAUCHNOGO TSENTRA VYSSHEY SHKOLY. SERIYA YESESTVENNYKH NAUK, Vol 3, 1977, p 34.

4. Vedenov, A. A., Drobyazko, S. V., Knizhnikov, V. N., Turundayevskiy, V. B., TEPLOFIZIKA VYSOKIKH TEMPERATUR, Vol 13, 1975, p 425.

5. Baranov, V. Yu., Lyubimov, B. Ya., Niz'yev, V. G., Pigul'skiy, S. V., KVANTOVAYA ELEKTRONIKA, Vol 6, 1979, p 184.

6. Reznikov, G. P., Fugol', N. Ya., Shevchenko, Yu. F., PIS'MA V ZHURNAL EKSPERIMENTAL'NOY I TEORETICHESKOY FIZIKI, Vol 8, 1968, p 64.

7. Skrebov, V. N., Eykhval'd, A. I., TEPLOFIZIKA VYSOKIKH TEMPERATUR, Vol 17, 1979, p 711.

8. Karabut, E. K., Kravchenko, V. F., Mikhalevskiy, V. S., OPTIKA I SPEKTROSKOPIYA, Vol 48, 1980, p 648.

6610
CSO: 1862/133

UDC 621.378.325

NEW WORKING SUBSTANCES FOR PHOTODISSOCIATIVE IODINE LASER

Moscow KVANTOVAYA ELEKTRONIKA in Russian Vol 9, No 2(116), Feb 82 (manuscript received 5 Feb 81) pp 253-259

[Article by G. A. Skorobogatov, B. N. Maksimov, V. G. Seleznev, O. N. Slesar', N. D. Torbin and L. N. Kostyreva]

[Text] The following fluorinated iodies are tested as working fluids for an iodine laser: C_4F_9I, $C_5F_{11}I$, $CF_3OCF_2CF_2I$ and $C_3F_7OCF_2CF_2I$. Energy output of 80-85 mJ/cm^3 was attained for stimulated emission on perfluorobutyl iodide (without an inert diluent), which is comparable with the energy output attained on n- and iso-perfluoropropyl iodides -- the most effective of known working fluids in iodine lasers. A theoretical analysis is done on the mechanism of quenching of stimulated emission in a laser using C_4F_9I.

The photodissociation iodine laser [Ref. 1] shows the greatest promise along with neodymium glass and carbon dioxide lasers for accomplishing laser-driven nuclear fusion [Ref. 2]. However, at present the maximum attainable efficiency of the iodine laser is only 0.5-1.4% [Ref. 3, 4], which is comparable with that of neodymium glass lasers. Since the attained efficiency of utilizing the working substance in the laser cell of the photodissociation iodine laser does not exceed 19% for CF_3I, 28% for C_3F_7I [Ref. 5] and 25% for $C_6F_{13}I$ [Ref. 6], there are considerable reserves for improving the efficiency of such lasers by finding more favorable working mixtures. There are also reserves for increasing efficiency by a fundamental change in the pumping arrangement [Ref. 7].

Since the time of publication of Ref. 1, stimulated emission in photodissociation iodine lasers has been realized on the following iodides: CF_3I, CH_3I, C_2F_5I, C_3F_7I, C_2H_5I, C_3H_7I, C_4H_5I, i-C_4H_9I [Ref. 1], i-C_3F_7I [Ref. 8], CD_3I [Ref. 9], $(CF_3)_3CI$ [Ref. 10], i-$C_5F_{11}I$, $C_6F_{13}I$ [Ref. 6], $(CF_3)_2AsI$, $CF_3(C_2F_5)AsI$, $CF_3(C_3F_7)AsI$, $(C_2F_5)_2AsI$, $(C_3F_7)_2AsI$, $(CF_3)_2PI$, $CF_3(C_2F_5)PI$, $CF_3(C_3F_7)PI$, $(C_2F_5)_2PI$, $(C_3F_7)_2PI$, $CF_3(CH_3)PI$, $CF_3PI(CN)$, $CF_3(CF_2Cl)(CFH)PI$, F_3PI, OPF_2I and $(CF_3)_2SbI$ [Ref. 11]. Attempts to achieve lasing with such gases as 2-C_3H_7I, HI, I_2 [Ref. 1], $(CH_3)_2AsI$ [Ref. 12] or with compounds that contain the N-I bond [Ref. 12] have been unsuccessful. Among all the tested iodides, just as before, the maximum specific energy output is observed for i-C_3F_7I (80-85 mJ/cm^3 [Ref. 6]) and C_3F_7I (80±3 mJ/cm^3 without diluent, and

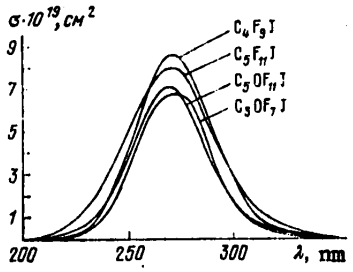

Fig. 1. Absorption spectra of gaseous fluorinated iodides at 20°C

125 ± 5 mJ/cm^3 when diluted with SF_6 [Ref. 5]). Therefore it seems logical to look for more effective working fluids for photodissociation iodine lasers among heavier perfluoroalkyl iodides, or among near analogs of C_3F_7I. In accordance with this, the lasing properties of the following series of iodides have been studied in this paper: C_4F_9I, $C_5F_{11}I$, $CF_3OCF_2CF_2I$ and $C_3F_7OCF_2CF_2I$.

These iodides were synthesized by methods described in Ref. 13. Before the laser tests, the iodides were purified by vacuum distillation 5-10 times, with collection of 4/5 of the volume of the substance each time in the middle of distillation. The test for purity of the substance was absence of spurious peaks on gas chromatograms. The spectra of the iodides (Fig. 1) were taken on a Perkin-Elmer-402 spectrophotometer. Table 1 summarizes spectral properties (obtained from the data on Fig. 1) and some other properties of the iodides used in the work.

TABLE 1

Some properties of gaseous fluorinated iodides RI[1)]

R	$\sigma^{2)}_{max}$, 10^{-19} см^2	$\Delta^{2,3)}$, nm	$\int \sigma_{RJ} d\lambda / \int \sigma_{CF_3J} d\lambda$	$C^{2)}_p$, cal/(mole·deg)	T_{boil}, °C	$p_{21°C}$, mm Hg
$CF_3OCF_2CF_2$	6,75±0,1	44±0,5	1,25±0,03	36	46,5±0,5	>221
$C_2F_5OCF_2CF_2$	7,06±0,11	45,5±0,5	1,36±0,03	54	86,5±0,5	44
C_4F_9	8,6±0,2	42±0,5	1,59±0,03	42	74±0,5	123
C_5F_{11}	8,9±0,2	49±0,5	1,65±0,04	50	94±0,5	37

[1)]Errors are normal; [2)]T = 293 K; [3)]Δ is width of the band at level 0.5.

The laser tests were done on a facility described in Ref. 14, with the difference that each of the four IFP-5000 lamps was placed in its own grid of return wires [Ref. 15], which increased the steepness of the pulse edge and the power of the pumping radiation in the first 5 μs (compare curve 3 of the figure in Ref. 14 with curves *1* and *3* in Fig. 2). The overall dimensions of the laser cell were reduced somewhat: inside diameter 5.2 ± 0.1 mm, irradiated length and volume 245 mm and 5.2 ± 0.1 ml respectively. The reflectivities of the cavity mirrors (100 and 10% on $\lambda = 1300$ nm) and their radius of curvature (1 m) were as before. The end windows of the laser cell were also placed as before: at an angle of 90° to the axis.

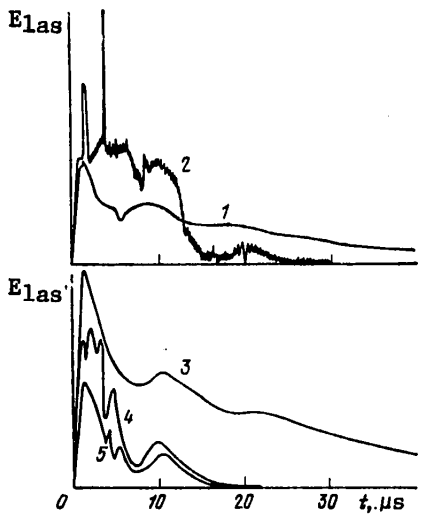

Fig. 2. Typical pulse shapes of pumping radiation ($\lambda = 250$–350 nm) (*1*, *3*) and stimulated emission (*2*, *4*, *5*): $E_{pump} = 2310$ (*1*) and 1300 J (*3*); $E_{las} = 81$ (*2*), 47 (*4*) and 42 mJ/cm^3 (*5*); working fluid C_4F_9I ($p = 123$ (*2*) and 74 mm Hg (*4*)) and i-C_3F_7I ($p = 74$ mm Hg (*5*))

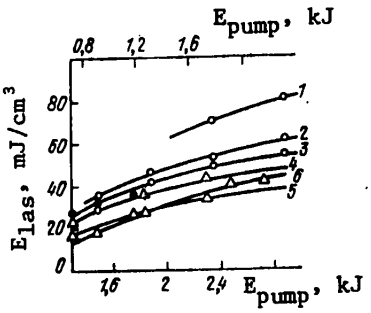

Fig. 3. Specific energy output E_{las} of RI lasers as function of pumping emission for cell with inside diameter of 5.2 ± 0.1 mm: 1--123 mm Hg C_4F_9I; 2--74 mm Hg C_4F_9I; 3--74 mm Hg i-C_3F_7I; 4--100 mm Hg C_3OF_7I; 5--44 mm Hg $C_5OF_{11}I$; 6--37 mm Hg $C_5F_{11}I$. The upper scale of E_{pump} refers to curves 1-3, and the lower -- to curves 4-6 and the black circles on curve 3; displacement of the upper and lower scales for E_{pump} is determined by registration of the black circles with curve 3.

Fig. 2 shows some typical oscillograms of lasing pulses, demonstrating that with all of the fairly high pumping radiation powers that we used, lasing was cut off due to quenching processes rather than merely by the termination of the pumping radiation pulse. Therefore the data that we have obtained on the lasing properties of iodides reflect not only their spectral-optical properties, but also the physicochemical processes that take place in the iodide undergoing photolysis.

Fig. 3 shows the specific energy yield of stimulated emission as a function of the electric energy fed to the pumping lamps. The number of points on each curve is not large. The trouble is that under the severe conditions that we used the luminous emittance of the IFP-5000 lamps as well as the transparency of the laser cell fall off noticeably after every 10-20 operations. Therefore to get undistorted results the entire experiment must be done with a minimum number of operations. Besides, under severe conditions there is a high probability of explosion of the lamps. It is for this reason that curves 1-3 on Fig. 3 were plotted with some lamps, while curves 4-6 and three points (dark circles) on curve 3 were plotted with other lamps (with poorer luminous emittance).

Fig. 4 shows the specific energy yield of stimulated emission as a function of pressure of the iodide in the cell for some fixed values of pumping energy. The data of Fig. 4 show that of the four newly tested iodides, only C_4F_9I

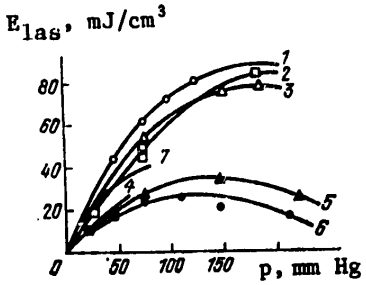

Fig. 4. Specific energy output E_{las} of RI lasers as function of working gas pressure for cell with inside diameter of 5.2 ± 0.1 mm: Working fluid C_4F_9I (*1*); i-C_3F_7I (*2*, *3*, *5*), $C_5OF_{11}I$ (*4*), C_3OF_7I (*6*) and $C_5F_{11}I$ (*7*); E_{pump} = 2310 (*1*, *3*), 2700 (*2*) [Ref. 6] and 1300 J (*4-7*)

shows E_{las} about 10% greater than that of the most effective iodides that are currently known: C_3F_7I and i-C_3F_7I. Since the vapor pressure of C_4F_9I at room temperature (123 mm Hg) is less than that of C_3F_7I or i-C_3F_7I (380 mm Hg), the actually attainable maximum energy output of 80-85 mJ/cm^3 is the same for undiluted C_4F_9I (see Fig. 3 and 4), i-C_3F_7I [Ref. 6] and C_3F_7I [Ref. 5].

In preceding papers [Ref. 6, 16-18] we established that for the high pumping rates that we used ($\sigma\phi \geqslant 10^3$ s^{-1}), stimulated emission of photodissociation iodine lasers based on iodides CF_3I, C_3F_7I, $C_6F_{13}I$ after reaching a maximum (t_{max}) drops by a considerable factor (or even to zero) due to photoinduced radial gasdynamic movements (oscillations) of the working gas in the laser cell. The instant of final cutoff of lasing t_c is determined by chemical quenching processes that develop in the laser cell [Ref. 19]. The contribution of radial movements of the working gas to the quenching of stimulated emission of photodissociation iodine lasers was first experimentally observed in Ref. 20, and experimental confirmations of the photodissociative mechanism of onset of radial movements of the working gas in such lasers were obtained in Ref. 21, 22. Since the iodides C_4F_9I, $C_5F_{11}I$, C_3OF_7I and $C_5OF_{11}I$ used in our research are analogous in physicochemical properties to C_3F_7I or $C_6F_{13}I$, for them as well one should expect an appreciable contribution of gasdynamic radial oscillations to quenching of lasing. In this research we have not brought up the problem of studying the mechanism of quenching of stimulated emission of the photodissociation iodine laser (therefore the pumping radiation pulse is not square as in Ref. 6, 16, and has irregularities, while the lasing pulses sometimes have a spike structure), but will nonetheless attempt to extract information on the mechanism of emission quenching in the photodissociation iodine laser from the resultant experimental data, e. g. for C_4F_9I.

First of all, let us estimate the temperature rise in the laser cell due to photodissociation and subsequent chemical reactions. For curves *2*, *4* of Fig. 2 the absolute pumping rate $\sigma\phi$ averaged over the cross section of the cell and the iodide absorption band was evaluated by the method of autophotometry [Ref. 23] (Table 2). To check the correctness of autophotometry, the lifetime τ_{st} of atoms $I(^2P_{1/2})$ with respect to the stimulated transition $I(^2P_{1/2}) + h\nu(1.3\ \mu m) \rightarrow I(^2P_{3/2}) + 2h\nu(1.3\ \mu m)$ for the instant t_{max} of maximum lasing is calculated in the seventh column of Table 2 by formula (2) from Ref. 6. Since τ_{st} is 4-5 times less than t_{max}, we can be sure that the autophotometrically determined pumping rate is understated in comparison with the true value due to this factor by no more than $100\% \cdot e^{-4} = 2\%$. By time

TABLE 2

Temperature rise in working volume of C_4F_9I laser by the time t_{min} of the first appreciable drop in lasing power and by the time t_c of lasing cutoff

Curves on Fig. 2	Γ_Σ^2, %	$\sigma_{max} \cdot 10^{-20}$, photon/cm²·s	t_{max}, μs	t_{min}, μs	t_c, μs	τ_{st}, μs	$\overline{\sigma\varphi}(t_{max})$, 10^4, s^{-1}	$t_{min}\int_0 \overline{\sigma\varphi}\,dt$*	$t_c\int_0 \overline{\sigma\varphi}\,dt$*	$T(t_{min})$·K	$T(t_c)$·K	Γ_c^{td}** μs	Γ_Σ^{td}, %
1	19,7	5,35±0,5	1	7	18	0,25	2,2±0,9	0,11±0,04	0,22±0,08	610±80	720±130	26 or 18	43 or 32
2	20,6	8,7±0,9	1	15	25	0,22	2,4±1,0	0,20±0,08	0,29±0,11	690±140	840±170	21 or 16	43 or 32

* $\overline{\sigma\varphi}(t) = \int_{200\ nm}^{350\ nm} \sigma_{C_4F_9I}(\lambda)\varphi(\lambda, t)d\lambda$ is the pumping rate averaged over the cross section of the cell and over the absorption band of the iodide; evaluated by the method of autophotometry.

**Calculations done for rate constant of thermal dissociation $k_{td} = A\exp(-23650/T)$ with two values of A: 10^{13} or 10^{15} cm^{-1}, Γ_Σ^2 is the integral euantum yield of stimulated emission (see formula (1), Ref. 23); Γ_Σ^{td} is the same calculated by formula (68) of Ref. 29, i. e. within the formalism of a kinetic model that accounts for only one quenching reaction--thermal dissociation (2).

$t_{max} = 2$-3 μs we should also not have developed processes of inversion annihilation due to dark reactions $I(^2P_{1/2}) \xrightarrow{k_{RI^*}} RI$ or $2I(^2P_{3/2}) + RI \xrightarrow{K_{I_2}} I_2 + RI$, $I(^2P_{1/2}) + I_2 \rightarrow I(^2P_{3/2}) + I_2$, since according to the data of Ref. 24-26 the corresponding characteristic half-reaction times ($t_{RI^*} = 1/k_{RI^*}\,[I(^2P_{1/2})] \cong 15$ μs and $t_{I_2} = 1/K_{I_2}\,[RI][I(^2P_{3/2})] \cong 15$ μs) are an order of magnitude greater than t_{max}. Since autophotometry is fundamentally approximate (up to ±50%) as a method of determining absolute pumping rate, we have disregarded (averaged out) the spikes on curve 2 of Fig. 2, and have not made corrections in the determined values of $\overline{\sigma\phi}$ for the possible understatement (up to 15% [Ref. 27, 28]) of the measured intensity of stimulated transitions due to losses of stimulated radiation within the cavity, or for possible overstatement (up to 20-30%) of the intensity of stimulated transitions due to the dark reaction $R + I(^2P_{3/2}) \xrightarrow{k_{RI}} RI$. (Rate constants $k_{RI} \cong 10^{-11}$ cm^3/mole·s [Ref. 24, 25], which leads to a characteristic half-reaction time of $t_{RI} = 1/k_{RI}[I(^2P_{3/2})] \cong 1$ μs, which is comparable with t_{max}).

Under the conditions of our experiments for reactions $R + R \xrightarrow{K_{R_2}} R_2$ and $R + I(^2P_{3/2}) \xrightarrow{k_{RI}} RI$, characteristic half-reaction times $t_{R_2} = 1/K_{R_2}[R]$ and $t_{RI} = 1/k_{RI}[I(^2P_{3/2})]$ do not exceed 1 μs (see K_{R_2} and k_{RI} in Ref. 24, 25). Therefore in the region up to 1200-1300 K, analytical expression (45) from Ref. 29

$$T(t) = T_0 + \frac{Q}{C_{RJ}}\left[1 - \exp\left(-\int_0^t \overline{\sigma\varphi}(t)\,dt\right)\right] \qquad (1)$$

gives the same law of temperature rise in the photolyzed iodide as the (fundamentally more exact) differential expressions of type (4) from Ref. 30 or (14) from Ref. 31. The rise in temperature of the working gas in Table 2 was calculated by formula (1) for $Q = 4$ eV and $C_{C_4F_9I} = 42$ cal/K mole (see Table 1) ($Q = 4.0 \pm 0.2$ eV is the amount of energy converted to heat in a single act of photodissociation as calculated on the basis of thermodynamic data [Ref. 32-34] with consideration of the fact that the characteristic pumping time $t_{pump} = 1/\overline{\sigma\phi} \cong 45$ μs is nearly two orders of magnitude longer than the characteristic times $t_{R_2} \cong t_{RI} \cong 1$ μs). Time t_c^{td} of thermodissociative lasing cutoff was calculated by formula (67) from Ref. 29 on the basis of approximation (1) for rate constant $k_{td} = A \exp(-\Delta E/kT)$ of thermal dissociation

$$C_4F_9I \rightarrow C_4F_9 + I(^2P_{3/2}), \qquad (2)$$

where we have assumed $\Delta E/k = 23650$ K and $A = 10^{13}$-10^{15} s^{-1} in accordance with current concepts [see Ref. 32-35].

It can be seen from the data of Table 2 that the experimental values of time t_c of lasing cutoff and especially time t_{min} of the appreciable drop in lasing power are several times lower than the theoretical value of t_c^{td}. For the less exponential curves *4* and *5* of Fig. 2, $t_{min} = 7$ μs, although it nearly coincides with the time $t'_{min} = 8$ μs, where the pumping pulse has a slight minimum, but lasing power $G(t_{min})$ is only 11-13% of $G(t_{max})$, whereas the pumping rate $\overline{\sigma\phi}(t_{min})$ is 50% of $\overline{\sigma\phi}(t_{max})$. Therefore, just as in Ref. 6, 36, we have come to the conclusion that in our experiments the rise in temperature of perfluorobutyl iodide undergoing flash photolysis has an effect on the intensity of stimulated emission and chemical reaction rate that is much stronger than directly implied by formula (45) from Ref. 29, or by formulas (4) from Ref. 30 and (14) from Ref. 31. It was shown in Ref. 16 and 17 that the reason for such intensified action of temperature increase (leading to acceleration of quenching chemical reactions and considerable attenuation of lasing power far before t_c) is to be found in radial gasdynamic oscillations of the working gas of the photodissociation iodine laser caused by the temperature gradient that arises in the iodide undergoing photolysis. Actually, in a first approximation in each element of volume of the working gas undergoing oscillations, density fluctuations are accompanied by temperature fluctuations around an average value (1). Since the rates of strongly endothermal (e. g. (2)) or exothermal reactions are exponentially (sharply nonlinearly) dependent on temperature, all processes of pyrolysis of iodide take place at a rate that corresponds to a noticeably higher temperature than (1). In a second approximation, corrections can be made in (1) that account for absorption and release of heat in the periodically accelerated chemical reactions and so on. Hwever, we did not undertake a quantitative accounting for the temperature contribution of gas dynamics to the reduction in amplitude of fluctuations of lasing power or a comparison of the contribution due to periodic misalignment of the optical cavity as a consequence of fluctuations of optical density of the gasdynamically oscillating gas. (The development of radial optical

TABLE 3

Theoretical and experimental parameters of radial oscillations of C_4F_9I laser

Curve on Fig. 2	ν	ρ, cm	r_0, cm	$\sigma[RJ]_0$, cm^{-1}	$\frac{Q/C_{RJ}}{T_0}$	τ_0, μs	τ_1^*, μs	τ_2^*, μs	τ_3^{**}, μs	a_2
1	1,05	0,26	0,160	1,72	7,5	50	34	22	16±1	4,80
2	1,05	0,26	0,151	2,83	7,5	50	35	24	16±1	4,14

*First period

**Experimental value of first period of radial oscillations; ρ is the inside radius of the laser cell

inhomogeneities in the working fluid of photodissociation iodine lasers was first experimentally observed in Ref. 37, and the possible gasdynamic nature of such inhomogeneities was first pointed out in Ref. 20).

In contrast to preceding papers [Ref. 6, 16], the use of a grid of return wires in this paper led to irregularity of pumping radiation pulse shape, and consequently to additonal irregularities of the pulses of stimulated emission. However, all three pulses of stimulated emission shown on Fig. 2 show a first appreciable minimum at t = 7-8 μs corresponding to the phase of maximum compression of the working gas on the axis of the cell, a second minimum for t = 15-17 μs corresponding to the phase of maximum departure of the working gas from the axis of the cell and (on curve 2) a third minimum for t = 23-25 μs corresponding to the second maximum of compression of the working gas on the axis of the cell.

Comparison of the experimental (by data of Fig. 2) and theoretical parameters of radial oscillations of the C_4F_9I laser is summarized in Table 3. The sense of r_0 and a_2 is given in Ref. 17. The values of the zeroth (τ_0), first (τ_1) and second approximations of the first period of radial oscillations of the iodide undergoing photolysis were calculated by formulas (9), (10) and (11) respectively from Ref. 17. Since τ_0, τ_1, τ_2 converge to the [experimental value] τ_3, it can be expected that exact solution of the corresponding equations of gas dynamics will yield total agreement between the theoretical and experimental values of the period of oscillations. Thus the experimental data of Fig. 2 are described by the very simple theory [Ref. 17] of nonlinear radial oscillations of the gas undergoing photolysis, so that we can take it as proven that there is a significant contribution of radial oscillations of the working gas to attenuation and cutoff of lasing of the C_4H_9I laser under the conditions of our experiments.

REFERENCES

1. Kasper, J. V. V., Pimentel, G. C., APPL. PHYS. LETTS, Vol 5, 1964, p 231; Kasper, J. V. V., Parker, J. H., Pimental, G. C. C., J. CHEM. PHYS., Vol 43, 1965, p 1827.

2. Basov, N. G., PRIRODA, No 6, 1978, p 26.

3. Hohla, K., Kompa, K. L., APPL. PHYS. LETTS, Vol 22, 1973, p 177.

4. Antonov, A. S., Belousova, I. M., Gerasimov, V. A., Danilov, O. B., Zhevlakov, A. P., Sapelkin, N. V., Yachnev, I. L., PIS'MA V ZHURNAL TEKHNICHESKOY FIZIKI, Vol 4, 1978, p 1143.

5. Danilov, O. B., Yelagin, V. V., Emdina, I. M., Yachnev, I. L., ZHURNAL TEKHNICHESKOY FIZIKI, Vol 35, 1975, p 1923.

6. Skorobogatov, G. A., Seleznev, V. G., Maksimov, B. N., Slesar', O. N., ZHURNAL TEKHNICHESKOY FIZIKI, Vol 45, 1975, p 2454.

7. Swingle, J. C., Turner, C. E., Murray, J. R., George, E. V., APPL. PHYS. LETTS, Vol 28, 1976, p 387.

8. Hohla, K., Kompa, K. L., Z. NATURFORSCH., Vol 27a, 1972, p 938.

9. Pirkle, R. Y., Davis, C. C., Mcfarlane, R. A., CHEM. PHYS. LETTS, Vol 36, 1975, p 305.

10. Zalesskiy, V. Yu., Kokushkin, A. M., KVANTOVAYA ELEKTRONIKA, Vol 3, 1976, p 1501.

11. Birich, G. N., Drozd, G. I., Sorokin, V. N., Struk, I. I., PIS'M V ZHURNAL EKSPERIMENTAL'NOY I TEORETICHESKOY FIZIKI, Vol 19, 1974, p 44.

12. Andreyeva, T. L., Birich, G. N., Sorokin, V. N., Struk, I. I., KVANTOVAYA ELEKTRONIKA, Vol 3, 1976, p 1442.

13. Tarfons, R., U. S. Patent No 3234294, 20 Dec 62; Rebfsdat, S., Sahuierer, E., West German Patent No 1915395, 26 Mar 69.

14. Skorobogatov, G. A., Komarov, V. S., Seleznev, V. G., ZHURNAL TEKHNICHESKOY FIZIKI, Vol 44, 1974, p 1996.

15. Volkov, V. N., Zubarev, I. G., Sorokin, V. N., ZHURNAL PRIKLADNOY SPEKTROSKOPII, Vol 7, 1972, p 735.

16. Skorobogatov, G. A., Komarov, V. S., ZHURNAL TEKHNICHESKOY FIZIKI, Vol 47, 1977, p 429.

17. Skorobogatov, G. A., ZHURNAL TEKHNICHESKOY FIZIKI, Vol 47, 1977, p 1551.

18. Dymov, B. P., Skorobogatov, G. A., ZHURNAL TEKHNICHESKOY FIZIKI, Vol 48, 1978, p 124.

19. Belousova, I. M., Gorshkov, N. G., Danilov, O. B., Zalesskiy, V. Yu., Yachnev, I. L., ZHURNAL EKSPERIMENTAL'NOY I TEORETICHESKOY FIZIKI, Vol 65, 1973, p 517.

20. Golubev, L. Ye., Zuyev, V. S., Katulin, V. A., Nosach, N. Yu., Nosach, O. Yu., "Kvantovaya elektronika" [Quantum Electronics], edited by N. G. Basov, No 6(18), 1973, p 23.

21. Ishii, S., Ahlborn, B., J. APPL. PHYS., Vol 47, 1976, p 1076.

22. Alekhin, B. V., Borovkov, V. V., Lazhintsev, B. V., Nor-Arevyan, V. A., Sukhanov, L. V., Ustinenko, V. A., KVANTOVAYA ELEKTRONIKA, Vol 6, 1979, p 1948.

23. Komarov, V. S., Seleznev, V. G., Skorobogatov, G. A., ZHURNAL TEKHNICHESKOY FIZIKI, Vol 44, 1974, p 875.

24. Skorobogatov, G. A., Slesar', O. N., VESTNIK LENINGRADSKOGO UNIVERSITETA, No 4, 1979, p 39.

25. Seleznev, V. G., Skorobogatov, G. A., VESTNIK LENINGRADSKOGO UNIVERSITETA, No 10, 1978, p 77.

26. Dymov, B. P., Skorobogatov, G. A., Khomenko, V. Ye., Shchukarev, S. A., ZHURNAL OBSHCHEY KHIMII, Vol 47, 1977, p 848.

27. Zuyev, V. S., Korol'kov, K. S., Nosach. O. Yu., Orlov, Ye. P., KVANTOVAYA ELEKTRONIKA, Vol 7, 1980, p 2604

28. Nosach, O. Yu., Orlov, Ye. P., Preprint No 7, Lebedev Physics Institute, Moscow, 1979.

29. Skorobogatov, G. A., VESTNIK LENINGRADSKOGO UNIVERSITETA, No 4, 1970, p 144.

30. ZALESSKIY, V. Yu., Moskalev, Ye. I., ZHURNAL EKSPERIMENTAL'NOY I TEORETICHESKOY FIZIKI, Vol 57, 1969, p 1884.

31. Zalesskiy, V. Yu., KVANTOVAYA ELEKTRONIKA, Vol 1, 1974, p 1819.

32. Laurence, G. S., TRANS. FAR. SOC., Vol 63, 1976, p 1155.

33. Tschunikow-Roux, E., J. PHYS. CHEM., Vol 69, 1965, p 1075.

34. Grygorcewicz, C., Laurence, G. S., J. PHYS. CHEM., Vol 72, 2968, p 1811.

35. Vedeneyev, V. I., Kibkalo, A. A., "Konstanty skorosti gazofaznykh monomolekulyarnykh reaktsiy" [Rate Constants of Monomolecular Gas-Phase Reactions], Moscow, Nauka, 1972.

36. Seleznev, V. G., Skorobogatov, G. A., Komarov, V. S., ZHURNAL OBSHCHEY KHIMII, Vol 44, 1974, p 1293.

37. Belousova, I. M., Danilov, O. B., Sinitsyna, I. A., Spiridonov, V. V., ZHURNAL EKSPERIMENTAL'NOY I TEORETICHESKOY FIZIKI, Vol 58, 1970, p 1481.

6610
CSO: 1862/133

OPTICS AND SPECTROSCOPY

UDC 551.466.3:535.31

THEORY OF OBSERVATION OF UNDERWATER OBJECTS THROUGH WAVE-COVERED SEA SURFACE

Moscow IZVESTIYA AKADEMII NAUK SSSR: FIZIKA ATMOSFERY I OKEANA in Russian Vol 18, No 4, Apr 82 (manuscript received 9 Dec 80, after revision 6 Apr 81) pp 408-415

[Article by S. V. Dotsenko, Marine Geophysical Institute, Ukrainian Academy of Sciences]

[Text]

Abstract: The article gives a theoretical analysis of the distortions introduced by the wave-covered sea surface in the image of underwater features observed from the atmosphere. It is postulated that the spatial structure of both observed features and waves has a random character. The quality of observation is evaluated using the magnitude of the error in measuring the spatial luminosity of the feature. It is shown that there is an optimum relationship between the statistical characteristics of the distribution of luminosity and waves and the parameters of the measuring instrument ensuring a minimum of this error.

The possibility of observing underwater features from the atmosphere is dependent on their contrast, degree of turbidity of the water and atmosphere, superposing of the brightness of air haze, light scattered in the sea and brightness of the water-air discontinuity on the image [1].

We will investigate the joint influence exerted on transmission of the image of underwater features by the wave-covered sea surface and the averaging effect of the measuring instrument, neglecting other interfering factors, allowance for which is possible independently.

A problem similar in its formulation was solved in [1], where the influence of the sea surface on image transmission was studied by an analysis of the scattering function, the energy distribution in the edge image and the frequency contrast of the transfer function. In source [2] a study was made of the image transfer of a point through a one-dimensional sinusoidal wave and formulas were given for computing the displacement of a point and the blurring of an object

with an increase in the exposure. An approximate model of image transfer through the wave-covered discontinuity of two media with different refractive indices was described in [3], where the author determines the multipoint statistical characteristics of the brightness image of a self-luminescent object or feature observed through the wave-covered discontinuity.

A feature of this study is that it examines the observation of random spatially elongated features using optical radiation detectors which perform spatial averaging of the image. Many natural formations on the bottom and in the water layer can be modeled by features of the mentioned structure whose investigation is possible by optical methods. The spatial averaging of the received image is a property of any real radiation detector. Accordingly, the combination of such initial premises makes it possible to obtain research results suitable for direct practical application. The quality of observation is evaluated using the mean square error between the initial and measured luminosity distributions [4]. It is shown that it is dependent on the choice of the degree of averaging and is the highest when it has a finite value. Here we will examine observations at the nadir as ensuring minimum image distortion [1].

In order to simplify the analysis we will examine a problem in which the object of measurement and waves are assumed to be one-dimensional (Fig. 1).

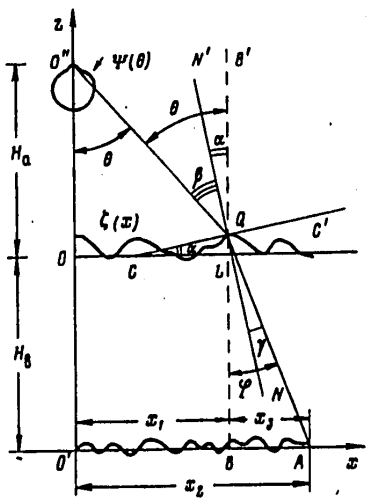

Fig. 1. Diagram explaining derivation of principal relationships.

Retaining the physical essence of the analyzed phenomena, such an approach makes it relatively simple to obtain final numerical results. The x-axis of the mean level of the wave-covered surface is stipulated in the figure by the point O.

The atmosphere is situated above it and the water below. At the depth H_w below the sea surface there is a diffuse self-luminescent object to be observed, extending in the direction of the x-axis, whose spatial distribution of luminosity is described by the random function f(x). At the height H_a above the sea surface at the point O" there is a detector of optical radiation whose optical axis is directed to the nadir. The difference in the level of the wave-covered surface from the mean is described by a centered random function of the space coordinate $\zeta(x)$.

An analysis of the process of observation of an underwater feature will be made on the basis of the premises of geometrical optics without allowance for the absorption and scattering of light in the water. The ray emerging from the point A of the observed feature and received by the detector at the point O" travels the following path. It is propagated in the water medium at the angle φ to the vertical BB' to the point Q at the water surface. The tangent CC' to the sea surface at this point is slanted to the horizontal at the angle α, whereas the normal NN' to this surface also is deflected by the angle α from the vertical BB'. At the point Q there is refraction of the ray and it emerges from the water at the angle β to the normal NN'. The detector at the point O" picks it up arriving at the angle θ to the vertical.

Since the $\zeta(x)$ surface is curvilinear and random, the picture picked up by the instrument differs from the f(x) function describing the distribution of luminosity of the observed object and this difference has a random character. We will find the error introduced by the wave-covered sea surface and instrument to the image sensed by the latter and we will evaluate the limits of applicability of such a method for observing underwater objects. For this purpose we will first obtain the correlation between the output signal Y of the measuring instrument and the investigated object f(x).

We will find the position of the point A, situated on the observed object, which is sensed by the instrument as visible at the angle θ to the vertical. The segment LQ is the $\zeta(x)$ value. Accordingly, the abscissa of the points L and B is

$$x_1=[H_a-\zeta(x_1)]\operatorname{tg}\theta. \tag{1}$$

Since the straight line CC' is the tangent to the $\zeta(x)$ curve at the point with the abscissa x_1, then

$$\operatorname{tg}\alpha=\frac{d\zeta(x)}{dx}\Big|_{x=x_1}=\zeta'(x_1).$$

It follows from Fig. 1 that the distance of the point A from the point B is equal to $x_3 = [H_w + \zeta(x_1)]\ \operatorname{tg}\varphi$. Accordingly, the abscissa of the point A is

$$x_2=x_1+x_3=[H_a-\zeta(x_1)]\operatorname{tg}\theta+[H_a+\zeta(x_1)]\operatorname{tg}\varphi, \tag{2}$$

where $\varphi=\alpha+\gamma$. Equation (1) can be regarded as an equation for finding the abscissa x_1. However, due to the random character of the $\zeta(x_1)$ parameter its precise solution cannot be obtained. We will take advantage of the circumstance that in actual practice the amplitude of the wave $|\zeta_{max}|$ is much less than the height H_a at which the measuring instrument is situated. From expression (1) we find that $x_1 = H_a \operatorname{tg}\theta$, and expression (2) assumes the form

$$x_2=[H_a-\zeta(H_a\operatorname{tg}\theta)]\operatorname{tg}\theta+[H_a+\zeta(H_a\operatorname{tg}\theta)]\operatorname{tg}\varphi. \tag{3}$$

Thus, at the angle θ to the normal the measuring instrument picks up the point of an object whose abscissa is given by expression (3). The luminosity $f(x_2)$ of the object at this point has the form

$$f\{[H_a-\zeta(H_a \operatorname{tg}\theta)]\operatorname{tg}\theta+[H_a+\zeta(H_a \operatorname{tg}\theta)]\operatorname{tg}\varphi\}. \tag{4}$$

The argument of this function is random since the parameters ζ and φ are random. Accordingly, the value (4) is random even for a specific f(x) record. We will simplify its argument. For this we use the notation $\xi = \operatorname{tg}\alpha$, $\eta = \operatorname{tg}\vartheta$. Remote optical instruments usually have a very high angular resolution. Accordingly, it can be assumed that $|\eta|_{max} \ll 1$. The angles of inclination of the waves are usually also small, that is $|\xi|_{max} \ll 1$. In this case $\operatorname{tg}\varphi = \xi + (\eta - \xi)/n$, where n is the refractive index of water and the distribution of luminosity (4) assumes the form

$$f\left[A_0 x_1 + \frac{n-1}{n} H_a \xi(x_1)\right], \tag{5}$$

where

$$A_0 = 1 + \frac{H_a}{nH_a} \tag{6}$$

[B = w(ater)]

and it is taken into account that $\eta = x_1/H_a$. Thus, with the mentioned assumptions the random character of parameter (5) is determined by the random form of the function f(x) and the random character of wave slope $\xi(x) = d\zeta(x)/dx$.

The total signal received by the optical instrument is a superposing of the signals (5), that is

$$Y(\xi) = \int_{-\infty}^{\infty} h(x) f\left[A_0 x + \frac{n-1}{n} H_a \xi(x)\right] dx, \tag{7}$$

where h(x) is the instrument function of the sensor of this instrument, which is the projection of the directional diagram of the optical receiver $\Psi(\Theta)$ onto the mean sea surface (Fig. 1), and characterizes the weight with which different parts of the image are sensed by the instrument. The $Y(\xi)$ parameter is dependent on the random function $\xi(x)$.

If the waves are absent and the resolution of the instrument is infinitely high, that is, the conditions $\xi(x) = 0$ and $h(x) = \delta(x)$ are satisfied, the instrument output signal is precisely equal to the value of the f(x) function at the nadir point, that is, $Y_0 = f(0)$. The difference between the $Y(\xi)$ and Y_0 value is determined by the presence of waves and a finite resolution of the measuring instrument. The mean square difference of the $Y(\xi)$ and Y_0 values is the dispersion of the measurement error

$$\varepsilon^2(\xi) = \overline{[Y(\xi)-Y_0]^2} = \overline{Y^2(\xi)} - 2\overline{Y_0 Y(\xi)} + \overline{Y_0^2}, \tag{8}$$

dependent on the random function of slopes $\xi(x)$. In expression (8) averaging is carried out for all possible cases of the random function f(x) with a constant record of the random function $\xi(x)$. Assuming the distribution of luminosity f(x) to be stationary and ergodic and using expression (7), we obtain

$$\overline{Y_0^2}=\overline{f^2(0)}=\sigma^2,$$

$$\overline{Y_0Y(\xi)}=\int_{-\infty}^{\infty}h(x)B\left[A_0x+\frac{n-1}{n}H_0\xi(x)\right]dx,$$

$$\overline{Y^2(\xi)}=\iint_{-\infty}^{\infty}h(x_1)h(x_2)B\left\{A_0(x_2-x_1)+\frac{n-1}{n}H_0[\xi(x_2)-\xi(x_1)]\right\}dx_1\,dx_2,$$

where σ^2 is the dispersion of the f(x) function; $B(\rho)$ is its correlation function. Expressing the latter through the S(k) spatial spectrum of the f(x) process, we find

$$\overline{Y_0Y(\xi)}=\int_{-\infty}^{\infty}h(x)S(k)\exp\left\{j\omega\left[A_0x+\frac{n-1}{n}H_0\xi(x)\right]\right\}dx\,dk, \tag{9a}$$

$$\overline{Y^2(\xi)}=\iiint_{-\infty}^{\infty}h(x_1)h(x_2)S(k)\exp\left\{j\omega\left[A_0(x_2-x_1)+\right.\right.$$

$$\left.\left.+\frac{n-1}{n}H_0(\xi(x_2)-\xi(x_1))\right]\right\}dx_1dx_2\,dk. \tag{9b}$$

Since the $\xi(x)$ function is random, the dispersion of measurement error $\varepsilon^2(\xi)$ is also random. We will find the mean value of the dispersion of measurement error $\varepsilon^2=\langle\varepsilon^2(\xi)\rangle$ for the set of records of the wave process; here the symbol $\langle\ldots\rangle$ denotes such averaging. According to formula (8),

$$\varepsilon^2=\sigma^2-2\langle\overline{Y_0Y(\xi)}\rangle+\langle\overline{Y^2(\xi)}\rangle. \tag{10}$$

We will compute the values of the terms entering here. The distribution of the probability of rises $\zeta(x)$ of the sea surface is described by the normal law [1, 5]. Therefore, the process $\xi(x)=\zeta'(x)$ is also normal and its probability density has the form [5]

$$w_1(\xi)=\frac{1}{\sigma_\zeta k_1\sqrt{2\pi}}\exp\left(-\frac{\xi^2}{2\sigma_\zeta^2k_1^2}\right).$$

Here σ_ζ^2 is the dispersion of the $\zeta(x)$ function, the value $k_1^2=-B_\zeta''(0)/\sigma_\zeta^2=-R_\zeta''(0)$, and $B_\zeta(\rho)$ and $R_\zeta(\rho)$ are the correlation and normalized correlation functions of the $\zeta(x)$ process. In accordance with expression (9a) we obtain

$$\langle\overline{Y_0Y(\xi)}\rangle=\int_{-\infty}^{\infty}\overline{Y_0Y(\xi)}w_1(\xi)d\xi=$$

$$=\int_{-\infty}^{\infty}S(k)\tilde{h}^*(A_0k)\exp\left[-\frac{(n-1)^2}{2n^2}(H_0\sigma_\zeta k_1)^2k^2\right]dk, \tag{11}$$

where $\tilde{h}(k)$ is the instrument function spectrum.

The computation of the $\langle\overline{Y^2(\xi)}\rangle$ value, in accordance with (9b), requires a knowledge of the two-dimensional probability distribution $w_2(\xi_1, \xi_2)$ for the values $\xi_1 = \xi(x_1)$ and $\xi_2 = \xi(x_2)$. Since the $\xi(x)$ process is normal, this distribution has the form [6]

$$w_2(\xi_1, \xi_2) = \frac{1}{2\pi\sigma_\xi^2\sqrt{1-R_\xi^2(\rho)}} \exp\left\{-\frac{\xi_1^2-2R_\xi(\rho)\xi_1\xi_2+\xi_2^2}{2\sigma_\xi^2[1-R_\xi^2(\rho)]}\right\}, \tag{12}$$

where σ_ξ^2 and $R_\xi(\rho)$ are the dispersion and normalized correlation function of the $\xi(x)$ process, and $\rho = x_2 - x_1$. Taking into account that $\xi(x) = \zeta'(x)$, we express the coefficients entering into formula (12) through the statistical characteristics of the initial wave process

$$B_\zeta(\rho) = -\sigma_\zeta^2 R_\zeta''(\rho), \quad \sigma_\zeta^2 = B_\zeta(0), \tag{13}$$

$$R_\zeta(\rho) = -R_\zeta''(\rho)/k_1^2, \quad \sigma_\zeta^2 = k_1^2\sigma_\zeta^2.$$

Thus,

$$\langle\overline{Y^2(\xi)}\rangle = \int_{-\infty}^{\infty} \overline{Y^2(\xi)}\, w_2(\xi_1, \xi_2)\, d\xi_1\, d\xi_2.$$

Substituting here the expression (9b), we obtain

$$\langle\overline{Y^2(\xi)}\rangle = \iiint_{-\infty}^{\infty} S(k)h(x_1)h(x_2)\times \times\theta_2\left(-\frac{n-1}{n}H_n k, \frac{n-1}{n}H_n k\right) e^{jkA_0(x_2-x_1)}dx_1\, dx_2\, dk, \tag{14}$$

where $\theta_2(v_1, v_2) = \langle\exp[j(v_1\xi_1 + v_2\xi_2)]\rangle$ is the two-dimensional characteristic function of the random parameters ξ_1 and ξ_2. For a normal distribution we have the expression [6]

$$\theta_2(v_1, v_2) = \exp\left[-\frac{1}{2}(\sigma_1^2v_1^2+2r_{12}\sigma_1\sigma_2v_1v_2+\sigma_2^2v_2^2)\right],$$

where σ_1^2 and σ_2^2 are the dispersions of the parameters ξ_1 and ξ_2, and r_{12} is their correlation coefficient. In our case $\sigma_1 = \sigma_2 = \sigma_\xi$ and $r_{12} = R_\xi(\rho)$. Accordingly, with expressions (13) taken into account, we reduce expression (14) to the form

$$\langle\overline{Y^2(\xi)}\rangle = \iiint_{-\infty}^{\infty} S(k)h(x_1)h(x_2)\exp\{-[k_1^2+R_\zeta''(x_2-x_1)]\times \times\left(\frac{n-1}{n}\sigma_\zeta H_n k\right)^2 + jA_0k(x_2-x_1)\Big\}\, dx_1\, dx_2\, dk. \tag{15}$$

We will assume that the instrument function for the sensor has a bell shape

$$h(x) = \frac{a}{2R_x}\exp\left(-\frac{\pi}{4}\frac{x^2}{R_x^2}\right), \tag{16}$$

where R_x is its characteristic radius, a is the amplification factor. Expression (16) is frequently used in order to approximate real instrument functions of optical instruments [7]. The spectrum of function (16) $h(k) = a\exp(-k^2R_x^2/\pi)$. Expressions (11) and (15) assume the form

$$\overline{\langle Y_0 Y(\xi)\rangle} = a\sigma^2 P_1, \quad \overline{\langle Y^2(\xi)\rangle} = a^2\sigma^2 P_2, \tag{17}$$

where

$$P_1 = \sigma^{-2}\int_{-\infty}^{\infty} S(k)\exp\left[-\left(\frac{A_0^2 R_x^2}{\pi}+\frac{1}{2}l^2k_1^2\right)k^2\right]dk, \tag{18}$$

$$P_2 = \frac{1}{2\sqrt{2}\,R_x\sigma^2}\iint_{-\infty}^{\infty} S(k)\exp\left[-l^4k_1^2q(x)k^2-\frac{\pi}{8R_x^2}x^2+jkA_0x\right]dx\,dk, \tag{19}$$

$$l^2 = \frac{n-1}{n}\sigma_t H_0, \tag{20}$$

$$q(x) = 1+R_t''(x)/k_1^2, \tag{21}$$

and formula (10) can be written as $\varepsilon^2 = \sigma^2(1 - 2aP_1 + a^2P_2)$. In the latter expression the ε^2 parameter is dependent on the a coefficient. It is minimum with $a = P_1/P_2$, and this minimum has the value

$$\varepsilon_0^2 = \sigma^2(1-P_1^2/P_2). \tag{22}$$

Further computations by the derived formulas are possible only when making specific the statistical characteristics of the observed object and the wave field.

We will assume that the distribution of luminosity f(x) subject to measurement has a bell-shaped spectrum

$$S(k) = \frac{\sigma^2 r_f}{\pi}\exp\left(-\frac{r_f^2k^2}{\pi}\right),$$

where r_f is the characteristic spatial scale of this distribution. Formulas (18) and (19) assume the form

$$P_1 = \left(1+A_0^2z^2+\frac{1}{2}c\right)^{-1/2}, \tag{23}$$

$$P_2 = \frac{1}{2\sqrt{2}\,R_x}\int_{-\infty}^{\infty}\exp\left\{-\frac{\pi}{4}\left[\frac{A_0^2}{r_f^2(1+cq(x))}+\frac{1}{2R_x^2}\right]x^2\right\}\frac{dx}{\sqrt{1+cq(x)}}, \tag{24}$$

where $z = R_x/r_f$ and $c = \pi l^4k^2/r_f^2$.

We will examine a case when inhomogeneities of the sea surface constitute a sinusoidal wave with the wave number k_0:

$$\zeta(x) = b\sin(k_0x+\alpha), \tag{25}$$

the phase α of which is uniformly distributed in the interval $[0, 2\pi]$. If the amplitude b is random, independent of the phase α and with a Rayleigh distribution, the $\zeta(x)$ function is stationary, ergodic and with a normal distribution [8]. Assuming that all these conditions are satisfied, we find that the correlation function of the $\zeta(x)$ process is $B_\zeta(\rho) = \sigma_\zeta^2\cos(k_0\rho)$, the value $k_1^2 = k_0^2$, and expression (21) assumes the form

$$q(x)=1-\cos(k_0 x). \tag{26}$$

We denote the wavelength (25) by λ_0, that is, $k_0 = 2\pi/\lambda_0$, and we introduce the coefficient

$$\varkappa=r_f/\lambda_0, \tag{27}$$

showing the ratio of the characteristic scale of the function f(x) to the wavelength of the surface wave. In this case

$$P_2=\frac{1}{2\sqrt{2}\pi z\varkappa}\int_0^\infty \exp\left\{-\left[\frac{A_0^2}{1+c\beta(t)}+\frac{1}{2z^2}\right]\frac{t^2}{16\pi\varkappa^2}\right\}\frac{dt}{\sqrt{1+c\beta(t)}}, \tag{28}$$

where $\beta(t) = 1 - \cos t$. We will transform the c parameter in the following way:

$$c=4\pi^2\left(\frac{n-1}{n}\varkappa W\right)^2,$$

where the dimensionless parameter

$$W=\frac{H_в}{r_f}\frac{\sigma_\zeta}{r_f}$$

[B = w(ater)]

is determined by the depth H_w at which the observed object is situated, the characteristic scale r_f and the mean square wave height σ_ζ. Taking into account that the refractive index n of water can be considered equal to 4/3 [9], we obtain $c = 1/4\,\pi^3(\varkappa W)^2$.

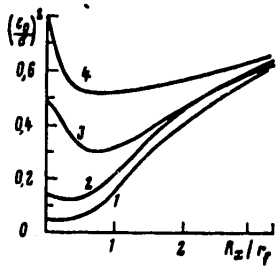

Fig. 2. Dependence of measurement error on relative averaging scale with $A_0 = 1$, W = 1: 1) $\varkappa$ = 0.1; 2) 0.2; 3) 0.5; 4) 1.0.

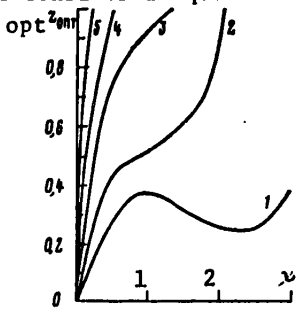

Fig. 3. Dependence of degree of optimum averaging on characteristics of observed object and waves: 1) W = 0.2; 2) 0.5; 3) 1.0; 4) 2.0; 5) 5.0.

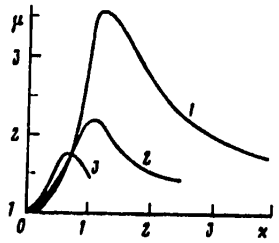

Fig. 4. Dependence of gain in measurement accuracy with optimum averaging on characteristics of observed object and waves: 1) W = 0.2; 2) 0.5; 3) 1.0.

Figure 2 shows an example of the results of computation of the error in measuring the distribution of luminosity on the basis of the determined relationships. It can be seen that the $(\varepsilon_0/\sigma)^2$ value in the case of small z with an increase in z and with the other parameters remaining constant decreases, attaining a minimum with some finite value $z = z_{opt}$. Accordingly, the measurement error is minimum not with an infinitely narrow directional diagram of the optical detector, but with some finite width. Such an increase in accuracy with an increase in $z = R_x/r_f$ is associated with the spatial filtering of the image by the detector. An increase in z leads to an averaging of both the luminosity distribution of the object f(x) and the observed wave pattern. In the case of small z an increase in z leads to an improvement of the image, but with a considerable increase in z the error increases due to the smoothing of image details with its great averaging. This circumstance is evidently one of the reasons for the well-known fact of an improvement in the image of underwater objects with an increase in observation height (to a definite level). Here the radiation detector plays the role of a filter restoring the image. In the case of very great heights the image quality again decreases. The effect of an improvement in the image by an averaging detector is particularly conspicuous in the case of large $\varkappa = r_f/\lambda_0$ (the length of the surface wave is small in comparison with the characteristic scale of the object).

It follows from Fig. 3 that the optimum averaging value is essentially dependent on the characteristics of the observed object and waves. This averaging is particularly great with large W.

It can be shown that with z = 0 (that is, for detectors with an infinitely narrow directional diagram)

$$\left(\frac{\varepsilon_0}{\sigma}\right)^2_{z=0} = \frac{c}{2+c}. \tag{29}$$

As the gain in measurement accuracy in the case of optimum averaging we have

$$\mu = \left(\frac{\varepsilon_0}{\sigma}\right)^2_{z=0} \Big/ \left(\frac{\varepsilon_0}{\sigma}\right)^2_{\text{мин}} \quad \text{min} \tag{30}$$

It shows by how many times the the square of the measurement error with use of a detector with an optimum width of the directional diagram is less than this same parameter with an infinitely narrow diagram. Figure 4 shows that this gain increases with a decrease in the W parameter, that is, with a decrease in the amplitude of the surface wave and the depth of the observed object and an increase in the characteristic scale of this object.

Therefore, there is not always justification for the striving to use apparatus with maximum spatial resolution for observing underwater features. The cited results of computations make it possible to determine in what cases there is assurance of a greater accuracy in measuring their luminosity distribution when there is finite spatial averaging, to find the optimum value of this averaging and to evaluate the accuracy gain occurring in this case.

BIBLIOGRAPHY

1. Mullamaa, Yu.-A. R., "Influence of the Wave-Covered Sea Surface on the Visibility of Underwater Features," IZV. AN SSSR: FAO (News of the USSR Academy of Sciences: Physics of the Atmosphere and Ocean), Vol 11, No 2, pp 199-206, 1975.

2. Levin, I. M. and Litvin, V. Kh., "Image Transfer Through a Sinusoidal Wave," IZV. AN SSSR: FAO, Vol 16, No 5, pp 490-495, 1980.

3. Veber, V. L., "Statistical Characteristics of Images Obtained During Observation Through an Uneven Interface Between Media With Different Refractive Indices," IZV. VUZov: RADIOFIZIKA (News of Institutions of Higher Education: Radiophysics), Vol 22, No 8, pp 989-1001, 1979.

4. Sondkhi, M. M., "Image Restoration: Aging of Spatially Invariant Distortions," OBRABOTKA IZOBRAZHENIY PRI POMOSHCHI TSIFROVYKH VYCHISLITEL'NYKH MASHIN (Image Processing Using Digital Computers), Moscow, Mir, pp 137-152, 1973.

5. Krylov, Yu. M., SPEKTRAL'NYYE METODY ISSLEDOVANIYA I RASCHETA VETROVYKH VOLN (Spectral Methods for Investigating and Computing Wind Waves), Leningrad, Gidrometeoizdat, 1966, 256 pages.

6. Levin, B. R., TEORETICHESKIYE OSNOVY STATISTICHESKOY RADIOTEKHNIKI (Theoretical Principles of Statistical Radio Engineering), Book I, Moscow, Sovetskoye Radio, 1969, 752 pages.

7. Levshin, V. L., PROSTRANSTVENNAYA FIL'TRATSIYA V OPTICHESKIKH SISTEMAKH PELENGATSII (Spatial Filtering in Optical Direction-Finding Systems), Moscow, Sovetskoye Radio, 1971, 200 pages.

8. Korn, G., MODELIROVANIYE SLUCHAYNYKH PROTSESSOV NA ANALOGOVYKH I ANALOGO-TSIFROVYKH MASHINAKH (Modeling of Random Processes on Analog and Analog-Digital Computers), Moscow, Mir, 1968, 315 pages.

9. Yerlov, N., OPTICHESKAYA OKEANOGRAFIYA (Optical Oceanography), Moscow, Mir, 1970, 224 pages.

5303
CSO: 1865/150

UDC 535.375:621.373

WAVEFRONT REVERSAL BY FOUR-WAVE MIXING IN RAMAN-NONLINEAR MEDIUM

Moscow KVANTOVAYA ELEKTRONIKA in Russian Vol 9, No 2(116), Feb 82 (manuscript received 27 Mar 81) pp 229-234

[Article by V. M. Izgorodin, S. B. Kormer, G. G. Kochemasov, V. D. Nikolayev and A. V. Pinegin]

[Text] A theoretical and experimental investigation is made of the feasibility of wavefront reversal by four-wave interaction in a Raman-nonlinear medium. For the case of planar waves, theoretical relations are found for the reflectivity of a four-wave mixer as a function of the increment of gain, phase detuning and the pumping asymmetry parameter. In experiments with a ruby laser and quasiplanar waves, a maximum reflectivity of 0.5% is obtained for a nonlinear mirror, which agrees with the theoretical estimate. An experimental investigation is made of the quality of wavefront reversal, and possibilities for improvement are discussed.

Recently considerable attention has been given to the investigation of wavefront reversal by stimulated Mandelstam-Brillouin scattering [Ref. 1] and four-wave interactions in media with cubic nonlinearity [Ref. 2, 3], as well as in media that are active in stimulated Mandelstam-Brillouin scattering [Ref. 11]. Possible uses of this phenomenon have been discussed in Ref. 4-6. We have considered the feasibility of wavefront reversal based on cubic Raman nonlinearity. This effect can be used for dynamic compensation of optical nonlinearities in stimulated Raman scattering installations.

The process of scattering in the presence of two pumping waves and two Stokes radiation waves

$$\vec{\mathcal{E}}_L = \tilde{\mathbf{E}}_{L1} + \tilde{\mathbf{E}}_{L2} = {}^1/_2 \exp(i\omega_L t)\,[\mathbf{E}_{L1}\exp(i\mathbf{k}_{L1}\cdot\mathbf{r}) + \mathbf{E}_{L2}\exp(i\mathbf{k}_{L2}\cdot\mathbf{r}), \quad (1)$$

$$\vec{\mathcal{E}}_s = \tilde{\mathbf{E}}_{s1} + \tilde{\mathbf{E}}_{s2} = {}^1/_2 \exp(i\omega_s t)\,[\mathbf{E}_{s1}\exp(i\mathbf{k}_{s1}\cdot\mathbf{r}) + E_{s2}\exp(i\mathbf{k}_{s2}\cdot\mathbf{r})] \quad (2)$$

is described by the equation [Ref. 7]

$$[\nabla[\nabla\vec{\mathcal{E}}_s]] - k_s^2\vec{\mathcal{E}}_s = gk_s(\vec{\mathcal{E}}_L\vec{\mathcal{E}}_s)\vec{\mathcal{E}}_L. \quad (3)$$

Here g is the amplification parameter in stimulated Raman scattering; ω, $\vec{k}$ are frequency and wave vector.

Assuming $\vec{k}_{S2} = -\vec{k}_{S1}$, $\vec{k}_S = \{0, 0, k_Z\}$, for slowly varying amplitudes we get from (1)-(3)

$$\frac{dE_{s1}}{dz} = \frac{g}{2}\left[\left(|E_{L1}|^2 + |E_{L2}|^2\right)E_{s1} + E_{L2}E_{L1}^{*}E_{s2}\exp\left(i\Delta\mathbf{k}\cdot\mathbf{r}\right)\right]; \quad (4)$$

$$\frac{dE_{s2}}{dz} = -\frac{g}{2}\left[\left(|E_{L1}|^2 + |E_{L2}|^2\right)E_{s2} + E_{L2}^{*}E_{L1}E_{s1}\exp\left(-i\Delta\mathbf{k}\cdot\mathbf{r}\right)\right]; \quad (5)$$

$$\Delta\mathbf{kr} = (\mathbf{k}_{L2} - \mathbf{k}_{L1})\,\mathbf{r} - 2k_s z. \quad (6)$$

When the synchronism condition is met, $\Delta\vec{k}\cdot\vec{r} = 0$, and for identical pumping wave amplitudes we have

$$\frac{dE_{s1}}{dz} = \frac{\Gamma}{2}\left(E_{s1} + \frac{1}{2}E_{s2}\right); \quad (7)$$

$$\frac{dE_{s2}}{dz} = -\frac{\Gamma}{2}\left(E_{s2} + \frac{1}{2}E_{s1}\right); \quad (8)$$

$$\Gamma = g\left(|E_{L1}|^2 + |E_{L2}|^2\right) = g\left(I_{L1} + I_{L2}\right). \quad (9)$$

Equations (7)-(9) coincide with those found in Ref. 8. In that paper it was also shown that near the angle of synchronism (Fig. 1)

$$\vartheta_0 = \pm\arccos\left(n\left(\omega_L\right)\omega_s / n\left(\omega_s\right)\omega_L\right) \quad (10)$$

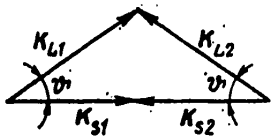

Fig. 1. Wave vector triangle

the threshold of stimulated Stokes radiation in the cavity decreases by a factor of 1.5, which is due to four-wave interaction.

Solving equations (4) and (5) with boundary conditions

$$E_{s1}(z=0) = E_0, \qquad E_{s2}(z=l) = 0, \quad (11)$$

at $\Delta\mathbf{kr} = (k_{L2})_z - (k_{L1})_z - 2k_s z = \Delta k z$, in the approximation of given pumping fields, we get

$$E_{s1} = A\exp(\lambda_1 z) + (E_0 - A)\exp(\lambda_2 z); \quad (12)$$

$$E_{s2} = \alpha_1 A\exp(\lambda_1 z) + \alpha_2\left(E_0 - A\right)\exp(\lambda_1 z), \quad (13)$$

where

$$\lambda_{1,2} = \frac{\Gamma}{4}\left(i\delta \pm \sqrt{3 + \beta^2 - \delta^2 - 4i\delta}\right); \quad (14)$$

$$\delta = 2\Delta k/\Gamma; \quad \beta = \left(I_{L1} - I_{L2}\right)/\left(I_{L1} + I_{L2}\right); \quad (15)$$

$$\alpha_{1,2} = 4\left(\lambda_{1,2} - {}^1/_2\Gamma\right)/\Gamma\sqrt{1 - \beta^2}; \quad (16)$$

$$A = E_0 \Big/ \left(1 - \frac{2\lambda_1 - \Gamma}{2\lambda_2 - \Gamma}\exp\left[\left(\lambda_2 - \lambda_1\right)l\right]\right). \quad (17)$$

The Stokes wave reflectivity and gain with forward Stokes wave propagation will be defined by the expressions

$$R=\left|\frac{E_{s2}(z=0)}{E_{s1}(z=0)}\right|^2=\frac{4}{1-\beta^2}\left|\frac{(2\lambda_1/\Gamma-1)(1-\exp[(\lambda_1-\lambda_2)l])}{1-(2\lambda_1-\Gamma)\exp[(\lambda_1-\lambda_2)l]/(2\lambda_2-\Gamma)}\right|^2,$$

$$K=\left|\frac{E_{s1}(z=l)}{E_{s1}(z=0);}\right|^2=\left|\frac{2(\lambda_2-\lambda_1)\exp(\lambda_1 l)}{(2\lambda_2-\Gamma)-(2\lambda_1-\Gamma)\exp[(\lambda_1-\lambda_2)l]}\right|^2. \quad (18)$$

In the case of exact phase matching, $\Delta\vec{k}\cdot\vec{r}=0$, and for identical intensities of the pumping beams ($I_{L1}=I_{L2}$, $\beta=0$)

$$R=\left|\frac{(2-\sqrt{3})[1-\exp(\sqrt{3}\Gamma l/2)]}{1-(2-\sqrt{3})\exp(\sqrt{3}\Gamma l/2)/(2+\sqrt{3})}\right|^2,$$

$$K=\left|\frac{2\sqrt{3}\exp(\sqrt{3}\Gamma l/2)}{(2+\sqrt{3})-(2-\sqrt{3})\exp(\sqrt{3}\Gamma l/2)}\right|^2. \quad (19)$$

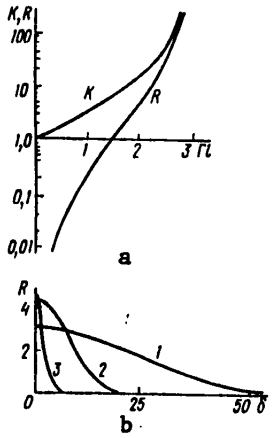

Fig. 2. Reflectivity R and gain K as functions of Γl for $\Delta\vec{k}\cdot\vec{r}=0$ (a), and R as a function of phase detuning δ at $\Gamma l=0.2$ (*1*, 10^3R), 0.6 (*2*, 10^2R) and 2 (*3*, R) (b)

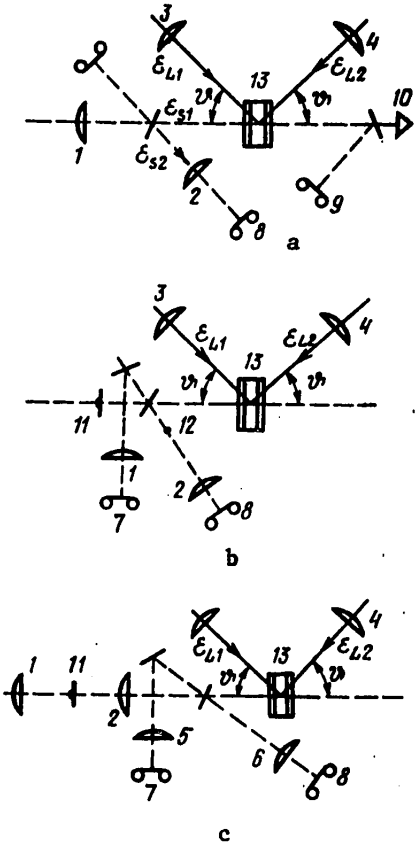

Fig. 3. Optical arrangements for measuring reflectivity of the Stokes signal (a), investigating reproduction of amplitude distribution (b) and wavefront reversal (c) with four-wave interaction (the broken lines show the Stokes beams, and the solid lines show the pumping beams)

Fig. 2 shows conductivity and gain as functions of Γl for case $\Delta\vec{k}\cdot\vec{r} = 0$, and R as a function of phase detuning $\delta = 4k_L \sin\theta_0\Delta\theta/\Gamma$ ($\Delta\theta = \theta - \theta_0$) at identical pumping beam intensities. An increase in the pumping asymmetry parameter β from 0 to 0.2 reduced R in the calculations by no more than 5%.

Thus as a result of four-wave interaction under conditions of phase synchronism one should observe conversion of an incident Stokes wave to a complex-conjugate wave with efficiency determined by the reflectivity (18), (19). Let us note that R may be considerably greater than unity.

Experimental verification of the above arguments was done in the arrangement shown in Fig. 3. The dependence of K and R on the power of the pumping beams and on detuning $\Delta\theta = \theta_0 - \theta$ of the angle of synchronism was studied in the arrangement shown in Fig. 3a. The source of the input Stokes radiation was a benzene Raman laser pumped by ruby laser light with pulse intensity of ~25 ns, emitting the first Stokes component of stimulated Raman scattering. The resultant beam 3-4 mm in diameter was focused by lens 1 ($f_1 = 0.5$ m) into cell with benzene 13 with length $l = 5$ mm. The pumping beams ($\lambda = 0.6943$ μm) were matched to the diameter of the input Stokes radiation beam (~3 mm) by focusing with lenses 3 and 4 ($f = 1$ m).

Focusing was also used to achieve approximate equality of the angular spectrum of all beams ($\theta' \cong 5\cdot10^{-3}$ rad) since the Stokes radiation and pumping were multimode. The pumping emission energy in one beam reached ~0.4 J, pumping asymmetry β did not exceed 0.25. Photographic films 7 and 9 placed at the focus of lenses 1 and 2 recorded the distribution of radiation in the far zone for the incident and reflected Stokes beams. The energy of the Stokes radiation passing through the cell was recorded by calorimeter 10 and film 9. The total energy in the incident and reflected beams was determined by integrating the distributions recorded on film. The radiation of the pumping beams was coupled into the cell at angles of θ and $\pi - \theta$ to the direction of the incident Stokes beam. The angle was set by a 2T2 theodolite with accuracy no worse than ~1'.

The reproduction of amplitude distribution of the incident Stokes radiation in the reflected beam was studied in an arrangement analogous to that of Ref. 9, 10 (Fig. 3b). A parallel beam of Stokes radiation passed through transparency 11 made in the form of an opaque letter K (letter size ~1 mm, characteristic line size ~0.2 mm). The image 12 of the transparency was transferred by lenses 1 and 2 to films 7 and 8, recording the incident and reflected Stokes beams respectively.

Wavefront reversal with phase modulation of the incident Stokes beam was studied by the arrangement shown in Fig. 3c [Ref. 9, 10]. In this case, transparency 11 was placed in the common focal plane of lenses 1 and 2 that formed a telescope. The distribution of the incident and reflected Stokes radiation in the far zone was recorded by lenses 5 and 6, and by films 7 and 8. In this arrangement, wavefront reversal should show up as rotation of the image of the transparency through 180° in the reflected beam with respect to the image in the incident beam.

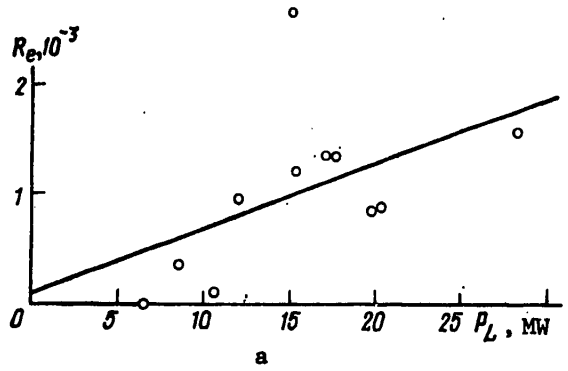

Fig. 4. Experimental values of energy-density reflectivity R_e as a function of maximum total pumping power P_L for $\theta_0 = 21°36.5'$; solid line shows the approximation by a linear function plotted by the method of least squares (a). The experimental values of R_e as a function of θ (b) at $P_L = 25$ (*1*) and 15 W (*2*), and also the theoretical curve for $\Gamma l = 0.4$ in a scale of 1:4 (*3*)

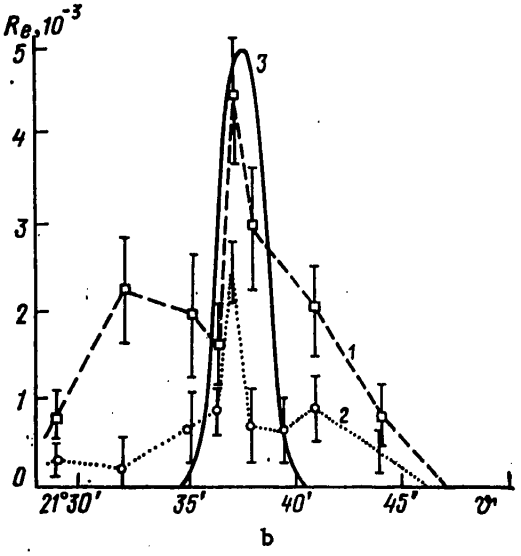

Fig. 4 shows the energy-density reflectivity R_e as a function of the maximum total pumping power ($P_L^{max} = P_{L1}^{max} + P_{L2}^{max}$ where $P_L^{max} = E_L/\tau$, $\tau = \int \varphi(t)dt$, $\phi(t)$ is the pumping pulse shape) for angle $\theta = 21°36.5'$, and also as a function of the angle θ. The quantity R_e was defined as the ratio of maximum energy densities in the reflected and incident Stokes beams. The figure also shows the theoretical dependence of R_e on θ for conditions close to experimental. The maximum on the distribution of $R(\theta)$ is observed at $\theta_0 = 21°37'$.

This value of θ_0 agrees with calculations by formula (10), but differs somewhat from the value of $\theta_0 = 21°24'$ found in Ref. 8. The total width of the maximum $\Delta\theta = 18'$ corresponds to the width of the angular pumping spectrum. The experimental width of the narrow maximum in the dependence $R_e(\theta)$ approximately coincides with the theoretical value of $R_e^{max} = 5 \cdot 10^{-3}$. The gain within the limits of error does not differ from unity. The angular distribution of radiation in the reflected beam is the same as in the incident beam within measurement accuracy (~20%).

The case of amplitude modulation is illustrated in Fig. 5a-c [photo not reproduced], showing patterns in the near zone for the incident Stokes beam, and for the beams reflected from nonlinear and conventional mirrors. It can be seen that the pattern is quite clearly reproduced in the near zone with reflection from the nonlinear mirror; the image of the modulating letter produced by the conventional mirror is blurred since the plane of the image does not coincide with that of the film in this case.

Fig. 5d, e [photo not reproduced] show the patterns in the far zone for incident and nonlinearly reflected beams with phase modulation. It can be seen that the image of the letter K is rotated through 180° relative to the image in the incident beam.

These experimental results in general confirm the theoretical conclusions about the feasibility of wavefront reversal of the Stokes wave in the arrangement described above. For the conditions of the experiment where R_e^{max} is achieved ($G = \Gamma l \cong 0.4$), the theoretical reflectivity $R \cong 2\%$, which is four times the experimental value. This is due to deviation of the experimental conditions from the ideal case of planar waves (multimodal pumping).

Attainment of higher R_e was precluded by the radiation strength of benzene. The use of a nonlinear medium with greater parameter of stimulated Raman scattering gain, with high radiation strength or with small difference between the pumping and Stokes radiation wavelengths (the latter leads to an increase in the interaction length) will give $R \gtrsim 1$. The use of a waveguide also increases the interaction length [Ref. 1], which should give an increase in R.

The results given above also demonstrate that there is a component in the reflected beam that is reversed with respect to the incident wavefront. The fraction of energy of the beam reflected from the nonlinear mirror in the angle that contains 84% of the energy of the incident beam fluctuates from 63 to 80%; therefore it can be assumed that the fraction of Stokes signal energy contained in the reversed wave amounts to 75-95%. The quality of reversal can be evaluated by a quantity analogous to visibility in evaluating contrast of an interference pattern: $\eta = (e - e_m)/(e + e_m)$, where e and e_m are the average exposures outside of an element of the transparency and within its limits. In our experiments, this quantity decreased from $\eta = 0.8$ in the incident beam to $\eta = 0.2$-0.3 in the reflected beam. Better coincidence of general outlines in the far zone of the incident and reflected beams with one another as compared with the details of the transparency is an indication of better reproduction of the low-frequency part of the spatial spectrum; quality of reproduction of the high-frequency part is much poorer. This is apparently due to the poor quality of the spatial spectrum of pumping radiation, which precludes satisfaction of the condition of phase synchronism for the entire spectrum of the incident radiation. Actually, the angle that characterizes diffraction by elements of the transparency that is used is about 15', and the width of the maximum on the experimental curve for $R_e(\theta)$ at a level of 20% of the base is also equal to 15'.

REFERENCES

1. Zel'dovich, B. Ya., Popovichev, V. I., Ragul'skiy, V. V., Fayzullov, F. S., PIS'MA V ZHURNAL EKSPERIMENTAL'NOY I TEORETICHESKOY FIZIKI, Vol 15, 1972, p 160.

2. Stepanov, B. I., Ivakin, Ye. V., Rubanov, A. S., DOKLADY AKADEMII NAUK SSSR, Vol 196, 1971, p 567.

3. Hellwarth, R. W., J. OPT. SOC. AMER., Vol 67, 1977, p 1.

4. Nosach, O. Yu., Popovichev, V. I., Ragul'skiy, V. V., Fayzullov, F. S., PIS'MA V ZHURNAL EKSPERIMENTAL'NOY I TEORETICHESKOY FIZIKI, Vol 16, 1972, p 617.

5. Borisov, Yu. N., Kruzhilin, Yu. I., Shklyarik, S. V., PIS'MA V ZHURNAL TEKHNICHESKOY FIZIKI, Vol 4, 1978, p 160.

6. Pilipetskiy, N. F., Popovichev, V. I., Ragul'skiy, V. V., PIS'MA V ZHURNAL EKSPERIMENTAL'NOY I TEORETICHESKOY FIZIKI, Vol 27, 1973, p 619.

7. Akhmanov, S. A., Khokhlov, R. V., "Problemy nelineynoy optiki" [Problems of Nonlinear Optics], Moscow, VINITI [All-Union Institute of Scientific and Technical Infromation], 1964.

8. Vokhnik, O. M., Odintsov, V. I., PIS'MA V ZHURNAL TEKHNICHESKOY FIZIKI, Vol 5, 1979, p 407.

9. Dolgopolov, Yu. V., Komarevskiy, V. A., Kormer, S. B., Kochemasov, G. G., Kulikov, S. M., Murugov, V. M., Nikolayev, V. D., Sukharev, S. A., ZHURNAL EKSPERIMENTAL'NOY I TEORETICHESKOY FIZIKI, Vol 76, 1979, p 908.

10. Sokolovskaya, A. I., Brekhovskikh, G. A., Kudryavtseva, L. D., DOKLADY AKADEMII NAUK SSSR, Vol 237, 1977, p 557.

11. Bespalov, V. I., Betin, A. A., Dyatlov, A. I., Kulagina, S. N., Manishin, V. G., Pasmanik, G. A., Shilov, A. A., ZHURNAL EKSPERIMENTAL'NOY I TEORETICHESKOY FIZIKI, Vol 79, 1980, p 378.

6610
CSO: 1862/133

UDC 621.378.325+537.523.9+533.915

STEADY-STATE THEORY OF OPTICAL STRIATIONS

Moscow KVANTOVAYA ELEKTRONIKA in Russian Vol 9, No 2(116), Feb 82 (manuscript received 18 Mar 81) pp 274-284

[Article by V. V. Breyev, L. A. Knizhnikova and A. F. Nastoyashchiy, Institute of Atomic Energy imeni I. V. Kurchatov, Moscow]

[Text] An examination is made of a steady-state theory of the laminar plasma column of a long laser spark. Modulation solutions of the steady-state problem are found and their stability is studied. Based on approximate analysis and numerical modeling results, general conditions are formulated for the existence of metastable optical striations. As a rule, the most long-lived are states with maximum possible amplitude of spatial temperature oscillations. A numerical solution of the problem is found for the case of a laser spark in air. When dust motes are present in air, each of them may become a center of nucleation of a striation; in this event the configuration of the striations will be chaotic.

1. Introduction

Let us assume that an extended plasma column has been set up in a gas. For the sake of simplicity we will assume that the column has cylindrical symmetry and its length is much greater than its radius. Let us consider the dynamics of behavior of the plasma column when it is exposed to intense laser emission. As was demonstrated in Ref. 1, in the case of weak ionization of the gas in a plasma column, a lengthwise homogeneous state of the optical discharge becomes impossible; the instability that arises leads to breakup of the plasma column into a chain of alternating "hot" and "cool" layers with considerably differing degree of gas ionization ("optical striations").

When the coefficient of absorption of laser radiation is exponentially dependent on temperature, the instability is explosive, i. e. formation of the hot layers is a self-accelerating process [Ref. 1]. Therefore it is to be expected that the development of an instability may slow down only in the case of nearly total ionization of the gas, when the absorption of light is determined by Coulomb collisions, and consequently the coefficient of absorption

is a decreasing function of temperature. It is also obvious that the states that arise should be distinguished by deep modulation of temperature, and especially of ionization in the direction of laser beam propagation.

It is natural to raise the question of whether the resultant laminar structure of the plasma column is stable (and whether the optical striations that arise are long-lived), and under what conditions. It is also clear that we are dealing with a strongly nonlinear problem where approximate analytical methods are ineffective. Therefore it becomes necessary to use numerical methods. Instead of solving the unsteady problem, a steady-state approach is used below that consists in finding steady-state solutions for a laminar column and simultaneously studying their stability. In doing this, use is made of both approximate analytical methods based on model representations of the coefficient of absorption and numerical modeling of optical striations. The combination of these two approaches enables a more complete understanding of the conditions of formation of optical striations, and also formulation of fairly general considerations on stability of a laminar plasma column in a laser radiation field.

2. Physical Formulation of the Problem

There are several possible methods of producing a plasma channel in a gas: electric explosion of a conductor, optical breakdown in the gas (or explosion of dust motes in a laser field with subsequent formation of a "halo" [Ref. 2] of ionization around each of them) and so on. Let us discuss the second method. We will assume that the gas is illuminated sequentially by two laser pulses: a short but intense "penetrating" pulse, and a pulse that is extended in time (Fig. 1).

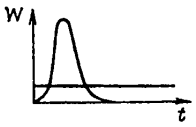

Fig. 1. laser pulse shape

In experiments (see e. g. Ref. 4, 5), the laser pulse frequently consists of a main spike and an extended tail in which a considerable part of the radiation energy is stored.

Let us recall that to set up a long laser spark in gas one ordinarily uses weakly focused laser beams in which the power density as a rule considerably exceeds the threshold value for gas breakdown: $w > w_n$. When these two conditions are met, propagation of the ionization boundary takes place in the breakdown wave state [Ref. 2], which ensures formation of an extended plasma column [Ref. 3].

The long laser pulse "catches up" with the ionization that arises after passage of the breakdown wave (or with the chain of ionization foci from individual dust motes [Ref. 5]) in the plasma column, and maintains this ionization for the required time. In the case of a long laser spark it can be assumed that the parameters of the laser beam in the direction of propagation remain unchanged for distances that are large compared with the transverse dimensions of the beam. This is in fact the physical definition of a "long spark."

It is useful to note that the laser emission power density needed for maintaining ionization in the plasma column is usually several orders lower than the threshold level for gas breakdown [Ref. 2].

Let us make some estimates. At gas pressures $p \sim 1$ atm, the temperatures of electrons and ions in the breakdown plasma are equalized in time $\tau_E \sim 1$ ns. Therefore with a sufficiently long laser pulse the electron temperature separation can be considered insignificant. At the same time, steady-state electron temperature separation usually necessitates high radiation power densities in the auxiliary pulse. Equalization of gas pressure across the plasma column and cooling of the plasma by heat exchange with the ambient cool gas take place in times $\tau_p \sim r_0/s$ and $\tau_\chi \sim r_0^2/\chi$ respectively, where r_0 is the radius of the laser beam, s is the speed of sound and χ is thermal diffusivity of the plasma. For air at atmospheric pressure at temperature $T \sim 10$ kK, assuming $s \sim 1$ cm/s, $\chi \sim 100$ cm^2/s and $r_0 \sim 0.1$ cm, we will have $\tau_p \sim 1$ and $\tau_\chi \sim 100$ μs. Thus even at relatively small laser beam radii $r_0 \gg 100$ μm, plasma cooling takes place relatively slowly. During time $\sim\tau_\chi$ noticeable ionization is also retained in the plasma; upon activation of the auxiliary laser pulse, the state of ionization in the plasma column can be maintained for a considerable length of time.

We will assume that gas pressure is equalized across the plasma column more rapidly than heat exchange takes place with the ambient cool gas. In this case, the equation of heat balance of the plasma column can be written as

$$C_p \frac{\partial T}{\partial t} = \frac{\partial}{\partial x} \lambda \frac{\partial T}{\partial x} + \mu_\omega w - \frac{1}{r_{\vartheta\phi}^2} \int_0^T \lambda dT, \qquad (1)$$

where C_p is the specific heat of the gas at constant pressure, λ is the coefficient of thermal conductivity, w is the laser emission power density, $\mu_\omega = \mu_\omega(N_0, T)$ is the coefficient of absorption of laser emission, N_0 being the density of neutral particles. Heat losses in the direction across the plasma column are accounted for in (1) by model term $r_{\vartheta\phi}^{-2} \int_0^T \lambda dT$ ($r_{\vartheta\phi}$ is the diffusion radius). Such an approximation is completely acceptable, at least for air [Ref. 2]. Model equation (1) is quite convenient for explaining the physical peculiarities of the problem.

The coefficient of absorption of laser radiation in the heated gas as a rule has a maximum at some temperature T*. For air at atmospheric pressure and neodymium laser radiation the curve of $\mu_\omega(T)$ takes the form shown on Fig. 2 [Ref. 2]. In principle, there are two possible steady states† of a plasma column: a "high-temperature" state with $T = T_0'' > T^*$, and a "low-temperature" state with $T = T_0 < T^*$. The first state is realized with complete ionization of the gas, and as implied by the results of Ref. 1, it will remain homogeneous in the direction of laser beam propagation. Otherwise we are dealing with the low-temperature regime where the degree of ionization of the gas in the column is less than unity; in this event the homogeneous state of the plasma column is impossible. The resultant stratification of the plasma column is

†In a strict sense, the term "steady-state" applies only to the case of a plasma column bounded by material walls with infinite specific heat. For a plasma filament in gas it would be more correct to use the term "quasi-steady state."

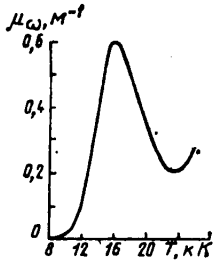

Fig. 2. Coefficient of absorption of laser radiation with wavelength of 1.06 μm in air at atmospheric pressure as a function of temperature

outwardly similar to the usual striations in a positive glow-discharge column, although the nature of the instability and the conditions of arisal of the striations are different.

3. Steady-State Theory of Optical Striations

Steady-state temperature distribution in a laminar plasma column must satisfy the equation

$$\frac{d}{dx}\lambda\frac{dT}{dx}+F(T)=0, \qquad (2)$$

where the function of the heat source is

$$F(T)=\mu_\omega(T)\,w-r_{s\phi}^{-2}\int_0^T\lambda dT. \qquad (3)$$

The second term in (3) accounts for heat losses from the plasma column to the ambient gas with temperature taken to be zero for the sake of simplicity. Thus as a result our assumptions give us a unidimensional model that in addition retains the main peculiarities of the problem. It is appropriate to recall that a unidimensional approximation has been used frequently in the literature: in problems of plasma "combustion" in a laser radiation field [Ref. 2], when considering striations in a positive column [Ref. 6], in studies of a thermonuclear combustion wave in a bounded plasma [Ref. 7] and elsewhere.

The heat conduction λ of an ionized gas is ordinarily a nonlinear function of temperature, and therefore the coefficient λ cannot be brought outside of the differential sign. In addition to this, by using the elementary substitution of variables $\theta=\int_0^T\lambda dT$ equation (2) can lead to the equation for the potential of heat flux θ:

$$d^2\theta/dx^2+F(\theta)=0,$$

which coincides in form with (2) when $\lambda=1$. Consequently, accounting for the dependence $\lambda(T)$ does not introduce anything fundamentally new. Therefore we will use for simplicity equation (2) with constant thermal conductivity:

$$\lambda\frac{d^2T}{dx^2}+F(T)=0. \qquad (4)$$

In recording the boundary conditions, we use the cyclic form

$$\left(\frac{dT}{dx}\right)_{x=0}=\left(\frac{dT}{dx}\right)_{x=L}\equiv 0, \qquad (5)$$

where $x=0$ and $x=L$ denote points at which the temperature reaches the minimum (T_1) and maximum (T_2) values.

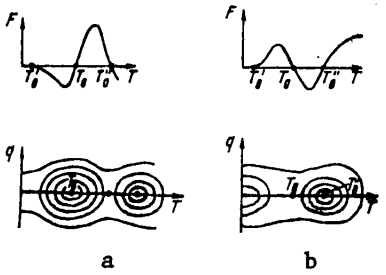

a b

Fig. 3. Family of integral curves of equation (6)

We can readily see that the problem of finding the temperature field becomes completely unambiguous only after assignment of space period 2L. However, since the quantity L itself is also to be determined, the problem is not closed; there are different solutions that are distinguished by their space period.

Using the phase plane method, let us map the family of integral curves (Fig. 3) of the equation

$$dq/dT=-F(T)/(\lambda q), \qquad (6)$$

where $q = dT/dx$.

The nature of behavior of the curves on Fig. 3 depends on the form of function F(T). The points of intersection of curve F(T) with the axis of abscissas T_0, T_0',... correspond to spatially homogeneous solutions. States with $T = T_0$ (Fig. 3a) and $T = T_0''$ (Fig. 3b)† are unstable with respect to small perturbations.

As we can see from Fig. 3, there is a set of periodic solutions of equation (4) that satisfy boundary conditions (5), including closed curves that enclose two singular points (two centers, see Fig. 3a). Thus the question of what states of the laminar column should be observed in an experiment remains open. In this connection it is suggested that the steady-state theory be supplemented by a principle of solution sorting based on studying the stability of laminar structures.

Two possibilities can be imagined. 1. Among the periodic solutions that have been found there are those that correspond to the stable (or metastable) state of the system. In this case, one should observe stationary striations with parameters that are constant or slowly varying in time. 2. In the second case, where there are no stable states, the parameters of the laminar column will apparently be inconstant in time.

Let us now turn to investigation of the stability of the laminar column. Assuming that T_1 (or T_2) is given, we find the space-periodic solution $T(x + 2L) = T(x)$ from (4), (5). Temperature perturbation can be represented as

$$T'(x,\ t)=T'(x)\exp(\Gamma t). \qquad (7)$$

After substituting (7) in the equation of unsteady heat conduction (1), we will have (coefficients C_p and λ are taken as constants for the sake of simplicity)

†Point T_0'' may correspond for example to the state of the plasma pertaining to the second maximum of the function $\mu_\omega = \mu_\omega(T)$ [Ref. 2].

$$d^2T'/dx^2 + [E - V(x)]\,T' = 0, \tag{8}$$

where $E = -\Gamma/\chi$ and $V(x) = -\lambda^{-1}dF/dT$. Equation (8) coincides in form with the Schrödinger equation for a particle in a periodic field $V(x+2L) = V(x)$, the quantity Γ being proportional to the energy of a particle with the opposite sign. $E = 0$ corresponds to the boundary of unstable states.

According to Bloch's theorem [Ref. 8] the solution of equation (8) with periodic potential can be represented in the form

$$T'_k(x) = u_k(x)\, e^{ikx}, \tag{9}$$

where k is the wave vector (quasi-momentum) of the particle, $u_k(x)$ is a periodic function, $u_k(x+2L) = u_k(x)$. The energy spectrum of the particle in a periodic field consists of a sequence of forbidden and allowed energy bands ("zones"), $k = 0$ corresponds to the lower edge of the energy band.

The boundary conditions for function (9) would, generally speaking, have to be assigned on the ends of the plasma column; unfortunately, this considerably complicates solution of the problem. Instead of this, we use cyclic boundary conditions (Born-Kármán conditions [Ref. 8]). It is assumed that the plasma column consists of a large number (N>>1) of sequentially arranged identical striations, and the influence of perturbations caused by the end striations extends no further than the nearest neighbors. In virtue of the identical conditions on both ends of the column $T'(x+2NL) = T'(x)$ or with consideration of (9), $\exp(2ikNL) = 1$, whence $k = \pi m/LN$ (m is an integer), i. e. when N>>1 there is a discrete set of closely spaced values of k.

Then in the periodic potential the functions $u_k(x)$ should have a certain parity.

Of greatest interest from the standpoint of instability is the ground state (with least energy), since the maximum increment corresponds to this state. The wave function of the ground state is even [Ref. 9], and hence

$$(du_0/dx)_{x=0} = (du_0/dx)_{x=L} \equiv 0. \tag{10}$$

It should be required in turn for odd functions that $(u_0)_{x=0} = (u_0)_{x=L} \equiv 0$.

Thus the stability problem reduces to finding the eigenvalues of equation (8) with boundary conditions (10). In the general case, such a problem can be solved numerically. At the same time, some general remarks can be made about the stability of a laminar plasma column. Let us assume that function F(T) near the point of stable equilibrium T_0 is linear, i. e. $F(T) = a(T - T_0)$, $a > 0$. Function V(x) in this case is a potential well with constant depth $V_0 = a/\lambda$. With accuracy to $\sim(NL)^{-2}$ for the lower state we have $E = -a/\lambda$, i. e. the fundamental mode will increase in accordance with the law

$$T = T'_0(x) \exp(at/C_p). \tag{11}$$

Higher modes with $k \neq 0$ rise at a slower rate. As we can plainly see, result (11) coincides with the conclusions of the linear theory of instability for a spatially homogeneous state.

Exponential behavior (11) of rising perturbations holds until the temperature oscillations go beyond the limits of the linear section of F(T). With a further increase in percentage modulation, the pace of the instability slows if $d^2F/dT^2 < 0$, and speeds up otherwise. Actually, in the former case there will be sections of less depth ("hills") that arise in the potnetial well, increasing the energy level; contrariwise, when $d^2F/dT^2 > 0$, "valleys" appear that lower the energy of the particle.

As the plasma is heated by laser emission, F(T) usually (see Fig. 3) is a nonmonotonic function of temperature; therefore beginning at some value of T, $dF/dT < 0$, and consequently the function V(x) is a sequence of wells of finite length separated by hills with $V > 0$. The width of the hills increases with increasing amplitude of the oscillations, which reduces the increments. It may turn out that at a sufficiently high percentage modulation the increments of instability become so small that the resultant periodic structure will be long-lived (metastable). The influence of two-dimensional effects associted with the finite radius of the plasma column ensures additional stability of the laminar column (see below).

4. Approximate Model and Conditions of Arisal of Stable Optical Striations

It is convenient to study the typical peculiarities of the problem on the basis of simplified models. Let us assume that the function of the heat source can be represented by a broken curve (Fig. 4), i. e.

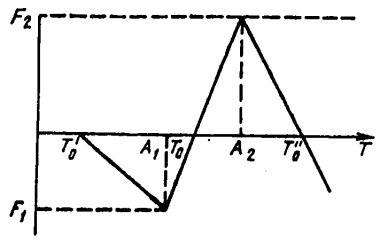

Fig. 4. Model function F(T)

$$F(T) = -\lambda k_0^2 (T - T_0'), \quad T_0' \leqslant T \leqslant A_1, \tag{12}$$

$$F(T) = \lambda k_1^2 (T - T_0), \quad A_1 \leqslant T \leqslant A_2, \tag{13}$$

$$F(T) = -\lambda k_2^2 (T - T_0''), \quad A_2 \leqslant T < \infty. \tag{14}$$

The meaning of symbols k_0, k_1, k_2 is clear from Fig. 4.

The solution of equations (4) with consideration of boundary conditions (5) in the corresponding regions takes the form

$$T = T_0' + (T_1 - T_0') \operatorname{ch} k_0 x, \tag{15}$$

$$T = T_0 + B_1 \sin k_1 (x - x_0), \tag{16}$$

$$T = T_0'' + (T_2 - T_0'') \operatorname{ch} k_2 (x - L). \tag{17}$$

Coordinate x_0 marks the point where the temperature assumes its equilibrium value T_0. From the condition of continuity of temperature and its derivative at points ($x = x_1$, $T = A_1$) and ($x = x_2$, $T = A_2$) we get six conditions for three unknown amplitudes and four coordinates x_0, x_1, x_2 and L:

$$k_1 \operatorname{th} k_0 x_1 + k_0 \operatorname{ctg} k_1 (x_1 - x_0) = 0, \tag{18}$$

$$k_1 \text{th}\, k_2(x_2 - L) + k_2 \text{ctg} k_1(x_2 - x_0) = 0, \quad (19)$$

$$F_2 \sin k_1(x_1 - x_0) + F_1 \sin k_1(x_2 - x_0) = 0, \quad (20)$$

$$(T_1 - T_0')^2 - (A_1 - T_0')^2 + k_1^2 k_0^{-2}[B_1^2 - (A_1 - T_0)^2] = 0, \quad (21)$$

$$(T_2 - T_0')^2 - (A_2 - T_0')^2 + k_1^2 k_2^{-2}[B_1^2 - (A_2 - T_0)^2] = 0, \quad (22)$$

where

$$B_1 = (A_1 - T_0)/\sin k_1(x_1 - x_0); \quad (23)$$

in (20) F_1 and F_2 are the values of the corresponding function at points A_1, A_2, i. e. $F_{1,2} = F(A_{1,2})$.

As pointed out above, the stability of the periodic solutions increases if the temperature oscillations go beyond the limits of interval (A_1, A_2). An exemplary graph of the periodic potential for this case is shown on Fig. 5. (The corresponding solid-state model is called the Kronig-Penny model [Ref. 8]). From equations (8), (10), by way of addition to system (18)-(23) we get two more conditions

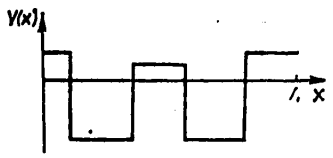

Fig. 5. Periodic potential for source function of Fig. 4

$$k_0^* \text{th}\, k_0^* x_1 + k_1^* \text{tg}\, k_1^*(x_1 - x_0^*) = 0, \quad (24)$$

$$k_2^* \text{th} k_2^*(x_2 - L) + k_1^* \text{tg}\, k_1^*(x_2 - x_0^*) = 0, \quad (25)$$

where x* is the point where the wave function† is maximum. (In getting solutions it is convenient to use the properties of symmetry of the initial equations with respect to the operation of inversion.)

The values of k_0^*, k_1^* and k_2^* in (24) and (25) are related to the energy of the level $E_\parallel$ by the expressions

$$k_{0,2}^{*2} = k_{0,2}^2 - E_\parallel, \quad k_1^{*2} = k_1^2 + E_\parallel. \quad (26)$$

Let us take note of one important circumstance. In the equation for temperature the influence of two-dimensional effects was accounted for by the model term $\lambda T/r_{\text{эф}}^2$, whereas this is insufficient for analysis of the instability of the resultant solutions. In fact, when studying stability it would be more correct to start from the very beginning with the two-dimensional formulation of the problem having cylindrical symmetry:

$$\frac{\partial^2 T'}{\partial x^2} + \frac{1}{\rho}\frac{\partial}{\partial \rho}\rho\frac{\partial T'}{\partial \rho} + [E - V^+(x, \rho)]T' = 0, \quad (27)$$

where $V^+ = w d\mu_\omega/dT$ is the two-dimensional potential.

Boundary conditions (10) must be supplemented by the conditions

---

†Using quantum-mechanical analogy, for the sake of convenience we will call the eigenfunctions "wave functions", and the corresponding eigenvalue E will be called the "particle energy."

$$\left(\frac{\partial T'}{\partial \rho}\right)_{\rho=0} = (T_1)_{\rho=r_{s\Phi}} \equiv 0. \tag{28}$$

Substituting the unknown solution in form

$$T'(x, \rho) = u(x)\, R(\rho) \tag{29}$$

in (27), we can reduce the problem to the one-dimensional case, where $E_\parallel$ will be replaced by the difference $E - E_\perp$, where $E_\perp > 0$ is the energy of transverse motion of the particle, which does not necessarily coincide with $r_{s\Phi}^{-2}$. In fact, in the general case, $V^+(\rho)$ is negative only in region $r_1 \leqslant \rho \leqslant r_2$, where r_1 and r_2 are the coordinates at which the temperature takes the values A_1 and A_2 respectively; over the remaining range of ρ we have $V^+(\rho) > 0$.

Thus the condition of stability within the framework of the one-dimensional model adopted above takes the form

$$E = E_\parallel + \Delta E_\perp \geqslant 0 \quad (\Delta E_\perp = E_\perp - r_{s\Phi}^{-2}). \tag{30}$$

It is convenient to solve system of equations (18)-(25) in the following order. By assigning some value of T_1, we find T_2 and B_1 from equations (21), (22), and then we find $k_1(x_1 - x_0)$, $k_1(x_2 - x_0)$, $k_0 x_1$ and $k_2(x_2 - L)$ in sequence from (23), (20), (18) and (19). This gives the distribution $T = T(x)$. We get the values of x^* and $E_\parallel$ from equations (24), (25) together with condition (26). (The appropriate calculations can be done without using a computer.) The question of stability of the resultant periodic solution can be answered, strictly speaking, only if the temperature distribution is given along the radius of the plasma column.

Consider a simple example. Assuming $k_0 = k_2 \equiv k$ and $F_2 = F_1$, we verify that $F(T)$ in this case is an odd function of difference $(T - T_0)$. At $E_\parallel = 0$ from equations (18)-(20) and (24), (25) we get $x_1 + x_2 = 2x_0, L$ and $\operatorname{th} k_0 x_1 = -\operatorname{th} k \times (x_2 - L)$. The latter equality is satisfied only at the limit $x_1 \to \infty$, $x_2 - L \to -\infty$, while the distance between points x_1 and x_2 remains finite. From (21), (22) we also find $T_1 = T_0'$ and $T_2 = T_0''$. Thus the temperature profile $T = T(x)$ consists of a finite section $x_2 - x_1$ on which T changes in accordance with (16) from A_1 to A_2, and of rather extensive "tails." With small changes in the parameters of the plasma column, including for example when $E_\parallel \neq 0$, the space period becomes finite.

The nature of the resultant solutions becomes clear if we refer to the mechanical analog (see Fig. 1c of Ref. 1). Actually, since the potential energy U of a "particle" and its derivative disappear at points T_1 and T_2, the particle will spend a long time in the process of oscillations near points T_1, T_2 (wide soliton [Ref. 12]). In view of the considerable spatial separation between two neighboring solitons, interaction between them practically disappears; as a consequence, the periodic nature of the laminar column will obviously be destroyed in this case.

The given example is notable in the respect that the stability boundary is attained even in the one-dimensional approximation, i. e. without considering

corrections $\Delta E_\perp$ for the energy of transverse motion of the particle. This conclusion is derived on the basis of the simplest model of the problem. Together with this, physical arguments of a more general nature can be given to support the conclusion. In the case of deep modulation of temperature, when T_2 is appreciably greater than the temperature at which F(T) is maximum, potential function V(x) within the limits of one period will consist of two separate wells. When there is a considerable distance between wells† the overlap of wave functions, and hence the splitting of energy levels will be small [Ref. 9]. Using the Barenblat-Zel'dovich method [Ref. 10]‡ we can verify that the ground state has energy $E_\parallel \cong 0$. As the wells get closer together, i. e. as the space period decreases, the energy level splits, one of the half-levels shifting into region $E_\parallel < 0$, generating an instability. At the same time, when a striation is very long the splitting will be minor, and consequently the instability will be stabilized, for example through a correction $\Delta E_\perp \neq 0$. Thus the stability of a laminar plasma column can be ensured only with deep modulation of the temperature and with a long striation.

In Ref. 11, self-similar solutions of equation (1) for a heat source of type $F(T) = q_0 T^\beta$ were considered. It can be concluded from the arguments given above that stable steady-state structures for a monotonic source function cannot arise even if the equilibrium steady state exists, e. g. for a function of the form $F = q_0 (T - T_0)^\beta$. Actually, when $q_0 > 0$ and $\beta > 0$, the potential function $V(x) = -\beta q_0 T(x)^{\beta-1}$ will be negative everywhere, and consequently the corresponding state will be unstable since there is always a bound state of the particle in a one-dimensional well [Ref. 9].

5. Numerical Modeling of Optical Striations

To find the steady-state temperature field in optical striations, we will start with a one-dimensional model in which heat exchange of the plasma column with the ambient gas is taken into consideration as above by the model term $\lambda T / r_{э\phi}^2$. In connection with the fact that there is actually a set of periodic solutions of the problem that differ in percentage modulation and space period, we will use a principle of solution sorting that is based on studying the stability of the resultant laminar column. If the optical striations are formed as a result of instability of an initially homogeneous plasma column, the consequent final steady state can be found from the condition that the nonlinear increment is equal to zero. It may turn out that even with the deepest temperature modulation the increment does not vanish; apparently in this case the striations should be irregular, and the state of the laminar column will be inconstant in time.

---

†As a rule, the distance between wells that belong to adjacent striations is even greater.

‡The method of Ref. 10 is as follows. Differentiating equation (4) with respect to x, we get an equation for function $\psi = dT/dx$ that coincides with (8) at $E_\parallel = 0$. Since function ψ does not have nodes within the limits of a well, we can conclude from this that the state with $E_\parallel = 0$ is the ground state.

Our numerical analysis will be based on two equations: an equation that describes the temperature distribution lengthwise of the column,

$$\lambda \frac{d^2T}{dx^2} + F(T) = 0, \quad \left(\frac{dT}{dx}\right)_{x=0} = \left(\frac{dT}{dx}\right)_{x=L} \equiv 0, \tag{31}$$

and an equation for eigenfunctions of perturbation of temperature T'(x):

$$\frac{d^2T'}{dx^2} + [E_\parallel - V(x)]\,T' = 0; \left(\frac{dT'}{dx}\right)_{x=0} = \left(\frac{dT'}{dx}\right) \equiv 0. \tag{32}$$

It is advisable to limit ourselves to solution of equations (31), (32) within the limits of one half-period, using cyclic boundary conditions and properties of symmetry of the equations relative to the operation of inversion.

If $E = E_\parallel + \Delta E_\perp < 0$, the state of the system is unstable. When $E = 0$, the instability stops growing.

Let us present the algorithm used in solving the formulated problem. The initial equations are written as a system of first-order equations:

$$\frac{dT}{dx} = \eta, \quad \lambda \frac{d\eta}{dx} = -F(T); \tag{33}$$

$$\frac{dT'}{dx} = v, \quad \frac{dv}{dx} = (V - E_\parallel)\,T'. \tag{34}$$

The Cauchy problem is formulated with initial conditions

$$(T)_{x=0} = T_1, \; (\eta)_{x=0} = 0; \; (T')_{x=0} = 0, \; (v)_{x=0} = 0. \tag{35}$$

For selected values of T_1 and $E_\parallel$ as a result of numerical integration of initial system of equations (33), (34) we find the point $x = L > 0$ at which the condition $\eta = 0$ is satisfied. Sorting through the values of parameter $E_\parallel$, we attempt to simultaneously satisfy the condition $v = 0$ at this point (we must also be careful that function T' does not have nodes in the interval $0 < x < L$). In this way, the values of T_2, L and $E_\parallel$ are found as a function of percentage modulation of T_1. The stability boundary is found from the condition $E = E_\parallel + \Delta E_\perp = 0$. (In connection with the fact that when $T_2 > T^*$, where T* is the root of equation $(dF/dT)_{T=T^*} = 0$, the quantity $|E_\parallel|$ decreases rapidly with increasing T_2, the results in some cases are not very sensitive to the method of estimating $\Delta E_\perp$.)

Most experiments on observation of long laser sparks have been done in atmospheric air (under laboratory conditions [Ref. 3, 5] or in the open air [Ref. 4]). Therefore it is of interest to calculate the structure of the plasma column of a laser spark in air. To do this, we use calculations of the coefficient of absorption based on the Biberman-Norman formula (the corresponding graph of $\mu_\omega(T)$ can be found for example in Ref. 2).

An example of numerical calculation for air at pressure p = 1 atm is shown on Fig. 6. The results correspond to neodymium laser emission power of 1 MW

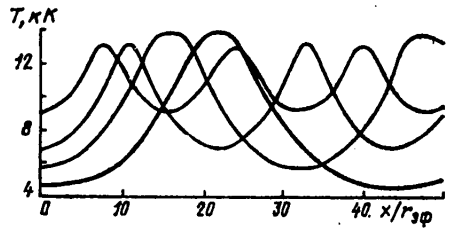

Fig. 6. Temperature modulation along plasma column

(or carbon dioxide laser power of about 10 kW). With increasing modulation amplitude there is an increase in the space period of the striations and a reduction in the increment of instability. Most long-lived are states with very deep modulation, where the temperature oscillates lengthwise of the plasma column between values of $T_1 \cong 4$ and $T_2 \cong 14$ kK (degree of ionization varies from $\sim 10^{-5}$ to ~1). Visually one should observe brightly luminescing layers of small dimensions separated by cool intermediate layers of considerable length. This pattern may be masked in part by an "ionization halo" arising next to each hot layer [Ref. 2].

An estimate of the correction to level energy E that accounts for two-dimensional effects shows that the resultant solution with deep modulation may be stable (or metastable). Calculations have shown that additional stability (or destabilization) of optical striations may result from small perturbations such as transport of the energy of self-radiation in the plasma, finite divergence of the laser beam, change in power of the laser pulse with time and the like. For example, laser illumination of the plasma column with power that decreases in time and $dC_p/dT < 0$ gives rise to additional stabilization of optical striations.

Atmospheric air always contains dust motes that are destroyed when exposed to laser radiation. After the dust motes are broken down in dense vapor [Ref. 13] each of them becomes a focus of ionization. Further evolution of the plasma cloud will depend on the initial size of a particle, its composition and the power density of laser irradiation. The largest motes may become a center of nucleation of striations. Naturally, the configuration of the striations will be chaotic. The remarks made above about the stability of striations apply in equal measure to these conditions since the interaction between neighboring striations is insignificant in the most interesting case of soliton-like solutions. (With high concentration of dust motes in air, overlapping of plasma foci from individual motes may make itself felt, which has been experimentally observed [Ref. 5].)

In conclusion let us note that the feasibility of comparing the numerical results with experimental data rests finally on the reliability of the cross sections used in the calculations (including coefficients of absorption of laser emission and so on). This applies primarily to conclusions about the lifetime of the striations that are formed, i. e. the question about whether the observed striations under given specific conditions will be regular (whether they will be like the standing striations in the positive column of a glow discharge [Ref. 6]), or whether the instability gives rise to hot layers that are chaotically configured along the laser spark and that have parameters fluctuating in time. At the same time, the very existence of

optical striations stems from fairly general physical considerations, and therefore it is to be hoped that we will soon have experimental observations of their formation.

REFERENCES

1. Nastoyashchiy, A. F., KVANTOVAYA ELEKTRONIKA, Vol 8, 1981, p 220.

2. Rayzer, Yu. P., "Lazernaya iskra i rasprostraneniye razryadov" [Laser Spark and Discharge Propagation], Moscow, Nauka, 1974.

3. Basov, N. G., Boyko, V. A., Krokhin, A. N., Sklizkov, G. V., DOKLADY AKADEMII NAUK SSSR, Vol 173, 1967, p 538.

4. Parfenov, V. A., Pakhomov, L. Ye., Petrun'kin, V. Yu., Podlevskiy, V. A., PIS'MA V ZHURNAL TEKHNICHESKOY FIZIKI, Vol 2, 1976, p 731; Vol 4, 1978, p 460.

5. Zakharchenko, S. V., Sintyurin, G. A., Skripkin, A. M., PIS'MA V ZHURNAL TEKHNICHESKOY FIZIKI, Vol 6, 1980, p 1065.

6. Nedospasov, A. V., Khait, V. D., "Kolebaniya i neustoychivosti nizkotemperaturnoy plazmy" [Fluctuations and Instabilities of Low-Temperature Plasma], Moscow, Nauka, 1979.

7. Nastoyashchiy, A. F., Shevchenko, L. P., ATOMNAYA ENERGIYA, Vol 32, 1972, p 451.

8. Peierls, R., "Kvantovaya teoriya tverdykh tel" [Quantum Theory of Solids], Moscow, IL, 1956 [English version, Oxford, 1955].

9. Landau, L. D., Lifshits, Ye. M., "Kvantovaya mekhanika" [Quantum Mechanics], Moscow, Fizmatgiz, 1963.

10. Barenblat, G. I., Zel'dovich, Ya. B., ZHURNAL PRIKLADNOY MATEMATIKI I MEKHANIKI, Vol 21, 1957, p 856.

11. Kurdyumov, S. P., Preprint No 29, Institute of Applied Mathematics, 1979.

12. Kadomtsev, B. V., "Kollektivnyye yavleniya v plazme" [Collective Phenomena in Plasma], Moscow, Nauka, 1976.

13. Bunkin, F. V., Savranskiy, V. V., ZHURNAL EKSPERIMENTAL'NOY I TEORETICHESKOY FIZIKI, Vol 65, 1973, p 21.

6610
CSO: 1862/133

UDC 535.375

WAVEFRONT REVERSAL THEORY FOR RADIATION WITH SPATIALLY INHOMOGENEOUS DISTRIBUTION OF AVERAGE INTENSITY

Moscow KVANTOVAYA ELEKTRONIKA in Russian Vol 9, No 3(117), Mar 82 (manuscript received 28 May 81) pp 548-553

[Article by I. M. Bel'dyugin and I. G. Zubarev, Physics Institute imeni P. N. Lebedev, USSR Academy of Sciences, Moscow]

[Text] Based on a spectral method, an attempt is made at a unified approach to description of the various modifications of wavefront reversal with induced scattering: in a light guide, with lens focusing of spatially inhomogeneous and single-mode radiation. It is shown that this necessitates consideration of a certain correlation between spatial spectral components and decomposition of the pumping field. Approximate solutions are found for the scattered field in the above-mentioned cases.

Principles of the process of wavefront reversal of radiation by stimulated Mandelstam-Brillouin scattering have now been fairly well covered both experimentally [Ref. 1-4] and theoretically [Ref. 5-10]. The result of this research has been formulation of the idea of existence of three modes of observation of wavefront reversal: in a waveguide [Ref. 1-3], and with focusing of multimode [Ref. 2, 4] and single-mode beams in a medium. This division of the effect of wavefront reversal by stimulated Mandelstam-Brillouin scattering into three sub-effects is dictated chiefly by the fact that in qualitative description of the phenomenon, each of the three modifications of wavefront reversal is described on the basis of its own theoretical concepts unrelated to the others.

For example, wavefront reversal in a waveguide is described on the basis of a spectral approach, and use of the fact that the scattering medium for the Stokes wave is an amplitude volumetric hologram that is recorded as a result of the laser beam setting up spatially inhomogeneous negative absorption in the medium on the Stokes frequency [Ref. 5, 6, 10]. This enables one to use volumetric hologram methods to get the pattern of formation of the scattered field correlated with pumping.

In describing wavefront reversal of focused multimode beams, a predetermined form is assigned to the scattered field correlated with pumping (based on

certain reasonable assumptions), and then the increment of amplification of such a field is calculated and the details of its form are refined [Ref. 7, 8]. In this approach, the form of the field correlated with pumping, and thus the judgments on the nature of the process of its amplification are to some extent arbitrary.

Wavefront reversal of focused single-mode beams is described on the basis of concepts of constriction of the active waveguide in the region of focusing, and strong discrimination of the modes of this waveguide as compared with the mode corresponding to the field of the focused beam [Ref. 9].

Each of these theoretical approaches, while satisfactorily describing its own modification of wavefront reversal, does not permit description of the others. At the same time, from the experimental viewpoint these versions of wavefront reversal are not fundamentally different, and there is the possibility that by varying experimental conditions we could achieve continuous transition from one of the methods of wavefront reversal to the others. This shows that wavefront reversal by stimulated Mandelstam-Brillouin scattering is conditioned by physical causes that are common to all three methods, and that the need for dividing the effect into sub-effects is due to inadequacy of the theoretical description of the process.

In this connection, it is of interest to describe wavefront reversal by stimulated Mandelstam-Brillouin scattering with consideration of the various methods of realization from a unified standpoint. In this paper, we solve the problem by using a spectral approach.

In the spectral approach to description of wavefront reversal by stimulated Mandelstam-Brillouin scattering, the slow amplitudes of the pumping field e_H and the scattered Stokes field e_C are represented (e. g. see Ref. 15, 10] as a sum of planar waves:

$$e_c = \sum_{n=0}^{N-1} a_n(z) \exp\left(i\mathbf{k}_n^c \mathbf{r}\right); \quad e_n = \sum_{n=0}^{N-1} A_n \exp\left(i\mathbf{k}_n^n \mathbf{r}\right).$$

Here it is assumed that the scattering medium is concentrated in the region occupied by the half-space $z \geqslant 0$;

$$k_{nx}^c = -k_{nx}^n = 2\pi n_x/D; \quad k_{ny}^c = -k_{ny}^n = 2\pi n_y/D,$$

where D is the transverse dimension of the region in which the problem is being considered; n_x, n_y are integers that satisfy conditions $n_x^2 + n_y^2 \leqslant \tilde{N}^2$, $N = [\pi \tilde{N}^2]$, and that take on all available values inside the indicated intervals.

Under these conditions, the equations for the amplitudes of plane waves of the scattered field take the form

$$\frac{da_n}{dz} = \frac{g}{2} \sum_{p=0}^{N-1} a_p \sum_{m=0}^{N-1} A_m^* A_{m+p-n} \exp\left(i\Delta k_{mpn}^{(z)} z\right). \qquad (1)$$

where

$$\Delta k^{(z)}_{mpn} = (4\pi^2/kD^2)\,[(n_x - m_x)(n_x - p_x) + (n_y - m_y)(n_y - p_y)];$$

k is the wave number of the pumping field.

In describing wavefront reversal in a waveguide, it is assumed that the slow amplitude of pumping $e_н(r_\perp, z)$ at the input to the waveguide, i. e. at $z = 0$, is a steady-state random process, so that

$$\langle e_н(r_\perp + \tau, 0)\, e^*_н(r_\perp, 0)\rangle = K(\tau),$$

where the angle brackets denote averaging over the set of realizations, and the correlation function $K(\tau)$ corresponds to the angle of divergence θ of the pumping laser emission. Satisfaction of this condition ensures statistically uniform illumination of the waveguide volume by the pumping radiation, which in terms of spectral analysis means satisfaction of the relations

$$I_{m'} = \sum_{m=0}^{N-1} A^*_m A_{m+m'} = I_н \delta_{0,m'}, \quad I_н = \sum_{m=0}^{N-1} A^*_m A_m$$

($\delta_{0,m'}$ is the Kronecker delta), that are the mathematical reflection of statistical independence of amplitudes of the planar pumping waves.

As shown in Ref. 6, in the case of statistically uniform illumination of the waveguide volume and satisfaction of conditions $(k\theta^2)^{-1} \ll z$, $gI_н/k\theta^2 \ll 1$ the only terms that may remain in the right-hand member of equation (1) are those for which $\Delta k^{(z)}_{mpn} = 0$ as a consequence of $n_{x,y} = m_{x,y}$ or $n_{x,y} = p_{x,y}$. The resultant equations satisfactorily describe wavefront reversal in the waveguide discussed in Ref. 5, 6, but they cannot be used to study wavefront reversal of focused beams.

In this connection, let us consider the problem of using equations (1) to describe wavefront reversal of fields with inhomogeneous spatial distribution of average intensity.

In most cases that are of interest for applications, a pumping field with spatially inhomogeneous distribution of intensity in plane $z = 0$ can be represented as a steady-state random process with correlation function $K(\tau)$ modulated by a regular function that varies slowly with respect to $r_\perp$. Here $\langle e_н(r_\perp, 0)\, e^*_н(r_\perp, 0)\rangle = f(r_\perp) K(0)$, where $f(r_\perp)$ is the square of the modulus of the regular function.

In terms of the spectral approach under these conditions we have the relations

$$I_{m'} = \sum_{m=0}^{N-1} A^*_m A_{m+m'} = I_н \rho_{m'};$$

$$\rho_{m'} = \frac{K(0)}{I_н D^2} \int_{-D/2}^{D/2}\int f(x, y) \exp\left\{i \frac{2\pi}{D}(m'_x x + m'_y y)\right\} dy dx.$$

This implies that $\rho_0 = 1$, and also that $\rho_{m'} = \delta_{0,\,m'}$ at $f(r_\perp) = \text{const}$, i. e. in the case of statistically uniform lighting of a region with transverse dimension D.

For the sake of definiteness we will assume that $f(r_\perp)$ is even and is a monotonically decreasing function with increasing $|r_\perp|$. It is just such a situation that is realized in focusing of multimode beams. Under these conditions, the spectral components of ρ_m are real. Moreover, since the envelope of $f(r_\perp)$ is a slowly changing function, for the range of values of index m: $m_x^2 + m_y^2 \leqslant M$, where the quantity ρ_m is concentrated, relation $(M/N)^{1/2} \ll 1$ is satisfied. Furthermore, since $\rho_0 = 1$ and $\rho_0 > \rho_m$ $(m \neq 0)$, we have the relations

$$N^{-1} \sum_{m=0}^{M-1} \rho_m = M_\rho / N \ll 1;\ M_\rho / M \lesssim 1.$$

Let us consider solutions of equations (1) in the region of space defined by inequalities

$$0 \leqslant z \ll kD^2/2\pi\,(MN)^{1/2} = l_{\rho g}, \tag{2}$$

i. e. in the region where the envelope practically has no time to change its form due to effects associated with divergence of pumping radiation. Under these conditions, plane pumping waves with indices m for which

$$\left(k\theta_{mn}^2\right)^{-1} \ll l_{\rho g}, \tag{3}$$

where θ_{mn} is the angle between the direction of propagation of planar pumping waves with indices m and n, will make an energy contribution to the Stokes wave with index n being amplified that is proportional to $\frac{1}{2} g I_{II} \sum_{m=0}^{M-1} a_{n+m} \rho_m$. This is due to the fact that when condition (3) is met, factor $\exp\left(i\Delta k^{(z)}_{m,\,n+m',\,n}\, z\right)$ in terms of form $a_{n+m'} \sum_{m=0}^{N-1} A_m^* A_{m+m'} \exp\left(i\Delta k^{(z)}_{m,\,n+m',\,n}\, z\right)$ in equation (1) is approximately equal to unity for practically all available values of index m', and for this reason

$$a_{n+m'} \sum_{m=0}^{N-1} A_m^* A_{m+m'} \exp\left(i\Delta k^{(z)}_{m,\,n+m',\,n}\, z\right) \approx a_{n+m'} \rho_{m'} I_{II}. \tag{4}$$

In the case where the pumping field is not modulated by a slow envelope, $\rho_m = \rho_{0,\,m}$; therefore the amplitudes of the plane waves are not phased in any way, and expression (4) becomes the expression $\frac{1}{2} g I_H a_\eta$ that is well known in the theory of wavefront reversal by stimulated Mandelstam-Brillouin scattering, and that is responsible for the increment in rise of the Stokes field that corresponds to the average value of pumping intensity.

Besides, when condition (2) is met, in view of the fact that the corresponding exponential factor is approximately equal to unity, the amplification of scattered waves will receive a contribution not only from the partial amplifying

gratings of interference origin situated at Bragg angles to the directions of propagation of plane scattered waves, but also from gratings situated at angles close to these directions. For a plane Stokes wave with index n, this means that the effective contribution to its amplification comes not so much from a term of form $A_n^* \sum_{p=0}^{N-1} A_p a_p$, as from a term of form $\sum_{m=0}^{M-1} A_{m+n}^* \sum_{p=0}^{N-1} a_p A_{m+p}$. Since the contribution of this term to amplification is appreciable only when the Stokes wave being amplified is correlated with the pumping wave, with consideration of the relation

$$\sum_{p=0}^{N-1} A_p^* A_{m+p} \approx \rho_m \sum_{p=0}^{N-1} A_p^* A_p$$

we can assume that

$$\sum_{m=0}^{M-1} A_{m+n}^* \sum_{p=0}^{N-1} a_p A_{m+p} \approx \sum_{m=0}^{M-1} \rho_m A_{m+n}^* \sum_{p=0}^{N-1} a_p A_p.$$

Summing up all the above discussion, we get the following equations for the amplitudes of plane Stokes waves in the region of z that satisfies (2):

$$\frac{da_n}{dz} = \frac{g I_{\text{н}}}{2} \sum_{m=0}^{M} \rho_m a_{m+n} + \frac{g}{2} \sum_{m=0}^{M-1} \rho_m A_{m+n}^* \sum_{p=0}^{N-1} a_p A_p. \tag{5}$$

Let us consider the function $S(z) = \sum_{p=0}^{N-1} a_p A_p$. Then after making the following substitution that does not significantly influence the final result,

$$\sum_{m=0}^{M-1} \rho_m a_{m+n} \approx a_n M_\rho, \tag{6}$$

we get an equation for S(z) from (5):

$$\frac{dS}{dz} = \frac{g I_{\text{н}}}{2} (M_\rho + N_\rho) S,$$

where $I_{\text{н}} N_\rho = \sum_{p=0}^{N-1} A_p \sum_{m=0}^{M-1} \rho_m A_{m+p}^*$ and $N_\rho \lesssim M_\rho$.

The solution of the given equation is

$$S(z) = \sum_{p=0}^{N-1} a_p(0) A_p \exp\left[\tfrac{1}{2} g I_{\text{н}} (M_\rho + N_\rho) z\right], \tag{7}$$

and finally from (5) with consideration of (6), (7) we find

$$a_n(z) = a_n(0) \exp\left\{\tfrac{1}{2} g I_{\text{н}} M_\rho z\right\} + \sum_{m=0}^{M-1} \left(\rho_m A_{m+n}^* / N_\rho I_{\text{н}}\right) \sum_{p=0}^{N-1} a_p(0) A_p \times \\ \times \exp\left\{\tfrac{1}{2} g I_{\text{н}} M_\rho z\right\} \left[\exp\left\{\tfrac{1}{2} g I_{\text{н}} N_\rho z\right\} - 1\right]. \tag{8}$$

The resultant solutions can be interpreted as follows. The first term in the right member of (8) describes uniform amplification of all plane Stokes waves in the pumping field. The increment of this amplification in view of appreciable spatial inhomogeneity of the average value of intensity of pumping is greater than the increment in the field of spatially uniform pumping of intensity I_H, and less than the increment corresponding to the maximum value of intensity of the pumping field.

The second term in (8) is responsible for formation of the field correlated with the pumping field. The increment of this field is somewhat less than twice the increment of uniform amplification of the plane waves. However, correlation with the pumping field is not complete due to the fact that the second term in (8) is proportional to $\sum_{m=0}^{M-1} \rho_m A^*_{m+n}$, rather than to A^*_n, which generally speaking means insufficiently exact reproduction in the reversed wave of the low spatial harmonics of the pumping wave that are responsible for formation of the slow envelope of its field.

Equations (5) and their solutions (8) are valid only when $z \ll l_{\rho g}$. When $z \gtrsim l_{\rho g}$, the exponential factors of $m' \neq 0$ in expressions (4) become oscillating. This means that the envelope of the pumping amplitude ceases to retain its shape, i. e. it blurs due to the finite divergence of the scattered radiation. For this reason equations (5) and their solutions (8) stop correctly describing the scattering process at $z > l_{\rho g}$. However for applications, in particular for experiments on observing wavefront reversal of focused multimode beams, of greatest interest is the region $z \lesssim l_{\rho g}$, where the resultant solutions (8) are valid.

Let us now consider the mode of wavefront reversal of focused single-mode beams. We will assume that the transverse dimension of the beam is D and the focal length of the lens is f. Using equations (1) we can describe the mode of wavefront reversal in the vicinity of the length of focal contraction $l_\Phi = \lambda f^2/D^2$, where λ is the wavelength of the pumping radiation. To do this, we must set $A_k = A_n = A$ for all k and n in equation (1), and also consider that the relation $\exp(i \Delta k^{(z)}_{mpn} z) \approx 1$ is satisfied at $0 \leqslant z \leqslant l_\Phi$. Under these conditions, equations (1) take the form

$$\frac{da_n}{dz} \approx \frac{g I_H}{2} \sum_{p=0}^{N-1} a_p,$$

where $I_H = N|A|^2 = |A|^2 D^4/\lambda^2 f^2$ is beam intensity on the lens surface.

The solution of this equation is

$$a_n(z) = a_n(0) + N^{-1} \sum_{p=0}^{N-1} a_p(0) \left[\exp\left(N \frac{g I_H}{2} z\right) - 1\right]. \qquad (9)$$

Here the second term corresponds to the field correlated with pumping. This is implied by the fact that both the amplitudes of the plane pumping waves and the second terms in the right-hand members of (9) are independent of index n. The increment of the rise in the part of the field that is correlated with

pumping is proportional to NI_H, which we can easily see is equal to the intensity of the pumping beam in the region of focal contraction.

Using solutions (9), we can evaluate the intensity of a single-mode beam at which wavefront reversal could be observed:

$$N^{-1}\exp(gI_H Nl_\phi)=f^2\lambda^2 D^{-4}\exp(gI_H D^2/\lambda)\gg 1.$$

However, it should be noted that this estimate has been obtained with the assumption that the angle of divergence of plane waves of the scattered field does not exceed the angle of divergence θ of the focused pumping, and that the amplitudes $a_n(0)$ of the plane waves are statistically independent. On the other hand, under actual experimental conditions the initiating radiation on the Stokes frequency arises mainly in the region of the focal contraction, and as a consequence the amplitudes $a_n(0)$ are phased to some extent, and the estimate given above requires some refinement.

REFERENCES

1. Zel'dovich, B. Ya., Popovichev, V. I., Ragul'skiy, V. V., Fayzullov, F. S., PIS'MA V ZHURNAL EKSPERIMENTAL'NOY I TEORETICHESKOY FIZIKI, Vol 15, 1972, p 160.

2. Bespalov, V. I., Betin, A. A., Pasmanik, G. A. PIS'MA V ZHURNAL TEKHNICHESKOY FIZIKI, Vol 3, 1977, p 215.

3. Zubarev, I. G., in: "Obrashcheniye volnovogo fronta opticheskogo izlucheniya v nelineynykh sredakh" [Wavefront Reversal of Optical Radiation in Nonlinear Media], Gor'kiy, Institute of Applied Physics, USSR Academy of Sciences, 1979.

4. Dolgopolov, Yu. V., Komarevskiy, V. A., Kormer, S. B., Kochemasov, G. G., Kulikov, S. M., Murugov, V. M., Nikolayev, V. D., ZHURNAL EKSPERIMENTAL'NOY I TEORETICHESKOY FIZIKI, Vol 76, 1979, p 908.

5. Bel'dyugin, I. M., Galushkin, M. G., Zemskov, Ye. M., Mandrosov, V. I., KVANTOVAYA ELEKTRONIKA, Vol 3, 1976, p 2467.

6. Sidorovich, V. G., ZHURNAL TEKHNICHESKOY FIZIKI, Vol 46, 1976, p 2168.

7. Bespalov, V. I., Betin, A. A., Pasmanik, G. A., IZVESTIYA VYSSHIKH UCHEBNYKH ZAVEDENIY: SERIYA RADIOFIZIKA, Vol 21, 1978, p 961.

8. Baranova, N. B., Zel'dovich, B. Ya., KVANTOVAYA ELEKTRONIKA, Vol 7, 1980, p 973.

9. Bespalov, V. I., Pasmanik, G. A., DOKLADY AKADEMII NAUK SSSR, Vol 210, 1973, p 309.

10. Bel'dyugin, I. M., Zubarev, I. G., KVANTOVAYA ELEKTRONIKA, Vol 7, 1980, p 743.

6610
CSO: 1862/145

UDC 538.3

STIMULATED MANY-PHOTON EFFECTS ON DIFFRACTION GRATING

Leningrad ZHURNAL TEKHNICHESKOY FIZIKI in Russian Vol 52, No 3, Mar 82 (manuscript received 11 May 81) pp 554-556

[Article by S. G. Oganesyan and V. A. Yengibaryan, Yerevan State University, Scientific Research Institute of Physics of Condensed Media]

[Text] Ref. 1-3 cover theoretical studies of stimulated many-photon processes in homogeneous and inhomogeneous media. However, breakdown of the medium and multiple scattering of a charged particle create additional difficulties for experimental observation. As noted in Ref. 2, vacuum effects are most suitable from this standpoint. Since a particle does not emit or absorb in vacuum, the use of diffraction effects is suggested, where an electron interacts with electromagnetic radiation on an opening in an opaque screen.

In this paper we examine stimulated effects when a particle passes over a diffraction grating [Ref. 4]. The percentage modulation of the electron beam and broadening of its energy spectrum are proportional to the number of lines N which in good gratings may be of the order of 10^5 [Ref. 5].

Classical Theory

Let a charged particle pass over a diffraction grating with period d and gap width a, at distance z_0 from the grating surface. Incident on the grating from below and normal to its surface is a monochromatic electromagnetic wave linearly polarized along the y-axis, which we take as parallel to the lines of the grating. With consideration of the reflected wave, we find the Fourier component of the vector potential

$$a(q_x;\ q_z) = -i\frac{A_0}{4\pi}\frac{\delta(q_x)}{q_z-\omega/c-i\delta}+i\frac{A_0}{4\pi^2}\frac{\exp\left[i(N-1)(q_xd/2)\right]\sin(Nq_xd/2)}{\sin(q_xd/2)}\times$$
$$\times\frac{\sin(q_xa/2)}{q_x}\frac{q_z+\omega/c}{(q_z+\sqrt{\omega^2/c^2-q_x^2}-i\delta)(q_z-\sqrt{\omega^2/c^2-q_x^2}+i\delta)}. \qquad (1)$$

The infinitesimal corrections $\pm i\delta$ select the pole when integrating with respect to wave vector q_z.

To find the change of energy and momentum of the electron, we use the equations

$$\frac{dp_x}{dt} = -ie\beta_y\int q_x a(q_x;\ q_z)\exp\{i\omega t - iq_x x - iq_z z\}\,dq_x dq_z + \text{comp. conj.}$$

$$\frac{dp_y}{dt} = -ie\int\left(\frac{\omega}{c} - q_x\beta_x - q_z\beta_z\right)a(q_x;\ q_z)\exp\left(i\omega t - iq_x x - iq_z z\right)dq_x dq_z + \text{comp. conj.}$$

$$\frac{dp_z}{dt} = -ie\beta_y\int q_x a(q_x;\ q_z)\exp\left(i\omega t - iq_x x - iq_z z\right)dq_x dq_z + \text{comp. conj.} \quad (2)$$

and also the expression

$$\Delta\mathcal{E} = v_x\Delta p_x + v_y\Delta p_y + v_z\Delta p_z. \quad (3)$$

Let us solve system (2) by perturbation theory, substithting the unperturbed trajectory

$$x = x_0 + v_x t,\ y = y_0,\ z = z_0 \quad (4)$$

in the right-hand part.

Integrating with respect to time from $-\infty$ to $+\infty$, we find

$$\Delta p_x = \frac{\Delta\mathcal{E}'}{v_x}\cos\left(\frac{\omega x_0}{v_x} + \alpha\right),\ \Delta p_y = 0,\ \Delta p_z = \frac{\Delta\mathcal{E}'}{v_x}\sqrt{1-\beta_x^2}\sin\left(\frac{\omega x_0}{v_x} + \alpha\right),$$

$$\Delta\mathcal{E} = \Delta\mathcal{E}'\cos\left(\frac{\omega x_0}{v_x} + \alpha\right), \quad (5)$$

where

$$\Delta\mathcal{E}' = \xi\beta_y\frac{mc^2}{\sqrt{1-\beta_x^2}}\sin\frac{\omega d}{2v_x}e^{(-\omega/v_x)\sqrt{1-\beta_x^2}z_0}\frac{\sin\left(N\omega d/2v_x\right)}{\sin\left(\omega d/2v_x\right)},$$

$$\alpha = -(N-1)\frac{\omega d}{2v_x} + \operatorname{arc\,tg}\frac{\sqrt{1-\beta_x^2}}{\beta_x}, \quad (6)$$

and $\xi = eA_0/mc^2$ is the dimensionless intensity parameter. When condition

$$\omega d/2v_x = n\pi, \text{ where } n = \pm 1;\ \pm 2;\ \pm\ldots \quad (7)$$

is satisfied, the quantity $\sin\left(N\omega d/2v_x\right)/\sin\left(\omega d/2v_x\right) = N$. In this case, broadening of the energy spectrum of the electron beam is proportional to the total number of openings N. Relation (7) corresponds to the result of Ref. 4 if the angle of spontaneous electron emission is set equal to $\pi/2$. At predetermined particle velocity and external field frequency $\omega = 2\pi c/\lambda$, we get the condition for the grating period from (7):

$$d = n\lambda\beta_x, \text{ where } n = 1;\ 2;\ \ldots\ . \quad (8)$$

The change in particle energy is minimum if

$$\left|\sin\left(\omega a/2v_x\right)\right| = 1. \quad (9)$$

Hence we get the condition for the gap size in the diffraction grating

$$a = (2r+1)\lambda\beta_x/2, \text{ where } r = 1;\ 2;\ \ldots\ . \quad (10)$$

With respect to order of magnitude

$$\Delta\mathcal{E}' \simeq N\xi mc^2 \exp(-8.9 z_0 mc^2/\lambda\beta\mathcal{E}) \tag{11}$$

(for relativistic particles the angle between the x-axis and the direction of electron motion is $\vartheta \sim mc^2/\mathcal{E}$).

Quantum Theory

An analogous result (6)--equiprobable broadening of the energy spectrum of a particle beam in the range $2\Delta\mathcal{E}'$--can be found on the basis of the Klein-Gordon equation

$$-\hbar^2 \frac{\partial^2\psi}{\partial t^2} = [c^2(p_x^2 - p_y^2 + p_z^2) - 2ecA_y p_y]\psi + m^2c^4\psi. \tag{12}$$

In the approximation where the change of energy and momentum $\Delta p \ll p$, $\Delta\mathcal{E} \ll \mathcal{E}$, we get

$$\psi = \rho_0^{1/2} \exp\left(i\frac{p_{0x}}{\hbar}x + i\frac{p_{0y}}{\hbar}y - i\frac{\mathcal{E}}{\hbar}t\right) \sum_{s=-\infty}^{+\infty} I_s\left(\frac{\Delta\mathcal{E}'}{\hbar\omega}\right) \exp[is\omega(t - x/v_x)]. \tag{13}$$

Consequently, the probability of encountering a particle with energy $\mathcal{E} + s\hbar\omega$ is

$$W = I_s^2(\Delta\mathcal{E}'/\hbar\omega), \tag{14}$$

where s takes on whole-number values, and z_0 in (6) is replaced by z.

A study of expression (14) shows that in contrast to the classical result at $s \simeq \pm \Delta\mathcal{E}'/\hbar\omega$ spikes show up with width $\simeq \hbar\omega\,(\Delta\mathcal{E}'/2\hbar\omega)^{1/3}$ [Ref. 1, 2].

If the fields are such that $\Delta\mathcal{E}'/\hbar\omega \leqslant 1$, a major role is played by first-order processes. Therefore we will seek the solution of equation (12) in the form

$$\psi = \rho_0^{1/2}\left[\exp\left(i\frac{p_{0x}}{\hbar}x + i\frac{p_{0y}}{\hbar}y - i\frac{\mathcal{E}}{\hbar}t\right) + b\exp\left(i\frac{p_{0y}}{\hbar}y - i\frac{\mathcal{E}t\hbar\omega}{\hbar}t\right) + d\exp\left(i\frac{p_{0y}}{\hbar}y - i\frac{\mathcal{E}-\hbar\omega}{\hbar}t\right)\right]. \tag{15}$$

Disregarding terms that are quadratic with respect to the field, we find

$$b = \frac{1}{2}\frac{\Delta\mathcal{E}'}{\hbar\omega}\exp\left[i\left(\frac{p_{0x}}{\hbar} + \frac{\omega}{v_x}\right)x\right], \quad d = -\frac{1}{2}\frac{\Delta\mathcal{E}'}{\hbar\omega}\exp\left[i\left(\frac{p_{0x}}{\hbar} - \frac{\omega}{v_x}\right)x\right], \tag{16}$$

and substituting in (15), we find that the wave function of the particle is modulated on frequency ω

$$\psi = \rho_0^{1/2}\exp\left(i\frac{p_{0x}}{\hbar}x + i\frac{p_{0y}}{\hbar}y - i\frac{\mathcal{E}}{\hbar}t\right)\left[1 - i\frac{\Delta\mathcal{E}'}{\hbar\omega}\sin\omega\left(t - \frac{x}{v_x}\right)\right]. \tag{17}$$

The percentage modulation is a purely imaginary quantity, and therefore the electron density remains constant as contrasted with the case of an interface [Ref. 1]. The stimulated diffraction effect leads to modulation of electron velocity. Calculating the current, we find

$$j = \frac{e}{m} \operatorname{Re} \psi^* \hat{p}_x \psi = e\rho_0 \left[v_x + \frac{\Delta \mathcal{E}'}{m v_x} \cos \omega \left(t - \frac{x}{v_x} \right) \right]. \qquad (18)$$

Conclusion

If the initial field is polarized along the x-axis, and electron velocity $v_x = v$, then

$$\Delta \mathcal{E}' = N \xi mc^2 \exp(-2\pi mc^2 z_0 / \mathcal{E} \lambda) \qquad (19)$$

when conditions (8) and (10) are met, where $\vartheta = 0$.

We see from (6) and (19) that only electrons located at distance $z_0 \sim \lambda (\mathcal{E}/mc^2)$ from the grating surface take part in induced processes. For nonrelativistic energies, the total number of interacting particles can be increased by focusing the beam over the grating surface. Things are simpler with relativistic particles. If $\lambda = 1$ μm, and $\mathcal{E} = 500$ MeV, then $z_0 \cong 1$ mm.

Let us now estimate the power of electromagnetic radiation necessary for increasing particle energy by 10%. Let the number of grating lines be of the order of 10^3 per millimeter, and the size of the light spot be of the order of 1 cm. Then, considering that this requires values of $\xi = \mathcal{E}/20\, Nmc^2$, we find that for nonrelativistic particles ($\beta = 0.1$) a power $P = 2.68$ kW/cm^2 is required, for energies $\mathcal{E} = mc^2$ -- $P = 120$ MW/cm^2, and for relativistic particles Mev -- $P = 67 \cdot 10^{13}$ W/cm^2.

To prevent momentum Δp_z from carrying the particle out of the interaction region, the electrons should pass over the grating at a small angle $\phi \sim \Delta p_z / p_0$.

Percentage modulation $r = \Delta \mathcal{E}' / mc^2 \beta^2$ reaches 10% for particles with $\beta = 0.5$ at $P = 67$ MW/cm^2 if the initial field is polarized along the gap, and 16.75 MW/cm^2 when polarization is perpendicular to the gap. At energies $\mathcal{E} = mc^2$ a power of 67 MW/cm^2 is required regardless of polarization.

The authors thank V. M. Arutyunyan for discussing the results.

REFERENCES

1. Arutyunyan, V. M., Oganesyan, S. G., ZHURNAL EKSPERIMENTAL'NOY I TEORETICHESKOY FIZIKI, Vol 72, 1977, p 466.

2. Arutyunyan, V. M., Oganesyan, S. G., Preprint No 76-06, PLRF [expansion not known], Yerevan State University, 1976.

3. Arutyunyan, V. M., Avetisyan, G. K., ZHURNAL EKSPERIMENTAL'NOY I TEORETICHESKOY FIZIKI, Vol 5, 1972, p 62.

4. Bolotovskiy, B. M., Voskresenskiy, G. V., USPEKHI FIZICHESKIKH NAUK, Vol 94, 1968, p 377.

5. Landsberg, G. S., "Optika" [Optics], Moscow, "Nauka", 1976.

6610
CSO: 1862/150

UDC 535.21:621.378

LASER DISPERSAL OF POLYDISPERSE WATER AEROSOL

Moscow KVANTOVAYA ELEKTRONIKA in Russian Vol 9, No 2(116), Feb 82 (manuscript received 10 Oct 80, after revision 20 May 81) pp 332-342

[Article by V. K. Pustovalov, G. S. Romanov and I. A. Khorunzhiy, Scientific Research Institute of Applied Physics Problems at Belorussian State University imeni V. I. Lenin, Minsk]

[Text] Based on results of numerical solution of a system of equations, an investigation is made of the process of dispersal of a polydisperse water aerosol under the action of cw laser emission on a wavelength of 10.6 μm with vaporization of water droplets in the diffusion mode. Space-time curves are obtained, and also the parameters that characterize the dispersal process. An analysis is made of the way that the parameters of the dispersal process depend on the emission energy flux density, the initial temperature of droplets, the coefficient of vaporization and the optical constants of water, the parameters of the function of the initial size distribution of the aerosol droplets. The efficiency of the dispersal process is studied and the results are compared with experiment.

Dispersal of a polydisperse water aerosol (clouds, mist) under the action of intense laser emission with wavelength $\lambda = 10.6$ μm has been theoretically studied in Ref. 1-8 by analytical and numerical methods. In the analytical description of the process of dispersal, fine-droplet ($r_0 \ll \lambda$ [Ref. 1-3, 7], where r_0 is the instantaneous radius of aerosol droplets) and coarse-droplet ($r_0 \gg \lambda$ [Ref. 2]) approximations were used under conditions of a quasi-steady process of droplet vaporization in the dispersal wave and rough accounting for the losses of radiation energy to scattering and heat conduction [Ref. 5, 7, 8]. However, within the framework of the analytical description it is impossible to clearly define the region of applicability of the assumptions that are used, and to study the most interesting case $r_0 \sim \lambda$. In the numerical study of the dispersal process [Ref. 4, 6], the above-mentioned assumptions were not used, and the process was described more completely. At the same time, no consideration was taken in Ref. 4 of energy losses to scattering and heat conduction, and an inexact equation of energy balance of vaporizing droplets was used in Ref. 6 (no consideration was taken of the thermal energy

of the droplets in the process of heating by radiation). Ref. 4, 6 do not give enough variants of the calculations for detailed tracing of the dependence of parameters of the dispersal process on the initial parameters of the problem.

In this paper, based on computer solution of a system of equations an investigation is made of dispersal of a stationary polydisperse water aerosol under the action of laser radiation with $\lambda = 10.6$ μm. The investigation of aerosol dispersal is based on correct consideration of the process of vaporization of isolated aerosol droplets by radiation. In contrast to Ref. 1-8, we have accounted for discontinuities of density and temperature on the surface of the vaporizing droplets, and have used actual relations for the thermophysical parameters of the problem as functions of temperature and for the factors of effectiveness of absorption and scattering of droplets as functions of r_0, which brings the considered model of the process much closer to reality. Our principal attention has been given to investigating the way that the parameters of the dispersal process depend on the energy flux density I_0 of the acting radiation on the boundary of the aerosol (at $x = 0$), initial droplet temperature T_∞, vaporization coefficient α and the indices of refraction n and absorption κ of water. An examination is made of the influence that the initial function of size distribution of the polydisperse aerosol droplets has on the dispersal process. Some of the results are compared with data of experiments on dispersal in Ref. 9 and 4.

Formulation of the Problem

Consider dispersal of a stationary polydisperse water aerosol with initial concentration N_0 and droplet size distribution $f_0(r_0)$ under the action of radiation with constant I_0. The system of equations that describes the process of dispersal includes quasi-stationary equations of the transfer of the acting ($\lambda = 10.6$ μm) and probing ($\lambda_p = 0.63$ μm) radiation in the approximation of single scattering by droplets, equations of energy balance and kinetics of vaporization of droplets in the approximation of uniform energy release and absence of a temperature profile through the volume of a droplet:

$$\left.\begin{aligned}
&\frac{\partial I}{\partial x} + \pi N_0 I \int_0^\infty r_0^2 \left(K_\text{п}(r_0) + K_\text{р}(r_0)\right) f(r_0)\, dr_0 = 0;\\
&\frac{\partial I_\text{з}}{\partial x} + \pi N_0 I_\text{з} \int_0^\infty r_0^2 K_0(r_0) f(r_0)\, dr_0 = 0;\\
&\bar{n}_0 c_2 V_0 \frac{\partial T_0}{\partial t} = \frac{1}{4} K_\text{п}(r_0) I S_0 - j_e S_0;\\
&\bar{n}_0 \frac{\partial V_0}{\partial t} = -j_m S_0,
\end{aligned}\right\} \qquad (1)$$

where I, $I_\text{з}$ are the energy flux densities of the acting and probing radiation, $K_\text{п}$, $K_\text{р}$ and K_0 are the factors of effectiveness of absorption and scattering of the acting radiation, and attenuation of the probing radiation for droplets with instantaneous radius r_0 [Ref. 10], c_2, $\bar{n}_0$ are the specific heat and density of water molecules, $V_0 = {}^4/_3\pi r_0^3$, $S_0 = 4\pi r_0^2$ are the volume and surface area

of a droplet. In the diffusion mode of vaporization, the densities of the fluxes of mass j_m and energy j_ε from the surface of the vaporizing droplet are defined by the relations

$$j_m = \frac{n_0 T_0^{1/2} - n_\infty \bar{T}^{1/2}}{(2\pi m/k\alpha^2)^{1/2} + br_0 \bar{T}^{1/2} \ln(\bar{T}/T_\infty)/D_{10}[(\bar{T}/T_\infty)^{p+1} - 1]};$$
$$j_\varepsilon = \frac{\varkappa_{10} T_\infty [(\bar{T}/T_\infty)^{p+1} - 1]}{(p+1) r_0} + j_m L(T_0), \qquad (2)$$

where n_0 is the density of saturated water vapor at drop surface temperature T_0 [Ref. 12, 13], $n_\infty = n_0(T_\infty)$, $\bar{T}$ is air temperature directly at the surface of the droplet determined with consideration of temperature discontinuity [Ref. 11], α is the coefficient of vaporization (usually taken as equal to the coefficient of condensation) of water, m is the mass of a vapor molecule, k is Boltzmann's constant, $L(T_0)$ is the heat of vaporization of a water droplet [Ref. 12, 13]. The coefficient of diffusion of water vapor in air is given by $D = D_{10}(T/T_\infty)^b$, $D_{10} = \text{const}$, $b = 1.8$, $\varkappa = \varkappa_{10}(T/T_\infty)^p$ is the coefficient of thermal conductivity of air, $\varkappa_{10} = \text{const}$, $b = p + 1$ [Ref. 12, 13].

The equation that describes the change in the polydisperse aerosol droplet size distribution function $f(r_0)$ as a consequence of droplet vaporization takes the form

$$\frac{\partial f}{\partial t} + \frac{\partial}{\partial r_0}\left(f \frac{\partial r_0}{\partial t}\right) = 0, \qquad (3)$$

where $\int_0^\infty f(r_0)\, dr_0 = 1$. The initial and boundary conditions for (1)-(3) are

$$T_0(x, 0) = T_\infty; \; r_0(x, 0) = r_\infty; \; f(r_0, x, 0) = f_0(r_0);$$
$$I(x, 0) = I_0 \exp\left[-\pi N_0 x \int_0^\infty r_0^2 (K_\Pi(r_0) + K_p(r_0)) f_0(r_0)\, dr_0;\right] \qquad (4)$$
$$I_3(x, 0) = I_{30} \exp\left[-\pi N_0 x \int_0^\infty r_0^2 K_0(r_0) f_0(r_0)\, dr_0\right].$$

Of considerable interest is the differential parameter (see third equation of (1))

$$D_1(r_0, x, t) = IK_\Pi(r_0)/4j_\varepsilon, \qquad (5)$$

that could be called the degree of quasi-steadiness of the process of droplet vaporization. It is the ratio of the energy release in the droplet to the energy losses due to vaporization and heat conduction, and characterizes the imbalance between energy release and energy losses, and also the rate of change in T_0. Let us also consider integral energy quantities that characterize the process of droplet vaporization from the time $t = 0$ of onset of action of the radiation to the given time t: the emission energy $Q_\Pi(r_0, x, t)$ and $Q_p(r_0, x, t)$ respectively absorbed and scattered by the droplet, and energy $Q_И(r_0, x, t)$ and $Q_T(r_0, x, t)$ respectively expended on vaporizing the droplet and released by the mechanism of thermal conductivity from the droplet:

$$Q_{\text{п}}=\pi\int_0^t IK_{\text{п}}(r_0)\,r_0^2dt;\qquad Q_{\text{р}}=\pi\int_0^t IK_{\text{р}}(r_0)\,r_0^2dt;$$
$$Q_{\text{и}}=4\pi\int_0^t j_mL(T_0)\,r_0^2dt;\quad Q_{\text{т}}=4\pi\frac{\varkappa_{10}T_\infty}{(p+1)}\int_0^t\left[(\overline{T}/T_\infty)^{p+1}-1\right]r_0dt, \tag{6}$$

the same energies for the aerosol as a whole:

$$S_{\text{п}}=\int_0^\infty\int_0^\infty Q_{\text{п}}f(r_0)\,dr_0dx;\quad S_{\text{р}}=\int_0^\infty\int_0^\infty Q_{\text{р}}f(r_0)\,dr_0dx;$$
$$S_{\text{и}}=\int_0^\infty\int_0^\infty Q_{\text{и}}f(r_0)\,dr_0dx;\quad S_{\text{т}}=\int_0^\infty\int_0^\infty Q_{\text{т}}f(r_0)\,dr_0dx \tag{7}$$

and the energy parameters T_1 that characterize the process of dispersal of the aerosol as a whole:

$$T_1=S_{\text{и}}/(S_{\text{и}}+S_{\text{т}});\ T_2=S_{\text{и}}/(S_{\text{п}}+S_{\text{р}});\quad T_3=S_{\text{п}}/(S_{\text{п}}+S_{\text{р}}). \tag{8}$$

A dimensionless spatial variable ξ will be used below that is associated with the spatial variable x by the equation

$$x=1{,}274\cdot10^6\ \xi/N_0, \tag{9}$$

where x is in centimeters, N_0 is in inverse cubic centimeters. Let us note that in the given problem the concentration of droplets N_0 appears only in (9) that relates x and ξ, and all results of calculations of the process of dispersal can be recalculated for any initial values of aerosol water content $\rho=\frac{4}{3}\pi N_0\rho_{\text{в}}\int_0^\infty r_0^3 f_0(r_0)\,dr_0$, where $\rho_{\text{в}}$ is the density of water, with selected initial function $f_0(r_0)$ corresponding to a change (increase or reduction) of N_0.

With the exception of specially stipulated cases, we will take the coefficient of water vaporization α as equal to unity, and the optical constants of water for $\lambda=10.6$ μm as $n=1.173$ and $\kappa=8.23\cdot10^{-2}$ [Ref. 10]. We will use the initial polydisperse aerosol droplet size distribution function in the form of a Γ-distribution [Ref. 14]:

$$f_0(r_0)=\frac{\mu^{\mu+1}}{\Gamma(\mu+1)}\,\frac{r_0^\mu}{R^{\mu+1}}\exp\left(-\mu\frac{r_0}{R}\right). \tag{10}$$

In numerical solution of the problem for approximating $f_0(r_0)$ (10) we used a multigroup approximation (from 12 to 24 groups of droplets) including drops with radius up to 30-60 μm depending on the specific form of $f_0(r_0)$. During the numerical computation, we checked the balance of radiation energies absorbed and scattered by the aerosol droplets, and also the balance of absorbed and initial thermal energies expended on vaporization and heat conduction, which were maintained with accuracy of ~0.5%.

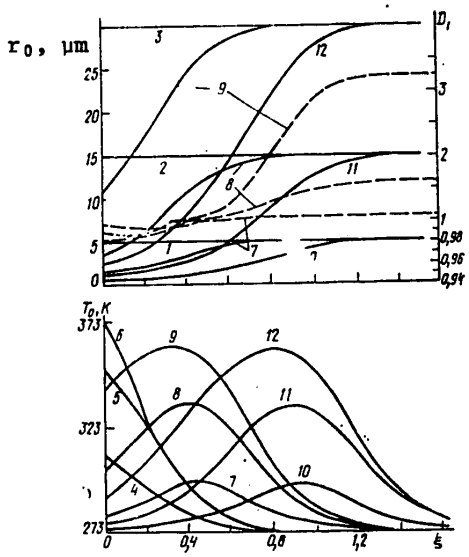

Fig. 1. Distributions of temperature T_0, radii r_0 (solid lines) and parameter D_1 (broken lines) for droplets with $r_\infty = 5$ (*1*, *4*, *7*, *10*), 15 (*2*, *5*, *8*, *11*), 30 (*3*, *6*, *9*, *12*) μm with respect to ξ at $I_0 = 500$ W/cm^2, $T_\infty = 273$ K for $t = 0$ (*1*, *2*, *3*), $4.7 \cdot 10^{-3}$ (*4*, *5*, *6*), $3.75 \cdot 10^{-2}$ (*7*, *8*, *9*) and $7.5 \cdot 10^{-2}$ (*10*, *11*, *12*) s

Discussion of the Results

1. Let us consider some results of numerical calculation of the process of dispersal of a polydisperse water aerosol with initial droplet distribution function $f_0(r_0)$ (10) with most probable droplet radius $R = 5$ μm, parameter $\mu = 2$, initial droplet temperature $T_\infty = 273$ K under the action of radiation with $I_0 = 500$ W/cm^2.

Fig. 1 shows distributions of T_0, r_0 and D_1 in a dispersal wave for aerosol droplet groups with $r_\infty = 5$, 15 and 30 μm with respect to ξ for several instants of time. From the instant that radiation begins to act on the aerosol the radiation energy starts to be absorbed and there is a rapid rise in T_0 (energy liberation is much greater than energy losses), giving rise to vaporization and an increase in heat losses by the droplets as a consequence of vaporization and thermal conductivity. Vaporization of droplets results in propagation of a dispersal wave into the aerosol. At times $t_m(r_\infty)$ for droplets of different initial radii r_∞ the energy liberation and energy absorption are in balance at $\xi = 0$. The temperatures of the droplets reach maximum values $T_m(r_\infty)(D_1(r_0, \xi = 0, t_m) = 1)$, after which the temperature of the droplet begins to fall in the process of quasi-steady vaporization [Ref. 11]. A similar pattern of attainment of $T_m(r_\infty)$ and subsequent reduction of temperature is

observed for droplets deep inside the aerosol as the dispersing and vaporizing waves propagate. With the passage of time, due to a drop in T_0 in the region of quasi-steady droplet vaporization ($T_0(r_0, \xi = 0) \leqslant T_0 \leqslant T_m(r_\infty)$) and an increase in T_0 in the region of dispersal, temperature waves are produced that advance into the aerosol (see also Ref. 4). In the steady state of dispersal wave propagation, e. g. for $r_\infty = 5$, 15, 30 μm we have $T_m = 295$, 332, 359 K respectively. In the region of decreasing temperature $0.98 \lesssim D_1(r_0) < 1$, i. e. energy losses are ~1-2% greater than energy liberation in the droplets.

In the region of temperature rise, up to the time of attainment of $\overline{T}_m$ and $D_1(r_0) = 1$, the aerosol droplets vaporize unsteadily under conditions of a considerable excess of energy liberation over energy losses at $1 < D_1(r_0) \leqslant \overline{D}_{1m}(r_\infty)$, where $\overline{D}_{1m} = D_1(r_\infty, \xi \to \infty)$ (see Fig. 1). In the given case $\overline{D}_{1m}(r_\infty)$ increases considerably with increasing r_∞ (Table 1). At $\overline{T}_m$ and $D_1(r_0) = 1$, the radii of droplets with $r_\infty = 5$, 15, 30 μm become equal to $r_0 = 3.6$, 11.2, 23 μm.

TABLE 1

I_0, W/cm²	T_∞, K	$\overline{D}_{1m}$ ($r_\infty = 5$)	$\overline{D}_{1m}$ ($r_\infty = 15$)	$\overline{D}_{1m}$ ($r_\infty = 30$)
200	273	1,02	1,2	1,8
500	273	1,07	1,6	3,4
500	293	1,04	1,35	2,55
1000	273	1,15	2,35	6,6

Consequently in the process of unsteady vaporization the aerosol droplets lose ~60% of their mass. At fixed $D_1 = 1.05$, $r_\infty = 5$, 15, 30 μm, we have $r_0 = 4.85$, 13.5, 27 μm respectively. In the interval $1.05 \leqslant D_1 \leqslant \overline{D}_{1m}(r_\infty)$ the aerosol droplets lose ~25% of their mass. Thus a reduction in droplet radii in the dispersal wave from r_∞ to ~$0.9r_\infty$ takes place at $1.05 \leqslant D_1 \leqslant \overline{D}_{1m}(r_\infty)$, i. e. for appreciably unsteady vaporization under conditions of considerable imbalance between energy liberation and energy losses. A further reduction of r_0 takes place at $0.98 \lesssim D_1 < 1.05$, i. e. for imbalance between energy liberation and energy losses that does not exceed ~5%.

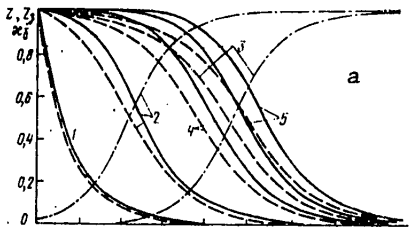

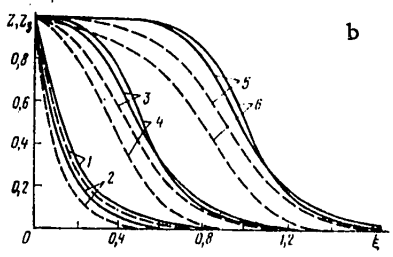

Fig. 2. Distributions of Z (solid lines), $Z_э$ (broken lines) and κ_δ (dot-and-dash) with respect to ξ for $T_\infty = 273$ K, $I_0 = 500$ W/cm², $t = 0$ (*1*), $3.75 \cdot 10^{-2}$ (*2*), $7.5 \cdot 10^{-2}$ (*3*) s; $I_0 = 200$ W/cm², $t = 1.875 \cdot 10^{-1}$ (*4*) s; $I_0 = 1$ kW/cm², $t = 3.75 \cdot 10^{-2}$ (*5*) s (a), and $T_\infty = 273$ K, $I_0 = 500$ W/cm², R = 5 μm, μ = 2 (*1*, *3*, *5*), 6 (*2*, *4*, *6*) and $t = 0$ (*1*, *2*), 3.75×10^{-2} (*3*, *4*), $7.5 \cdot 10^{-2}$ (*5*, *6*) (b)

Fig. 2a shows the distributions of dimensionless energy flux densities of the acting $Z = I/I_0$ and probing $Z_э = I_э/I_{э0}$ radiation, and the dimensionless coefficient of attenuation of the acting radiation $\kappa_\delta = \kappa(r_0)/\kappa_0(r_0)$ with respect to ξ for several t, where $\kappa = \pi N_0 \int_0^\infty r_0^2 (K_n(r_0) + K_p(r_0)) f(r_0) dr_0$, $\kappa_0 = \kappa(t = 0)$. As a result of droplet vaporization under the action of radiation, dispersal waves on λ and λ_p propagate into the aerosol with different degrees of aerosol dispersal on these wavelengths.

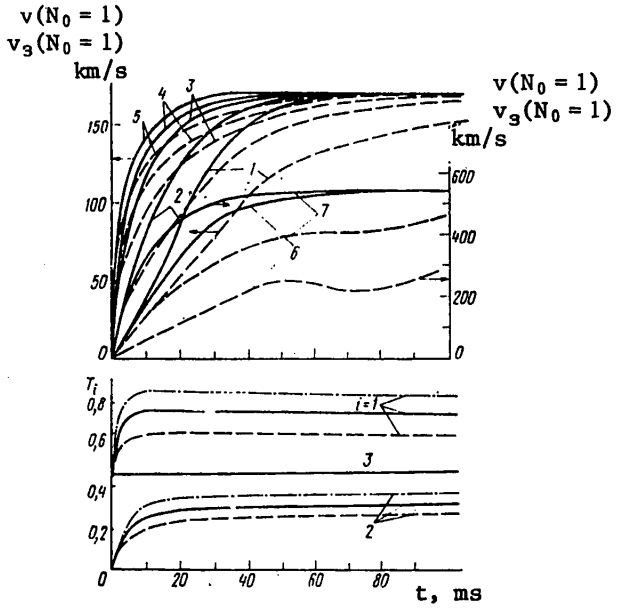

Fig. 3. Time dependences of v and $v_э$ for transparency levels $Z_ф$, $Z_{эф} = 0.9$ (*1*, *6*), 0.75 (*2*, *7*), 0.5 (*3*), e^{-1} (*4*), e^{-2} (*5*) of the acting (solid lines) and probing (broken lines) radiation at $I_0 = 500$ W/cm^2, $T_\infty = 273$ K, $R = 5$ μm, $\mu = 2$ (*1-5*, axis of ordinates on the left), and $R = 5$ μm, $\mu = 6$ (*6-7*, axis of ordinates on the right), the parameters T_i at $I_0 = 500$ W/cm^2, $T_\infty = 273$ K (solid lines) and $T_\infty = 273$ K (broken lines)

Fig. 3 shows the dependences on time t for velocities v and $v_э$ of propagation of the dispersal wave at several fixed levels of transparency for the acting ($Z_ф$) and probing ($Z_{эф}$) radiation and for parameters T_i. Here and below, v and $v_э$ are calculated at $N_0 = 1$ cm^{-3}, and conversion to other values of N_0 is done by the formula $v(N_0) = v(N_0 = 1)/N_0$. Velocity v increases monotonically during the unsteady stage of the dispersal process ($0 < t \leqslant t_y$), v(t) being the greater, the lower the $Z_ф$. The steady state of dispersal wave propagation on λ and λ_p (steady state of the dispersal process) settles down asymptotically at sufficiently long times t_y, $t_{эy}$ for which we take the times of settling of the steady value of v for rates of propagation of levels $Z_ф$, $Z_{эф} = 0.9$. Velocity $v_э$ at $0 < t < t_{эy}$ is less than v for the same $Z_ф$ and t, while $t_{эy} > t_y$, which is due to the difference in $K_п(r_0)$, $K_p(r_0)$ and the oscillatory dependence $K_0(r_0)$ [Ref. 10]. The steady-state value $\bar{v}$ of the velocity of dispersal wave propagation on λ and λ_p is the same: $\bar{v} = 171/N_0$ (km/s); e. g. at $N_0 = 2 \cdot 10^2$ cm^{-3}, $\bar{v} = 0.855$ km/s. Times of settling of the steady state of dispersal are $t_y \cong 85$ ms, $t_{эy} \cong 0.13$ s. Parameters T_1, T_2 during the unsteady stage depend on time, T_1 having a maximum in the interval 0, t_y. At $t \gtrsim t_y$, parameters T_i acquire constant values $\bar{T}_i$ that characterize the steady stage of the dispersal process. Parameter T_3 changes little over time interval 0, t_y.

Droplet vaporization by radiation deforms distribution function $f_0(r_0)$: the function is shifted toward smaller r_0 along the axis of radii, $f(r_0)$ is sharply narrowed, and there is a rise in the maximum of $f(r_0)$ (see Ref. 4).

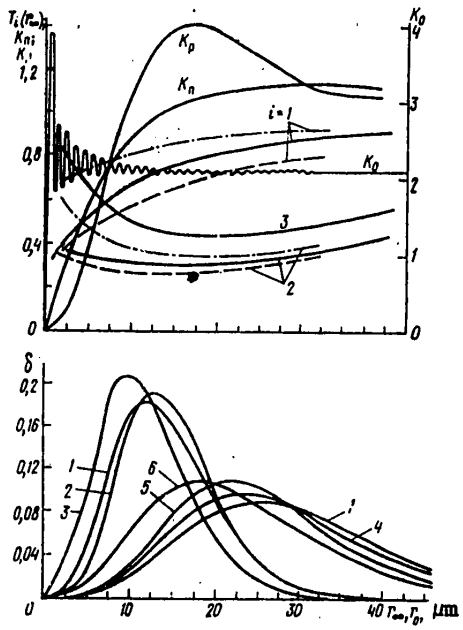

Fig. 4. Distributions of parameters $T_i(r_\infty)$ at R = 5 μm, μ = 2, $I_0 = 500$ W/cm^2, $T_\infty = 273$ (solid lines) and 293 K (dot-and-dash), $I_0 = 200$ W/cm^2, $T_\infty = 273$ K (broken lines); at R = 10 μm, μ = 2, $I_0 = 500$ W/cm^2, $T_\infty = 273$ K (solid lines) and specific contributions of groups of droplets $\delta_П$ and $\delta_И$ (*1*, *4*), δ_p (*2*, *5*), δ_T (*3*, *6*), δ_B (*1*, *7*) at $I_0 = 500$ W/cm^2, $T_\infty = 273$ K, R = 5 μm, μ = 2 (*1-3*) and R = 10 μm, μ = 2 (*4-7*) with respect to r_∞ at $t = 7.5 \cdot 10^{-2}$ s, and distributions of effectiveness parameters $K_П$, K_p, K_0 with respect to r_0

Fig. 4 shows the distributions of parameters $T_i(r_\infty)$ and specific contributions of individual groups of droplets to absorption ($\delta_П$), scattering (δ_p), vaporization ($\delta_И$), thermal conductivity (δ_T) and initial water content of the medium (δ_B) with respect to radius r_∞. Parameters $T_i(r_\infty)$ are determined analogously to parameters T_i (8), but they were calculated for individual groups of droplets with fixed initial radius. The values of $T_i(r_\infty)$ and all δ make sense only for the reference radii r_∞ of the groups of droplets indicated by the marks on Fig. 4, since the specific contribution of a group of droplets depends on the interval of partitioning Δr_∞ of the aerosol droplet spectrum into groups (in the given case $\Delta r_\infty = 2.5$ μm). Here $\Sigma\delta_П(r_\infty) = 1$, $\Sigma\delta_p(r_\infty) = 1$, $\Sigma\delta_И(r_\infty) = 1$, $\Sigma\delta_T(r_\infty) = 1$, $\Sigma\delta_B(r_\infty) = 1$. Let us note that the specific contributions of the groups practically do not depend on time. We see from Fig. 4 that in the given case $\delta_П$, δ_p and $\delta_И$ are determined by the specific contribution of each group of droplets to the initial water content of the medium. The specific contribution of groups of droplets to thermal conductivity is shifted toward lower r_∞ compared with the other specific contributions. Parameter $T_1(r_\infty)$ increases monotonically with increasing r_∞. All this is due to

the considerable reduction in the contribution made by thermal conductivity to the energy balance of the vaporizing droplets as r_∞ increases [Ref. 11].

2. Consider the influence that radiation energy flux density I_0 and initial droplet temperature T_∞ have on the dynamics and fundamental parameters of the dispersal process. Numerical calculations were done on the process of dispersal of a polydisperse aerosol with R = 5 μm, μ = 2 at I_0 = 50, 200, 500 W/cm^2, and 1 kW/cm^2, T_∞ = 273 and 293 K. The results are summarized in Table 2. When an aerosol is exposed to radiation with different I_0 and durations of action t_B, of fundamental interest is the attainment of the maximum effectiveness of the action at constant energy density, i. e. at

$$I_0 t_B = \text{const.} \qquad (11)$$

TABLE 2

R = 5 μm, α = 1, n = 1.173, κ = $8.23 \cdot 10^{-2}$ [Ref. 10]

I_0, W/cm^2	50	50	200	200	500	500	1000	1000	500	500
μ	2	2	2	2	2	2	2	2	4	6
T_∞, K	273	293	273	293	273	293	273	293	273	273
$\bar{T}_1$	0,49	0,73	0,62	0,78	0,74	0,84	0,82	0,88	0,67	0,64
$\bar{T}_2$	0,23	0,32	0,27	0,34	0,31	0,36	0,34	0,38	0,32	0,32
$\bar{T}_3$	0,47	0,47	0,47	0,47	0,47	0,47	0,47	0,47	0,51	0,54
$T_m (r_\infty = 5)$, K	275	294	283	297	295	304	307	311	296	297
$\bar{T}_m (r_\infty = 15)$, K	289	301	312	317	332	334	348	350	333	334
$\bar{T}_m (r_\infty = 30)$, K	306	313	335	338	359	360	374	375	360	361
$\bar{v} (N_0 = 1)$ km/s	11,3	16,7	55,7	72	166	194	366	407	374	540
t_y, s	1,33	0,84	0,255	0,2	$8,5 \cdot 10^{-2}$	$7,3 \cdot 10^{-2}$	$3,9 \cdot 10^{-2}$	$3,5 \cdot 10^{-2}$	0,1	0,11
t_{sy}, s	2	1,3	0,38	0,3	0,13	0,11	$6 \cdot 10^{-2}$	$5,3 \cdot 10^{-2}$	0,17	0,21

Fig. 2a shows the distributions of Z and Z_3 with respect to ξ for I_0, t_B that satisfy condition (11). The greater the I_0 (and the smaller the t_B), the greater will be the degree of dispersal of the medium, and the velocity of the dispersal wave, and the higher will be the effectiveness of the action of radiation on the aerosol (see Fig. 2a, 4, Table 2). Action of radiation with greater I_0 on the aerosol appreciably decreases $S_П$, S_p, S_T due to more intense vaporization of droplets and a sharp reduction in the contribution of thermal conductivity to the energy balance of the vaporizing droplets. Failure to account for thermal conductivity and scattering of radiation by droplets overstates $\bar{v}$ and understates t_y by a factor of ~3 [Ref. 4].

At moderate values of I_0 = 50, 200 W/cm^2, an increase in T_∞ noticeably accelerates the dispersal process and increases $\bar{v}$, T_1 and T_2. However, with increasing I_0 (e. g. at I_0 = 1 kW/cm^2) there is an appreciable decrease in the influence of T_∞ on parameters of the dispersal process. This is due to the fact that with increasing I_0, energy $Q_T(r_0)$ becomes small compared with $Q_П(r_0)$, $Q_p(r_0)$, $Q_Н(r_0)$, and decreasing Q_T with increasing T_∞ has little effect

on $\bar{v}$. Parameters T_3 and $T_3(r_\infty)$ show practically no change with variation in I_0, T_∞, just as $\delta_п(r_\infty)$, $\delta_р(r_\infty)$, $\delta_и(r_\infty)$, $\delta_т(r_\infty)$.

TABLE 3

I_0, W/cm^2	$n=1{,}173$, $\varkappa=8{,}23\cdot10^{-3}$ [10]							$n=1{,}144$, $\varkappa=6{,}7\cdot10^{-3}$ [14]		
	$R=10$ μm, $\alpha=1$			$R=5$ μm, $\alpha=3{,}6\cdot10^{-2}$				$R=5$ μm, $\alpha=1$		
	500	500	500	50	200	500	1000	50	200	500
μ	2	4	6	2	2	2	2	2	2	2
T_∞, K	273	273	273	273	273	273	273	273	273	273
$\bar{T}_1$	0,83	0,79	0,77	0,40	0,55	0,69	0,80	0,48	0,61	0,73
$\bar{T}_2$	0,34	0,31	0,31	0,18	0,24	0,29	0,32	0,21	0,27	0,31
$\bar{T}_3$	0,47	0,45	0,45	0,47	0,47	0,47	0,47	0,48	0,48	0,48
$\bar{T}_m$ ($r_\infty=5$), K	291	294	295	276	288	303	310	275	281	293
$\bar{T}_m$ ($r_\infty=15$), K	327	330	331	289	316	338	351	287	310	330
$\bar{T}_m$ ($r_\infty=30$), K	354	357	358	306	338	362	375	303	333	357
$\bar{v}$ ($N_0=1$), km/s	24	51	68	8,9	49,5	154	360	10,7	55,5	165
t_v, s	0,1	0,11	0,12	1,6	0,29	$9{,}2\cdot10^{-2}$	$3{,}95\cdot10^{-2}$	1,35	0,26	$8{,}6\cdot10^{-2}$
t_{sv}, s	0,12	0,13	0,14	2,4	0,44	0,14	$6\cdot10^{-2}$	2	0,4	0,13

The steady-state maximum values of $\bar{T}_m(r_\infty)$ depend appreciably on I_0, T_∞, the dependence of $\bar{T}_m(r_\infty)$ on T_∞ becoming weaker with increasing I_0. At $I_0 = 1$ kW/cm^2 for droplets with $r_\infty = 25$–30 μm $\bar{T}_m$ somewhat exceeds the limit of the diffusion mode of vaporization; however, the contribution of droplets with $r_\infty = 25$–30 μm to processes of dispersal is small (less than 5%) and the above-mentioned excess practically introduces no error. The $\bar{T}_m(r_\infty)$ given in tables 2 and 3 for different variants enable us to estimate the interval of temperature change for droplets of different initial dimensions as they vaporize in a dispersal wave.

For the entire range of initial intensities used $I_0 = 50$ W/cm^2–1 kW/cm^2 and temperatures $T_\infty = 273$, 293 K at $\bar{T}_m$ we have $r_0 \cong 3.5$, 11, 23 μm for $r_\infty = 5$, 15, 30 μm respectively, i. e. the radius of droplets in the dispersal wave at $\bar{T}_m$ is about 0.7 r_∞. Consequently, for the case of unsteady vaporization of polydisperse aerosol droplets over a range of the degree of quasi-steadiness $1 < D_1 \leqslant D_{1m}$ the aerosol loses about 60% of its water content, and this value is practically independent of changes in I_0, T_∞, α, n, $\varkappa$. The process of vaporization inside the aerosol is appreciably unsteady, and the quasi-steadiness parameter $\bar{D}_{1m}(r_\infty)$ depends on the initial parameters of the problem. Parameter $\bar{D}_{1m}(r_\infty)$ increases sharply with increasing I_0, r_∞ and depends on T_∞ (see Table 1). For the entire set of initial parameters used at fixed $D_1 = 1.05$, r_0 depends weakly on I_0, T_∞, and for $r_\infty = 5$, 15, 30 μm we have $r_0 \cong 4{,}85$, 13.2, 26.5 μm, i. e. r_0 at $D_1 = 1.05$ is about 0.9 r_∞. Thus in the range of $1.05 \leqslant D_1 \leqslant D_{1m}$ in the case of appreciably unsteady vaporization in the dispersal wave the aerosol droplets lose ~25% of their water content, and this value is practically independent of changes in the initial parameters of the problem.

Let us consider the influence that the coefficient of vaporization α and the optical constants of water have on the dispersal process. The values of α, and of the indices of refraction n and absorption κ of water on $\lambda = 10.6$ μm differ noticeably from one another. The value of $\alpha = 1$ used above is apparently the most exact according to the results of the latest experiments [Ref. 15]. To determine the influence that α has on the dispersal process, calculations were done at the minimum known $\alpha = 3.6 \cdot 10^{-2}$ (see Ref. 15) using the previous values of $n = 1.173$ and $\kappa = 8.23 \cdot 10^{-2}$ [Ref. 10]; the results are summarized in Table 3. Let us note that the minimum $\alpha = 3.6 \cdot 10^{-3}$ was used in Ref. 6 for all the calculated versions except for one. The use of $\alpha = 3.6 \cdot 10^{-2}$ leads to slower vaporization of aerosol droplets under the action of radiation, an appreciable reduction in the velocity of the dispersal wave and a considerable change in parameters of the dispersal process (see Table 3) with the exception of parameter $\overline{T}_3$. Consequently, a change in α can appreciably influence the parameters of the dispersal process. To determine the effect of optical parameters n, κ on the dispersal process, calculations were done at $\alpha = 1$ and the minimum known $n = 1.144$, $\kappa = 6.7 \cdot 10^{-2}$ [Ref. 14]; the results are summarized in Table 3. When n, κ from Ref. 14 are used, the main parameters of the dispersal process $\overline{T}_1$, v are similar or identical to the corresponding parameters at n, κ from Ref. 10. Thus a change in n, κ within the given limits has nearly no effect on the main parameters of the dispersal process.

Let us determine the spatial dimensions $\Delta\xi$ of the transition zone in which the aerosol properties change from the state of total dispersal (on the left boundary of the zone $Z = 0.99$) to the practically undisturbed state of the aerosol (on the right-hand boundary $r_0 = 0.99 r_\infty$), and the dependence of on I_0, T_∞ for the steady state of the dispersal process. During the unsteady stage of the process of dispersal, the dimensions of the transition $\Delta\xi$ increase; at $t \gtrsim t_y$, $\Delta\xi$ is constant. The aerosol at $r_0 \lesssim 0.1 r_\infty$ practically does not attenuate radiation, i. e. the coefficient of attenuation of radiation as a result has decreased by $\sim 10^2$-10^3 times. The spatial dimensions of the transition zone $\Delta\xi$ for different variants at $R = 5$ μm, $\mu = 2$ are: $\Delta\xi \cong 1$-1.2 ($\Delta x = 1.274 \cdot 10^6 \Delta\xi / N_0$ cm, e. g. at $N_0 = 2 \cdot 10^2$ cm^{-3}, $\Delta x \cong 63$-76 m) and are practically independent of I_0, T_∞.

3. Of considerable interest in the investigation of the process of polydisperse aerosol dispersal under the action of radiation is analysis of the influence that the form of the initial aerosol droplet distribution function has on the dispersal process. Function $f_0(r_0)$ (10) with different R, μ satisfactorily describes real droplet size distribution functions in clouds and mist [Ref. 14]. Variations of R and μ appreciably change the initial values of aerosol water content and coefficients of attenuation of the acting and probing radiation, and accordingly cause a noticeable change in parameters of the dispersal process.

Let us use the freest possible change in N_0 for objective comparison of the effectiveness of dispersal with different functions $f_0(r_0)$. Consider the process of dispersing a polydisperse zerosol with constant initial water content

$$\rho = \frac{4}{3} \pi \rho_n N_0 \int_0^\infty r_0^3 f_0(r_0) dr_0 = \text{const}, \qquad (12)$$

but with different droplet concentrations N_0 and parameters R, μ of distribution function $f_0(r_0)$. Calculations were done on the process of dispersal of a polydisperse aerosol at $I_0 = 500$ W/cm^2, $T_\infty = 273$ K, R = 5 and 10 μm, $\mu = 2$, 4, 6. The results of the calculations demonstrate the influence of a change in parameter μ at fixed R on the dispersal process. At R = 5, 10 μm with consideration of the constancy of ρ (12), for every 100 droplets of aerosol with distribution function $f_0(r_0)$ (10) at $\mu = 2$, there are 228 aerosol droplets at $\mu = 4$, and 319 droplets at $\mu = 6$ respectively. Fig. 2b shows distributions $Z(\xi)$, $Z_3(\xi)$ at R = 5 μm and $\mu = 2$, 6 for several t. The initial distributions $Z(\xi)$ and $Z_3(\xi)$ at t = 0 and different μ are near each other, i. e. the initial coefficients of attenuation of the acting and probing radiation by the aerosol in the given case are approximately identical. In the process of aerosol dispersal the distributions $Z(\xi)$ also practically coincide, i. e. at R = 5 μm with condition (12), μ has no appreciable effect on aerosol dispersal on λ. This is also confirmed by the equality of dispersal wave velocities calculated with consideration of constancy of ρ (12) at $N_0 = 1$ cm^{-3}, $\mu = 2$: $\bar{v}(\mu = 2) \cong \bar{v}(\mu = 4)/2.28 \cong \bar{v}(\mu = 6)/3.19 \cong 166$ km/s (see Table 2). Consequently, only the water content ρ has a decisive effect on the process of aerosol dispersal on λ at R = 5 μm. However, distributions $Z_3(\xi)$ in the dispersal process for $\mu = 2$, 6 differ from $Z(\xi)$ and from each other, i. e. an increase in μ may influence the aerosol dispersal on λ_p.

Fig. 3 shows the time dependences of v and v_3 for some Z_Φ, $Z_{3\Phi}$ at R = 5 μm, $\mu = 6$. An increase in μ appreciably reduces the number of groups of droplets that make the main contribution to the water content of the medium, absorption, scattering and so on, and the polydisperse aerosol begins to approach a monodisperse condition. This situation as the radii r_0 of the droplets decrease as a consequence of vaporization with consideration of the oscillatory dependence of $K_0(r_0)$ (see Fig. 4) in the given case $\mu = 6$ leads to nonmonotonic behavior of $v_3(t)$ and a considerable reduction of t_{3y} as compared with t_y.

An increase in R to 10 μm shifts function $f_0(r_0)$ (10) toward larger r_0 and appreciably changes the parameters of the dispersal process $\bar{T}_i$, v, t_y, t_{3y} (as compared with R = 5 μm). Fig. 4 shows distributions $T_i(r_\infty)$ and δ_Π, δ_p, δ_H, δ_T, δ_B, with respect to r_∞ at R = 10 μm, $\mu = 2$. Parameters $T_i(r_\infty)$ practically ($T_3(r_\infty)$ exactly) coincide at R = 5 and 10 μm. The maxima of distributions of specific contributions of groups to processes shift toward larger r_∞, the main contribution being made by droplets with $r_\infty \sim$ 10-40 μm. At R = 10 μm and constant water content ρ (12), an increase in μ reduces the steady-state velocity of the dispersal wave $\bar{v}$, e. g. at N = 1 cm^{-3} analogously with the case R = 5 μm, at $\mu = 2$, 4, 6 respectively we have $\bar{v} = 24$, 22.4, 21.2 km/s. Consequently at R = 10 μm and constant ρ, parameter μ may influence aerosol dispersal on wavelength λ as well as $\bar{v}$.

It is of interest to compare the values of the principal parameter $\bar{v}$ of the dispersal process at fixed μ for R = 5 and 10 μm. At $\mu = 2$, 4, 6 with consideration of constancy of ρ (12), for every 100 aerosol droplets with function $f_0(r_0)$ (10) at R = 10 μm there are about 800 droplets at R = 5 μm. Velocity $\bar{v}$ calculated with consideration of (12) for an aerosol with R = 10 μm is greater than at R = 5 μm for the same μ. With increasing μ (at $\mu = 6$) the difference in values of $\bar{v}$ decreases (see tables 2, 3). Consequently, parameter R has

an influence on $\bar{v}$. The spatial dimensions of the transition zone $\Delta\xi$ depend on R, μ: at R = 5 μm, $\mu = 6$, $\Delta\xi \cong 3$-3.7; at R = 10 μm, $\mu = 2$, $\Delta\xi = 0.2$-0.30, and at $\mu = 6$, $\Delta\xi \cong 0.35$-0.45.

The results of calculations given in tables 2, 3 show that parameter $\bar{T}_3$ (the ratio of the absorbed radiation energy to the sum of the energies of radiation absorbed and scattered by the aerosol) does not depend on I_0, T_∞, α, but only on the parameters R, μ of the function $f_0(r_0)$ and to a lesser extent on the optical constants n, κ. The parameter $\bar{T}_3$ also changes very little in the interval 0, t_y (see Fig. 3). All this shows that $\bar{T}_3$ is apparently determined by the initial parameters of the problem R, μ, n, κ and does not depend on the dynamics of processes of vaporization and dispersal. Of interest is derivation of an approximate formula for $\bar{T}_3$ that describes the dependence of $\bar{T}_3$ on the initial parameters of the problem. Let us set

$$\bar{T}_3 = \varkappa_{n0}/\varkappa_0, \tag{13}$$

where $\varkappa_{n0} = \pi N_0 \int_0^\infty r_0^2 K_n(r_0)\, f_0(r_0)\, dr_0$ is the coefficient of absorption of radiation by the aerosol. For example at n = 1.173, $\kappa = 8.23 \cdot 10^{-2}$ [Ref. 10], R = 5 μm, $\mu = 2$, 4, 6, $\tilde{T}_3 = 0.455$, 0.49, 0.494 respectively; at R = 10 μm, $\mu = 2$, 4, 6, $\tilde{T}_3 = 0.47$, 0.443, 0.437 respectively. At n = 1.144, $\kappa = 6.7 \cdot 10^{-2}$ [Ref. 14], R = 5 μm and $\mu = 2$, T_3 (13) is equal to 0.455. From a comparison of $\tilde{T}_3$ and $\bar{T}_3$ from tables 2, 3 it is clear that (13) correctly describes the dependence of $\bar{T}_3$ on the initial parameters of the problem and agrees satisfactorily with the numerical values of $\bar{T}_3$.

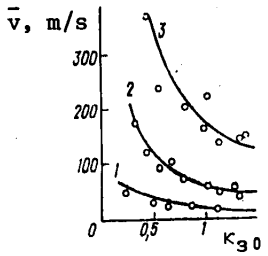

Fig. 5. Experimental (points) [Ref. 9] and theoretical (curve) dependences of $\bar{v}$ on κ_{30} for $I_0 = 50$ (*1*), 180 (*2*) and 500 (*3*) W/cm^2

Fig. 5 shows the calculated and experimental dependence [Ref. 9] for the velocity $\bar{v}$ of the dispersal wave as a function of the initial coefficient of attenuation of the probing radiation κ_{30} for some I_0. It can be seen that the results of calculations agree satisfactorily with experiment.

REFERENCES

1. Glickler, S. L., APPL. OPTICS, Vol 10, 1971, p 644.

2. Sukhorukov, A. P., Shumilov, E. N., ZHURNAL TEKHNICHESKOY FIZIKI, Vol 43, 1973, p 1029.

3. Bukatyy, V. I., Zuyev, V. Ye., Kuzikovskiy, A. V., Khmelevtsov, S. S., DOKLADY AKADEMII NAUK SSSR, Vol 217, 1974, p 52.

4. Romanov, G. S., Pustovalov, V. K., "Prosvetleniye oblachnoy sredy, soderzhashchey kapli vody, pod deystviyem intensivnogo monokhromaticheskogo izlucheniya" [Dispersal of Cloudy Medium Containing Water Droplets Under the Action of Intense Monochromatic Radiation], Preprint, Institute of Physics, BSSR Academy of Sciences, Minsk, 1975; ZHURNAL TEKHNICHESKOY FIZIKI, Vol 47, 1977, p 168.

5. Korotin, A. V., Svetogorov, D. Ye., Sedunov, Yu. S., Semenov, L. P., DOKLADY AKADEMII NAUK SSSR, Vol 220, 1975, p 829.

6. Gordin, M. P., Strelkov, G. M., KVANTOVAYA ELEKTRONIKA, Vol 3, 1976, p 2427.

7. Volkovitskiy, O. A., Manonov, V. K., KVANTOVAYA ELEKTRONIKA, Vol 4, 1977, p 1123.

8. Yegorov, K. D., Kandidov, V. P., Prakhov, M. S., KVANTOVAYA ELEKTRONIKA, Vol 6, 1979, p 2562.

9. Volkovitskiy, O. A., Matveyev, O. M., Pechorin, V. T., Skripkin, A. M., TRUDY INSTITUTA ELEKTROMEKHANIKI, No 13, 1976, p 108.

10. Zel'manovich, I. L., Shifrin, K. S., "Tablitsy po svetorasseyaniyu, t. 3. Koeffitsiyenty oslableniya, rasseyaniya i luchevogo davleniya" [Tables on Light Scattering, Vol 3. Coefficients of Attenuation, Scattering and Radiation Pressure], Leningrad, Gidrometeoizdat, 1968.

11. Pustovalov, V. K., Romanov, G. S., KVANTOVAYA ELEKTRONIKA, Vol 4, 1977, p 84.

12. Bargaftik, N. B., "Spravochnik po teplofizicheskim svoystvam gazov i zhidkostey" [Handbook on Thermophysical Properties of Gases and Liquids], Moscow, Nauka, 1972.

13. Kay, J., Luby, T., "Tablitsy fizicheskikh i khimicheskikh postoyannykh" [Tables of Physical and Chemical Constants], Moscow, GIFML, 1962.

14. Zuyev, V. Ye., "Rasprostraneniye vidimykh i infrakrasnykh voln v atmosfere" [Propagation of Visible and Infrared Waves in the Atmosphere], Moscow, Sov. radio, 1970.

15. Neizvestnyy, A. I., DOKLADY AKADEMII NAUK SSSR, Vol 243, 1978, p 626; IZVESTIYA AKADEMII NAUK SSSR: SERIYA FIZIKA ATMOSFERY I OKEANA, Vol 15, 1979, p 74.

6610
CSO: 1862/133

MATHEMATICS

UDC 681.5.015.26

OPERATIVE IDENTIFICATION OF CONTROL OBJECTS

Moscow OPERATIVNAYA IDENTIFIKATSIYA OB"YEKTOV UPRAVLENIYA in Russian 1982 (signed to press 2 Dec 81) pp 4-12, 271-272

[Annotation, preface, introduction and table of contents from book "Operative Identification of Control Objects", by Iosif Isaakovich Perel'man, Energoizdat, 6000 copies, 272 pages]

[Text] Methods of operative identification are described and analyzed: procedures for gathering, restoring and processing a posteriori information coming from an object for the purpose of getting a running mathematical model that is necessary for control. Principal attention is given to construction and analysis of dynamic models that provide a quantitative description of the object in input-output terms.

For engineers, technicians and scientists in the field of automatic control. Will be of use to upperclassmen and graduates in the corresponding areas.

Preface

At the present time, object identification is one of the most intensively developing divisions of control theory. The extensive literature on this problem has been enriched in recent years by a number of detailed monographs that have deservedly become well known among specialists. Nevertneless, new problems have arisen and been solved with the further development of theory and practice in identification. Advances in modern computer technology and the extensive use of computers in control systems have eliminated numerous difficulties that had been a major topic of discussion until recently in the literature on identification. At the same time, more fundamental and important unsolved problems have appeared. First among these is the problem of a comprehensive approach to identification procedures, and methods of applying the results to control algorithms; and secondly, the problem of creating identification methods that are adequate for actual practice of automated control system design (especially automatic systems for controlling complicated technological objects), i. e. under conditions where a model of the object is to be reconstructed on the basis of a limited volume of noisy experimental data and rather vague a priori information on the internal structure of the object, and on statistical characteristics of perturbations applied to the object. In many cases, these difficulties are aggravated still

more by drifting of the characteristics of the object. The enumerated topics constitute the principal subject matter of the book.

This book has been written for specialists working in the field of designing and introducing automated systems for control of technological processes. It is assumed that the reader is acquainted with the principles of automatic control theory (including elements of the theory of random processes).

The author takes this opportunity to express sincere gratitude to S. B. Dement'yeva, N. K. Kachko and N. A. Usiyevich for assistance in preparing the manuscript for publication, and to B. G. Borchik and O. A. Polyakov for a number of constructive comments made in editing and discussing the book.

The author

Introduction

Given a formulated goal of control and a predetermined quality criterion for its attainment, the development of any control system, be it in engineering, economics or any other field of application, reduces to solution of two interrelated problems: the problem of constructing a model of the object, and the problem of constructing a control algorithm corresponding to the given model and to the predetermined goal of system operation. Here the term "model" is used in a broad sense: it is understood to mean such a minimum volume of information on the object and the medium acting on it as will be sufficient for consturcting an optimum, or at least workable control procedure.

If the first part of the problem of constructing the system, i. e. the model, has been obtained, then the second part reduces to synthesis of a control algorithm when all information for this is available. Development of the automatic control theory has come about historically in such a way that until relatively recently attention has been concentrated mainly on the second part of the problem.

The generally known advances made in this direction are the core of the present theory of control. Such are the classical methods of analysis and synthesis of closed systems of regulation, filtration and extrapolation of random processes, optimum control in the presence of constraints, game theory, queueing theory and the like.

In the enumerated divisions of the theory, for the most part questions remain open on how information on the model necessary for realizing the given control system is obtained under real conditions; how this information can be supplemented and refined in the course of operation of the system and how the design of the system should depend on accuracy of initial information. We must assume that this omission is indeed one of the main reasons for such a glaring gap between the advances in control theory and their practical application. These same circumstances are the cause of the continuously rising interest in the theory of identification of control objects, and especially in the problem of reconstructing unknown characteristics of an object from results of observation of its output signals.

The development of identification theory has proceeded at a rapidly accelerating pace over the last 15 years. The availability of a large number of definitive papers on the subject (e. g. monographs 47, 52, 65 in the list of references) permits us to circumvent detailed enumeration of the advances that have been made in this area. Nonetheless, a number of gaps remain that prevent the present theory of identification from fully meeting the requirements of practice in designing control systems, and above all -- designing highly efficient automated control systems for complicated technological facilities. It is the main goal of this book to narrow some of these gaps. The approach developed herein consists in methods of reconstructing a mathematical model that gives a description of objects in input-output terms, and directly using this reconstructed model of the object in different control algorithms. in doing this, both in designing and using the reconstructed model there is absolutely no need for the model to reflect the internal properties of the object (such as values of intermediate phase coordinates or of the individual parameters of the transfer function of the object). As we will see later, on the one hand the elimination of these requirements appreciably simplifies the identification problem. On the other hand, getting rid of these requirements necessitates moving to control systems specially adapted to the use of reconstructed models.

To explain the additional possibilities opened up by the approach developed in this book, let us consider the problem area associated with designing systems for controlling linear dynamic objects. In its traditional formulations, the problem of identifying such objects is usually taken as that of statistical estimation of coefficients of the transfer function (or coefficients of the system of controls in Cauchy form) at a given order of the object.† At first glance, such a formulation completely corresponds to practical requirements since the information on coefficients of a differential (or difference) equation of the object is necessary and sufficient for constructing classical control algorithms (up to those as complex as optimum algorithms with the use of a Kalman filter). However, we can point out the following two circumstances that appreciably limit the possibility and advisability of such an approach.

There are fundamental difficulties involved in finding consistent statistical estimates of coefficients of the transfer function of the object from noisy experimental data. The fact is that getting such estimates requires using the maximum likelihood method, which reduces to forming a likelihood function $S_n(\theta)$ that depends on the vector of unknown parameters θ and on the volume n of the experimental sample in such a way that in the asymptotic limit it has an extremum at point θ corresponding to the true value of parameters of the object. However, unfortunately the likelihood function used in identification of a dynamic object in the general case is not unimodal, i. e. in addition to the mentioned true extremum there are false extrema whose number, location and depth usually cannot be accounted for ahead of time.‡ As a

†In addition, some papers (e. g. Ref. 67) examine the problem of estimating the unknown order of the transfer function.

‡It can be shown [Ref. 44] that the number of extrema of the function $S_n(\theta)$ is a random quantity with distribution that depends on n. The upper

consequence, finding the true extremum is a practical possibility only when there is considerable a priori information on the object (mainly information that enables preliminary isolation of the region of attraction of this extremum). At the same time, as will be shown later, the mentioned fundamental difficulties are not typical of the problem of synthesizing a reconstructed model of the object. This advantage is not bestowed gratis, but is achieved by the fact that the reconstructed model of the object carries less complete (rougher) information on the object. However, as it turns out, the latter disadvantage is of no significance with appropriate choice of control methods.

As was stated above, a model in the form of a differential equation (or transfer function) is needed for constructing traditional control algorithms. At one time, these algorithms were worked out with consideration of rigid constraints stemming from the fact that they were to be realized on then available analog computer facilities. However, simplicity of realization, which was the principal advantage of classical control algorithms, has lost its former importance. Thanks to the use of computers in modern automated systems for controlling technological processes, capabilities have been brought about for going on to more universal control methods enabling expansion of the class of problems that can be solved in the automated control system, and improving the economic effectiveness of these systems. As demonstrated in this book, the information on the object that is necessary for realization of these methods can be assigned as a reconstructed model of the object, and in the given case the entire model (rather than individual parameters) is directly included in the control algorithm.

Clearly, to set up systems based on using reconstructed models, we need first of all to have methods of identifying these models, procedures that are workable under conditions typical of actual automated control system design practice. In particular, as applied to problems of controlling complex technological processes this means that the model must be reconstructed on the basis of a limited volume of noisy experimental data and rather vague a priori information on the object. Moreover, in some cases in addition to these difficulties the characteristics of the object may drift in time so that the model becomes obsolete.

It is natural that the mentioned circumstances cause some specific peculiarities in the methodology of reconstructing models intended for describing the behavior of an object in input-output terms. Thus the central issue in synthesizing the reconstructed model of the object becomes selection of the structure of the model. The essence of this problem is briefly as follows.

All models of identification that are used in practice (including the methods considered in this book) in spite of all their diversity can be reduced to a combined scheme: on the basis of certain arguments (based mainly on the available a priori information on the object) the structure of the model is chosen, i. e. the future reconstructed model of the object is assigned except

---

limit of this distribution, i. e. the maximum possible number of extrema of the likelihood function, increases in proportion to n although the probability of reaching this boundary then approaches zero.

for a certain number of unknown parameters. Then these parameters are estimated by the corresponding methods of mathematical statistics on the basis of available experimental observations of operation of the object.

At first glance it would seem that the more complex the selected structure of the model, i. e. the greater the number of its parameters that can be varied (the number of degrees of freedom), the greater will be the possibilities for improving accuracy of the reconstructed model. In fact this is not the case. As will be shown later in this book, if the time of gathering experimental data is limited (and under real conditions this always occurs), the accuracy of the reconstructed model (as a whole) is an extremum function of the complexity of the structure: other things being equal, as the complexity of the structure increases the accuracy of the reconstructed model of the object at first increases, and then falls off; the optimum complexity depends on the volume of available experimental information, and on the characteristics of the object. In view of the fact that with respect to formulation of the identification problem itself these characteristics are a priori unknown and can be estimated only by using the reconstructed model, a vicious circle arises in selecting the structure that makes a formal approach to optimum construction of the model impossible. Furthermore, the available information under real conditions is often inadequate even for sound application of relatively complicated statistical methods of evaluating the parameters of the model (such as minimizing the Bayes risk).

Thus on some stages of identification (and especially on the stage of choosing the structure), the developer is faced with a creative task -- the necessity of making a decision under conditions that are not strictly formalized, i. e. under conditions where an attampt at optimality (like the concept of "optimum decision" itself) loses its connotative meaning and is replaced by the more capacious and less specific concept of a rational decision.

At this stage of our presentation it might be advisable to move away from our main topic and examine the following question, that is in some sense philosophical: what part is played by theory, and first of all by exact mathematical methods, in the solution of creative engineering problems in general, and in the problem area that we are considering in particular?

Before going on to a specific answer, we should point out the fundamental difference in the goals of theoretical studies relating to a system with complete information and the problems that are being considered here. In the former case, the goal is to get an unambiguous operating method that leads tc optimum solution of the formulated problem. Although the results of the theory are formally addressed to a human operator, in actuality this situation can be circumvented by putting the appropriate theoretical results in the form of a computer program into which the engineer who is developing the system has only to enter specific numerical material. In other words, application of theoretical results to solution of practical problems in the given case does not require the intelligence of the developer. Let us note that this advantage is typical of many divisions of the technical sciences; for example: calculation and design of electrical machines, electronic amplifiers, standard machine components and the like are strictly programmable.

However, this is not the part played by theory in the other area of practice where elements of uncertainty make it impossible to establish a strict program of optimum operations, and one must make do with rational decisions that are arrived at by application of human intelligence to a specific practical problem. This area covers such processes of practical activity as scientific research, diagnosis, administrative management and so on. Here the applied value of theory consists in providing the human operator with summary representations that show the comparative advantages and disadvantages of each of these strategies under various conditions of use, and enable analysis of the possible results of applying each of these strategies. Thus in contrast to problems with complete information where the synthesis of optimum solutions is of principal significance, in problems that contain an element of creativity the main purpose of theory is to provide methods of analysis and to evaluate the quality of decisions.

All this is applicable to the specific problem under consideration. In solving the problem of reconstructing a model under conditions of insufficient a priori information, the designer of the model must rely on theoretical knowledge that is provided mainly by the following material:

knowledge of basic patterns in the way that the choice of structures affects quality of the reconstructed model;

the formalism of theoretical analysis of the quality of identification algorithms, and the principal facts established on the basis of such analysis concerning the comparative advantages of these algorithms when the models reconstructed with their aid are used in control problems.

This problem area is the main topic of this book.

Basic notation in the text follows theses principles:

matrices are denoted by boldface upper-case letters;
vectors (column matrices) -- by boldface lower-case letters;
A^T--transposed matrix;
$\|\cdot\|$--norm of a matrix (vector);
sp A--Spur of a matrix;
$\triangleq$--equality by definition;
$M\{f(\cdot)\}$--mathematical expectation of $f(\cdot)$ taken over sets of all random arguments of this function; $M_{x,y}\{f(x, y, z\}$ and $M\{f(x, y, z)|z\}$--conditional mathematical expectation of function $f(x, y, z)$ taken over the set of random variables x and y at given z;
$\forall$--quantor of generality ($\forall x \in X$ corresponds to the formulation "for all x that belong to the set X").

Contents page

6610
CSO: 1862/157

UDC 62-501.163

METHODS OF SYNTHESIZING LOW-SENSITIVITY LINEAR CONTROL SYSTEMS

Moscow METODY SINTEZA LINEYNYKH SISTEM UPRAVLENIYA NIZKOY CHUVSTVITEL'NOSTI in Russian 1981 (signed to press 26 Oct 81) pp 2-9, 100-103, 105

[Annotation, introduction, conclusion and table of contents from book "Methods of Synthesizing Low-Sensitivity Linear Control Systems", by Aleksandr Ivanovich Yermachenko, Izdatel'stvo "Radio i svyaz'", 1920 copies, 105 pages]

[Text] The book examines the theory and practical methods of synthesizing control systems with low sensitivity to parametric perturbations. Algorithms are proposed for synthesizing linear singly connected and multiply connected automatic systems with consideration of requirements for fundamental and additional motions. They enable development of modern engineering methods of design with the use of computers. Examples are given.

The book is intended for scientists and engineers working in the field of synthesizing control systems.

Table 1, figures 37, references 36.

Introduction

The increasing complication of functions performed by automatic control systems and rising requirements for working quality of these systems under conditions of limited resources make it necessary to improve known methods and develop new ones for designing technical systems. Several approaches have been used in research on synthesizing automated control systems with consideration of requirements for insensitivity to changes in the parameters of components [Ref. 1].

The first approach is synthesis of systems according to criteria of parametric invariance and zero sensitivity [Ref. 1-9], and in the second [Ref. 3, 10, 11] the structure of the system is selected such that the point of inclusion of an object as the least stable link is determined by sensitivity requirements. The third approach [Ref. 6, 12] is based on introducing redundant components (correcting links) that give rise to an additional degree of freedom in the system. Such systems with redundant components were called systems with two degrees of freedom in Ref. 12. The redundancy in these systems is used for simultaneous satisfaction of requirements for fundamental and additional

motions. We will consider synthesis of optimum crude systems [Ref. 1, 6, 13, 14] as a fourth approach. The new factor here with respect to methods of optimum control synthesis is the presence of a crudeness functional that may be minimized or used as a constraint, depending on the formulation of the problem. The fifth approach is based on introducing additional feedback into the system: feedback with respect to sensitivity functions [Ref. 1, 6, 14, 15-20].

Analysis of all these approaches shows that each of them assumes a change in structure of the control device such that one of the properties of the system -- sensitivity to variations of system component parameters -- varies in a certain way. Sensitivity is closely interrelated with other characteristics of the system such as stability, the quality indicators of transient processes and the like. This relationship does not always permit attainment of arbitrary sensitivity of the system when other characteristics are assigned, and requires introduction of constraints on additional variables (sensitivity functions) when calculating low-sensitivity control of an object.

But introduction of constraints does not mean that they are met. Often such additional constraints make the problem of choosing the necessary control unsolvable. Hence an important problem arises: finding the conditions under which predetermined constraints on sensitivity or additional motion can be ensured. Only when we have such conditions can we go on to calculate the required low-sensitivity control with firm conviction that such a control exists. Otherwise the designer will be doomed to prolonged and fruitless searches for a nonexistent control.

One of the mandatory conditions of meeting arbitrary restrictions on sensitivity is its controllability [Ref. 7-9]. Controllability of the vector function of sensitivity to some parameter means the capability of converting it in the space of sensitivity functions from any arbitrary state to the zero state (coordinate origin).

Disregard of the sensitivity controllability factor when synthesizing low-sensitivity systems may lead to an unsuccessful search for a usable solution in the structure of the control device that in principle does not permit reduction of sensitivity to the required level.

Let us consider in more detail methods of synthesizing automated control systems with regard to sensitivity requirements.

Solutions for the problem of synthesizing systems with respect to criteria of parametric invariance and zero sensitivity in Ref. 1-4 lead to very rigid and often unrealizable conditions under which zero sensitivity is attained. For example, requirements of infinite gain, ideal differentiation and others are extremely difficult to satisfy in real automatic control systems. Other solutions [Ref. 1, 6] of the given problem are more accessible of realization, but have a limited range in the space of parameters of the zero-sensitivity system. This may be an advantage for simultaneous satisfaction of requirements for sensitivity and for the quality indices of principal motion.

The Italian authors of Ref. 7-9 have used the principles of higher algebra and functional analysis as a basis for deriving general conditions of existence of subspaces with zero sensitivity and of the possibility of conversion of the vector function of sensitivity in such spaces for linear automatic control systems.

We should note the limitation of the range of application of results of Ref. 2-4 with respect to synthesizing zero-sensitivity systems, as they deal with singly connected control systems, whereas any fairly complex objects are multidimensional and multiply connected systems.

On the basis of the above discussion we can conclude that it is more realistic to formulate the problem of reducing sensitivity to some limited level meeting our requirements rather than to zero. Problems of reducing sensitivity or additional motion to a predetermined value are considered in Ref. 1, 3, 6, 10-20 (the second to fifth approaches).

The possibilities of the methods of synthesis by the second approach (Ref. 3, 10, 11) are limited since frequently from practical considerations or in accordance with conditions of physical realizability it is impossible to introduce multiple feedbacks on the least stable component of the system (the object of control is usually such a component).

In the methods of synthesis proposed in Ref. 6, 12, which apply to the third approach, it is assumed that we are given the maximum variations of system parameters, the desired sensitivity functions or the requirements for additional motion caused by maximum deviations of parameters. The requirements for additional motion or sensitivity are usually assigned in the frequency region or in the region of a complex variable; the requirements for additional motion that occurs in the system in the absence of variations of parameters are analogously assigned.

Solution of the problem of synthesis with consideration of requirements for sensitivity (additional motion) is sought in a predetermined class of system structures (applying to systems with two degrees of freedom). This solution leads to the use of two types of correcting devices with large gains and high orders of the numerator and denominator of their transfer functions. A consequence of this is considerable broadening of the passband of the system, and hence poor interference immunity. Thus high gain and a wide passband are the price that the designer must pay for the achieved reduction of sensitivity.

In Ref. 6, the method of synthesis with consideration of sensitivity requirements that is based on using redundant correcting devices is developed for the case where there are redundant parameters in the system. Usually this takes place when calculating the parameters of correcting components, the above-mentioned redundancy being used to satisfy requirements for sensitivity of the individual characteristics of the system (it is assumed here that the structure of the system and the form of the correcting elements are assigned).

Methods of synthesis belonging to the fourth approach in principle enable us to find the structure and parameters of the controlling device that ensure

a given stability. However, they require complicated and labor-consuming calculations, and lead to complex realizations of the controlling device. They are applicable (considering the capabilities of modern computers) to objects of relatively low order of complexity. Furthermore, in published papers the results are mainly theoretical, and what is very important, many of them lack the conditions of existence of the desired controls by which the given sensitivity is realized.

The approach based on introducing additional feedbacks with respect to sensitivity functions into the system has been defended in some research by Soviet and other authors [Ref. 1, 6, 14-20] (including the author of this book), and has now received recognition and the right to life. The idea of this approach [Ref. 15] consists in assigning the structure of the controlling device and subsequent selection of its parameters from the condition of satisfying requirements for principal and additional motions. The controlling device proposed in Ref. 15 for linear steady-state singly connected systems contains feedback with respect to sensitivity functions. Since then, it has been successfully demonstrated that the given approach is applicable to synthesis of low-sensitivity multiply connected automatic control systems. Conditions have been derived for the existence of a control that ensures meeting of predetermined constraints on additional motion, and on the basis of these conditions algorithms have been developed for synthesizing multiply connected automatic control systems with consideration of principal and additional motions. Although the control derived on the basis of these conditions is rather complicated, its existence was guaranteed, and this opened up the way for further simplification with a certain degree of precision in hardware realization of the given controlling device. The proposed algorithms of synthesis, including solution of nonlinear programming problems, systems of linear and nonlinear equations and inequalities, enable computer automation of all operations with respect to calculation of the necessary low-sensitivity control. Analytical solutions (with consideration of relative complexity of the calculations and the large dimensionality of the problem) were found by considering linearized systems of equations.

The introduction of constraints on the sensitivity functions does not require high gain or a wide passband for reduction of system sensitivity, therefore the given method may find application in cases where for some reason it is impossible to appreciably increase the gain or when there is a high level of interference at the input of the system or in the feedback circuit, and a certain degree of interference immunity is required.

Summing up our brief analysis, we should especially emphasize that in view of the extreme complexity of the problem of synthesizing control systems with onsideration of insensitivity, the methods of calculation now known have been developed chiefly for linear systems, and are mostly theoretical. The majority of these are still a long way from direct engineering applications.

Among the few methods that have been brought to the point of engineering techniques, we can take notice of methods based on introducing redundant correcting components and leading to systems with two degrees of freedom. One of the authors of this approach (A. M. Horowitz, Ref. 12) has developed the method

to an engineering technique. However, his proposed graphic analysis procedure requires a large number of trial versions in the search for a usable solution, and the designer has to do the work by hand (without a computer).

Therefore in this book the author has attempted to use the available literature and his own research as a basis for working out modern engineering procedures for synthesis with consideration of additional motion, based on introducing constraints on sensitivity functions and use of the principle of two degrees of freedom, to substantiate these procedures, and to apply them to singly and multiply connected automatic control systems.

The term modern will be understood to mean synthesis procedures based on analytical and numerical methods of calculation and extensive use of computers. Computer technology, which assists in automating a number of calculations and additional operations that engineers until recently had done by hand, considerably extends the capabilities of engineering methods of design, makes them more penetrating, comprehensive and therefore more reliable.

The principal results of development of the methods are presented in Ref. 15-20.

The book consists of three chapters. The first investigates the feasibility of reducing additional motion caused by variations of parameters in the class of structures that contain feedbacks with respect to sensitivity functions. The problem of synthesizing systems with consideration of principal and additional motions is formulated as applied to linear steady-state singly connected automatic control systems (systems for automatic regulation). The conditions of existence of their solution are considered. An engineering synthesis technique is presented and computational algorithms are given that are used in this problem. The feasibility of simplifying constraints with respect to the sensitivity functions are studied.

The second chapter is dedicated to presenting a method of synthesizing singly connected systems with consideration of requirements of principal and additional motions in the class of structures that contain two types of correcting components: series and parallel. This chapter describes how the required (desired) characteristics of the system are obtained, and investigates conditions of solvability of the formulated synthesis problem.

The third chapter gives a method of limited synthesis of multiply connected automatic regulation systems that retain required dynamic properties and stability reserves when component parmaters are varied (within certain limits) in the class of structures that contain feedbacks with respect to sensitivity functions. It is shown that the principle of equivalence can be used in calculating multiply connected automatic regulating systems with consideration of principal and additional motions, methods are described for obtaining sensitivity functions (constructing sensitivity models), and a synthesis procedure for linear multiply connected automatic regulating systems with consideration of principal and additional motions based on the results of the first and second chapters.

All chapters are illustrated by examples.

The author thanks Doctor of Technical Sciences R. M. Yusupov whose work and attention were conducive to the appearance of this book, and also Doctor of Technical Sciences, Professor Ye. N. Rozenvasser for useful advice and for comments made in editing.

The work was done at the Institute of Automation and Control Processes of the Far Eastern Science Center, USSR Academy of Sciences. The author will welcome readers' comments on inadequacies:

Comments and suggestions should be addressed to: Moskva, Gl. pochtamt, a/ya 693, izd-vo "Radio i svyaz'".

Conclusion

Research in the field of synthesizing low-sensitivity automatic control systems has been mainly theoretical. At the same time, developers of precision and high-quality systems need engineering techniques for designing automatic control systems with consideration of additional motion that are based on extensive use of computers. Considering the needs of practice, an attempt has been made in this book to develop modern engineering methods of synthesizing systems with consideration of principal and additional motions that are based on introducing constraints with respect to sensitivity functions and using the principle of two degrees of freedom.

An investigation was made of the problem of synthesizing (in the frequency region) linear automatic control systems that retain their required operational quality in the presence of uncontrollable variations (over certain limits) of parameters, as applied to singly connected and multiply connected automatic control systems. Two classes of structures have been used to solve this problem. In the first, additional feedbacks with respect to sensitivity functions are introduced into the initial system. The second uses two correcting links -- series and parallel. The purpose of using the latter class of structures is to simplify the structure of a system of the first class. In doing this, the frequency responses of the automatic control systems with constraints on sensitivity functions were taken as the desired characteristics for which requirements on principal and additional motions are met. The frequency response curves of control systems with a structure of the second class approach these characteristics in the process of calculation.

The suggested approach to synthesis of singly connected automatic regulating systems was then applied to multiply connected automatic regulating systems using the equivalence principle.

In chapter 1 of the book, we derived conditions of existence of a control in the automatic control system enxuring satisfaction of predetermined requirements in the system being synthesized on principal and additional motions. They enable formulation of algorithms for calculating the necessary correction for singly connected and multiply connected automatic control (regulating) systems realizable by using computers.

Conditions were also obtained whose satisfaction in automatic control systems of the second class of structures ensures the desired frequency responses

(i. e. the characteristics shown by automatic control systems with constraints on sensitivity functions for which requirements are satisfied on dynamics and on stability reserves of the system, as well as on additional motion in the frequency region). These constraints are conditions of replacement of restrictions on sensitivity functions with simpler correcting links, i. e. conditions of simplification of the constraints on sensitivity functions. On their basis, an algorithm can be formulated for calculating the necessary correcting links (series and parallel). It is noted that when the given conditions cannot be met, the constraints on sensitivity functions cannot be simplified, and the correction that accounts for the requirements on the additional motion must be retained in its original form.

It must be especially noted that the proposed methods of synthesizing automated control systems and multiply connected automatic regulating systems with consideration of principal and additional motions are analytical. This means that when calculating controls (correcting links) we can use effective algorithms and make extensive use of modern computers. This capability is a great advantage of the techniques.

The search for necessary solutions (correcting links) in the given synthesis techniques requires a comparatively small number of trial versions and calculations. In calculations of the parameters of correcting links, methods of optimization are used (nonlinear programming methods). Since the formalism of nonlinear programming has now been rather well developed, and the computational capabilities of modern computers are extensive, the given methods make the work of designers in synthesizing automatic control systems more effective.

An important advantage of the proposed methods is the possibility offered to the designer at the beginning of synthesis to answer the question: can I use the given class of structures to get the desired characteristics in the system with respect to both principal and additional motion? This considerably reduces the time of search for the necessary structure of the controlling device, and hence reduces the time for designing the automatic control system.

Despite the advantages of the given methods of synthesis, their application necessitates a fairly large volume of manual preparatory work (involving unavoidable errors) and leads to rather complicated control devices (especially in the first class of structures). Although it is difficult to avoid the first disadvantage, the second can be overcome, considering the rapid pace of development and introduction of microprocessor control devices for complex and decisive objects, as well as microprocessor LSI chips.

Realization of the proposed correction, including sensitivity models, correcting links and so on, based on the microprocessor family of LSI chips will present no particular difficulties, the moreso as at the present time the cost of such a chip is no more than 10-20 dollars [Ref. 36], and the selection of microprocessor LSI chips is constantly expanding (and at an increasing pace).

Contents page

6610
CSO: 1862/158

UDC 519.6

ADAPTIVE CONTROL

Moscow ADAPTIVNOYE UPRAVLENIYE in Russian 1981 (signed to press 5 Oct 81) pp 2-12

[Annotation, preface, introduction and table of contents from book "Adaptive Control", by Vladimir Grigor'yevich Sragovich, Izdatel'stvo "Nauka", 6400 copies, 384 pages]

[Text] The book gives a fairly complete exposition of the present state of the mathematical theory of adaptive control. Controllable random processes are taken as a model of control objects. Adaptive control algorithms are presented in a form convenient for computer realization. These algorithms are intended for a variety of jobs (optimization and stabilization) in discrete and continuous time.

The book is written for specialists in cybernetics, applied mathematics and control theory. It may be of use to undergraduate and graduate students with majors in the appropriate areas.

Preface

In problems of a number of scientific disciplines relating to decision making and data processing, more and more research is being done on situations of "uncertainty", insufficiency of a priori information. Situations of this kind have arisen in problems of control, recognition, identification, forecasting and filtration. This has prompted the search for methods of solving the corresponding problems that are insensitive to scatter of the properties of the objects of control or identification, recognition patterns and so on. Such methods have been developed and given special names: in control theory -- "adaptive methods", in identification theory -- "robust methods". This book deals with adaptive methods of control.

When there is insufficient a priori information in control theory, the problem of reaching a predetermined goal should be solved for an arbitrary object from some class or set rather than for a specific, completely defined object. In accordance with this principle, adaptive control algorithms differ from algorithms of classical control theory (where the object is completely known) in that it may not be known just what object of a class is to be controlled and guided to a target. In such cases, it is often said that the algorithm

must be "adapted" or "adjusted" to the object, and the goal is attained after "learning".

Over a period of nearly thirty years, many groups of researchers have been developing methods of adaptive control for different classes of objects. The work has been done chiefly in the applied aspect, and the results attained as a rule have been published in monographs. At present there are several dozen monographs in Russian and English. The predominant style of exposition -- "by engineers for engineers" -- should, as the authors intended, be conducive to popularization of the methods among the representatives of various technical disciplines, and thereby should promote practical application of these methods. This research (and consequently the monographs) has not always given due attention to the mathematical aspect of the problems considered. However, a considerable fraction of adaptive research certainly has appreciable mathematical significance, and in future the role of such research will be even more considerable. Therefore it is both desirable and necessary to sum up at least some of the development of mathematical aspects of adaptive control theory. This book seems to be a first attempt to do just that. Here we have summed up a considerable percentage of the exact results of adaptive control from a unified standpoint. Probably the time has not yet come for an exhaustive, encyclopedic presentation.

The material is divided into three parts. In the first -- "General Problems" -- we have formulated major concepts (controllable random process, strategy, adaptive control), pointed out a useful representation of adaptive controlling systems (in discrete time) as automata, introduced "associated Markov processes" and discussed the peculiarities of adaptive control and its difference from classical control. Chapter 3 examines the identification method of forming adaptive control algorithms.

The second part -- "Controlling Classes of Processes With Discrete Time" -- occupies the most space. In order of increasing complexity of the classes of controllable random processes, algorithms are synthesized and investigated first for the simplest processes, and then for control of classes of Markov chains and functionals on them, and finally methods of controlling classes of steady-state processes. Chapter 5 studies a specific problem -- games of automata.

The third part -- "Controlling Classes of Processes With Continuous Time" -- is comparatively brief. Chapter 11 deals with optimization problems: one relates to "optimalizing controllers", and the other refers to semi-Markov processes with incomes. Chapter 12 is devoted to problems of stability of solutions of ordinary and sotchastic differential equations.

Some of the results given in the book are new, which is indicated in each case in the "Notes" at the end of the book. As a rule, references are limited to works that are reflected in the main text.

The attempt to cover the subject as broadly as possible has entailed diversity in the sense that the book uses methods and facts from different branches of mathematics. This makes elevated demands on education of readers.

The monograph is addressed primarily to mathematicians and pursues the goal of turning their attention to a new field of research. It is the author's hope that the book will be useful to all those interested in control theory, and also to engineers working in design of automated control systems.

I was assisted in preparing the materials for the book by M. G. Konovalov and A. A. Burtsev. They have my sincere gratitude.

Introduction

The basic concepts of control theory are "control object", "control target" and "control algorithm" (strategy). Examples of objects are differential equations (ordinary and sotchastic) that incorporate controls, and controllable Markov chains with functionals that are defined on them, etc.

The controls must be selected so that a certain problems is solved that consists in the object having a certain property: that the solution of a differential equation be stable in some sense, that a functional on a Markov chain be extremum, etc. This problem is called the control target.

The problem of synthesizing controls consists in finding algorithms (strategies) that solve the problem of the required properties of the object. Sometimes for the sake of brevity it will be stated that such algorithms "bring the object to the target" or "ensure attainment of the target".

The present divisions of control theory indicate methods (algorithms) for controlling specific, completely defined objects. "Specificity" of an object denotes completeness of its description within the framework of the formal requirements of the corresponding division of control theory, and does not allow the presence of unknown parameters and functions. This premise was mandatory in the formalism of the "classical" theory, and was no impediment to diverse applications in the 1950's as long as it was not necessary to control objects whose description suffers from incompleteness. Under conditions of such "uncertainty" there may be three approaches to the control problem: a) wait to get exhaustive information on the object; b) attempt to combine control of the imprecisely defined object with acquisition of all lacking information about it; c) synthesize a theory of adaptive control. These possibilities have indeed been historically realized, the second of them being the impetus to development of the identification method of control, which consists in combining estimates of the characteristics of an object with classical methods of solving control problems. In the simplest cases where the structure of the control object is known beforehand, identification methods enable ascertainment of values of the unknown coefficients (for example in linear difference or differential equations). In addition to such problems, it is frequently necessary in practice to find not only the parameters, but also the functions that describe an object, and even to try to establish the form of the functional dependence of the output signal and state of the object on applied controlling actions. Being self-evident in principle, the identification method immediately became popular and was used in solving the first problems of adaptive control. The limits of applicability of this technique subsequently became evident (consistent estimates of the parameters of the

object do not always exist and the algorithm of solution of the problem of classical control is not necessarily known). Therefore specific "adaptive" methods of control that do not require detailed investigation of the properties of the object began to move into first place. A simple idea became clear: the control system must ensure attainment of the formulated target, and the "gathering, storage and processing of information" about the object are necessary only in minimum measure as the information is required for reaching the target. We now know many different adaptive controlling systems that do not provide information on the properties of the control object no matter how long they may operate.

A universal means of representing control objects is "controllable random processes" that may be assigned by a family of conditional probability distribution functions that depend on a "control". Uncertainty of assignment of the object consists in the fact that the family of conditional probabilities contains unknown parameters or functions. Indication of the possible ranges of these parameters or the form of the unknown functions delineates the class of families of conditional distributions, i. e. the class of controllable random processes. Operating with such classes distinguishes adaptive control theory from classical control theory. The adaptive control algorithm rests on information about the states of the process to be controlled coming through a feedback channel, and it ensures attainment of the assigned target by any object of the class, even though it remains unknown just exactly what object is an element of this class. In other words, algorithm A can be considered an adaptive control algorithm only in cases where we have a specified class K of controllable objects and a target Z such that algorithm A brings any object of K to this target.

Another difference between adaptive and classical control methods is that the adaptive methods ensure attainment of the designated target for any object of a certain class rather than for just one precisely known object. In the course of control, these methods evaluate certain parameters of the object from observations of the object. These estimates are frequently statistical, and therefore the duration of the estimation cannot be specified beforehand without loss of reliability in the result. This implies the necessity of formulating adpative control algorithms for an unrestricted time interval. Let us add that the instant when the object begins to be close to the designated target is a "non-Markov time", i. e. it is determined by the future evolution of the object, and its arrival cannot be observed. Consequently at no instant of the control process can an outside observer state that the adaptive system has already served its purpose, and its functions can be turned over to a controlling system of classical type.

The content of the overwhelming majority of results of the mathematical theory of adaptive control consists in indication of sufficient conditions of existence of adaptive control. For a class of objects K and control target Z, such conditions not only state the existence of an adaptive control algorithm, but also give its description, i. e. the sufficient conditions are constructive. Necessary conditions of existence of adaptive control are known so far only for a small number of cases.

In conclusion, let us call attention to the uneven development of adaptive control theory for objects evolving in discrete and continuous time. Despite the fact that the theory had its inception with research on objects of the second type, advances in this direction have been much more modest than in the investigation of control of objects with discrete time. This is because of the considerable difficulties that arise in the case of continuous time. So far we have been successful in relatively ambitious advancement of research on algorithms that ensure stability of solutions of linear differential equations.

At the present time, numerous problems in the control of "distributed objects" with description by partial differential equations and integrodifferential equations remain nearly untouched. Control of such objects has been dealt with for a considerable time in the nonadaptive theory.

Contents page

6610
CSO: 1862/138

END